Development of high-temperature firebrick resistance-heated energy storage (FIRES) using doped ceramic heating system

By

Daniel Christopher Stack

B.S., Mechanical Engineering (2014)
Syracuse University

S.M., Nuclear Science and Engineering (2017)
Massachusetts Institute of Technology

SUBMITTED TO THE DEPARTMENT OF NUCLEAR SCIENCE AND ENGINEERING IN PARTIAL FULFILLMENT OF THE REQUIREMENTS FOR THE DEGREE OF

DOCTOR OF PHILOSOPHY IN NUCLEAR SCIENCE AND ENGINEERING
AT THE
MASSACHUSETTS INSTITUTE OF TECHNOLOGY

February 2021

Signature of Author:_____
Daniel Christopher Stack
Department of Nuclear Science and Engineering
January 22, 2021

Certified by:_____
Charles W. Forsberg
Principal Research Scientist, Department of Nuclear Science and Engineering
Thesis Supervisor

Certified by:_____
Michael P. Short
Associate Professor, Department of Nuclear Science and Engineering
Thesis Co-supervisor

Accepted by:_____
Ju Li
Battelle Energy Alliance Professor of Nuclear Science and Engineering
And Professor of Materials Science and Engineering
Chairman, Department Committee on Graduate Students

This page left intentionally blank.

Development of high-temperature firebrick resistance-heated energy storage (FIRES) using doped ceramic heating system

By

Daniel C. Stack

Submitted to the Department of Nuclear Science and Engineering on January 22, 2021 in partial fulfillment of the requirements for the degree of Doctor of Philosophy in Nuclear Science and Engineering

Abstract

Towards combating climate change, the widespread replacement of fossil fuel energy with zero-carbon energy has two main requirements: (1) the ability to reach very high temperatures using zero-carbon energy to perform a variety of continuous industrial processes, such as iron smelting and cement clinker production; (2) the ability to match electricity supply with demand. Firebrick resistance-heated energy storage (FIRES) is a previously proposed technology capable of meeting both requirements by storing zero-carbon electricity as high-temperature heat, and delivering it to industrial plants or power plants as needed in place of fossil fuels. The capability limits of FIRES is set by existing electrical heater options, which limit the temperatures and heat rates of the system.

The work herein describes the development of a novel high-temperature FIRES system using cation-doped ceramic firebricks as the basis of the electrical heating system. The firebricks are directly resistance heated (DRH), enabling peak temperatures equal to that of flame temperatures, and allowing FIRES to electrify and decarbonize the hottest industrial processes and power the highest efficiency turbines.

The fundamentals of semiconductor joule heater design were reviewed, and the material option space was evaluated. Chromia doped with nickel was identified as a promising material candidate for a DRH-style FIRES system. Commercial and doped lab-fabricated chromia samples were prepared. Electrical resistivity was measured as a function of temperature, and brick-brick contact resistivity was measured as a function of temperature and contact load, up to 1500ºC, to determine viability of electrically heating a freely stacked brick mass. A proof of concept of DRH was successfully demonstrated by electrically heating a small stack of doped samples.

Calculations and simulations of brick-brick contact temperature rise, short circuit failure conditions, and thermal runaway were developed and undertaken using the experimentally measured electrical properties and the expected operating conditions of a FIRES system as inputs. Results informed the development of an electrically conductive brickwork design, including the brick dimensions and patterns of interlaid insulative and conductive firebrick to form an electrical circuit resistant to thermal runaway. The bricks and brickwork were designed with the intention of being compatible with hot blast stoves (heat regenerators) commonplace in the steel industry to provide a pathway for commercial development using existing industrial experience. Specific modifications necessary for coupling FIRES with blast furnaces, cement kilns, and gas turbines were explored.

Thesis Supervisor: Charles W. Forsberg
Title: Principal Research Scientist, Department of Nuclear Science and Engineering

Thesis Co-supervisor: Michael P. Short
Title: Associate Professor, Department of Nuclear Science and Engineering

Acknowledgements

I would like to thank Exelon Corporation for their sponsorship of this work and their commitment to developing sustainable energy solutions. A special thanks to Dr. Ugi Otgonbaatar of Exelon for our discussions of the research and the possibilities of the FIRES technology.

I would like to thank Don Abrino and HarbisonWalker International for engaging in discussions about the firebrick option space, and for providing many firebrick samples as a valuable commercial reference. Also, a special thanks to Dr. Zachary Hood, formerly of the Electrochemical Materials Lab at MIT, for a great deal of help with the doped sample fabrication process.

I would like to thank my co-advisor, Prof. Mike Short, for offering a wealth of insights, support, and enthusiasm throughout this project, especially through the highs and lows of the experimental portion.

I owe a great debt of gratitude to my advisor, Dr. Charles Forsberg, for his inspirational thinking, guidance, patience, and unwavering support over many years of research. Six years ago, I did not join the nuclear science and engineering department expecting to work on thermal energy storage; in hindsight, I cannot imagine a more fulfilling path. It has been an honor to be your student, to explore such a promising concept, and to work towards this “small” energy revolution.

Finally, thank you to all of my colleagues and friends who have entertained far too many hours of talk over the years on the topic of heating up bricks, and to my family, for their unconditional love and support that has sustained me through these years.

This page left intentionally blank.

Table of Contents

List of Figures

List of Tables

1 Introduction

To mitigate the threat of climate change and transition to a more sustainable way of life, it has been acknowledged by the broader scientific community and the majority of national governments [1] that greenhouse gas emissions must be dramatically reduced. The bulk of the emissions takes the form of carbon dioxide produced by fossil fuel power plants and industrial heat processes. Decarbonization of these energy sectors poses many technological challenges, most of which may be considered in two categories: (1) the ability to reach very high temperatures using zero-carbon energy to perform a variety of continuous industrial processes, such as iron smelting and cement clinker production; (2) the need to match electricity supply with demand using variable generators (VG), particularly intermittent wind and solar electricity production. The present technology options for accomplishing these tasks are very few, and are typically either prohibitively expensive, technologically immature, unproven at scale, or limited in their application by geography. This technology shortfall necessitates the focus of researchers to address the many issues of implementing technology options beyond the laboratory, into the energy sector.

One class of technology that shows great promise for addressing both challenges above, and the focus of this work, is known as electrically-heated thermal energy storage (E-TES). The function of E-TES is to capture surplus electrical energy, typically from VG or non-load following nuclear plants, and store the energy as heat. This heat can then be delivered to (1) an industrial plant that needs process heat, or (2) a power plant that can regenerate electricity at times of high demand, acting as a battery that can manage the supply-demand mismatch. In both cases, the stored heat of E-TES replaces the combustion of fossil fuels with the energy of zero-carbon sources, opening a pathway to transition away from fossil fuels.

Firebrick resistance-heated energy storage (called "FIRES") is an E-TES system based on commonplace industrial materials that was conceived to replace fossil fuels with zero-carbon energy in even the hottest power cycles and industrial plants. Previous work [2] has established the relative robustness of ceramic brickworks to store 100s-1000s of MWh and achieve cycle times of either a few hours or days depending on the market demand, with comfortable storage times of a week. System cost estimates came to approximately $10/kWh, far below long-term battery projections near $150/kWh [3, 4], using commercially available firebricks and metallic heaters that typically operate near 1000ºC.

While 1000ºC is acceptable for many industrial processes, the production of steel, glass and cement require temperatures of 1500ºC or more, with flame temperatures near 2000ºC [5], hotter than any commercially available heaters [6-8]. Moreover, operating near the peak temperatures of commercial heater options causes them to burn out relatively quickly in an air environment, requiring frequent and potentially costly replacements, thereby limiting their practicality. Heaters are designed to deliver heat to surroundings, typically in relatively rapid fashion, and relatively frequent replacement; this is contrary to the application of thermal energy storage, which desires the gradual deposition of heat into a thermal mass over the course of hours, does not benefit from a rapid heat-up, and is hindered economically if heaters must be frequently replaced.

The goal of this doctoral work is to develop a new type of FIRES system, which operates without the limitations of traditional heaters and instead employs a new approach: electrically conductive firebricks. Such bricks would serve as both the charge medium and heat storage medium of FIRES, and holds promise for very long life, high temperatures, and reliable charging capabilities. A hypothesis was developed that a mass of electrically conductive bricks, composed of a cation-doped oxide material, may be stacked to form a large thermally insulated electrical circuit in the form of a brickwork. The brickwork may pass an electrical current through freely stacked bricks to volumetrically resistance-heat the mass near 2000ºC, with long-term thermo-mechanical stability and controllable electrical charging.

The work herein follows along the steps taken towards developing a FIRES system that uses electrically conductive firebrick. It embodies a holistic effort to bring this technology closer to commercialization, which includes testing of commercial firebricks, design, fabrication, and testing of custom ceramics to match requirements, proof of concept experiments, system charging simulations, and conceptual design and discussion.

To begin, the motivation of this work is presented (Section 2), by clarifying why E-TES is a class of devices that can make great strides towards decarbonizing the energy sectors, and why further innovation is required. A discussion of current and future energy needs is presented, both in terms of the challenges of achieving an electricity grid with high VG penetration and the inadequacies of current technology options to deliver zero-carbon high-temperature heat to industrial processes. The existing E-TES options are discussed in more detail, the need for hotter E-TES is established, and the FIRES system is described. Following this, the relevant technical background is presented (Section 3). The fundamental physics and engineering of ceramic joule-heater design is reviewed, and

properties desirable for a FIRES storage medium are discussed. An evaluation of materials options is provided (Section 4), culminating in selection of doped chromia for further investigation.

The experimental portion of the work is presented next. Experimental methods (Section 5) for sample preparation and electrical property measurements are detailed for some existing commercially available firebricks and lab-fabricated doped ceramics. Results are reported (Section 6) and discussed in terms of performance characteristics. The section concludes with results of a joule-heating experiment of a small stack of ceramic bricks, serving as a proof of concept for the direct resistance-heating of freely stacked firebricks for energy storage applications.

Next the modeling and simulation portion of this work is presented, which uses the experimental results to examine key aspects of spatial heat generation and heat transfer during charge cycles. Modeling and simulations focus on three specific concerns: the excessive heating of brick-brick electrical contacts in a large stack (Section 7), the length scale of short circuit failures for the candidate chromia material (Section 8), and the timescale of thermal runaway (Section 9).

Fourth, the preliminary design and dimensioning of FIRES is detailed, informed by the simulations and by state-of-the-art of industrial systems and practices. The bricks, brickwork regions, and electrically conductive flow path are designed to ensure resistance to thermal runaway while maintaining an overall geometry compatible with existing industrial hot blast stove technology (Section 10). Further design considerations regarding retrofits and modifications to target application, specifically, cement, steel, and Brayton power cycles, are discussed in Section 11.

The work concludes (Section 12) with a summary of findings and the next steps in commercializing the FIRES technology, different applications the technology may see use in that were not already discussed, and high level discussion of the role regulation may play in the adoption of E-TES systems.

2 Background

2.1 Electricity sector challenges

In the absence of affordable electricity storage, the addition of large volumes of renewable energy to electricity grids has created an unprecedented volatility in electricity supplies, which has caused balancing challenges to the system. Figure 1a shows the change in net electricity load in California from 2012 to 2020. The addition of more solar energy over the years has caused the net load to dip dramatically in the middle of the day. Net load is the load after subtracting wind and solar, which have near-zero operating costs. This drop in net load corresponds to a drop in the wholesale market price near zero (Figure 1b), reflecting the low value of the electricity at these times. The low sale price hurts the economics of solar generators as well as any other generators operating at the time, such as wind, nuclear or hydro plants. There is little revenue to pay for the capital and maintenance costs. This dip also creates an overgeneration risk where the combined generation of solar power and "must run" thermal and hydro plants produces more than what is demanded. To prevent overgeneration, solar generation must be curtailed, further hindering its ability to reach high penetration.

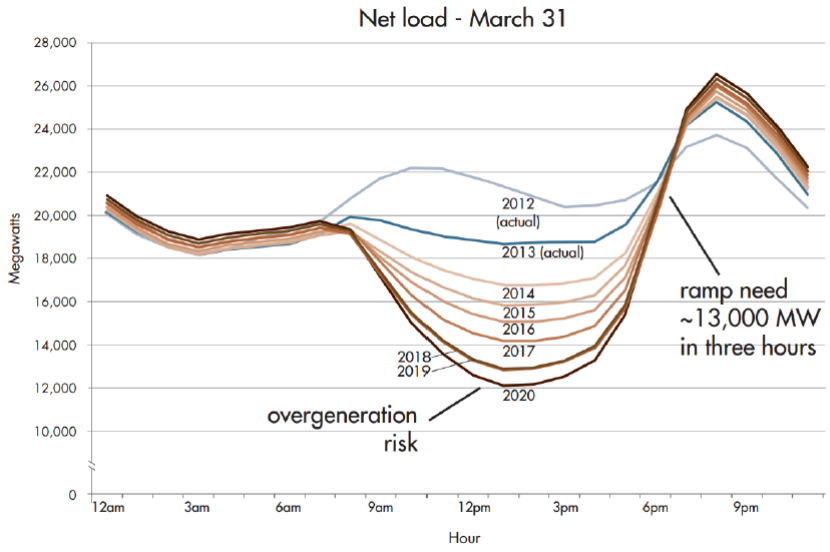

Figure 1. The CAISO duck chart

a)

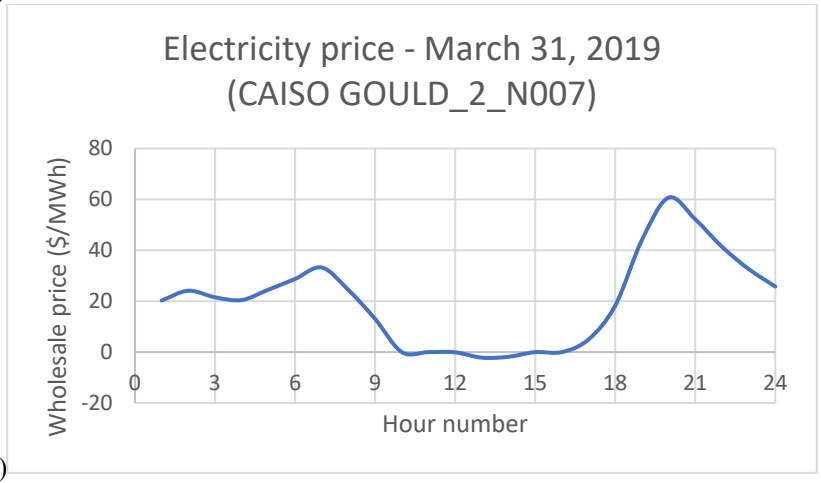

b)

Figure 1: Effect of solar energy on California electrical load and wholesale electricity prices during a spring day.
a): Projected electrical load in subsequent years with more solar energy penetration (the "duck curve") [9]. b): Wholesale electricity price data at a southern California node, March 31, 2019. As more solar energy is installed, risk of overgeneration at the peak of sunny days increases, and electricity value decreases.

a)

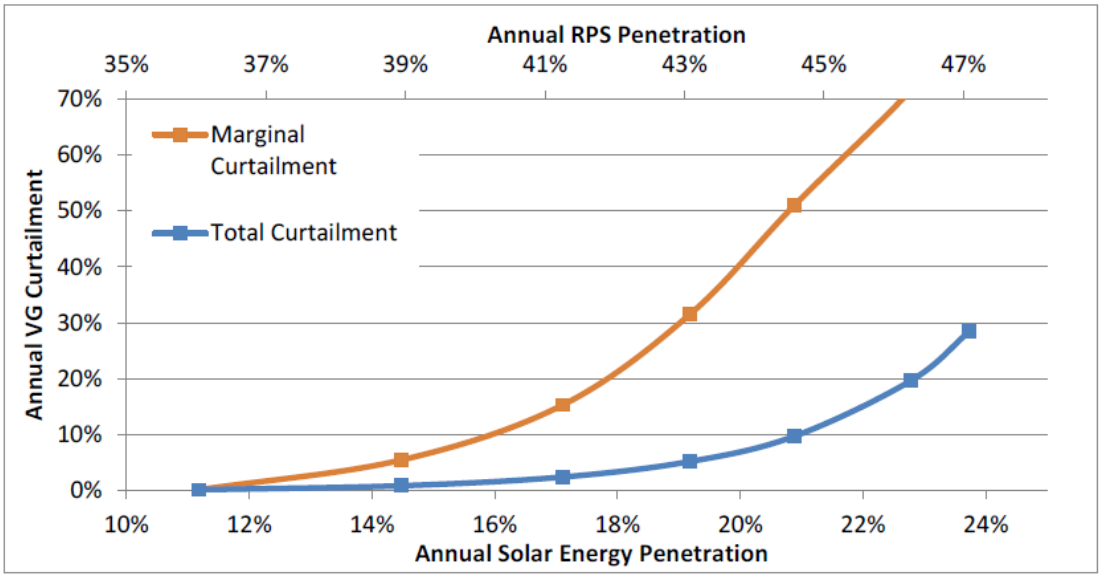

b)

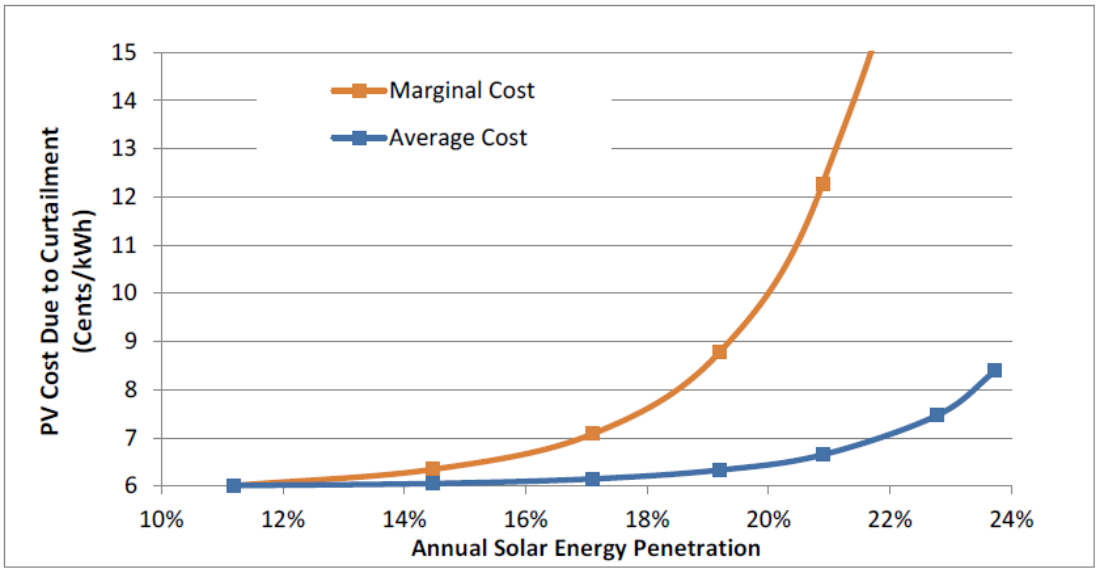

Figure 2: solar curtailment and levelized cost of energy (LCOE) as a function of greater solar energy penetration. a): Annual curtailment. b): Solar LCOE. [9]

As regions such as California drive towards greater renewable penetration in the grid, unfavorable sales prices and curtailment become rapidly unsustainable. Figure 2 shows the effects of greater solar energy penetration on the amount of energy curtailed from solar generators (Figure 2a) and the associated rise in levelized cost of energy (LCOE) due to less lifetime generation (Figure 2b). Curtailment levels and cost rise rapidly past 20% solar penetration. In the case where typical "must run" plant capacity is cut in half, and solar power is allowed to make up 80% of power demand, curtailment and cost instead rise rapidly past 28% solar penetration. Figure 3 shows the reductions of wholesale price of electricity in a simulated grid scenario as the solar power penetration is increased. The average sale price of solar energy drops by half near 30% power penetration.

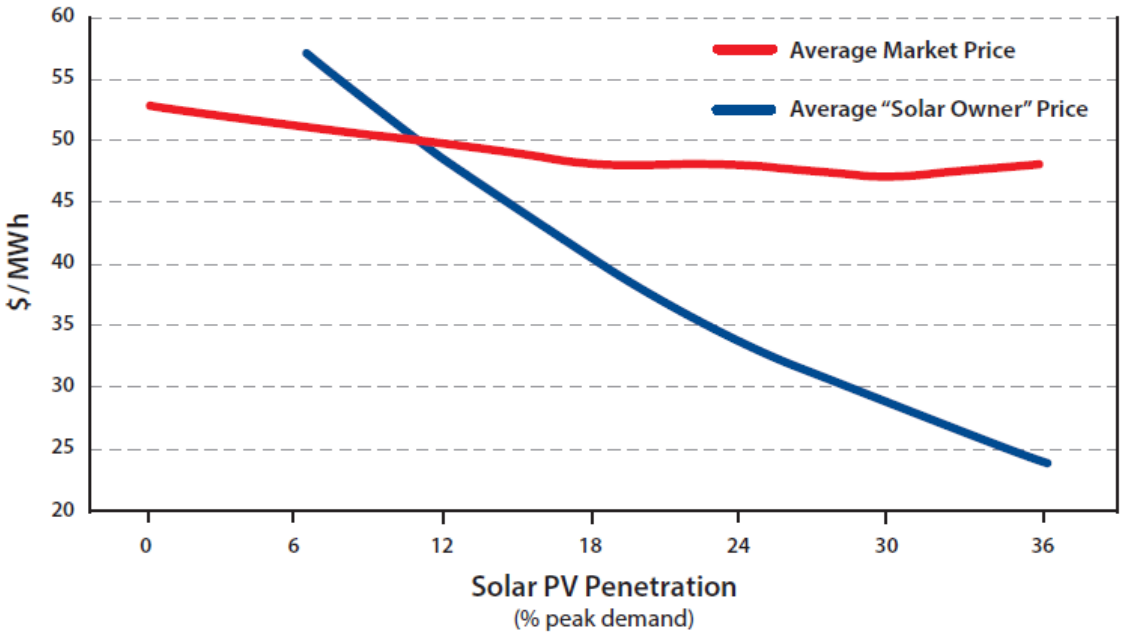

Figure 3: Average market price of energy as a function of solar power penetration. [10]

To achieve electricity grids with a large share of VG, challenges of supply and demand mismatch must be met with energy storage. Denholm and Margolis found that California would require an additional 15-25 GW of storage capacity to economically reach solar PV penetration of 50%, matching or exceeding the installed storage capacity nationwide [11]. This storage would be required to enable an LCOE of $70/MWh$_e$ for solar PV, somewhat more costly than the average wholesale price of California $40-$50/MWh$_e$ [12]. But the study does not consider the cost of the storage itself, which if expensive may be just as cost prohibitive as heavily curtailed VG. Current capital costs for Li-ion batteries, the most deployable option, are typically between $250-$500/kWh, and are likely to stay above $150/kWh in the future [3, 4]. Recent work by Schmidt et al. [13] predicts that Li-ion batteries or vanadium redox-flow batteries will be the cheapest storage option for energy arbitrage with long-term projected levelized costs of storage (LCOS) of $150/MWh$_e$. Storage at this cost would effectively triple the cost of stored solar energy, and even more dramatically increase the total LCOE of a high-penetration solar PV grid. The current state and projections portend an expensive electricity grid if new storage solutions are not pursued.

2.2 Industrial heating sector challenges

Although given less attention, the heating sectors pose a comparable threat to the climate as the electricity sector, with a larger energy burden. The different energy sources and sinks of the US is shown in Figure 4. Non-electricity fuel consumption in the residential, commercial, and industrial sectors account for 28% of the CO_2 emissions in the US, compared to 38% for electricity generation [14]. However, the CO_2 from electricity is only associated with approximately 13 quads (quadrillion Btu) of delivered electricity, while the heating sectors are associated with approximately 27 quads of delivered heat [15], roughly double. This discrepancy arises because making electricity from traditional power plants requires 2 or 3 units of fossil fuel heat per unit of electricity, depending on plant efficiency. Because wind and solar generators produce electricity directly and are replacing traditional power plants, 1 quad of VG capacity will remove 2-to-3 quads of fuel emissions.

The 27 quads of the heating sector will not generally have this feature when replacing fossil fuels with zero-carbon energy, except where heat pumps may be used. Heat pumps only operate at lower temperatures, based on the capabilities of existing refrigerants. The largest share of this energy is in the industrial sector, which requires approximately 18 quads[1] of heat at elevated temperatures, far above typical maximum heat pump temperatures of 75ºC [17].

[1] A portion of the 23 quads of industrial fuel consumption are used as feedstock rather than heat. Feedstock was estimated as 5 quads, based on estimations of the Energy Information Administration [16].

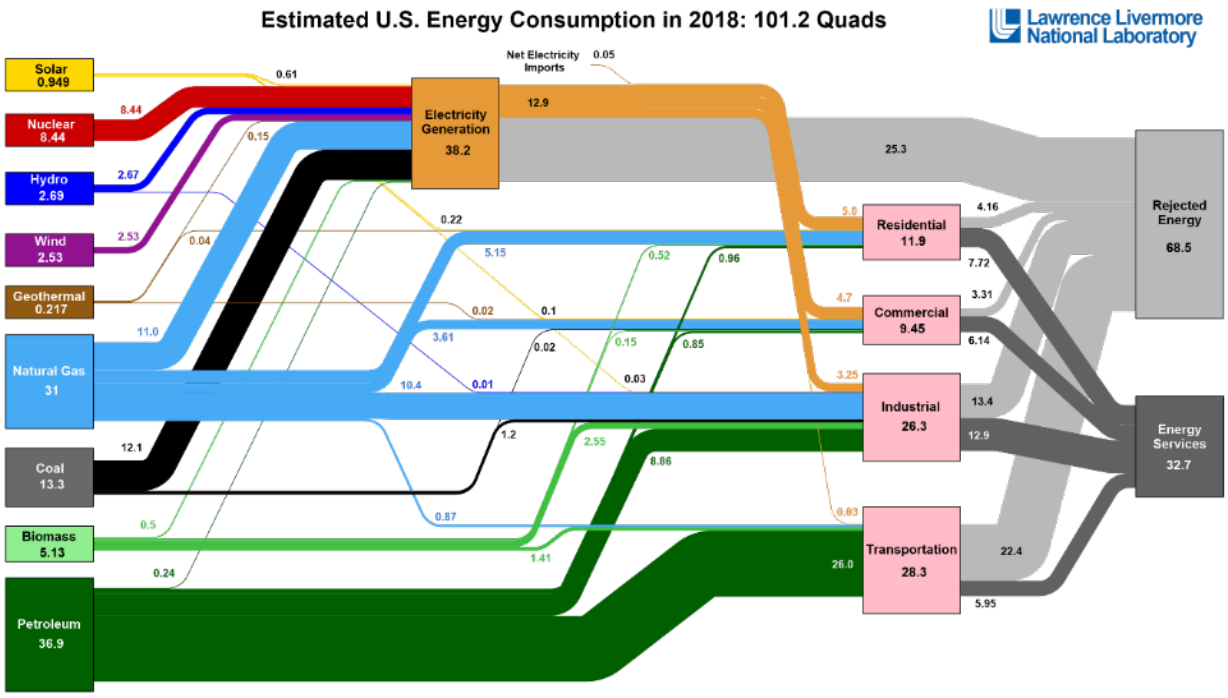

Figure 4: energy flow diagram of United States, 2018. [15]

Figure 5 shows global energy projections to 2050. World energy usage is expected to increase from approximately 600 quads today to 900 quads in 2050, with the industrial sector making up one third of energy consumption or more throughout. Energy-intensive manufacturing is expected to rise substantially as large populations of the world continue substantial development.

a)

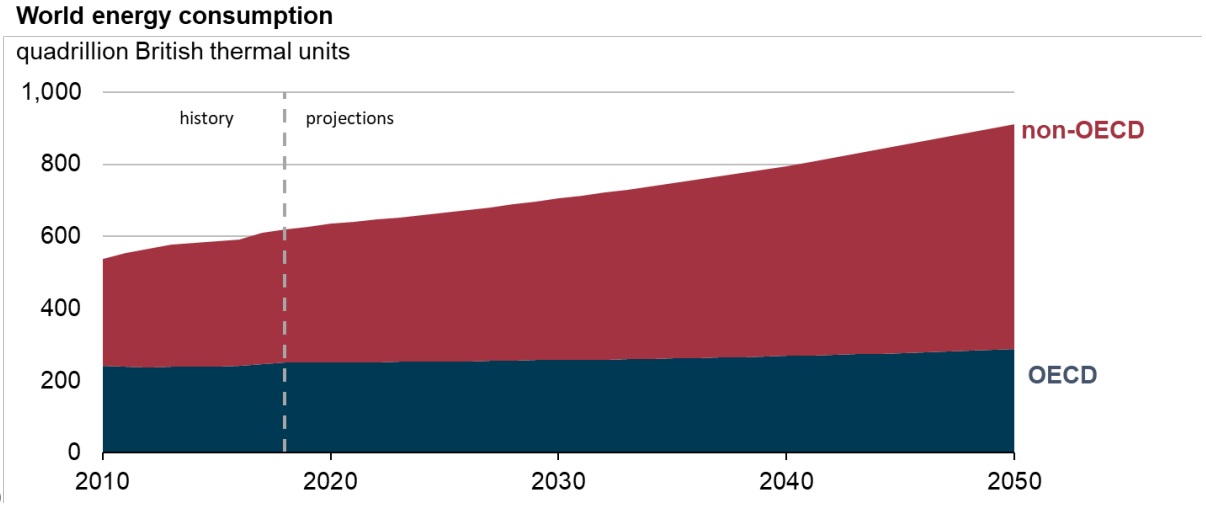

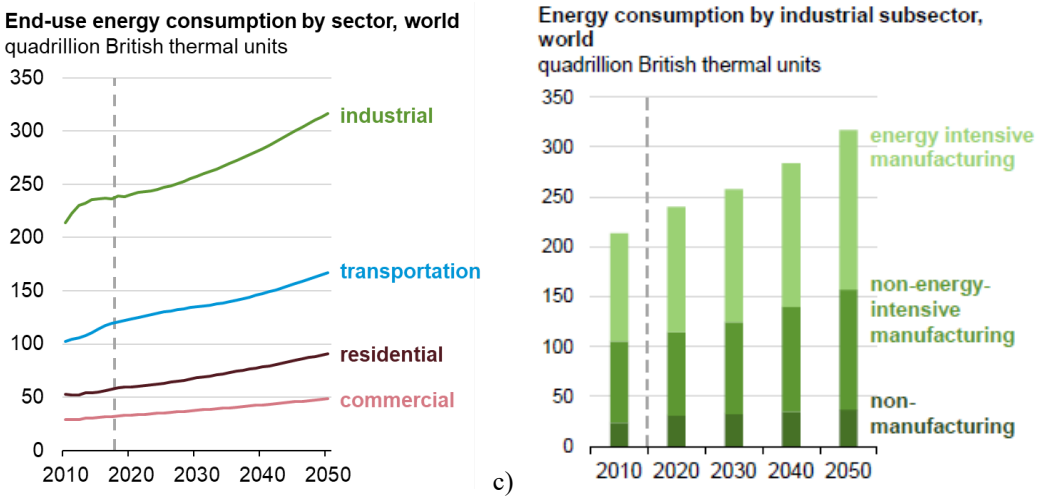

Figure 5: global energy projections to 2050.
a): Total energy consumption. b): End-use breakdown by energy sector. c): Breakdown of industrial subsectors. [18]

Three of the largest energy consumers and CO_2 producers of the industrial sector are chemical processing, steel, and cement production, accounting for 4%, 7%, and 7% of global energy system emissions, respectively [19]. Chemical production primarily uses steam at temperatures of a few hundred Celsius, while cement, glass, and steel manufacturing require temperature between 1000°C and 1800°C. [5, 20].

The options to decarbonize the heat inputs of these processes are limited to only a few existing or proposed technologies. Friedmann et al. recently published a study of low-carbon heating options for industry in terms of cost, temperatures, carbon footprint, and technical feasibility. Figure 6 shows the temperature capabilities of potential zero-carbon heat sources, as well as operating temperatures of the industrial processes of interest. Traditional or advanced nuclear reactors have some potential for use in chemical and paper process heat. For cement, glass and steel, nuclear heat can be used for preheating but the options for higher temperature heat are limited to electricity, hydrogen, or biomass.

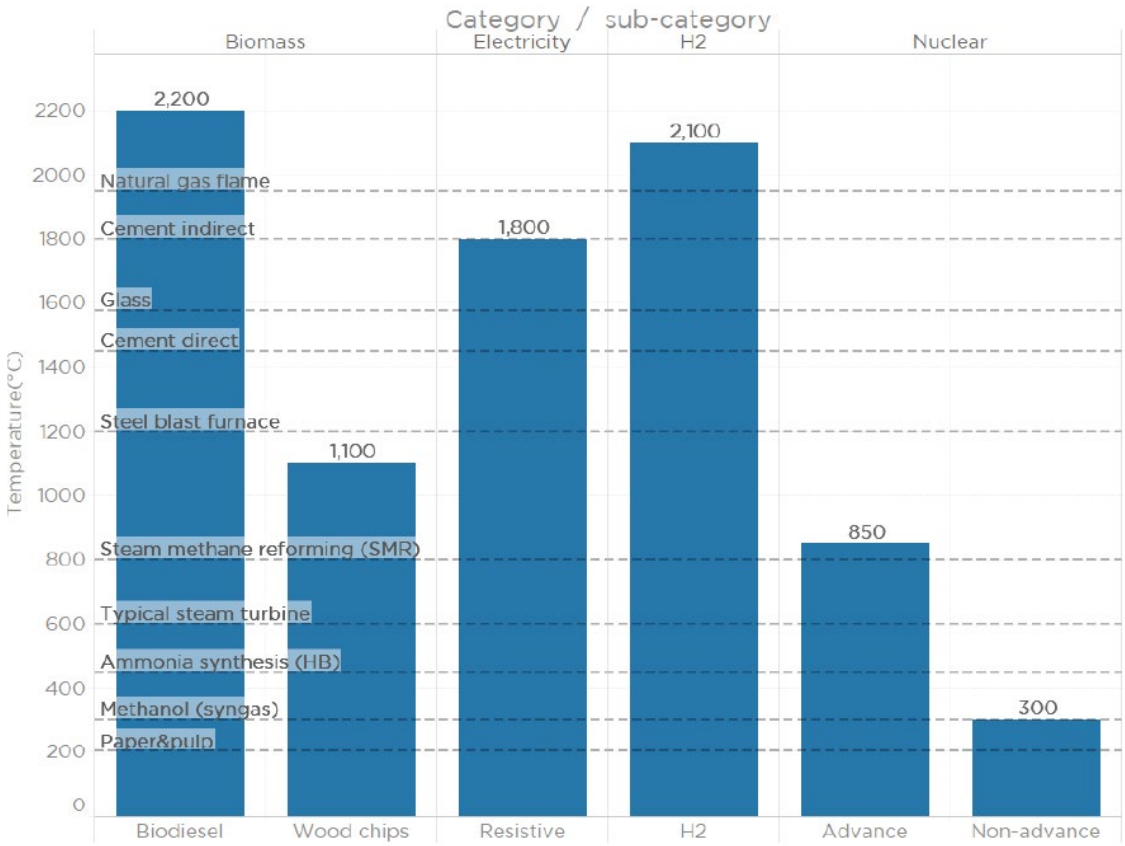

Figure 6: Temperature capabilities of potential zero-carbon heat sources compared to application requirements. [5]

Each of these options have costs and carbon intensity dependent on their generation process. Figure 7 shows estimates of cost and carbon footprint. With the exception of nuclear reactors, the cost of most other heating options is expected to far exceed fossil fuel costs. Hydrogen via steam methane reforming (SMR) with 89% carbon capture is considered the least expensive "low carbon" heating option that can run the hottest applications, and is approximately $16/MMBtu fuel (twice or three times that of typical fossil fuel costs in the US). It is dependent on natural gas extraction and carbon capture infrastructure that may be geography dependent, and still has some emissions. Although renewably generated hydrogen via electrolysis has a low carbon footprint, each option is expected to cost a factor of five or ten more than typical fossil fuels. An inherent disadvantage of hydrogen generation via electrolysis is the efficiency loss of the process; the eventual heat from combustion will be only 67-84% of the electricity input for most systems, even with further developments of low and high-temperature electrolyzers through the year 2030 [17]. Many carbon footprint analyses of biomass options remain controversial, and biomass options vary widely in price range. "biodiesel 100" is approximately four to eight times as expensive as fossil fuels.

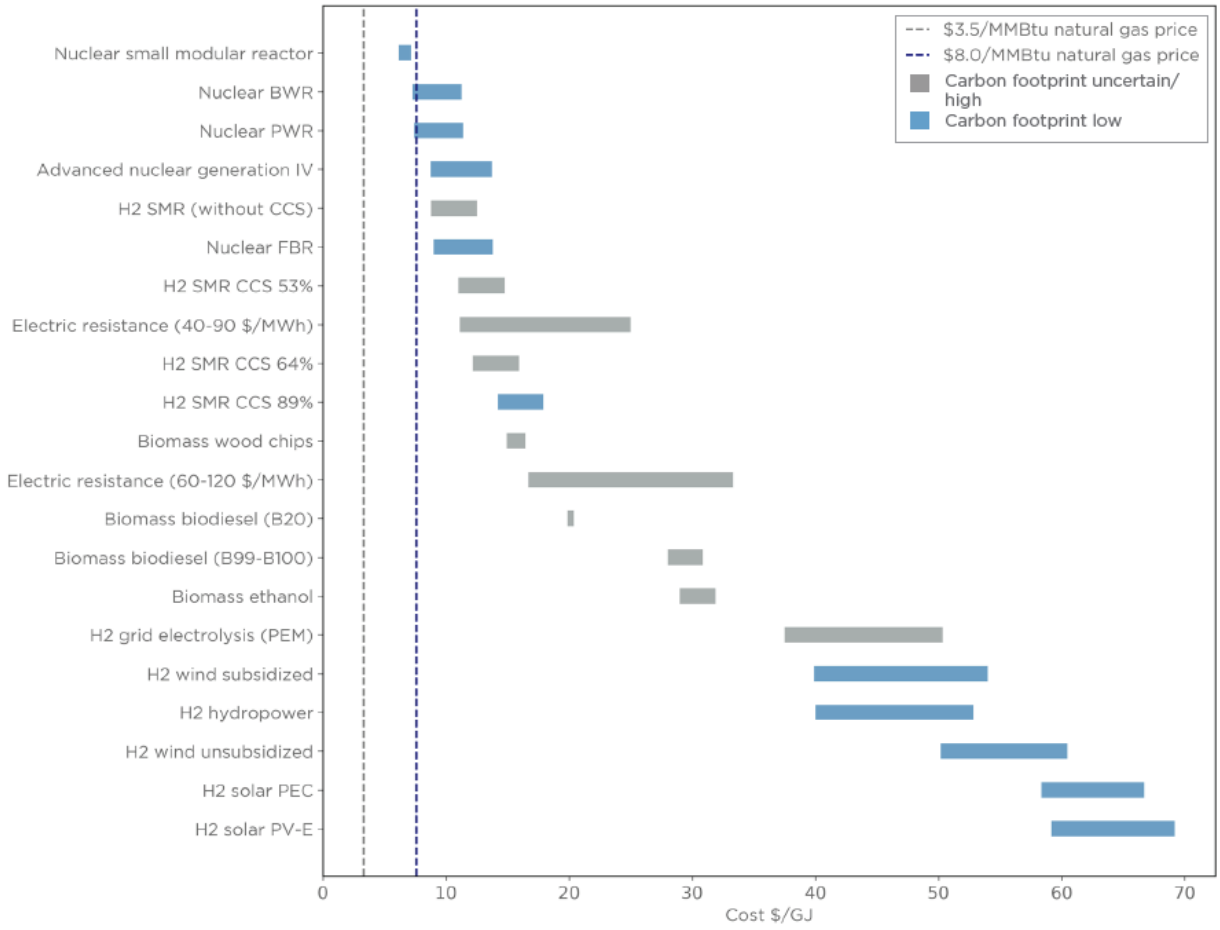

Figure 7: Cost comparison of different heating options. [5]

Although shown with a large cost range and uncertain carbon intensity, electric resistance heating is potentially the lowest cost heating option capable of running the hottest applications. If operated in high renewable penetration grids at times when the vast majority of electricity is generated by zero-carbon sources (e.g., the peak of sunny days in California), electricity may be the most competitive zero-carbon heat source. One inherent advantage over fuel production is the 100% efficiency of joule heating. The electrical heat may be stored for later use in a thermal mass with low heat leakage.

However, implementation of electricity as a heat source is more complicated than other options. While hydrogen and biodiesel still generate and transfer heat via combustion, electric heat generation and transfer requires the integration of heating elements and an electrical infrastructure that may not fit conveniently into existing processes. For lower temperatures driven by heat exchangers and steam generators, the implementation of heaters may be simpler than in the case of high temperature systems that rely on radiative heat transfer of flames. These challenges are reflected in the qualitative feasibility chart in Figure 8, also from the work of Friedmann et al. [5].

The combinations of either high cost or low feasibility of different low-carbon heating options makes clear the need for more work on developing technologies that enable decarbonization of the industrial heating sector.

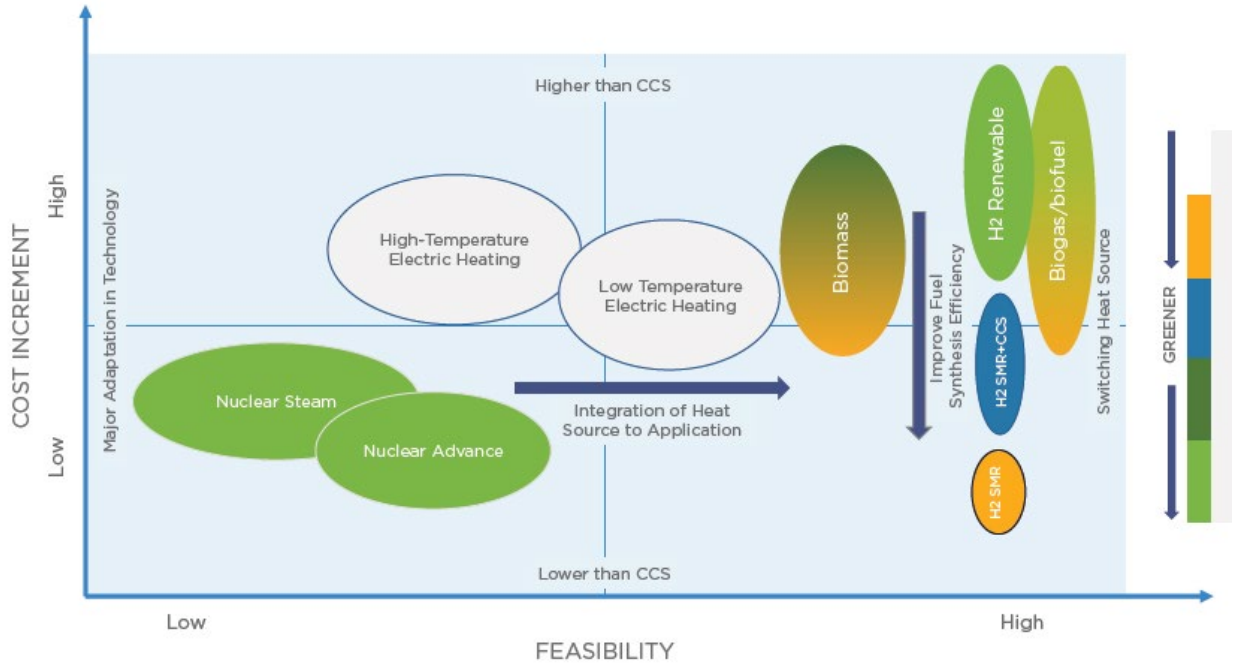

Figure 8: Qualitative feasibility chart for different industrial heating options. [5]

2.3 Description of firebrick resistance-heated energy storage (FIRES)

Firebrick resistance-heated energy storage (FIRES) [2, 21, 22] is an electrically heated thermal energy storage (E-TES) concept designed to couple with high-temperature industrial plants or power plants. The system consists of a large mass of heat-resistant ceramic bricks known as firebricks, an electrical heating system capable of heating up the firebricks, a blower system capable of removing heat from the bricks via convective heat transfer, and a steel vessel lined with ceramic insulation capable of housing the hot bricks. The system is "charged" by heating the firebricks using electricity. The system is "discharged" by blowing air through the hot bricks, which are laid as a brickwork that forms chimney-style air channels. Figure 9 shows a simple schematic of how FIRES is operated to deliver heat to applications that traditionally use fossil fuels.

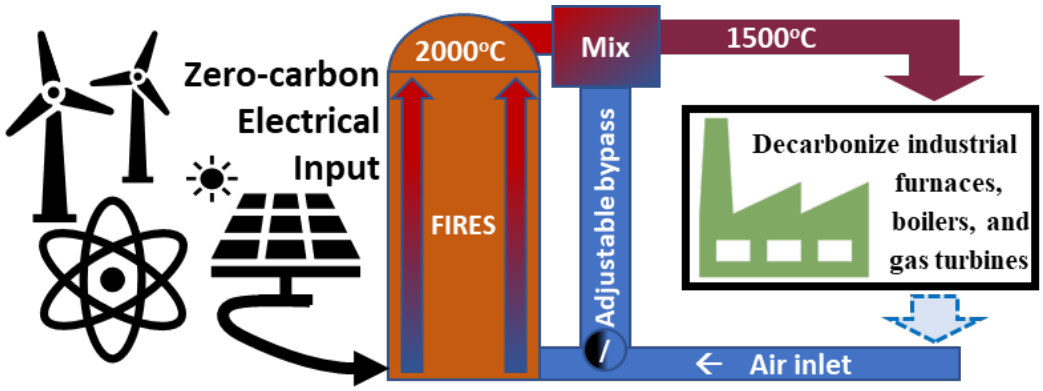

Figure 9: Schematic of FIRES coupled with generic industrial heating application.

The brickwork, insulation, steel vessel, and plumbing of FIRES is modeled after existing high-temperature firebrick regenerators that are commonplace in industrial glassmaking and steelmaking [2], which are used to capture and store the heat of hot flue gases to reduce fuel consumption. Figure 10 below shows the regenerative "hot blast" or "Cowper" stoves used in blast furnaces for steelmaking, and several common brick geometries that make up their

chimney-style brickworks. Hot blast stoves operate with peak temperatures of 1600ºC, heat rates up to 300 MW [23], hourly cycling, and near-continuous operation [24], with a 20-30 year lifetime [25].

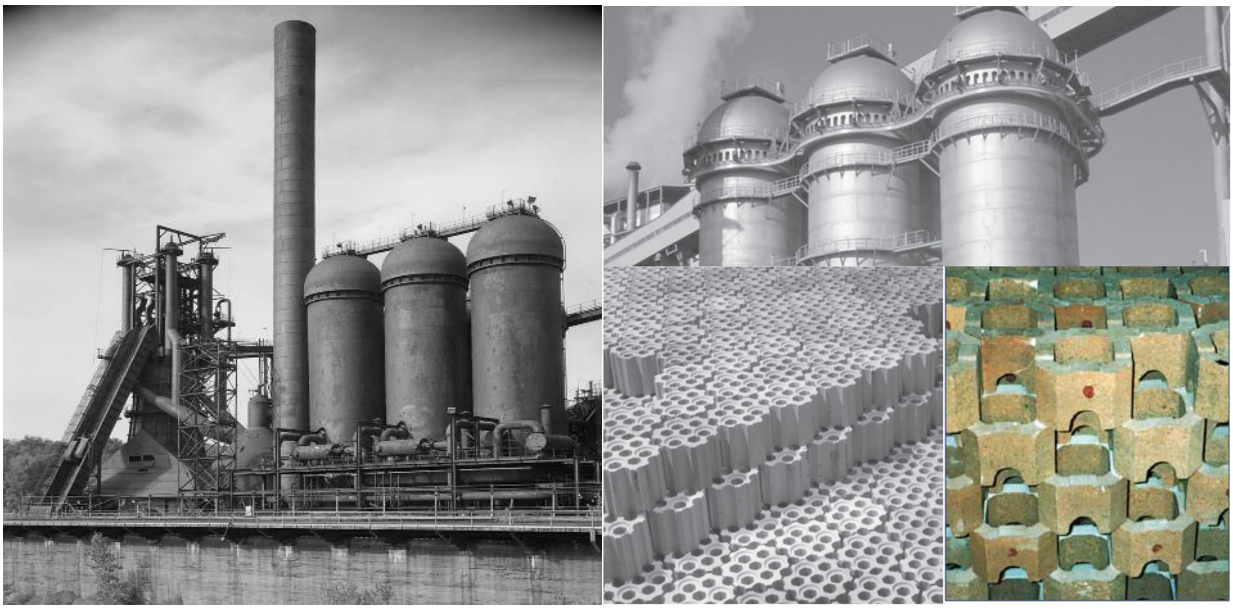

Figure 10: Existing basis of FIRES system. [23, 26]

In industrial applications, hot exhaust gas from steel and glass furnaces is routed through the regenerators, heating the brick and cooling the furnace gas before it is exhausted to the atmosphere. After the firebrick is heated, ambient air is sent through the firebrick and heated. After heating, fuel is added to raise the gas temperatures to those required by the industrial process. This results in large energy savings. The firebrick goes through multiple cycles per day. In many industrial processes the hot gas is corrosive and contains particulates. Firebrick is used because it is the only material able to withstand the high temperatures. There is more than a century of large-scale industrial experience with these systems.

The main difference between FIRES and hot blast stoves, and the key point of necessary innovation, is the inclusion of an electrical heating system for charging. Brickworks integrated with electric heating systems have been deployed at residential and commercial scales for the purposes of space and water heating, in E-TES systems known as firebrick storage heaters. Units as large as 10 MWh for commercial complexes have been deployed in China as part of national “coal to electricity” anti-pollution policies [27]. Figure 11 shows residential and commercial firebrick storage heaters. At the industrial scale, Siemens Gamesa has recently launched a pilot plant of an E-TES technology that couples an electric heating system with a crushed rock storage medium [28]. The system charges by blowing air through a heater chamber and then through the crushed rock to heat it. The system discharges by again blowing air through the rock. The heated air is used to run a steam turbine to produce electricity. The full scale system is intended for gigawatt-hours of storage for steam power plants.

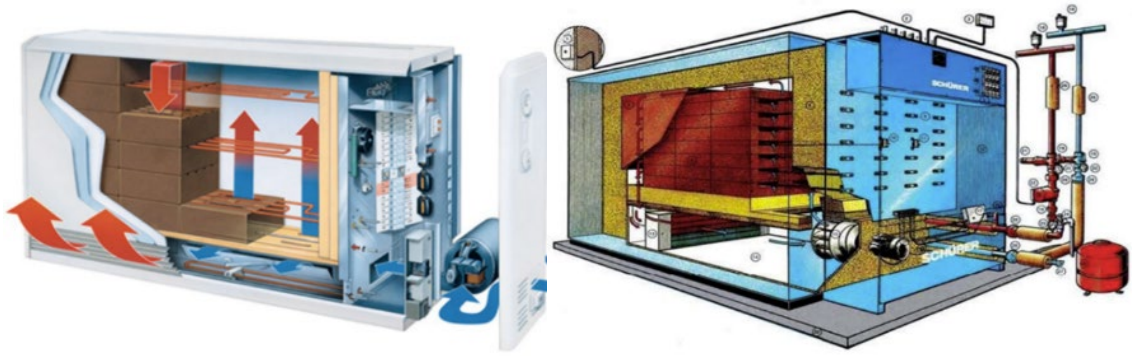

Figure 11: Residential scale (left) and commercial scale (right) firebrick storage systems available today. [29, 30]

The limiting feature of these E-TES systems is the type of electric heating elements they use to heat the firebrick or other storage media. Each is based on metallic heating elements. The key properties of existing metallic and ceramic heater options are shown in Table 1. Metallic heaters have maximum operating temperatures of 1300-1400ºC, but they are regularly operated several hundred degrees colder to maintain a longer heater life; the oxidation of the metals increases exponentially with temperature [6]. In practice, each of the metallic-based E-TES systems store at peak temperatures of 750-850ºC. Although effective for many industrial processes that use steam, these temperatures are too low for cement, glass, and steel production. For electricity production, E-TES systems coupled with steam turbines are limited to a maximum of 45% roundtrip efficiency, more typically 35-40%, which represents a relatively large waste of the electricity inputted compared to the efficiencies of natural gas combined cycle (NGCC) plants, near 60% efficient with peak temperatures of 1600ºC [31]. A FIRES unit capable of powering steel, cement, and glass plants, as well as NGCC plants, must possess a heating system that outperforms metallic heaters.

Another large benefit to higher temperature storage is greater energy density and smaller system size. Heat storage materials such as firebrick can go to very high temperatures, far above metallic heater limits, meaning a great deal more sensible heat may be stored. If one doubles the temperature swing from hot to cold, the quantity of firebrick, weight, and size of the storage system may be reduced by approximately half. This creates economic incentives to increase storage temperatures for even low-temperature applications.

Table 1: Typical heater operating capabilities [2]

Key Performance Aspects of Candidate Resistance Heaters			
Heater Type	Peak Operating Temperature	Max Recommended Surface Load	
		@ Typical Temp	@ High Temp
-	ºC	kW/m^2	kW/m^2
Nichrome (Ni-Cr) [6]	1250	35-100 (800ºC)	10-25 (1100ºC)
Kanthal (Fe-Cr-Al) [6]	1425	50-120 (800ºC)	20-35 (1300ºC)
Silicon Carbide (SiC) [7]	1650	100-150 (1200ºC)	25-30 (1600ºC)
Molybdenum Disilicide ($MoSi_2$) [8]	1850	200-220 (1500ºC)	80-120 (1750ºC)

The ceramic heater options, silicon carbide (SiC) and molybdenum disilicide ($MoSi_2$), exceed metallic heaters in peak temperatures and heat flux capabilities, and generally have longer life. This is because of their higher temperature stability and slower oxidation kinetics. However, ceramic heaters have several limitations of their own. Whereas metallic heater wires can be easily produced to any length to span long lengths and follow firebrick channel paths, ceramic heaters are each prefabricated and must penetrate the insulated wall of the storage chamber such that their electrodes are kept cool; this makes it difficult to reach the innards of a large brickwork. The length restrictions also imply more electrical penetrations into the heat storage systems with more heat losses through those penetrations. While SiC heaters can be cantilevered against the external wall, $MoSi_2$ heaters do not have the mechanical strength to be cantilevered and must be supported against gravity. SiC heaters can operate only slightly hotter (1650ºC) than the applications FIRES aims to power, which makes sustained delivery of heat difficult. This is again exacerbated by oxidation kinetics, which demands that in practice SiC heaters be operated a couple hundred degrees Celsius below peak [32]. For a high temperature FIRES unit, it was concluded that a charging system based on existing heater options could not match the same reliable performance as the discharge system demonstrated in hot blast stoves.

To achieve a FIRES charge system similarly robust as the discharge system, a novel approach was considered, in which the firebrick acts as both the electrically conductive charge medium and the storage medium, and the brickwork is charged via direct resistance heating (DRH). By using electrically conductive firebrick, electricity can flow directly through the brickwork, generating heat volumetrically, and avoiding major temperature gradients, as well as heater wattage loading limits. A DRH charge system may also be most simplistically incorporated without major adaptation of existing hot blast stove designs, by avoiding the need to fit new components into the brickwork, such as with cantilevered heaters. The design burden of a DRH-style FIRES unit is therefore the design of the electrically conductive firebrick itself.

2.4 Requirements of firebrick for DRH-style FIRES

A DRH FIRES unit where the firebrick acts as both the energy storage media and joule-heating media has unique requirements for the firebrick, which merges the attributes of both traditional firebricks and joule heaters. This section discusses these attributes in more detail. The final three attributes discussed, which all pertain to electrical properties, are the focus in this doctoral work. Table 2 lists the attributes of an ideal firebrick for DRH, as well as the relative capabilities in existing hot blast stoves and ceramic heaters with respect to each attribute.

- **High operating temperature:** The starting point of evaluating candidate materials is whether they are capable of operating at high temperatures, which at a minimum requires a high melting point and sufficient mechanical strength to withstand the weight of the storage media stacked on top. Operating temperatures in practice are set by several other considerations as well. Hot blast stove materials, which consist of high-alumina firebricks, routinely reach 1600°C, with ratings near 1800°C and melting points over 2000°C. Other oxide options have similar temperature ranges.
- **Bulk chemical stability (in air):** Rapid oxidation is a common disqualifier of materials for high temperature applications. Most firebricks are already oxides which cannot be oxidized further. Existing ceramic heaters are not oxides but form SiO_2 layers on the outside that protect the bulk material. SiC heaters fail due to gradual growth of this layer as oxygen penetrates further inward, increasing heater resistance and causing stresses between the protective layer and the bulk material. This is commonly called aging [32]. $MoSi_2$ heaters have a slower oxidation rate.
- **Thermal shock resistance:** A key challenge in the design of heaters and hot blast stoves, thermal shock resistance is the ability of a material to resist crack formation and propagation due to temperature-induced stresses, particularly during thermal cycling of materials. Smaller and more thermally conductive objects such as SiC and $MoSi_2$ heater rods have better thermal shock resistance than larger oxide bricks for the same operating conditions, such that heaters can generally handle higher heat rates than firebricks. Hot blast stoves have been designed to operate on the order of 10^4 cycles, for decades of operation with some regular maintenance. SiC heater life is generally limited by oxidation rather than thermal shock. $MoSi_2$ failure sometimes occurs from thermal stresses during cooldown, caused by material embrittlement after long periods of operation [33].
- **High heat transfer rate:** The heat transfer rate achieved in practice is tied to thermal shock limits, where very high heat transfer rates induce too much stress. Based on previous analysis [2], typical brickworks of hot blast stoves are estimated to have heat transfer rates up to several 10s of kW/m^2, where heaters may reach over 100 kW/m^2 (Table 1). In a DRH system, this heat transfer rate pertains to the convective heat transfer that the brickwork walls may handle from an airstream during discharge. Charge rates are far less constrained by thermal shock because heat is generated volumetrically through the conductive brickwork rather than transferred by surface convection/radiation.
- **High energy density:** A higher energy density makes heat storage more practical by storing more energy in less mass/volume. This is secondary to all the attributes necessary for surviving high temperatures in hot blast stoves, and is not considered in heater applications. Typical high-alumina low porosity firebricks have a thermal mass between 0.5 and 1 MWh/m^3 of sensible heat capacity for a temperature change of 1000°C.
- **Bulk electrical conductivity:** Electrical conductivity is an essential requirement not seen in most commercial firebricks, which are large bandgap semiconductors, classified for most purposes as electrical insulators. Even at temperatures of 1000°C, alumina-silica refractories generally have resistivities of 10^5 ohm-cm. Meaningful heat generation at these resistivities is generally impractical. This high resistivity is due to the covalent bonding and lack of free charge carriers in oxide crystal structures. Heaters made of SiC, also a relatively large band gap semiconductor, have far lower electrical resistivities, near 10^{-2} ohm-cm. This

effect is achieved by doping the crystal structure with atoms of different valency, creating freely moving electrons or holes. $MoSi_2$ heaters have electrical resistivities near 10^{-5} ohm-cm, because $MoSi_2$ is an intermetallic compound with no energy band gap, meaning valence electrons will freely move through the crystal under an applied voltage.

- **Small resistivity-temperature derivative (RTD):** In addition to being sufficiently electrically conductive, candidate firebricks must also have a relatively constant resistivity with temperature, i.e., a relatively small resistivity temperature derivative (RTD). Most commercial firebricks have sharp exponentially decreasing resistivities, which may change by four orders of magnitude over the temperature ranges of interest. This makes it very challenging to controllably heat a large mass of the material. As the temperature goes up, the electrical resistivity goes down. This implies that most of the current goes through the hottest part of the ceramic creating the risk of run-away heating and heater failure. SiC heaters have a sharp negative RTD up until approximately 600°C, at which point resistivity levels out and the RTD turns positive and small. It is therefore typically recommended to operate SiC heaters above 600°C [7]. $MoSi_2$ heaters possess a relatively constant positive RTD throughout the temperature range, with a factor of 10 or 12 change in resistivity over the temperature range. The control challenges created by different RTDs and the theory behind the different behaviors are discussed in the following section.
- **Surface electrical conductivity:** Surface electrical conductivity is necessary for the flow of electricity between stacked firebricks. The protective SiO_2 layers that form on ceramic heaters are highly insulative, and does not allow current to flow between contacting materials. This makes the prospect of simply stacking doped SiC bricks to form the DRH-style FIRES unit likely unworkable, in addition to the other shortcomings of SiC (an idea explored early in the project). Oxide firebricks in clean air undergo minimal changes in surface chemistry but are generally not electrically conductive.

Table 2: Attributes of ideal firebrick for DRH-style FIRES system

Ideal attributes	Relevant material properties	Hot blast stove experience	Ceramic heater experience
High operating temperature	Melting point, mechanical strength	routinely 1600°C ratings near 1800°C melting points over 2000°C.	SiC: 1650°C, strength for cantilever. MoSi2: 1850°C, hang vertically or support by hooks.
Bulk chemical stability (in air)	Oxidation/other reaction rates, diffusivity rates	10s of years in contact with air and flue gases at elevated temperatures.	Oxide layer formation protects bulk material, typically 100s-1000s hours life.
Thermal shock resistance	Thermal conductivity, young's modulus, thermal expansion coefficient, tensile strength	10^4 thermal cycles	100s-1000s thermal cycles
High heat transfer rate	Thermal conductivity (thermal shock-limited)	1s-10s kW/m2.	10s-100s kW/m2.
High energy density	specific heat, density, operating temperature range	0.5-1 MWht/m3 for 1000°C temperature range.	not necessary for joule heater applications.

Bulk electrical conductivity	electrical resistivity	10^4 - 10^7 ohm-cm.	10^-5 - 10^-2 ohm-cm
Small resistivity-temperature derivative (RTD)	electrical resistivity, operating temperature range	Exponentially negative RTDs.	MoSi2: positive RTD SiC: negative RTD < 600°C, positive RTD > 600°C
Surface electrical conductivity	Surface chemistry, oxidation/other reaction rates, diffusivity rates	Generally stable, oxides	Surfaces oxidize to form SiO2, highly electrically insulative

2.5 Strategy of DRH-style firebrick development

Of the many attributes necessary for a DRH-style firebrick, the three most critically lacking are the electrical properties, which demand a far higher conductivity, and a smaller RTD compared to the exponential trends seen in most commercial firebricks. On the other hand, existing oxide firebricks would likely overcome the problem of the resistive surface oxide layer experienced by SiC heaters if their bulk were electrically conductive, due to their already oxidized state. Doping oxides to create the necessary electrical attributes while maintaining the many other positive attributes of hot blast stove firebricks arose as a promising approach to developing a DRH-style firebrick.

First, a review of oxide options was undertaken with respect to their relevant properties and prospects for effective doping (physics are reviewed in Section 3), in addition to other practical considerations of each candidate. Next, the electrical properties of some commercial bricks were tested as a baseline to candidate materials. Finally, the top candidate bulk-dopant combination was home-fabricated and tested.

3 Joule heater fundamentals

The principles of design for effective resistive heating devices involve the intersection of semiconductor physics and materials science. This section begins with a review of semiconductor electrical conductivity, and discusses the capabilities to predict and design for specific properties. Then an evaluation of the material option space for DRH-style firebricks is presented, with respect to the relevant semiconductor and material properties.

3.1 Electrical conductivity in semiconductors

The electrical conductivity of a material can be generally expressed as the product of the available charge carriers, and mobility of the carriers:

$$\sigma(T) = q * \mu_c(T) N(T) \tag{1}$$

where T is the temperature, q is the carrier charge, μ_c is the carrier mobility, and N is the charge carrier concentration. Typical units for charge, carrier concentration, and mobility are Coulombs C, #/cm^3, and cm^2/V-s respectively. The charge carrier may be an electron or an electron hole. The properties of mobility and carrier concentration heavily depend on the class of material, particularly with regard to its electron band structure. A brief review of semiconductor electronic band theory is given here.

3.1.1 Carrier concentration

In the electronic band structure of pure semiconductors, there is an appreciable band gap between the energies of the valence band edge E_v and the conduction band edge E_c. The creation of a free electron charge carrier, unbound from the valence shell and free to move in an electric field, requires the thermal excitation of valence electrons across the band gap E_g, where $E_g = E_c - E_v$. This excitation leaves a hole in the valence shell that is also a carrier, free to migrate through the solid as adjacent valence electrons hop to its location. Figure 12a shows a simplified band structure of an undoped semiconductor.

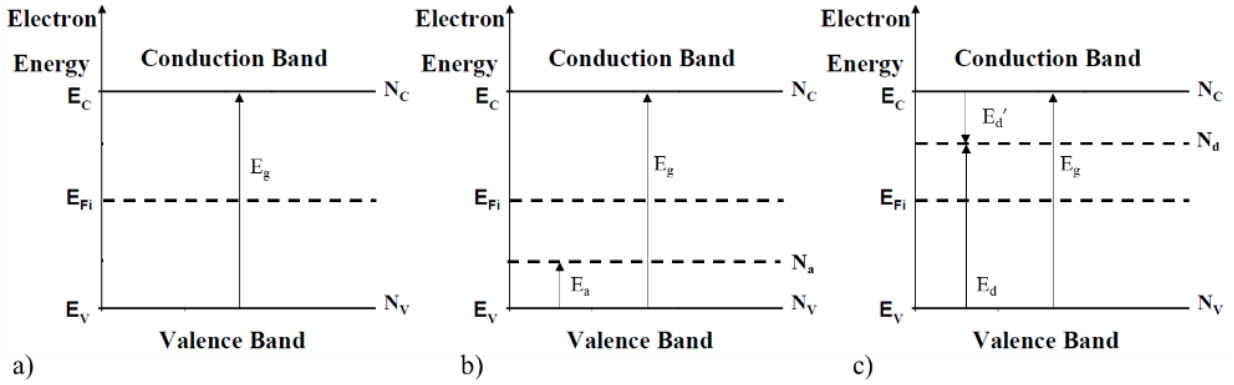

Figure 12: simplified band structures of semiconductors.
a) undoped intrinsic semiconductor. b) p-type doped semiconductor, with an acceptor ionization energy near the valence band. c) n-type doped semiconductor, with the donor energy level near the conduction band. E_{Fi} denotes the Fermi level in the intrinsic case. Adapted from [34].

The number of carriers that exist at a given temperature is determined by density of possible electron states over the energy range of interest, and the probability that the state is (or is not) occupied. The number of free electrons (holes) in the conduction band (valence band) at a given temperature can be obtained by integrating the product of the density of states in the band and the probability that the state is occupied (unoccupied) by an electron:

$$n_o(E) = \int_{E_c}^{\infty} g_c(E) f(E) dE \quad and \; p_o(E) = \int_{-\infty}^{E_v} g_v(E)\big(1 - f(E)\big) dE \tag{2}$$

Where n_o is the number of free electrons at thermal equilibrium, p_o is the number of free holes a thermal equilibrium, E is energy, $g(E)$ is the density of states function, $f(E)$ is the Fermi-Dirac distribution, and the subscripts c and v signify conduction band or valence band. Note that in the case of holes, the probability is represented by $1\text{-}f(E)$. The Fermi-Dirac distribution is written:

$$f(E) = \frac{1}{\exp\left(\frac{E - E_F}{kT}\right) + 1} \tag{3}$$

where E_F is the Fermi level. An energy state at the Fermi level corresponds to a 50% chance of being occupied by an electron. For semiconductors where the Fermi level is farther than 3kT from the edge of the valence band and conduction band (referred to as "non-degenerate" semiconductors), the Fermi-Dirac distribution may be simplified to the Maxwell-Boltzmann distribution:

$$f(E) \approx \exp\left(\frac{E_F - E}{kT}\right) \tag{4}$$

This allows for the analytical solution of equation (1), with the following result of free electron and hole concentrations:

$$n_o = N_c \exp\left(\frac{E_F - E_c}{kT}\right) \; and \; p_o = N_v \exp\left(\frac{E_v - E_F}{kT}\right) \tag{5}$$

where N_c is the effective density of states in the conduction band, and N_v is the effective density of states in the valence band:

$$N_c = \frac{2(2\pi m_n^* kT)^{\frac{3}{2}}}{h^3} \; and \; N_v = \frac{2\left(2\pi m_p^* kT\right)^{\frac{3}{2}}}{h^3} \tag{6}$$

where h is Planck's constant, and m_n^* and m_p^* are the density of states effective masses of electrons and holes, respectively. The Fermi level, temperature, electron and hole concentrations are related by:

$$E_F = E_v + kT * ln\left(\frac{p_o}{N_v}\right) = E_c + kT * ln\left(\frac{n_o}{N_c}\right) \tag{7}$$

By the law of mass action, the product of free electrons and free holes must be a constant at equilibrium. In an intrinsic semiconductor, where the creation of a free electron in the conduction band also creates a hole in the valence band ($n_o = p_o$), the constant value may be designated the square of n_i, the intrinsic carrier concentration:

$$p_o n_o = constant = \; n_i^2 \tag{8}$$

It follows that the Fermi level for an intrinsic semiconductor, denoted E_{Fi}, changes with temperature as per the relation:

$$E_{Fi} = \frac{E_c + E_v}{2} + kT * ln\left(\frac{N_v}{N_c}\right) \tag{9}$$

In an intrinsic semiconductor, where the creation of a free electron in the conduction band also creates a hole in the valence band, $p_o = n_o$.. and the square root of their product yields the generic intrinsic carrier concentration, which can be expressed as:

$$n_i = \sqrt{n_o p_o} = \sqrt{N_c N_v} \exp\left(\frac{E_v - E_c}{2kT}\right) = \sqrt{N_c N_v} \exp\left(\frac{-E_g}{2kT}\right) \tag{10}$$

Note that, by this manipulation, the Fermi level is eliminated from the equation, and the intrinsic carrier concentration relates to the band gap E_g.

An intrinsic semiconductor shows an exponential increase of charge carrier concentration with temperature, which is impractical for most resistance-heated devices. The exponential trend continues until the material melts, creating no regime where carrier concentration is constant.

To modify the electrical behavior of semiconductors, small amounts of impurities are added, i.e, dopants, which change the band structure of the semiconductor. Dopants most commonly substitute atoms of the pure lattice and have one more or one fewer electron in their valence shell. The net effect of the dopant is the donation of one free electron to the conduction band (n-type doping), or the acceptance of an electron from the valence band to form a free hole (p-type doping). Figure 12b and Figure 12c show the relative positions of the dopant energy levels which will donate or accept electrons from the neighboring band edges. An effective p-type dopant will have usually one fewer valence electron and an energy level near the valence band edge; an effective n-type dopant will have usually one more valence electron and an energy level near the conduction band edge. The creation of these free carriers requires the ionization of the dopant, again a thermally activated process, but with lower temperature requirements, as per the smaller energy gap that exists between the band edges and the energy level of the dopant. The number of dopant sites ionized as a function of temperature, which yields an equal number of free carriers, is expressed as [34]:

$$N_d^+ = \frac{N_d}{1 + g_d \exp\left(\frac{E_F - E_d}{kT}\right)} \; and \; \; N_a^- = \frac{N_a}{1 + g_a \exp\left(\frac{E_a - E_F}{kT}\right)} \tag{11}$$

where N indicates concentrations of dopants, + and – superscripts indicate ionized dopants, and d and a subscripts indicate acceptor or donor dopants. g_d and g_a are the donor and acceptor ground state degeneracy of the bulk material, i.e., the number of ways in which the ionization can occur.

The presence of free holes, free electrons, and ionized acceptor and donor sites in the bulk material must obey the local charge neutrality equation:

$$p_o - n_o - \sum_{l=1}^{M_a} N_{a_l}^- + \sum_{l=1}^{M_d} N_{d_l}^+ = 0 \tag{12}$$

where the summations are over *M* kinds of p-type or n-type dopant materials. When combined with equations (5) and (11), all terms are defined to solve for the Fermi level that satisfies (12). The Fermi level will move as more dopant is activated. In single-doped systems (Figure 12b or Figure 12c), the Fermi level will typically be located in between the dopant energy level and the nearest edge of the band gap at low temperatures. As the dopant becomes activated, the Fermi level will generally move towards the center of the band gap.

The resulting carrier concentration of a single-doped semiconductor over the temperature range is shown in Figure 13. The temperature dependence of carrier concentration has three distinct regimes: ionization, extrinsic, and intrinsic. At low temperatures, the free carriers increase exponentially as the dopant is ionized, such that carrier concentration is driven mostly by equation (11). As nearly all the dopant sites are ionized, i.e., $N_a^- \approx N_a$, the material enters the extrinsic regime, where increasing temperature has a negligible effect on carrier concentration. This is also referred to as exhaustion. Throughout this temperature regime, the excitation of electrons across the bandgap is exponentially increasing, but negligible. At a high enough temperature, the intrinsic electron-hole generation overtakes the base dopant as the dominant charge carrier, and the carrier concentration again increases exponentially, following the n_i line.

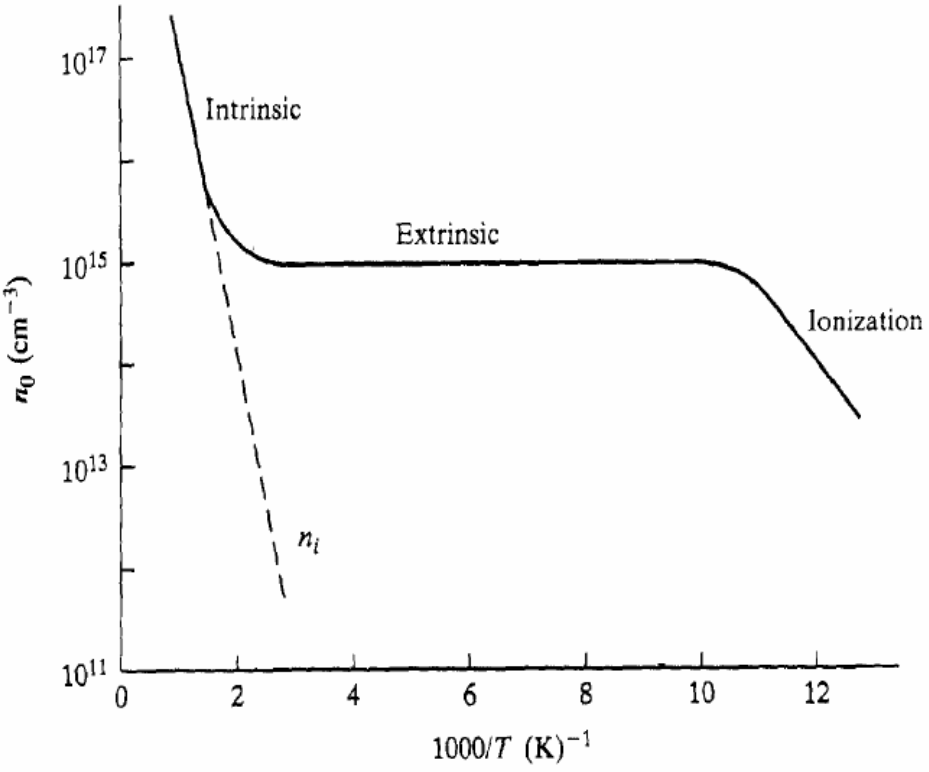

Figure 13: Carrier concentration of a doped semiconductor as a function of inverse temperature. [35]

When designing joule heaters as well as other electronic devices, the extrinsic region is generally the area in which the device is operated, due to the vast changes in resistivity that may occur in the exponential regions. To change this operating range, one may add more or less dopant. Figure 14 shows the effect of varying the amount of dopant added. More dopant shifts the upper temperature limit T_U and lower temperature limit T_L higher. The envelope of the extrinsic region where the dopant is fully exhausted generally shrinks as more dopant is added, as the onset of exhaustion occurs at higher temperatures and is more gradual. Earlier exhaustion occurs with dopants whose energy

levels are close to the band gap edge. More dopant also has the added effect of proportionally higher conductivity. A balance must be struck between the width of the extrinsic region, the onset of the extrinsic region, and the overall conductivity of the system. The specific application must be considered carefully when deciding the amount of dopant.

One must also consider the higher and lower bounds of doping, namely the solubility limit of the dopant within the material, and the starting purity of the material, respectively. Doping beyond the solubility limit will introduce undesirable phases and unintended properties. Research and development of higher performance transparent conducting oxide (TCO) films, i.e films that may cover a solar cell to efficiently conduct carriers away without blocking sunlight, often involve pushing the solubility limits of dopants in order to maximize electrical conductivity. Equilibrium solubility limits have been surpassed by forming and depositing doped oxides at non-thermodynamic conditions, creating metastable compositions that do not show undesirable phases [36]. Such metastable compositions may be suitable for lower temperature applications such as solar cells, but are not an option for joule-heating devices, which would lose metastability upon heating to high temperatures. Doping at very low levels in an impure material will likely result in dilution of the intended effect with the impurities. For example, the presence of an unintended p-type impurity may cancel the effect of an n-type dopant. These factors set the stringent purity requirements of most of the semiconductor industry. While devices for such applications may typically be expected to operate at a range of -50°C to 150°C [35], joule-heating applications aim to create an exhaustion region of 1000°C or more.

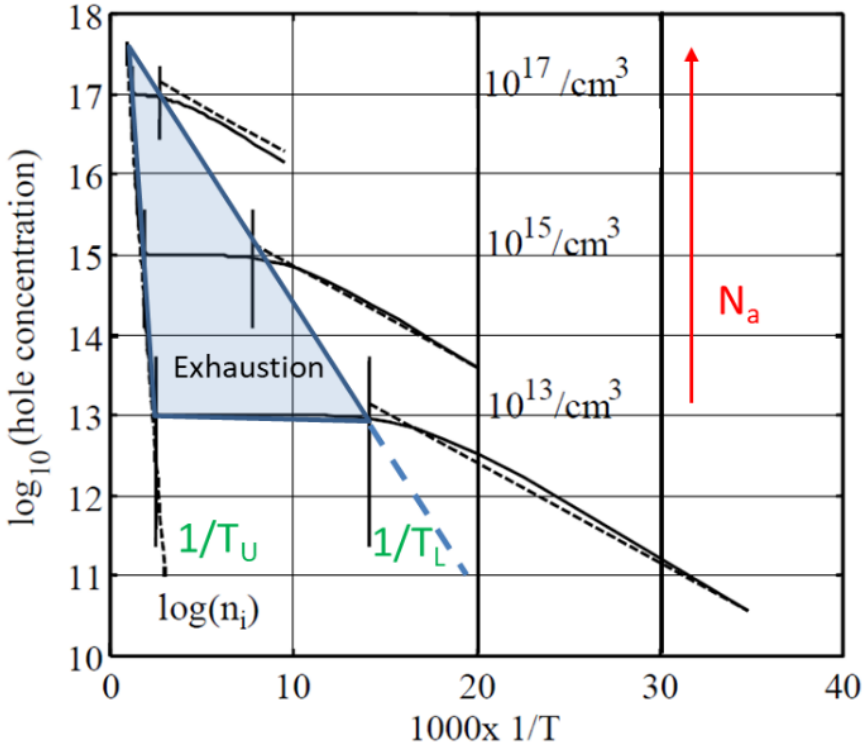

Figure 14: The effect of greater dopant on lower and upper temperature limits T_L and T_U of the fully exhausted extrinsic region in silicon.
Adapted from [34].

3.1.2 Carrier mobility

The mobility of carriers in semiconductors is affected by several complex interactions of the electrons and holes with impurities, phonons, and lattice distortions, which have competing effects. The relative magnitude of each changes with temperature and dopant amount, and vary widely by the character of the semiconductor. The mobility derivative $d\mu_c/dT$ is of special significance because it determines the resistivity-temperature derivative RTD in the extrinsic regime where $N(T) \approx$ constant. Considerations of the RTD will be discussed more in Section 3.3.

Once a free electron or hole is formed, its mobility is understood in terms of the polaron quasiparticle, which captures the coupled movements of both the electron and the lattice ions as they shift from their equilibrium positions to screen the charge. Polarons formed during movement are characterized as a large polarons, or that small polarons.

Large polarons exhibit band conduction, which refers to relatively easy movement of carriers between closely spaced energy levels that form an effectively continuous band of energies. This behavior is affected by several forms of scattering events. In addition to the scattering effects experienced by large polarons, small polarons are hindered by an effect called "self-trapping." The scattering phenomena will be discussed first, then self-trapping.

Carrier mobility in band conduction is affected by a number of different scattering events. The net effect of scattering events are related by [37]:

$$\frac{1}{\mu_{c,eff}} = \frac{1}{\mu_1} + \frac{1}{\mu_2} + \cdots \tag{13}$$

Such that the effect causing the lowest mobility dominates. The most common scattering phenomena include impurity scattering, acoustic phonon scattering and optical phonon scattering.

Impurity scattering refers to the scattering of free charge carriers by electrostatic forces of ionized impurities, which hinders carrier mobility. Greater dopant levels increase the magnitude of this effect. As temperature increases, the interaction time of the carriers with impurities is reduced, as is the scattering effect, but the thermally activated ionization of dopant creates more scattering sites. To first order, the effect of impurity scattering on mobility is [38]:

$$\mu_{c,impurity} \propto \frac{T^{\frac{3}{2}}}{N_{ion}} \tag{14}$$

Whether the effect of impurity scattering causes mobility to increase or decrease with temperature depends on $d(N_{ion})/dT$, as informed by the discussion in the previous section. In the ionization region (Figure 13), the exponential increase of N_{ion} will cause a sharp decrease in mobility as a function of temperature. The temperature at which exhaustion is reached depends on the amount of dopant (Figure 14). Once in the extrinsic region, the numerator effect will overtake the denominator. In many commercial semiconductors exhaustion is reached well below typical ambient temperatures, such that only the numerator is of concern.

Phonon scattering refers to the scattering of free electrons and holes with vibration modes of the crystal lattice, which may consist of acoustic and optical phonons. Acoustic phonons are coherent movements of atoms, while optical phonons are out-of-phase movements. The phonon density in the lattice increases with temperature, such that carrier mobility decreases. Optical phonons are more prevalent in polar semiconductors such as metal oxides, i.e., opposite motions of positive and negatively charged ions. In covalent semiconductors such as silicon, acoustic phonon scattering is the dominant scattering feature. The temperature dependencies of mobility on acoustic phonon scattering and optical phonon scattering are estimated as [38]:

$$\mu_{c,ac} \propto T^{-\frac{3}{2}} \quad and \quad \mu_{c,opt} \propto T^{-\frac{1}{2}} \tag{15}$$

where *ac* and *opt* subscripts refer to acoustic and optical scattering respectively. The phonon scattering effects overtake impurity scattering at most temperatures of interest. The overall effect for large polaron mobility may simply be taken as:

$$\mu_{c,LP} \propto T^{-n} \tag{16}$$

where *LP* denotes large polaron. *n* may range from 1.0 to 2.5 for different commercial semiconductors at temperatures of interest [38]. Semiconductors that exhibit band conduction therefore possess a negative mobility derivative $d\mu_c/dT$.

Self-trapping is an effect that occurs when a free carrier, upon its creation, becomes localized at one or few atoms. In terms of band structure, the lattice distortion causes the movement of the free carrier energy level into the band gap, where there it again requires extra energy to move. The self-trapping is often attributable to the changing of oxidation state of an ion, such as may commonly occur in transition metal oxides [39]. Unlike band conduction, characterized by relatively easy movement through an energy band, the small polaron transport mechanism is referred to as "small polaron hopping," indicative of the greater effort required for a carrier to move between states. The extra energy required to move, sometimes called the "hopping energy" E_h, has an effect on mobility similar to carrier concentration. The resulting mobility trend of semiconductors that exhibit small polaron hopping may be expressed as:

$$\mu_{c,SP} \propto T^{-n} \exp\left(\frac{-E_h}{kT}\right) \tag{17}$$

Where *sp* denotes small polaron. The leading T^{-n} term represents the collective scattering effects discussed for large polarons, as in equation (16). In much of the literature on small polaron mobility the scattering term is often omitted, because the hopping exponential typically dominates behavior over the temperature ranges of interest. When scattering effects are considered, n is usually prescribed as 3/2 [40, 41], because acoustic phonon scattering will ultimately dominate the other scattering effects. Nonetheless, careful attention must be paid to the competing effects, with the understanding that generalizations of a given temperature or dopant level to a broader range may lead to faulty conclusions regarding the dominant effects.

Depending on the specific dopant level, temperature, and hopping energy E_h, a small polaron conductor will typically have a positive mobility derivative $d\mu_c/dT$. but may experience a negative derivative at high enough temperatures. Figure 15 shows the behavior of $\mu_{c,SP}$ over a large temperature range at hopping energies of 0.1eV, 0.2eV, and 0.3eV, with n = 3/2.

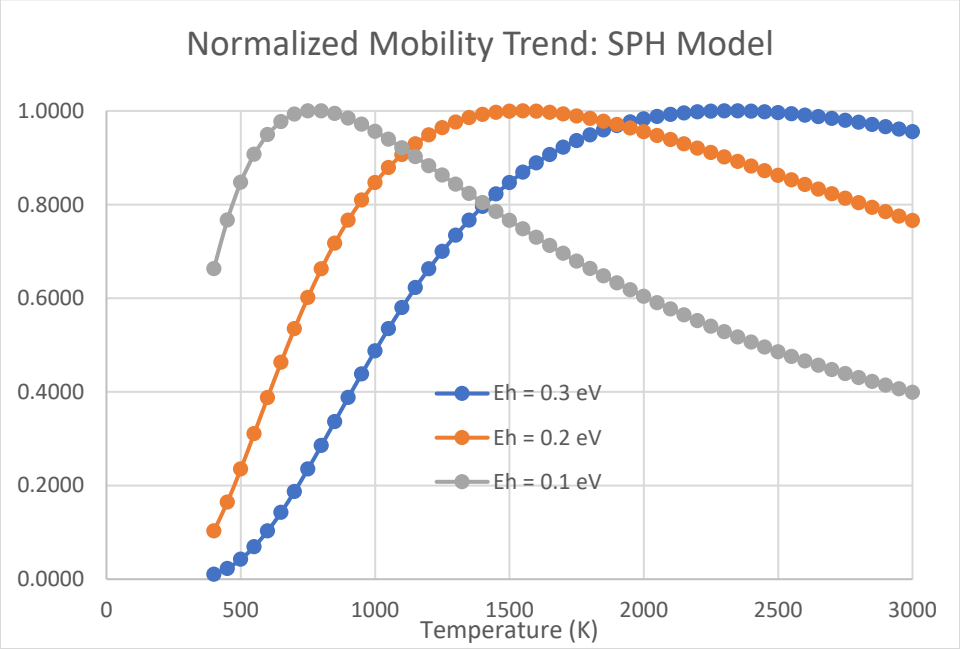

Figure 15: Normalized trend of small polaron mobility with temperature.
Equation (17) is plotted for three different hopping energies and the scattering exponential n = 3/2.

3.2 Operating range maximization of a joule heater

The operating range of a joule heater is set by the width of the exhaustion region, where carrier concentration $N(T) \approx$ constant and a small RTD is possible. From the application of the relations in Section 3.1.1, T_L and T_U can be predicted as a function of dopant level and material properties, and the desirable material attributes that maximize the temperature bounds can be identified. This section begins by presenting the ideal properties that maximize operating range, followed by the application of theory to Si and SiC to demonstrate the concepts, and show the predictive capability of the approach, by demonstrating that the performance of an SiC heater can be recreated with fair accuracy using the formulations and inputs roughly estimated from literature. Finally, the limitations of the approach are discussed.

3.2.1 Ideal semiconductor joule heater properties

For an ideal joule heater, a large envelope of dopant levels would be acceptable, spanning several orders of magnitude, where the operating temperature range has T_L near room temperature and T_U near flame temperatures, e.g., near 2000°C. The ideal candidate would possess the following characteristics, using notation of a p-doped semiconductor:

- **Shallow dopant energy level E_a:** A shallow acceptor (or donor) energy level near the valence band (or conduction band) edge determines the ease with which dopants may be ionized. A small ionization energy dramatically lowers T_L, since all dopant may be ionized at lower temperatures.
- **Large band gap E_g:** The band gap is the dominant factor in determining the onset of the intrinsic zone, T_U. A large band gap results in a very low intrinsic carrier concentration even at very high temperatures.
- **Small minor carrier effective mass m_n^*:** For a p-doped semiconductor, a small m_n^* increases T_U without an effect on T_L.
- **Large dominant carrier effective mass m_p^*:** For a p-doped semiconductor, a large m_p^* decreases both T_L and T_U, with a net effect of a larger operating range.
- **Low degeneracy g_a:** A higher degeneracy of states in the valence band (or conduction band) causes the T_L edge to "bend" towards the T_U edge with increasing dopant concentration, shrinking the operating range. A low degeneracy of states is therefore desirable.
- **Large polaron mobility:** The mobility derivative $d\mu_c/dT$ in part qualifies what level of dopant exhaustion is sufficient to say "$N(T) \approx$ constant." Because large polaron mobility is generally characterized by a less steep, slightly negative mobility derivative $d\mu_c/dT$, it counteracts the positive carrier derivative dN/dT as exhaustion sets in. This has the net effect of reducing the resistivity-temperature derivative RTD and widening the effective operating range of the joule heater.

The effects of different parameters are best understood by looking at real material candidates. In practice, there are a finite number of material options to choose from, each with a set of intrinsic properties that must be accepted as a whole. Identification of compatible bulk-dopant combinations is a key starting point. Regarding dopant activation, dopant energy levels E_a or E_d in equation (11) are not typically reported relative to a valence band edge or conduction band edge as depicted in Figure 12. Rather, an "activation energy" E_{act} is often reported, which is typically calculated for a generic Arrhenius fit to electrical resistivity data. This fit represents the net effect of potentially multiple exponential terms, though is usually characterized by a dominant effect, namely ionization (11). An activation energy characteristic of dopant ionization should be measured far from the onset of exhaustion. For a given E_{act} from literature, one can iterate on the input of dopant energy level E_a or E_d until the resulting E_{act} is similar to the experiment. A dopant option with a sufficiently low dopant energy level typically correlates to an activation energy E_{act} of 0.05eV to 0.5eV. Otherwise a material is essentially an insulator at most relevant temperatures and dopant levels, and will not reach exhaustion.

Effective masses of both carrier types can vary widely from approximately $0.2m_0$ to $20m_0$ [39], where m_0 is the rest mass of an electron. Dominant and minor carrier masses on the opposite ends of this spectrum exist but are uncommon. Mass ratios m_p^*/m_n^* of 1.5 to 2.5 are typical. For a given set of parameters, an increase in mass shifts the temperature operating range proportionally in dopant space. That is, a factor of 10 increase in both masses results in the same T_L and T_U with a factor 10 more dopant.

Depending on the parameters, an envelope of acceptable dopant level can be seen where the operating temperature range is relatively wide and T_U is located near flame temperatures, e.g., near 2000ºC. This dopant envelope may be very narrow for some materials or very wide for others. The envelope will be further constrained on the upper side by the solubility limit of the dopant in the bulk material, and on the lower side by the impurity content of a reasonably priced bulk material, which may include effects of native impurities and non-stoichiometry. Once this envelope is understood, the dopant level may be selected, which will set the operating range of the joule heater. Section 4 evaluates different oxides and maps their operating ranges as a function of dopant concentration.

3.2.2 Exhaustion region prediction in materials: Si and SiC reference

Figure 16 shows the lower and upper temperature limits T_L and T_U for different dopant levels in Si and SiC. Four scenarios are shown: n-type Si, p-type Si, n-type SiC, and p-type SiC. Here, formulations offered by Pieper and Michael [34, 35] are used to calculate dopant ionization and carrier activation for a single impurity. The exhaustion region has been defined where T_L and T_U indicate free carriers at a level of 80% of the dopant level and 120% of the dopant level, respectively. Generic dopant energy levels of 0.05eV and 0.10eV were used for Si and SiC, respectively. Table 3 shows all model inputs.

In all cases shown, doping at higher levels has the effect of shrinking the width of the operating range and shifting it to higher temperatures. T_U was limited to at or below T_{max}, selected for each material relative to their approximate solid stability temperatures. SiC possesses a far greater T_U and operating temperature range than Si (even before T_{max} is reached), owed mostly to its larger band gap.

Doping n-type or p-type affects T_L based on the relative effective masses of the major and minor carriers. In the case of Si, $m_n^* > m_p^*$, and favors n-type doping. The opposite is true for SiC. This assumes the dopant energy levels are similar, which were kept the same in the n-type and p-type scenarios for each material.

Table 3: property inputs of Si and SiC for carrier activation calculations

Property		Si [35]	SiC [42]
E_g	eV	1.1	3.0
E_a, E_d	eV	0.05	0.1
m^*_n/m_0	-	1.1	0.3
m^*_p/m_0	-	0.56	1.5
g_d	-	2	2
g_a	-	4	4
T_{max}	K	1600	3000
T_L condition	-	-20% $N_{a,d}$	-20% $N_{a,d}$
T_U condition	-	+20% $N_{a,d}$	+20% $N_{a,d}$

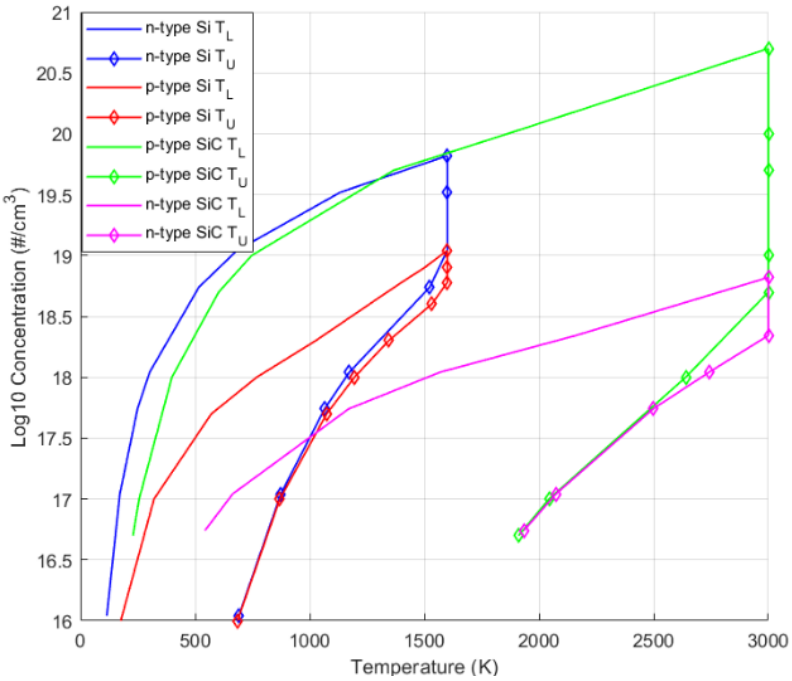

Figure 16: Modeling of exhaustion region for Si and SiC. T_L and T_U of exhaustion region for p-type and n-type doping of Si and SiC at different levels, corresponding to carrier concentrations between 80% and 120% of dopant level.
Table 3 contains inputs.

To test the validity of these results, the formulations will be used to reconstruct the resistivity curve of a typical SiC heater by estimating trends of mobility and dopant energy level from different literature. At this time it is worth further discussing what qualifies as "exhaustion," which does not have a rigorous definition. Indeed, the carrier concentration is never *truly* constant. Considering exhaustion as a region where free carriers are within a certain percentage (e.g., +/-20%) of the dopant concentration can be a useful metric, but the ultimate merit of the exhaustion region in the context of joule heating is a temperature range where the RTD can be small enough for controllable heating. Although the upper limit of a "small enough RTD" involves in-depth considerations of thermal properties, heat rate and geometry, RTD = 0 certainly meets the burden of "small." An RTD of zero may occur at two different temperatures in the case of large polaron band conductors with $\mu_c \propto T^{-n}$: once when the rate of decreasing mobility overtakes the rate of activating extrinsic carriers, and again when the rate of intrinsic carrier activation overtakes the

effect of decreasing mobility. The region between these temperatures will be non-Arrhenius, instead defined by the mobility trend. A more useful framing of the exhaustion region can therefore be the region between the two temperature points where RTD = 0.

This new definition of exhaustion region is shown alongside the previous one (adjusted here to +/-30%) in Figure 17. Here, nitrogen-doped SiC (i.e., N-doped SiC, with a capitalized N) is examined, from $N_d = 5\text{x}10^{16}/\text{cm}^3$ to $N_d = 10^{19}/\text{cm}^3$, with exact solutions of free carrier concentrations superimposed. These cases are of interest because n-type doping with nitrogen is common in SiC heaters, despite apparently worse performance than p-type doping based on Figure 16. The nitrogen dopant energy level was estimated from a simple Arrhenius fit of data from Lely and Kroger [43]. Typical heater dopant levels are near $10^{19}/\text{cm}^3$ [42], which is above the dopant levels where exhaustion is achieved defined by the +/-30% criteria. However, carrier level-off can be seen in the exact solutions as low as 500K, above which carriers remain the same order of magnitude. When accounting for the mobility trend of SiC, estimated as $\mu_c \propto T^{-1.13}$ from data presented in [32], an RTD of zero is found near 1180K (900ºC) for $N_d = 10^{19}/\text{cm}^3$.

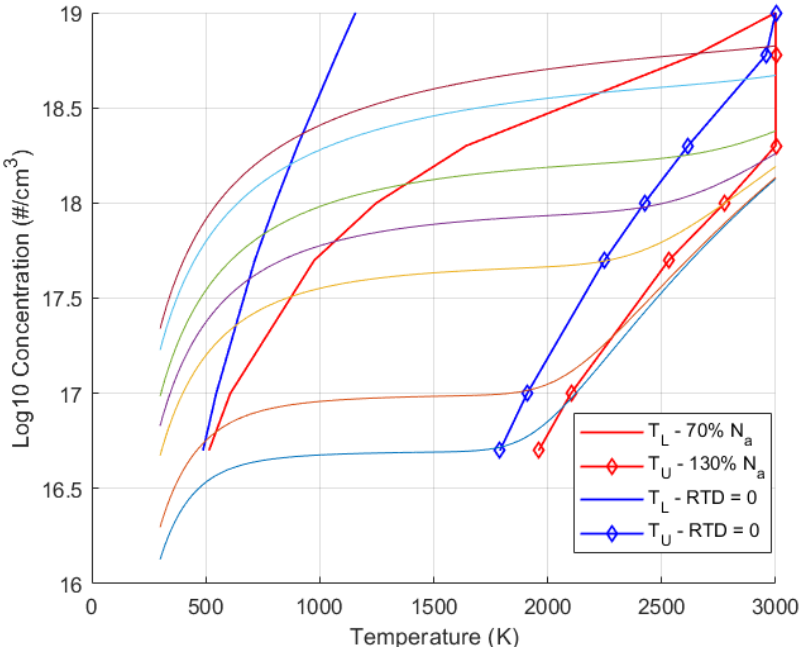

Figure 17: Comparison of exhaustion region criteria for N-doped SiC with $E_d = 0.125$eV, with exact carrier concentration overlayed. One method (red) shows T_L and T_U corresponding to carrier concentrations between 70% and 130% of dopant level. Another method (blue) shows where resistivity-temperature derivative RTD = 0. The SiC temperature dependence of mobility was estimated as $\mu_c \propto T^{-1.13}$, based on the temperature range above 1200ºC of a typical SiC heater in the assuming $N(T) \approx$ constant, from [32]. E_d estimated based on data from [43]. Exact carrier concentration lines are overlayed from formulations in [34].

The RTD near 900ºC is not far from existing heater data. By combining the carrier concentration trend and mobility trend of $N_d = 10^{19}/\text{cm}^3$ with a reference resistivity $\rho = 0.1$ ohm-cm at $T = 1000$K, a modeled resistivity curve has been produced in Figure 18a. The overall shape and magnitude compare well to the result of heater measurements for a variety of SiC heaters in Figure 18b, with a deviation that can be attributed largely to the simplified assumptions and data fitting used to calculate the mobility trend. The similarity serves as a validation of the relatively simple formulations used here to model exact carrier concentration as a function of temperature. This model will serve as a basis when evaluating oxide candidates.

They key aspects and aims of joule heater design thus far are summarized in Figure 19. Another typical resistivity-temperature curve of SiC is shown with labels of the different dominant effects in the ionization, extrinsic, and intrinsic regimes. The onset of the intrinsic regime here is added qualitatively for instruction, and is not generally observed in in the operation of SiC elements, due to the high doping content [42].

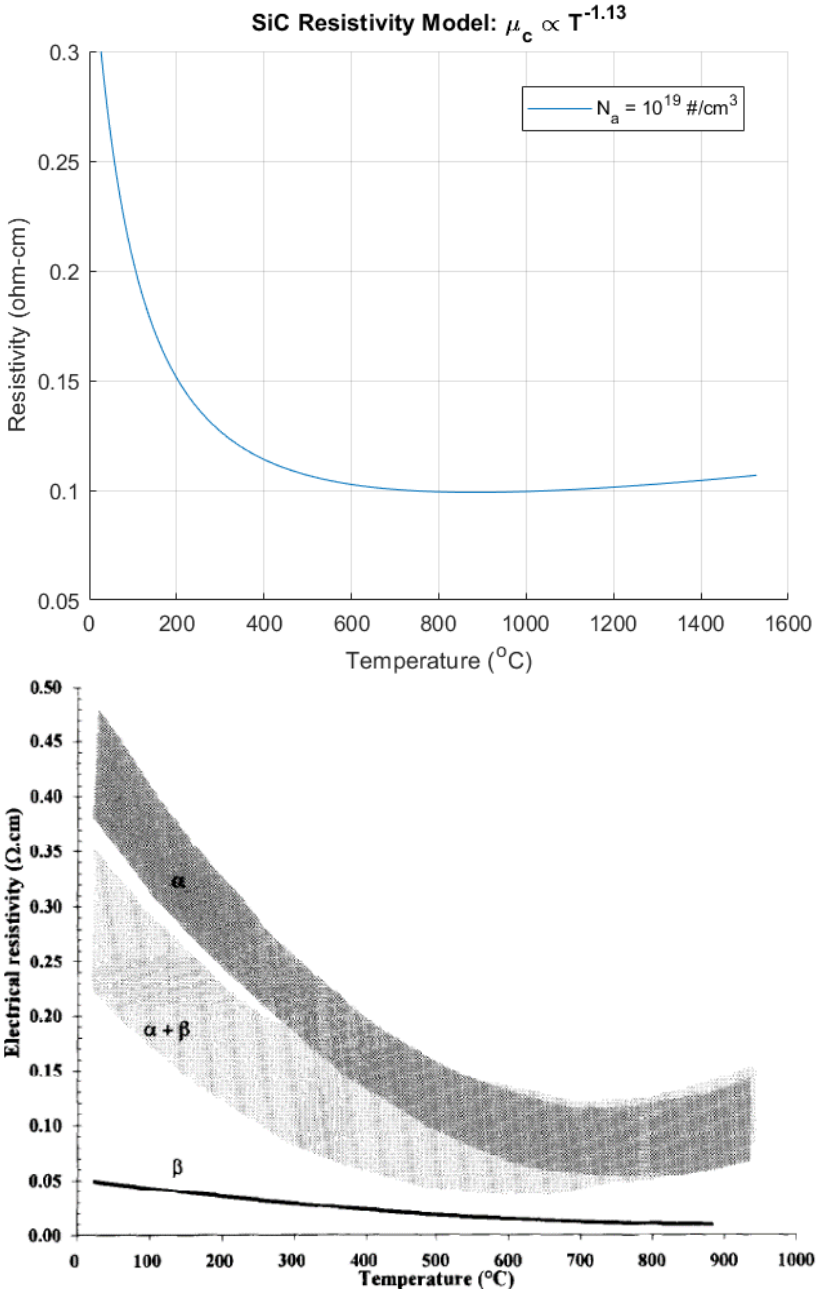

Figure 18: Comparison of modeled resistivity and measurements of SiC.
a): Modeling of resistivity of 10^{19}/cm^3 N-doped SiC with mobility trend based on same properties of (b), with prescribed resistivity $\rho = 0.1$ ohm-cm at $T = 1000$K, informed by [44]. b): Resistivity-temperature behavior of commercial SiC heater elements from [44].

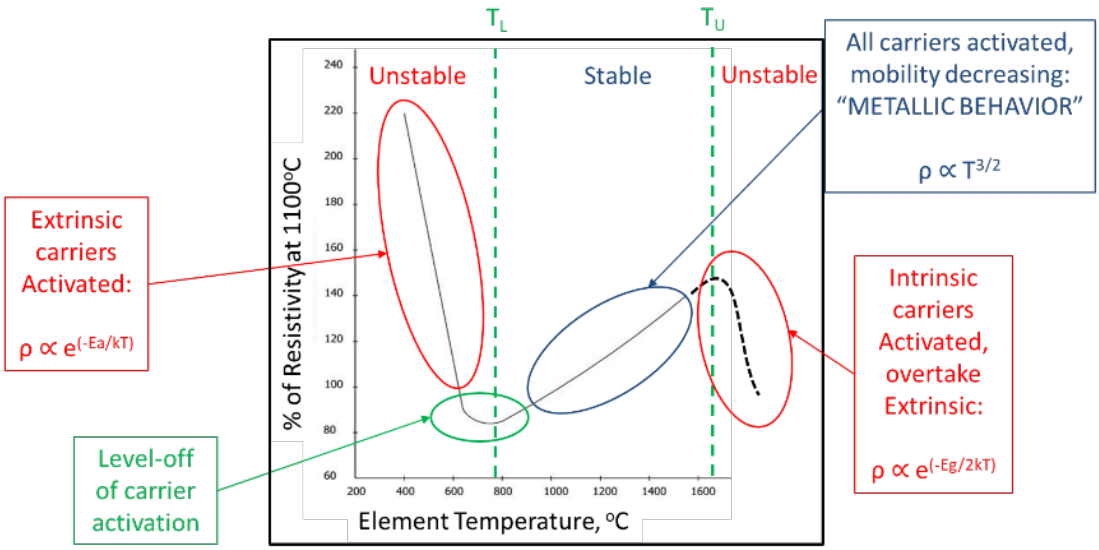

Figure 19: Electrical resistivity versus temperature of a typical SiC heater element.
"T_L" and "T_U" denote the approximate lower and upper bounds of the stable "exhaustion" region, where all dopant has been ionized.In this region, the tendency of thermal runaway is reduced, as RTD is more gradual. Adapted from [32].

3.2.3 Limitations of semiconductor theory in predicting behavior

Much of the semiconductor physics and parameters discussed here are well-defined for the most common semiconductors used in industry such as silicon and silicon carbide, but are poorly defined for many other ceramics, particularly oxides. Common features of industry semiconductors include shallow dopant energy levels, covalent bonding, and achievability of high purities. This leads to clear distinction between the ionization region and exhaustion region, and mobility-temperature trends attributable to the relative magnitude of scattering events. By contrast, many oxide semiconductors possess relatively deep dopant energy levels [39], are ionically bonded, and have been historically difficult to fabricate at high purities [45].

These features create difficulty in interpreting experimental results of electrical measurements, which has led on many occasions to contradicting conclusions about the electrical character of various oxides, particularly whether one exhibits band-like conduction or small polaron hopping [39, 41, 46, 47]. The Arrhenius behaviors of dopant ionization (11) and small polaron hopping (17) may coexist or be mistaken for one another at higher temperatures. Without clearly attributing E_{act} to that of a dopant activation, deriving a characteristic energy level of a dopant using a simple Arrhenius fit will be less reliable. The activation of other unintended impurities or dopant sites also convolutes results. This includes native impurities, such as oxygen vacancies or interstitials, i.e. "oxygen non-stoichiometry" commonly exhibited by transition metal oxides, as well as cation vacancies or interstitials.

Beyond just lack of clarity in estimating dopant energy levels, oxygen non-stoichiometry causes an actual increase in "effective dopant added" with temperature, which is considered a constant in the methods outlined. This occurs in the sense that the material and the atmosphere will reach different equilibria of oxygen in the non-stoichiometric lattice as temperature changes. This may add constructively with the intended dopant if they generate the same carrier type, or counteract the dopant added if they generate opposite carriers, known as compensation. This addition of dopant via changing oxygen content is a thermally activated process as new equilibria are reached, and is well documented in chromium oxide [48-50] and nickel oxide [46]. One way to avoid the effect is to dope far above the expected oxygen non-stoichiometry.

Parameters such as effective masses are not well-established experimentally for many oxides [39]. The use of density functional theory (DFT) calculations has recently led to approximations of such parameters, which may be used for preliminary predictions of electrical behavior for some insight. However, the nuances of effective mass determination, beyond the scope of the present study, involve assumptions and approximations to generalize band theory that may be poor estimates of actual behavior in the methods used here.

Despite the noted shortcomings of these method for predicting exhaustion regions of different ceramics, it can nonetheless serve as a starting point for materials exploration, both for applications in FIRES and other novel joule-heating applications where other ceramics may have advantages over existing ceramic heaters, particularly as

electrification in a variety of high-heat industrial environments becomes a global trend. It is applied herein to a variety of metal oxides in Section 4.

3.3 Considerations of resistivity-temperature derivative (RTD)

The resistivity-temperature derivative (RTD) has serious implications in joule heating compared to most other semiconductor applications, because the material or system response to electricity will heavily depend on the RTD and geometric configuration. For a given starting condition, careful attention must be given to the RTD and the circuit geometry, such that the evolution of heating does not result in failures of runaway heating, which may crack, melt or destroy components of the electric heating system. Figure 20 shows the response of joule-heated materials to an uneven temperature profile in different configurations.

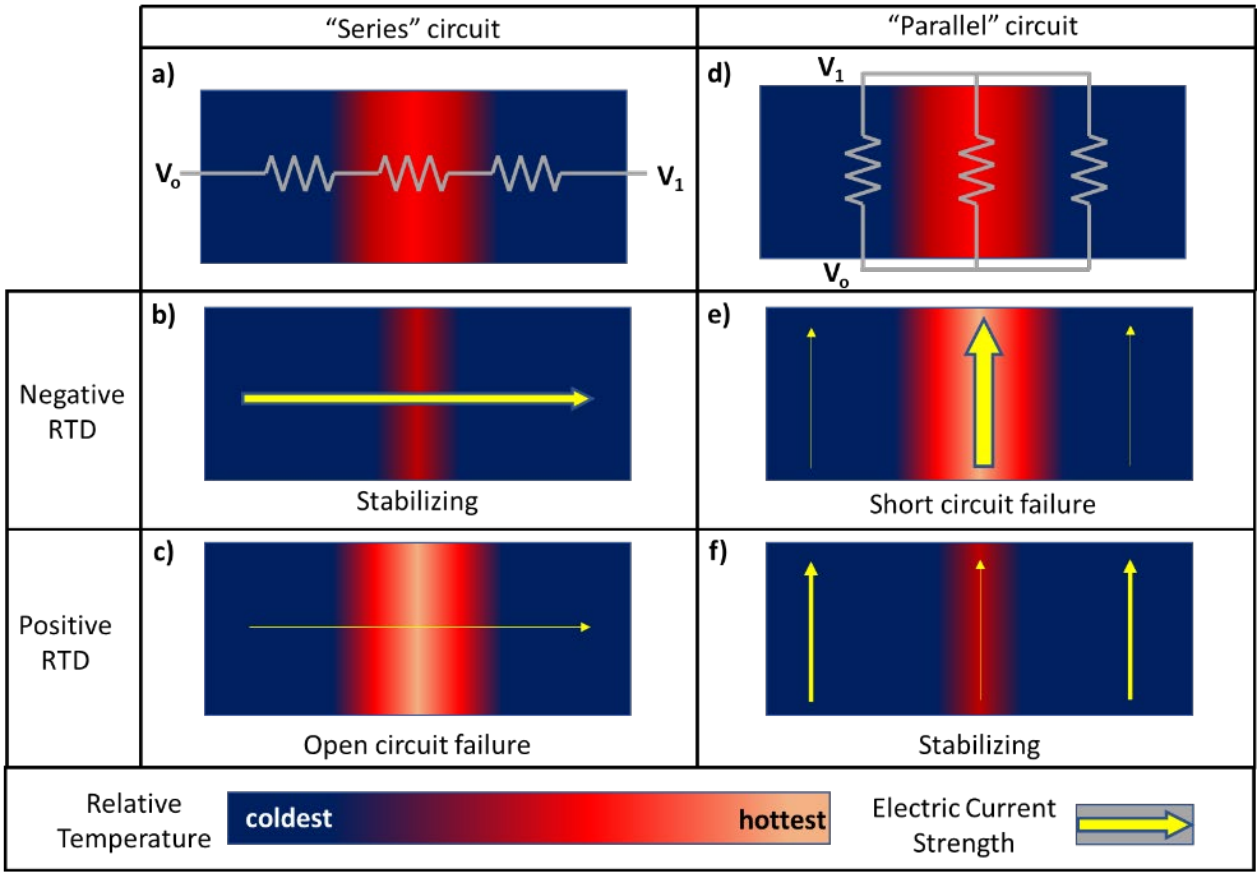

Figure 20: Characteristic thermal runaway behavior in series circuits and parallel circuits with materials of positive and negative RTD.
In an idealized series circuit with a hot zone (a, b, c): If the material has a negative RTD, the hottest region will experience a lower voltage drop, generate less heat, and equilibrate via heat conduction. If the material has a positive RTD, the hottest region will experience a greater voltage drop and generate more heat, causing thermal runaway and resulting in an open circuit failure. In an idealized parallel circuit with a hot zone (d, e, f): if the material has a negative RTD, the hottest region will draw more current because it has lower electrical resistance and heat up further, causing a short circuit failure. If the material has a positive RTD, the hottest region will draw less current, generate less heat, and equilibrate via heat conduction.

In a system where the joule-heated material is relatively long and thin with respect to the electrical current path, the system behavior may resemble a "series" circuit (Figure 20a). In the series circuit scenario, the joule-heating of a negative RTD material (Figure 20b) will experience less voltage drop in the hot locations. The hot region will receive less heat compared to the surrounding cooler regions, and the temperatures will equilibrate as heating continues. In the same scenario, a positive RTD material (Figure 20c) will experience a greater voltage drop in the hottest region, causing greater heat generation and a large resistance. Continued operation would result in an open

circuit-type failure, where the resistance increases until little power can be delivered to the device. This effect can lead to failure in metallic heater wire, exacerbated by the faster oxidation of the hot region.

In a system where the joule-heated material is relatively short and wide with respect to the electrical current path, the system behavior may resemble a “parallel” circuit (Figure 20d), where the current may take the path of least resistance. With a negative RTD (Figure 20e), the hot region will receive more electrical current than the adjacent cold regions, causing more heat generation. With continued operation, a short circuit failure would occur, where the hottest region becomes increasingly conductive and draws dramatically more current, causing a runaway heating effect. This serious instability condition is of concern in SiC heaters below 600ºC, which is why manuals routinely recommend operating above this temperature. In the case of a positive RTD (Figure 20f), the hottest region would instead have a higher resistance than colder material. A larger current will flow through colder regions, resulting in the equilibration of temperature.

The simplified scenarios considered above offer several insights. For operational stability, it is beneficial to configure positive RTD materials in a parallel-type configuration and negative RTD materials in a series-type configuration. There are however other practical considerations for what configurations are adopted, such as matching the circuit resistance with the voltage of the power supply available. It is also very difficult to create stabilizing conditions when working with doped semiconductors that exhibit both positive and negative RTDs at temperatures of interest. Moreover, real materials have a continuum of electrical flow paths rather than discrete paths as depicted above, where either failure mode could occur under different conditions. For these reasons, it is generally best for the RTD to be small, whether it is positive or negative.

Beyond our limited ability to modify the resistivity-temperature derivative of materials with doping, runaway heating threats must be mitigated by designing and operating the system in a way that allows adequate coping time to let temperatures equilibrate via heat transfer. The achievable RTD is therefore a key constraint in the design of FIRES. The different design considerations and options for FIRES are discussed in more detail in Sections 8, 9, and 10.

4 Evaluation of oxide materials for joule heater devices

In this section, different oxide materials are evaluated with respect to their semiconductor properties, their use in electronic applications, and their use and compatibility in refractory applications. Materials that may serve as the electrically active basis of DRH-style firebricks are modeled for carrier exhaustion and operating temperature range as a function of dopant levels, to serve as a basis of comparison for the different options. The results are analyzed and the section concludes with the selection of a material for further investigations.

4.1 Review of candidate oxide materials

Some aspects of interest for different oxide candidates are discussed here. The candidates considered are abundant and generally affordable. Oxides identified as potential candidates are at the intersection of the refractories industry, transparent conducting oxide (TCO) thin film applications, solid oxide fuel cell (SOFC) applications, and others. A number of common oxides not discussed herein were ruled out primarily due to low melting temperatures, such as silica and iron oxide.

Table 5 at the end of this section shows the major material properties of interest of the oxides discussed herein.

4.1.1 Chromium oxide (Cr_2O_3)

Chromium oxide, i.e. chromic oxide or chromia, is a bulk material in firebricks used for high temperature corrosive environments such as gasifiers [51, 52], with a melting point of 2330ºC [53]. Chromia is a preferred material for liners in slag regions due to its excellent chemical stability and spalling resistance [54]. In commercially available firebrick, mixtures ranging from 10% to 90% exist, with the remaining composition consisting mostly of Al_2O_3 and small amounts of sintering aids. The chromia-alumina mixture forms a solid solution in the corundum structure [54, 55].

Chromia, among other metal oxides, has been developed for gas sensing [49] and p-type transparent conducting oxide (TCO) applications [36], where doping with shallow energy levels is a priority. Although past studies have proposed small polaron hopping as the likely mobility mechanism for both p-type and n-type carriers [56, 57], more recent studies and DFT analysis support band conduction as the mobility model for holes [39, 58]. The mobility of chromia has been predicted to be similar to Rh_2ZnO_4, which has been found to have an essentially constant mobility with temperature [47]. Mg and Ni have both been proven as effective p-type dopants in chromia. Doped materials have been fabricated as powders, small pellets, and pulsed laser deposition (PLD) targets using bulk powder mixing [49, 50, 59], and sol-gel methods involving water ethanol and ammonia [60]. Thin films have also been deposited using the PLD targets [59] and spray pyrolysis [61]. Activation energies of these thin films were as low as 0.17eV and 0.07eV for Mg and Ni dopants, respectively, though these values are for thin films in non-equilibrium conditions [36]. Bulk ceramics in thermodynamic equilibrium will likely behave differently. Different studies have shown solubility limits of several atomic percentage (at%) on a cation basis, or $N_a = 10^{21}/cm^3$. Li dopant has also been attempted [62], though with a solubility limit an order of magnitude lower. Ti dopant, an n-type dopant in chromia, is commonly used as a sintering aid at 1-3 at% [63, 64], though no activation energy was found in literature. Chromia is a nonstoichiometric oxide, where excess oxygen acts as a native impurity and increases with temperature, forming holes at $10^{19}/cm^3$ before intrinsic behavior dominates around 1200ºC [48-50]. Dopants should therefore be added at concentrations of approximately $10^{20}/cm^3$.

One challenge in using chromia in high temperature oxidizing gas flows is a tendency to vaporize by oxidation to chromium (VI) oxide, by the reaction:

$$Cr_2O_3(s) + \frac{3}{2}O_2(g) \rightleftharpoons 2CrO_3(g) \tag{18}$$

This reaction has been documented as a problem for alloys that rely on oxide layer formation to protect from further oxidation [65]. The formation and high vapor pressure of CrO_3 gas has also been identified as the cause of poor densification of chromia bodies when sintering in air [66]. The CrO_3 dissociates to Cr_2O_3 on deposition. Despite this reaction, firebrick mixtures of chromia and alumina have recommended operating temperature limits above 1700ºC [54]. It is expected that the mixture of chromia with a sufficient alumina content can dramatically reduce the reaction rate by creating a diffusion barrier. There are also engineering options such as coatings on brick surfaces facing gas flows but not on surfaces where bricks contact each other.

Supposing the vaporization reaction is manageable, the combination of chromia's commercial availability, proven performance as a firebrick, doping potential with Mg or Ni, high melting temperature, and solid solution with alumina make it an excellent candidate for a DRH-style firebrick.

4.1.2 Nickel oxide (NiO)

Nickel oxide is used industrially as an intermediate material for producing other nickel substances. It has historically been investigated as part of refractories industry research [48]. It bonds in the rock salt structure, and has a melting point of 1955ºC. Nickel oxide forms a solid solution with the common refractory oxide MgO. At NiO-MgO molar ratios near 75-25 this can increase the melting point to 2100ºC [67].

Like chromia, nickel oxide was once mistaken as exhibiting small polaron hopping mobility for both n-type and p-type carriers, but has been found to exhibit band conduction for p-type carriers, with a supposed slight decrease in mobility at higher temperatures [39, 41, 46]. Nickel oxide has been researched for use as a TCO, and as an electrochromic (EC) thin film [68], which may be used to change transmittance of glass under an electric field. The most common dopants of NiO are Li and Cu. Li has been demonstrated to have an activation energy from 0.25eV to 0.30eV [46]. The high reactivity of Li has sometimes posed challenges in doping processes [62]. Activation energies for Cu-doped NiO have not been found, but both Li and Cu are 1+ valency and have nearly identical ionic radii with octahedral coordination. Both dopants have solubility limits above several at. %, or $10^{21}/cm^3$. Nickel oxide is a nonstoichiometric oxide. As temperatures rise, the equilibrium changes such that more oxygen enters the NiO lattice,

creating holes in concentrations of $10^{18}/cm^3$ [46]. Dopant levels should therefore be approximately $10^{19}/cm^3$ or higher to avoid effects of exponentially increasing hole concentration.

Although not used in the refractory industry today, nickel oxide is an excellent candidate for DRH-style firebricks because of its relatively active dopant options, and its ability to be blended with MgO, which may be used to lower the material cost and increase its melting point.

4.1.3 Titanium dioxide (TiO_2)

Titanium dioxide, i.e. titania, is used industrially in the production of a wide variety goods, including white paint and sunscreen. In the context of the refractories industry, it is used as an additive sintering aid in some firebricks, specifically chromia-alumina bricks. Otherwise, it is an unintended impurity in firebricks, which may set the temperature limits of a given grade of material, due to the formation of lower melting point phases in the bulk, particularly in the case of silica brick [54]. As with nickel oxide, sintering and electrical resistivity measurements of bulk TiO_2 and mixtures with SiO_2 were explored in earlier research focused on applications for the refractories industry [48]. Titania is stable in the rutile structure, with a melting point of 1855ºC [53]. The lower melting point of titania limits the capabilities of a FIRES unit built from TiO_2-based DRH bricks. Moreover, unlike chromia and nickel oxide, titania does not form a solid solution of another cheaper or more refractory oxide, such as SiO_2 or ZrO_2.

Titania has been commercialized as a UV light-absorbing photocatalyst for many applications, especially for environmental and air purification. There has been significant research for applications in opto-electronics as an n-type TCO, photocatalytic water splitting, and visible spectrum photocatalysis via doping [69-71]. It is worth noting however that much of the interest in titania is not in the rutile phase, but rather the metastable anatase phase, which exhibits high conductivities consistent with band conduction for n-type carriers [39]. TiO_2 in the anatase phase changes irreversibly to rutile at 700ºC [53], which exhibits less mobility via small polaron hopping for both n-type and p-type carriers. Niobium (Nb) is a common n-type dopant in titania. Titania exhibits n-type oxygen non-stoichiometry, where a slight decrease of oxygen in the lattice causes free electrons. At atmospheric pressure, 0.1 at% or more of Nb dopant, i.e. $10^{18}/cm^3$, can become the dominant source of carriers over that of the oxygen effect [72], potentially creating an exhaustion of carriers. From resistivity measurements taken at 1200ºC and 1450ºC, an activation energy likely related primarily to the "hopping" energy was found to be 0.3eV. This creates a large positive RTD that will likely lead to heating instability issues.

Compared to others, a TiO_2-based firebrick is a less desirable candidate, due to lack of maturity as a bulk material in the refractory industry, relatively low melting temperature, and small polaron hopping that leads to challenges in controllable heating.

4.1.4 Zinc oxide (ZnO)

Zinc oxide has many similarities to titania in its industrial use, including white paint, cosmetics, sunscreen, and others. Despite its high melting temperature near 1969ºC, no mainstream use of zinc oxide in the refractories industry was found at the time of writing. It is stable in the wurtzite structure, though thin films at high pressure have been grown in the rock salt structure [73].

Zinc oxide has a large range of applications in optoelectronic devices, such as transparent thin film transistors, photodetectors, light emitting diodes and laser diodes [59, 73, 74]. It is a nonstoichiometric oxide that exhibits n-type band conductivity [75], with reported room temperature carrier concentrations as high as $10^{21}/cm^3$ in supposedly undoped samples [73]. The source of the free electrons has been debated for some time. The most commonly attributed sources are native Zn interstitials or O vacancies, or unintentional doping with hydrogen or other elements. Janotti and Van de Walle [74] conducted a critical review of the DFT literature and concluded that neither native defect can be the dominant source of n-type conductivity; instead, unintentional hydrogen in the form of interstitial or O-substitutional defects is suggested to be most likely source of the high number of carriers. This is considered plausible because hydrogen is present in the most common ZnO fabrication processes, and can easily diffuse [73, 74]. To overcome the unintentional dopant behavior, doping in excess of the hydrogen impurities with Al is common, at levels of several at%, or $10^{21}/cm^3$ [58, 76].

The O vacancies and the presence of unintentional hydrogen both function as a source of compensation, which make attempts to dope ZnO p-type very difficult. This is further exacerbated by the small ionic radii of most lower valency cations that could substitute Zn, namely Li, Na, K, or Cu. The small ionic radii causes them instead to partially occupy the interstitial sites of the wurtzite structure, where they instead act as donors [73]. Should p-type doping be achieved, hybrid functional calculations suggest the hole transport mechanism would be that of small polaron hopping [77].

There remains a fair bit of uncertainty about the practicality of zinc oxide in its application as a high temperature joule heater, given that a great deal of the research reviewed is focused on thin films at relatively low temperatures, with a large dependency on native impurities and unintended hydrogen doping that may behave very differently in a bulk high temperature regime. Zinc oxide remains a potential candidate.

4.1.5 Aluminum oxide (Al_2O_3)

Aluminum oxide, i.e. alumina, is a ubiquitous material in the refractory industry. Mixtures of alumina in bricks range from 18% to 99%. Alumina is commonly mixed with silica, chromia, and carbon. Alumina-silica firebricks are used in hot blast stoves, with higher alumina content bricks being used in hotter portions. Pure alumina has a melting point near 2054°C [53]. Solid solution alumina-chromia corundum mixtures are used to resist acidic slags, where a higher chromia content grants greater performance, though at higher cost [54]. In Cr_2O_3-based DRH firebricks, the blending of chromia with alumina may lower the overall material cost, with the tradeoff of lowering the melting temperature closer to that of alumina. A survey of online prices and discussions with vendors have indicated that Cr_2O_3 is typically a factor 10 more expensive than Al_2O_3, such that the material cost will be sensitive to the exact composition.

Alumina is a highly insulative material, with a band gap near 8eV and no shallow energy dopants. A variety of p-type and n-type dopants, such as Mg, Ti, and Co, have been reported to have activation energies ranging from 2-4eV [78, 79], which never display an exhaustion region through high temperature measurements [80]. It has proven uniquely challenging to characterize charge carrier transport mechanisms in highly insulative materials such as alumina, due to measurement difficulties involved with measuring few carriers and low mobilities [81, 82], and limited modeling capabilities for predicting the occurrence of self-trapping in oxides [83, 84]. One widely cited 1990 review of Al_2O_3 electronic band structure, while commenting on the limitations of current density functional methods and calculations, stated that electrons and holes in Al_2O_3 would both be expected to form large polarons, based on the relatively wide oxygen 2p energy band [85]. Around the same time, time-resolved microwave conductivity measurements were taken on Al_2O_3 powder, in which radiation pulses of 3 MeV electrons were used to excite carriers. The result was an intrinsic mobility of 3e-4 cm^2/Vs [81], many orders of magnitude below large polaron mobilities [41]. Decades later, the application of newer "hybrid functionals" in density functional theory has predicted that self-trapped holes are more energetically stable than delocalized holes in Al_2O_3 along with several other common oxides, and that p-type conduction in these materials is prohibited [86]. Despite the lack of clarity regarding the transport mechanisms in alumina, some practical questions of the interaction between alumina and chromia in a p-type doped system were explored in a broad experimental study of oxide mixtures [48]. The alumina-chromia mixtures showed p-type conduction, due to the non-stoichiometry of the chromia. With mixtures of only 37% chromia or more, the relative shape of the resistivity-temperature trend was far more similar to that of pure chromia than that of pure alumina. Another mixture added 1% Mg dopant, to a nearly 50-50 ratio of Al_2O_3-Cr_2O_3; the result was a similar shape to the undoped case, with a factor 50 lower resistivity. This study displayed an exponential RTD, but shows promise for the chromia-alumina system.

4.1.6 Magnesium oxide (MgO)

Magnesium oxide, i.e. magnesia, is a common and inexpensive bulk material in firebricks and other refractory ceramics. It possesses a very high melting point of 2852°C [53]. Basic firebricks, i.e. firebricks that resist corrosion of chemically basic slags, may have magnesia contents of 90+%. Magnesia is also commonly mixed with chromia to form the spinel phase $MgCr_2O_4$, and more recently mixed with carbon in quantities of 2.5-30% for functions in the hearth of electric arc furnaces [54]. Although highly electrically insulative and having no shallow dopant options, the mature application of magnesia in firebricks as well as its potential to form a solid state solution with NiO-based DRH firebricks makes it a promising candidate, with benefits of lower cost and an increased operating temperature.

Although not a site of dopant activation, the increased presence of Mg in the NiO-MgO rock salt structure will alter the electrical behavior from that of pure NiO, making carrier mobility in MgO important. As with alumina, the mobility character of holes and electrons in magnesia has been debated for decades, due to a lack of appropriate models for describing the relatively complex interactions of ions in oxides [83, 84], and the experimental challenges of observing charge carrier behavior in highly insulative materials [81, 82], with added challenges of impurities and surface non-stoichiometry. In the case of [81], time-resolved microwave conductivity techniques were used to generate carriers: radiation pulses of 3 MeV electrons were used to excite carriers in MgO powders. The primary carrier possessed a mobility of 20 cm^2/Vs, several orders of magnitude above the carrier mobility associated with small polaron hopping, typically estimated by the Bosman-Van Daal limit of $<< 0.1$ cm^2/Vs [39, 41]. However, the radiation itself played a role in "trap deactivation." As recently as 2017, a study of mobility in MgO for applications in a

magnesium-air battery noted the transport mechanisms of MgO remained a matter of debate; the study concluded that the MgO-MgO_2 system exhibits sluggish charge transport, that the little conductivity that does exist is electronic rather than ionic in nature, and that the carriers are holes that exhibit thermally activated polaron hopping [87]. The small polaron hopping of holes in MgO may turn the RTD exponential in the NiO-MgO system, while also lowering the overall mobility. This may limit the amount of Mg that may be used in NiO-based DRH firebricks.

4.1.7 Zirconium dioxide (ZrO_2)

Zirconium dioxide, i.e. zirconia, was of interest due to its use in refractory ceramics and ionic conduction applications such as solid oxide fuel cells (SOFC). Although highly refractory and possessing excellent chemical inertness, and having a high melting point of 2710°C, zirconia has three temperature-dependent phases: monoclinic up to 1205°C, tetragonal from 1205°C to 2065°C, and cubic from 2065°C to 2710°C [53]. These phase changes, along with high cost, has limited the wide-spread use of zirconia in refractories [54]. Phase changes are generally undesirable due to density and property changes. For use as a firebrick that spans these temperature ranges, bulk zirconia must either be stabilized in one phase, such as with yttria (Y_2O_3) calcium oxide (CaO), or ceria (Ce_2O_3), or bonded at higher compositions into a different phase entirely, such as zircon ($ZrSiO_4$). In its typical stabilized phases, zirconia sees use as an electrolyte in SOFCs, where the stabilizing material also improves the mobility of ionic charge carriers in the electrolyte.

The electronic mobility in stabilized zirconia is characterized by small polaron hopping for both n-type and p-type dopants [88, 89]. The lower valency of yttrium, calcium and cerium also act as p-type dopants within the structure. The activation energies of these dopants are in the range of 0.85eV to 1.4eV [89-91], indicative of very deep energy levels that will not achieve exhaustion. Additionally, stabilized zirconia has a tendency to thermally age, where the stabilizer tends to migrate out of the material at temperatures of 800-1400°C [54]. Because zirconia does not form a solid solution with the rutile structure, it is also a poor fit to enhance the melting point of a high-TiO_2 mixture.

4.2 Exhaustion region prediction in candidate oxides

As a companion to the qualitative review of materials above, it is informative to use the methods outlined in Section 3.2.2 here to compare the relative behavior of the candidate oxides in terms of their expected exhaustion regions. Based on evaluations of the different oxides, only four materials are examined here: chromia, nickel oxide, titania, and zinc oxide. A generic dopant energy level of 0.3eV was used in all cases, except in the case for n-type ZnO, which has been reported as having an ionization energy level of 0.12eV for Al dopant [74]. A T_{max} for each material was loosely set near their melting point. In the case of NiO, T_{max} was set near 2100°C because of the potential to be mixed with a small amount of MgO to increase the melting temperature. In practice, all materials would likely be operated a margin below their respective T_{max}. Table 4 shows the model inputs. Results are shown in Figure 21.

Table 4: Inputs to carrier concentration calculations as a function of temperature for candidate materials.

Property [39]		Cr_2O_3	NiO	TiO_2	ZnO [92]
E_g	eV	3.2	3.5	3.0	3.3
Dopant type	-	p-type	p-type	n-type	n-type
E_a, E_d	eV	0.3	0.3	0.3	0.12 [74]
m^*_n/m_0	-	6.5	4.6	2	0.24
m^*_p/m_0	-	13.3	7.2	5.1	0.78
g_a, g_d	-	6	6	2	2
T_{max}	K	2500	2400	2200	2300
T_L condition	-	-30% $N_{a,d}$	-30% $N_{a,d}$	-30% $N_{a,d}$	-30% $N_{a,d}$
T_U condition	-	+30% $N_{a,d}$	+30% $N_{a,d}$	+30% $N_{a,d}$	+30% $N_{a,d}$

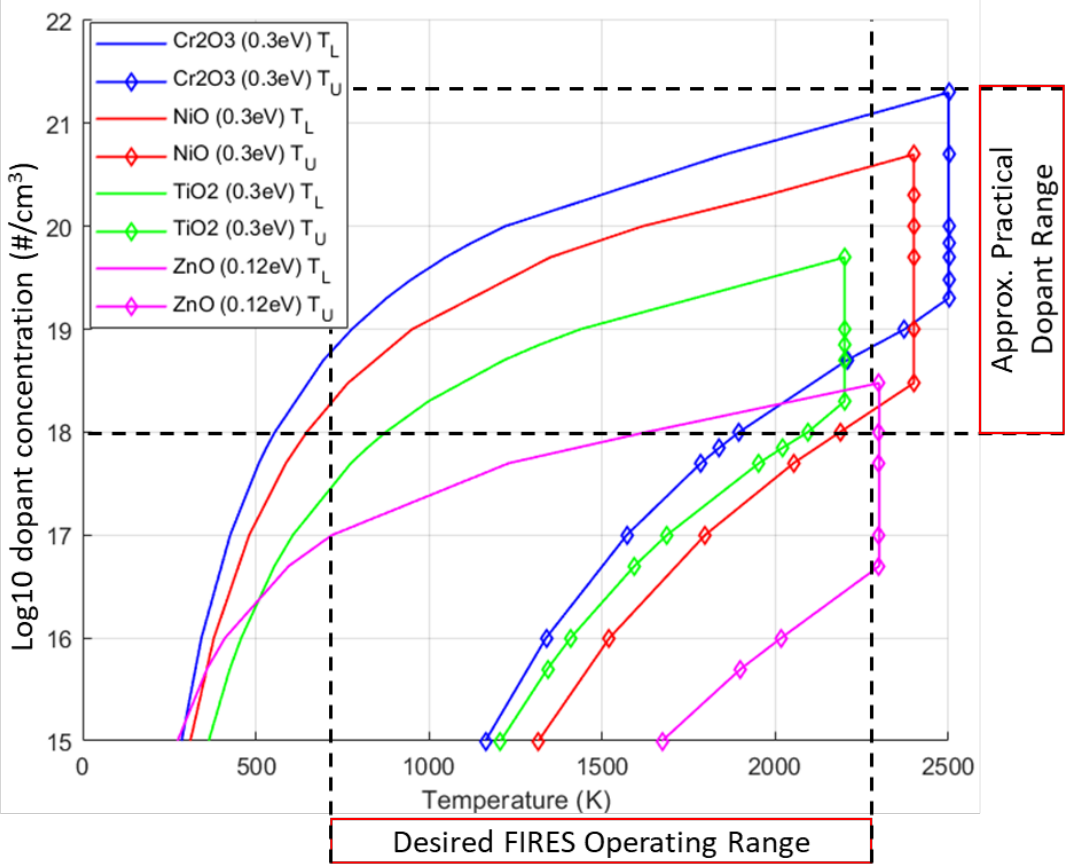

Figure 21: Comparison of exhaustion range of oxide candidates at different dopant concentrations.
Inputs are in Table 4. A generic dopant energy of 0.3eV was use except for ZnO, where the 0.12eV was used, based on that reported for Al-doped ZnO [74]. Calculations are based on formulations from [34].

Each material can be seen to have an optimal dopant regime, above which they show no exhaustion region, and below which they have not yet reached $T_U = T_{max}$, In the case of ZnO and TiO_2, the exhaustion region vanishes in $10^{18}/cm^3$ and $10^{19}/cm^3$, respectively. This corresponds to dopant levels of approximately 0.005% and 0.05%, respectively. This is of concern when considering that impurity content may disrupt the dopants added at these low levels, as will unavoidable effects of non-stoichiometry, which are not accounted for in these calculations.

In the case of titania, which is a known small polaron conductor of electrons that exhibits hopping mobility, thermally activated carriers and thermally activated mobility throughout most of the operating range of interest will likely create a large exponential RTD unacceptable for joule heating applications such as FIRES. This analysis may thus disqualify n-type doping of TiO_2 from use in joule heater applications.

In the case of ZnO, known to be an n-type band conductor, the T_L and T_U shown here may again be misleading as it was with SiC, where the negative mobility derivative $d\mu_c/dT$ substantially broadened the envelope of exhaustion, and the criteria RTD = 0 was a truer indicator of a T_L and T_U that sets an operating regime. As such, zinc oxide may find doping above $10^{19}/cm^3$ acceptable.

The operating envelopes of nickel oxide and chromia are shifted upward relative to titania and zinc oxide due to their large effective masses. The tops of their exhaustion regions appear at $10^{20}/cm^3$ and $10^{21}/cm^3$, respectively. It is worth noting that despite both these materials being theorized as heavy hole band conductors, the mobility derivatives of Cr_2O_3 and NiO are not strongly negative (indeed, if they were strongly negative, decades of debate would have likely been avoided). Chromia and nickel oxide will likely have an operating region defined by a slightly positive RTD, relating to the continued gradual activation of dopant until intrinsic character activation overtakes the extrinsic carriers. It is therefore expected that, unlike SiC and perhaps ZnO, the criteria of exhaustion used here is a reasonable one for chromia and nickel oxide.

Based on observed oxygen non-stoichiometry of chromia [49], intentional doping with Mg or Ni at $10^{20}/cm^3$ may be required to dominate the oxygen effect and see exhaustion. this results in a T_L near 1300-1500K, with the

assumption of a 0.3eV acceptor level. Similarly, the effect of excess oxygen levels observed in NiO may be overcome by dopant levels of $10^{20}/cm^3$, corresponding to a T_L of 1000-1200K. This is not far from the dopant levels and T_L of SiC. The result will have great sensitivity to the actual dopant energy levels achievable by the dopant options in bulk sintered bodies. Chromia and nickel oxide are therefore considered two of the most promising candidates.

4.3 Summary and material selection

From the oxides examined, chromia, nickel oxide, and zinc oxide have large polaron mobilities for their primary carriers. Chromia, nickel oxide and titania show compatibility or operational experience within the refractory applications, though the latter exhibits small polaron hopping for both p-type and n-type carriers.

Alumina and magnesia are expected to both serve as useful electrically inactive materials to be blended with chromia or nickel oxide in solid solutions that may have potentially little negative effect on the electrical character of the constituents. In the case of chromia, alumina lowers the melting point somewhat, but also lowers cost, and can serve as a barrier to vaporization of Cr_2O_3 via reaction (18). MgO may be blended with NiO to both lower cost and increase operating temperature. Stabilized zirconia was considered a potentially attractive candidate for use in DRH firebricks, with excellent peak temperatures, but has dopant levels that are too deep, and does not have phase compatibility with the other options identified.

Chromia was selected as the most promising candidate to serve as the basis for a doped directly resistance-heated firebrick heating system. As such, the focus of the remainder of the study is primarily on chromia. The key factors in the decision were the recent publications on highly active p-type dopants and the commercial use of the material as a refractory oxide in contrast to nickel oxide. Nickel oxide is considered a promising secondary candidate and is expected to be well-suited for DRH-style firebricks. The review of zinc oxide herein suggests that a great deal more qualification is needed of the electrical properties for prolonged operation at high temperatures.

Table 5: properties of oxide materials of interest.

Bulk Material		Crystal Structure [53]	Cation Charge	Stability Range (°C) [53]	Band gap (eV) [39]	DOS m_n* [39]	DOS m_p* [39]	n-type mobility model [39]	p-type mobility model [39]	Dopant Options	n-type activation energies	p-type activation energies
Aluminum Oxide	Al_2O_3	Corundum	3+	2054	8 [93]			BC [79, 85] SPH [86]	BC [78, 85] SPH [86]	Ti, Mg, Co [80]	Ti: 3.48-3.78 eV [79]	Mg: 2.03 eV [78]
Magnesium Oxide	MgO	Rock salt	2+	2852	8 [94]				SPH [86, 87]			
Nickel Oxide	NiO	Rock salt [67]	2+	1955 [67]	3.5	4.6	7.2	SPH	BC	Al, Li, Cu	Al: 0.3-0.5 eV [95]	Li: 0.3 eV [46]
Chromium (III) Oxide	Cr_2O_3	Corundum	3+	2330	3.2 [96]	6.5	13.3	SPH	BC [39, 58] SPH [56, 57]	Mg, Ni, Ti [64] Li [62]	Ti: N/A	Mg: 0.17 eV; Ni: 0.07 eV [36]
Titanium Dioxide Rutile	TiO_2	Tetragonal	4+	1855	3	5.1	2	SPH	SPH	Nb [72]	Nb: 0.17-0.35 (E_h) [72]	
Zirconium Dioxide: Yttria-Stabilized	$Y:ZrO_2$	Cubic	4+,3+	2710				SPH [88]	SPH [89]			Y: 0.85-1.05 eV [90] Ca: 1.3-1.4 eV [91] Ce in YSZ: 0.89 eV [89]
Zinc Oxide	ZnO	Wurtzite	2+	1969	3.37 [92]	0.24 [92]	0.58-0.78 [92]	BC [73, 97]		Al, H, Li, Zn [76, 97]	Al: 0.01 eV [59] Other: 0.05 eV [97, 98]	

BC = Band conduction, SPH = small polaron hopping.

5 Experimental methods

The experimental efforts of this work can broadly be split into two phases: testing of commercial firebricks, and testing of lab-fabricated samples. By testing commercial firebricks, the current state of high-chromia and other firebricks could be better understood in the context of the broader aims of this work. The findings of commercial brick testing helped guide the lab-fabricated phase, and served as a basis of comparison for performance. The lab-fabricated phase aimed to determine the relevant properties and behaviors of chromia-based ceramics that may be used to simulate broader system behaviors of a DRH FIRES unit in later sections.

Each phase generally consisted of testing bulk resistivity and brick-brick contact resistivity, as a function of load, temperature, cycling, or dopant levels. The lab-fabricated experimental phase culminated in the proof-of-concept direct resistance heating of a small stack of samples. The more specific aims and experimental methods of each phase are discussed herein.

5.1 Commercial chromia firebrick methods

Samples of a variety of commercial firebrick were provided by Harbison-Walker International (HWI). The commercial firebrick of focus was SERV® 95 DC, due to its high chromia content. The appendix, Section 13, contains results of some other firebricks tested including SiC varieties. The samples were provided as 4x4x5cm^3 bricks. Each sample weighed 260(+/-5) g, owing to slightly different dimensions of their cut. Product data is shown in Table 6.

Table 6: product data of SERV®95 DC, provided by HWI

SERV® 95 DC	
Approximate Chemical Analysis (Calcined Basis)	
Chromium oxide (Cr_2O_3)	92.2%
Alumina (Al_2O_3)	5.1%
Titania (TiO_2)	1.1%
Others	1.6%
Physical Data (Typical)	
Maximum Service Temperature	1760°C
Bulk Density	3.73 g/cm^3
Modulus of Rupture	21.4 MPa
Apparent Porosity	25%

5.1.1 Room temperature testing of bulk resistance and brick-brick contact resistance

The samples were tested for bulk resistance and brick-brick contact resistance under load. Figure 22 shows the experimental setup. The brick or brick stack (known hereon as the stack) was placed in a load test machine between two metal foils, where there were three types of resistances: the bulk resistance of the brick R_b, the brick-brick contact resistance $R_{b\text{-}b}$, and metal-brick contact resistance $R_{m\text{-}b}$. The stack resistance R_{stack} can be generally expressed as:

$$R_{stack} = \sum_{1}^{X} R_{b,x} + \sum_{1}^{X-1} R_{b-b,y} + 2R_{m-b} \tag{19}$$

where X denotes the number of bricks in the stack. The load machine was used to change the load on the brick stack and measure the contact resistance response. In general, contact resistance is a function of the effective area of electrical flow created by two contacting surfaces, which increases with load as surface asperities are flattened out by plastic deformation, elastic deformation, or fracture [99, 100]. The crumbling or flattening of taller asperities can also cause more asperities to participate, increasing the contact area. All these mechanisms follow a power law function, such that a generic contact resistance can be related to load by:

$$R_{contact} = kP^{-\alpha} \tag{20}$$

where P is the contact pressure, and k and α are material-dependent constants relating to the deformation mechanisms of the materials involved. Elastic deformation of asperities is associated with a load exponent of 1/3; fracturing of asperities that cause more contact sites is associated with a load exponent of 1; fracturing of asperities that causes a larger contact area per site is associated with a load exponent of 1/2. The load exponent α is typically between 1/3 and 1 depending on the relative magnitude of each mechanism [99]. In the cases of two different materials, the behavior of the material more easily deformed by load tends to dominate.

A test voltage V_{test} was applied across the stack in series with a known resistor R_{known}. By the voltage divider law R_{stack} was determined based on the relative voltage drops across the stack and the known resistor:

$$R_{stack} = R_{known} * \frac{V_{meter}}{V_{test} - V_{meter}} \tag{21}$$

The test voltage was applied using a Keysight 6611C DC power supply, and the voltage was measured using a Keysight 34420A nano volt/micro ohm meter.

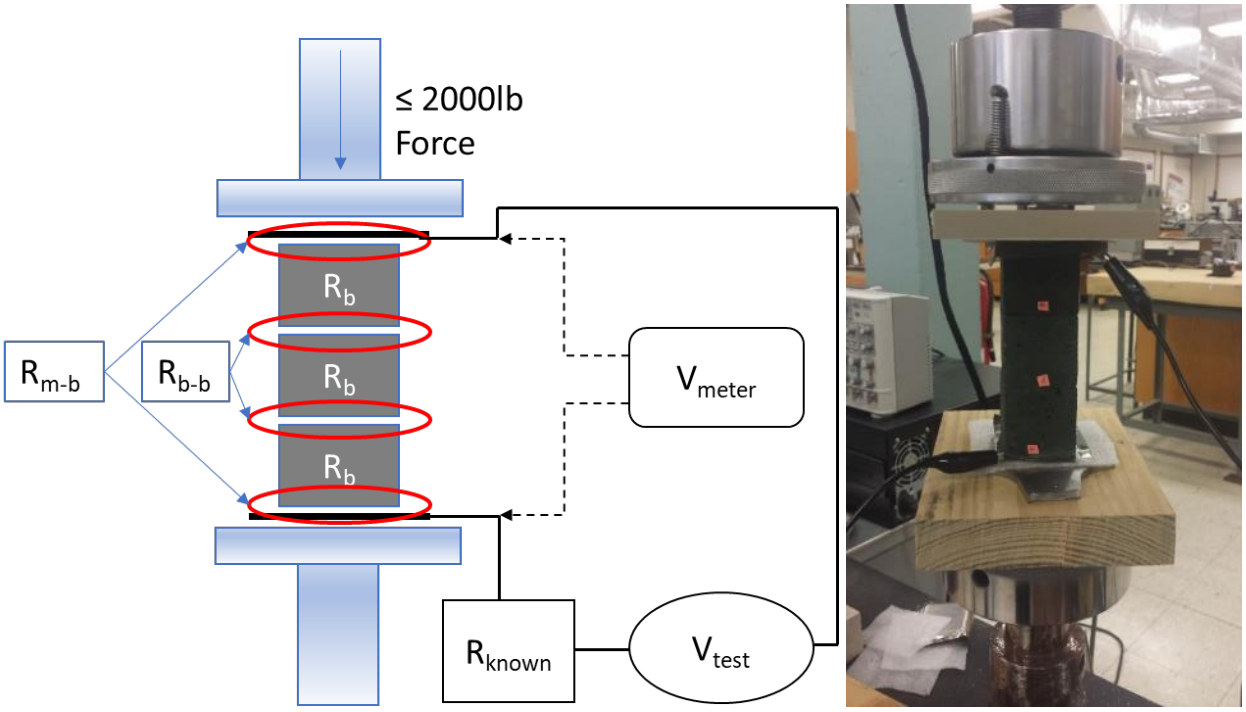

Figure 22: Room temperature bulk and contact resistance experimental setup.

Several testing approaches were taken to separately determine the resistances of equation (19). Five samples were tested in different stack configurations of one, two, or three bricks. Load was applied up to 2000lb, or approximately 4500 kPa, via the load test machine. Load was changed by 25lb increments at low load, then increasing by increments of 50, 100, and 200lb at higher load. A time-dependent electrical response to the changing resistances was observed, presumably due to some capacitance. Load-up was done steadily, with a few seconds between measurements, with little settling time. During load-down, a longer settling time of several minutes was permitted at each point.

After bare brick-brick and metal-brick tests, two samples were platinized via evaporation with 0.2 μm of platinum (Figure 23), with the intention of dramatically reducing both types of contact resistances for the isolation of the bulk brick resistance in the previous measurements. The results of the two platinized samples were extrapolated to the other samples without further need for platination. As a precautionary step, the samples were heated in the furnace up to 1200ºC for 12 hours and measured again prior to platination, to ensure no electrically resistive layers would form underneath a platinized surface during heating; this had previously ruined the bulk resistivity-temperature

measurements of SiC bricks tested (Section 13). The combination of measurements was used to determine with fair accuracy the resistances of the brick samples, as well as the brick-brick contact resistance as a function of load, fitted with an appropriate load exponent α.

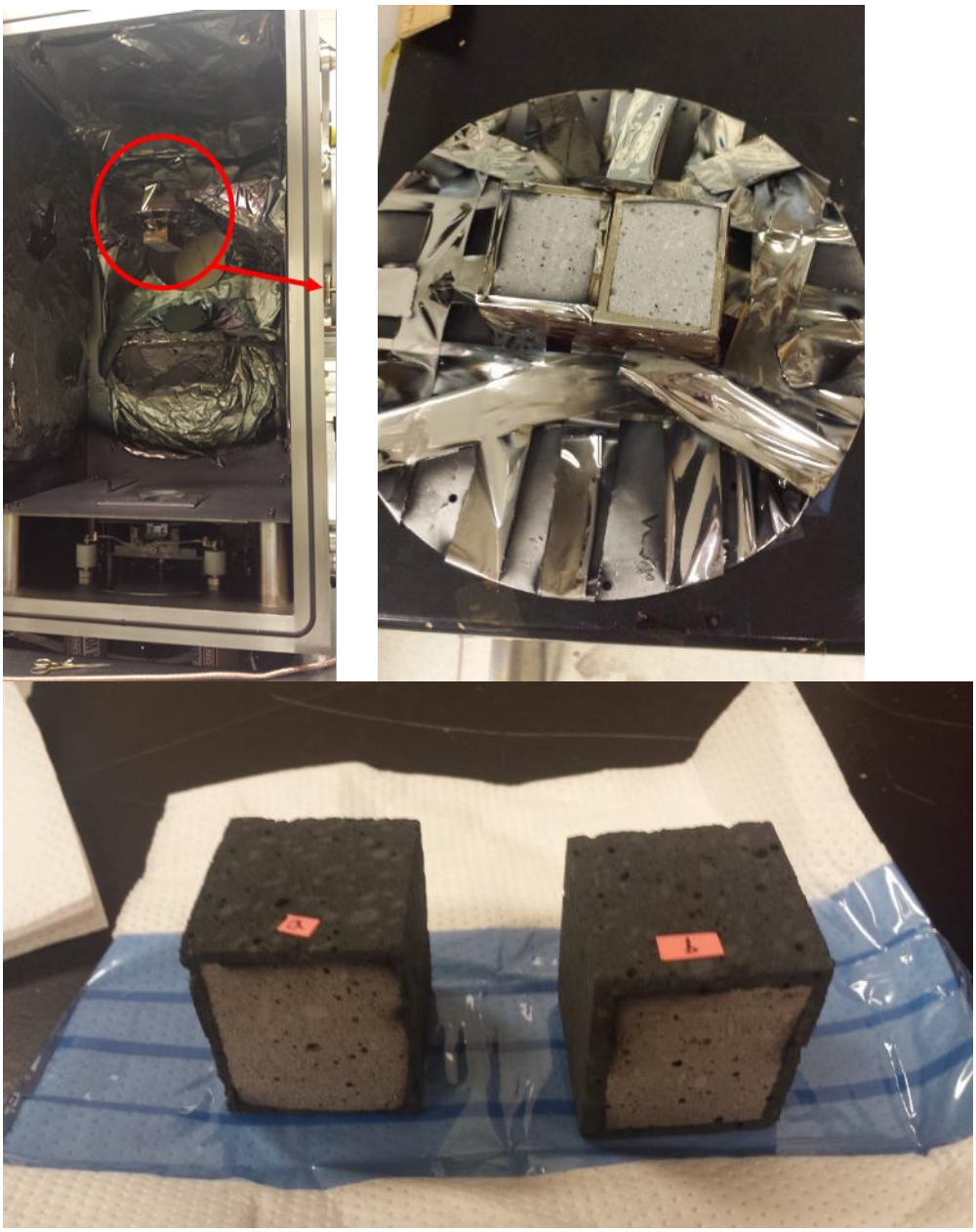

Figure 23: Platination of brick samples in evaporator.
Top left: bricks are suspended from sample holder upside down, secured by Kapton tape. Top right: Sample plate after evaporation. Bottom: Finished result.

5.1.2 Resistivity-temperature measurements

Following room temperature testing, the electrical resistivity of a platinized SERV® 95 DC sample was measured as a function of temperature in a Lindberg BlueM box furnace. In total the sample was cycled 13 times. The measurement setup is shown in Figure 24.

The firebrick was placed in the furnace between two platinum foils (Figure 24a), with a small weight placed on top to hold the top foil in place and make good contact. Platinum wires were spot welded to the foils, and led out of the furnace chamber. The platinum foils and wires are necessary to survive the high temperatures.

For the first 5 cycles, a setup was used very similar to that of the resistivity-load test (Figure 24b). As the firebrick resistance dropped exponentially (sometimes by 9 orders of magnitude), this setup created lingering capacitance across the brick as the voltage drop changed dramatically. The result was measurements of "negative" resistance at high temperatures, even with hours of soak time. The problem was lessened but persisted even when using relatively low known resistance values R_{known}.

After the first 5 cycles, the room temperature resistance of the sample dropped below 1 M-ohm, within the measurement limits of the ohmmeter capabilities of the Keysight 34420A. For cycles 6 through 13, the ohmmeter was used to measure resistance in a 2-probe configuration (Figure 24c), where the device automatically altered the test current depending on resistive load. In this configuration, the Keysight 34420A was also used to measure the temperature within the chamber using a type-R thermocouple.

In both setups there is an additional resistance of the platinum wires R_{Pt}, which had a slight impact on results at higher temperatures. This was found to be of little consequence in analysis of the commercial brick testing but is addressed in the measurement setup and analysis of the lab-fabricated samples.

a) 

b) 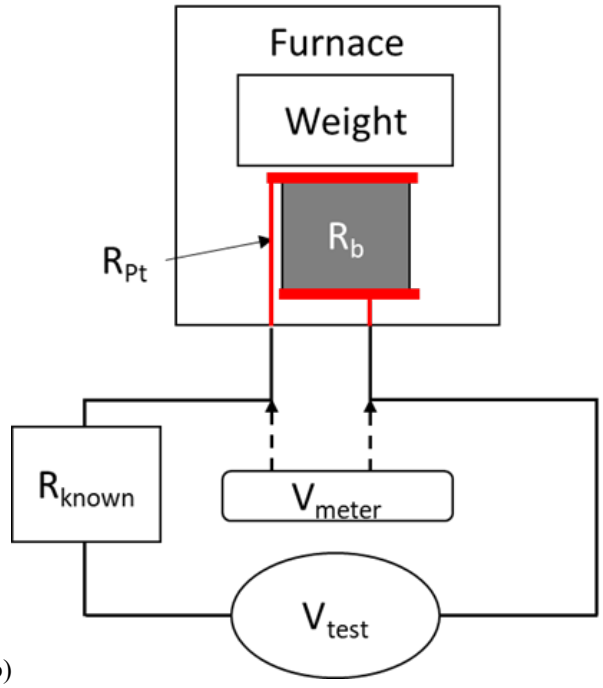

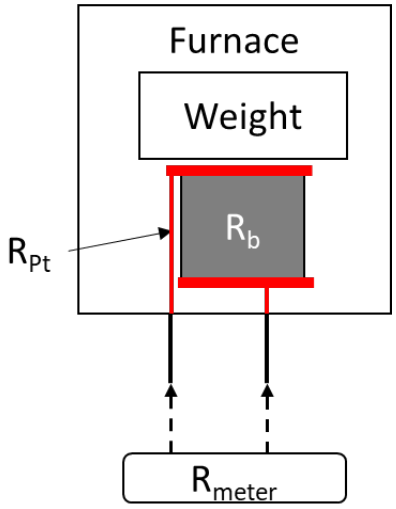

c)

Figure 24: resistivity-temperature measurement setup.
a) image of firebrick sample in the furnace. b) measurement setup for cycles 1 through 5. c) measurement setup for cycles 6 through 13.

The furnace ramp/soak program is shown in Figure 25. Furnace temperature was ramped at 200ºC/hour, and soaking times of 3 hours was used at each point, with the exception of the ramp up to 1500ºC, which was ramped at 100ºC/hour. Soak points at 300, 600, 900, 1200, and 1500ºC during heat-up, and 1200, 900, and 600ºC during cool-down. For cycles 1 through 5, a soak time of 1 hour was used at all points. For cycles 6 through 13, the soak was extended to 3 hours, except at 1500ºC, which was held for 5 hours. Following the soak period at 600ºC during cool-down, the program ended and data was collected until temperature was near ambient.

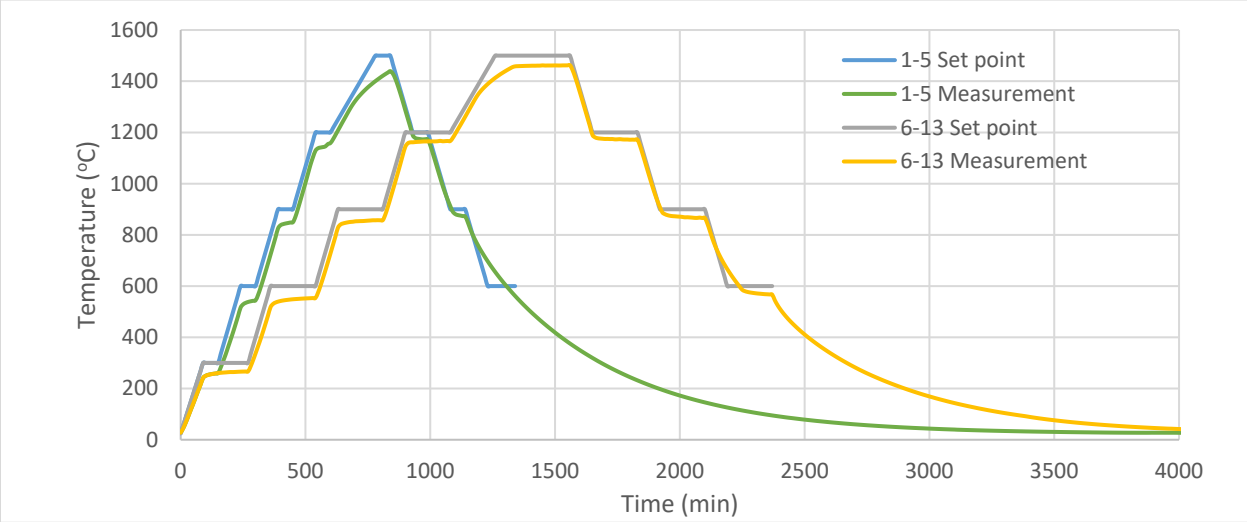

Figure 25: Ramp/soak cycle of commercial firebrick resistivity-temperature measurements.

5.2 Lab-fabricated chromia firebrick methods

The lab fabrication of doped chromia was undertaken with the goals to understand and demonstrate how doping alters chromia to enable a DRH-style FIRES unit. The experimental activities included measuring electrical resistivity data over a large temperature range of interest (from room temperature up to 1500ºC), determining contact resistivities between bare brick-brick surfaces, and performing proof-of-concept experiments that demonstrate the direct resistance-heating of a small stack of electrically conductive ceramic oxides. In the context of developing a DRH-style FIRES unit, these measurements inform broader considerations of system design, and serve as inputs to

the simulations of joule heating large-scale systems in Sections 7, 8, and 9, which examine the threats of excessive heating of brick-brick contacts, and thermal runaway mitigation as a function of the material RTD and geometry.

Secondary goals of the fabrication and measurements included exploring the dopant space of chromia and fill in some gaps within literature. Points of interest included low temperature measurements and activation energies, solubility limits, and the prospects of measuring a positive RTD at high enough temperatures, which would solidly support the claims that chromia exhibits band conduction rather than small polaron hopping.

Much of the resistivity-temperature data reported for bulk doped chromia begins at 500°C or higher, and ends at or below 1400°C [49, 50, 62]. The largest temperature range found was that of Hensler and Henry [48], who reported one MgO-doped chromia-alumina mixture from approximately 600°C up to 1500°C. Without data below 500°C the lower operating limit of these materials as joule-heating devices or DRH-style firebricks cannot be determined, and no activation energy can be calculated. In TCO applications of doped chromia, resistivity is reported at lower temperatures, typically from room temperature up to a few hundred degrees Celsius. From [36], activation energies of Ni and Mg-doped chromia, confirmed to be entirely the corundum phase, are reported as 0.07 and 0.17 eV, respectively. But these results are for sheet resistance of thin films at non-equilibrium conditions, and are likely not representative of bulk behavior. This is supported by the very low resistivity reported of the thin films, several orders of magnitude lower at room temperature than that of high temperature bulk samples. The work herein has therefore aimed at measurements over the entire temperature range, including near-room temperatures, with activation energies.

Doped chromia green bodies were prepared via the Pechini sol-gel method. The Pechini method was not found to be used for Ni or Mg-doped chromia powder fabrication in the literature review. Doped pellet production generally consisted of powder mixing Cr_2O_3 with MgO or NiO [48-50]. Solubility limits for powder mixing methods have been reported as 1 and 4 mol% of MgO and NiO, or approximately 0.5 at% and 2 at% of Mg and Ni on a cation basis, respectively. Beyond these amounts, the $NiCr_2O_4$ or $MgCr_2O_4$ spinel were found to form at the grain boundaries, reducing electrical conductivity. Citing the inadequacies of powder mixing to reach molecular homogeneity and the slow and tedious processing of coprecipitation methods, Chen and Colbow [60] reported an improved solubility limit of 1.25 at% for Mg-doped Cr_2O_3 using a time-consuming sol-gel process that predates the Pechini method by 20 years. The Pechini method, with a focus particularly on nickel doping, was used here for its ease of producing high-purity and homogeneous bodies at laboratory scale, and for testing the relative performance and solubility limit of samples compared to the literature on powder mixing.

Dopant levels of 0.05%, 0.25%, 0.5%, 1.0%, 2.0%, and 4.0% were attempted. However, resistance measurements of the lower dopant samples of 0.05%, 0.25%, 0.5%, 1.0% and 4.0% were muddied by poor contacts and unfavorable geometry, causing non-physical results that could not be compared on the basis of the dopant present. A later series of exclusively 2% doped samples addressed many of these shortcomings, and is the focus of most analysis and discussion. Some discussion and analysis will be presented for others.

5.2.1 Fabrication

Table 7 shows a summary of all samples fabricated, denoted by different series, i.e. “S1-1” denotes series 1, sample 1. Doped chromia samples were produced with cation ratios, i.e. “Do/(Do+Cr)” of 0.05%, 0.25%, 0.5%, 1%, 2% and 4%, where “Do” represents the dopant element. The 0.05% sample was doped with Mg, using relatively impure precursors of chromium nitrate nonahydrate (Sigma-Aldrich, 99% pure) and magnesium nitrate hexahydrate (Sigma-Aldrich, 99.9% pure). all other samples were doped with Ni, using chromium nitrate nonahydrate (American Elements, 99.99% pure), and nickel nitrate hexahydrate (Sigma-Aldrich, 99.999% pure).

Homogeneous powders were prepared by means of the Pechini sol-gel method [101]. In the process, steric stabilization of the cations is achieved by trapping them in a polymer network. A mixture of typically citric acid and ethylene glycol triggers poly-esterification at elevated temperatures. The resulting gel maintains the cations in a homogeneous mixture such that no secondary phases form. The gel can be further heated until it a hardened body that may be crushed into powder.

First the dry nitrate salts were massed and combined in the appropriate ratios. Citric acid was added with a molar nitrate salt:citric acid ratio of 60:40, which serves as the chelating agent. Ethylene glycol was then added in a 2/3 mass ratio of ethylene glycol per citric acid. All components were then dissolved in water, stirred and heated at approximately 100°C for 4 hours. The temperature was then increased to 400°C for approximately one more hour or until the gel was fully solidified. Before the gel became very viscous the stir bars were removed from the beakers. Figure 26 shows the Pechini processing and pressed and sintered samples of the 2% doped samples.

Each body was crushed to fit in a crucible then calcined for 12 hours at 900°C. The material was then ground to a powder in an agate mortar. The powders were uniaxially pressed into cylindrical pellets and rectangular bricks with 2 tons of force, or 90 to 150 MPa depending on sample dimension dimensions. The pressed forms were

sintered for 12 hours, with temperature depending on the sample (Table 7). The samples were pressed in a variety of shapes to achieve different length-to-area ratios to more confidently separate bulk resistivity behavior from that of varying platinized contact resistances between samples.

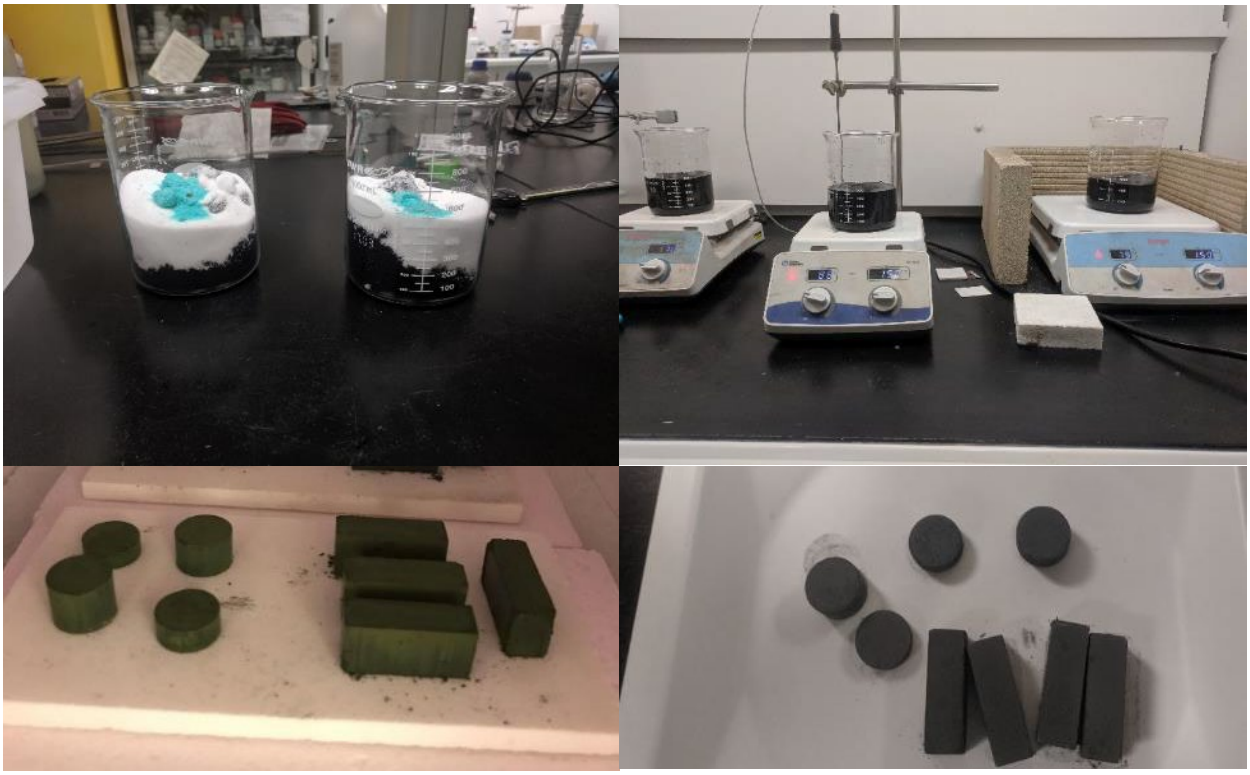

Figure 26: Lab fabrication of Ni-doped chromia pellets and bricks.
Top: Pechini process dry chemicals and solution on hot plate. Bottom: Pressed bodies before and after sintering at 1400°C for 12 hours.

Table 7: Lab-fabricated chromia sample descriptions

Series-Sample	Dopant type	Dopant amount	Shape	Diameter or Width	Thickness	Length	Sinter Temperature	Mass	Relative density
-	-	at%	-	Cm	cm	cm	°C	g	-
S1-1	Mg	0.05%	Cylinder	2	0.3	-	1600	2.4	0.49
S2-1	None	-	Cylinder	-	-	-	1750	3.63	-
S2-2	Ni	0.25%	Cylinder	2	0.4	-	1750	3.22	0.49
S2-3	Ni	0.5%	Cylinder	2	0.4	-	1750	3	0.46
S2-4	Ni	1%	Cylinder	2	0.4	-	1750	2.6	0.40
S2-5	Ni	2%	Cylinder	2	0.4	-	1750	2.94	0.45
S3-1	Ni	4%	Cylinder	2	0.59	-	1400	4.36	0.45
S3-2	Ni	4%	Cylinder	2	0.60	-	1400	4.44	0.45
S3-3	Ni	4%	Cylinder	-	-	-	1400	-	-
S3-4	Ni	4%	Cylinder	-	-	-	1400	-	-
S4-1	Ni	2%	Brick	0.83	2.51	1.13	1400	5.76	0.47
S4-2	Ni	2%	Brick	0.84	2.50	1.15	1400	5.85	0.47
S4-3	Ni	2%	Brick	0.84	2.51	1.20	1400	5.88	0.45

S4-4	Ni	2%	Brick	0.84	2.50	1.16	1400	5.76	0.45
S4-5	Ni	2%	Cylinder	1.30	0.46	-	1400	1.64	0.52
S4-6	Ni	2%	Cylinder	1.30	0.57	-	1400	1.99	0.51
S4-7	Ni	2%	Cylinder	1.30	0.84	-	1400	3.01	0.52
S4-8	Ni	2%	Cylinder	1.30	1.03	-	1400	3.69	0.52

Each sample is denoted by different series, i.e. "S1-1" signifies series 1, sample 1.

Sample densities were generally between 40% and 50% that of theoretical. The samples were relatively fragile, and required delicate handling. Low densities and fragile bodies in pure air-sintered chromia has been widely reported [48, 63, 64]. Although not clearly reflected in the density, samples sintered at 1400ºC were generally stronger than those sintered at 1750ºC. This is attributable to the greater production of CrO_3 at high temperatures by reaction (18), which hinders sintering mechanics [66].

5.2.2 Bulk and contact resistivity-temperature measurements

The setup used for measuring bulk and contact resistivity as a function of temperature was very similar to that used for commercial testing. The setup is shown in Figure 27. The samples were platinized with platinum paint (SPI Supplies, item 04990-AB), and placed in the furnace between two small foils with weight to make good contact. The capacitance issue experienced in commercial brick testing was avoided here with a choice of much smaller known resistor.

The different geometries of fabrication series 4 allowed for the isolation of the bulk resistivity. Similar to the commercial brick analysis, the measurement of a single brick is described as:

$$R_{meas} = R_b + 2R_{m-b} + R_{Pt} \tag{22}$$

where R_b is the bulk brick resistance, $R_{m\text{-}b}$ is the contact resistance between the leads and the platinized brick surfaces, and R_{Pt} is the platinum resistance associated with the portion of platinum leads beyond the nodes of V_{meas}. The platinum resistance is considered here because it is no longer negligible at this sample geometry and dopant level. To reduce the effect of the platinum resistance as much as possible, the voltmeter leads were replaced with platinum leads that could also enter the furnace. The leads were fastened as close as possible to the sample. The remaining platinum resistance was estimated by making room temperature measurements of the contacting foils. The average room temperature measurement was 0.008(+/- 0.002) ohm. Figure 28 shows the equation fitted to literary data of platinum resistivity over the temperature range.

The bulk brick resistance R_b of each identically doped sample can be related by the bulk resistivity ρ_b, which should be constant between samples, by the geometric relation:

$$\rho_b = \frac{R_{b,1}A_{eff,1}}{t_1} = \frac{R_{b,2}A_{eff,2}}{t_2} = \cdots \tag{23}$$

where the numbered subscripts denote different samples, t is the sample thickness from Table 7, and A_{eff} is the effective cross sectional area after accounting for the relative density ρ_{rel} of each sample:

$$A_{eff} = A_{nom} * \rho_{rel} \tag{24}$$

A_{nom} is the nominal cross sectional area of the cylindrical or rectangular samples, as described by the diameter or the length and width in Table 7, respectively. This correction assumes that the porosity can be approximated as a constriction of electrical flow area without significantly affecting flow length.

Similarly, the metal-brick contact resistance $R_{m\text{-}b}$ can be related to a metal-brick contact resistivity ρ_{m-b} , by the relation:

$$\rho_{m-b} = R_{m-b,1}A_{nom,1} = R_{m-b,2}A_{nom,2} = \cdots \tag{25}$$

Here A_{nom} is chosen to define a metal-brick contact rather than A_{eff} because the metal-brick contact resistivity may be associated with poor platinum spreading and on the surface as well as lower effective surface contact area.

The relations here are sufficient to isolate ρ_b and ρ_{m-b} between two different samples if ρ_{m-b} is the same in each case. However, results from earlier series showed ρ_{m-b} is not the same between samples. Multiple samples were therefore compared, and an average was obtained, $\rho_{b,avg}$ and $\rho_{m-b,avg}$.

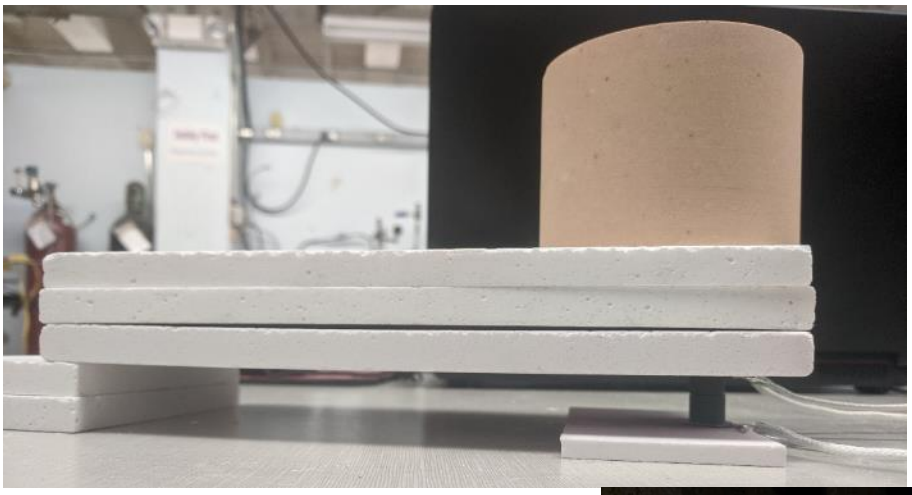

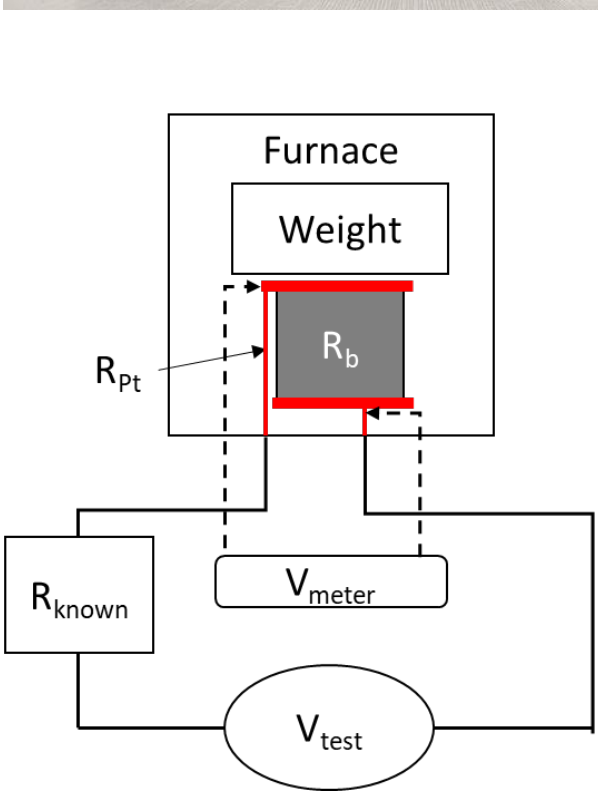

Figure 27: Bulk and contact resistivity-temperature measurement setup for lab-fabricated samples.
Two additional platinum leads were run into the furnace chamber to measure voltage as close as possible to the sample.

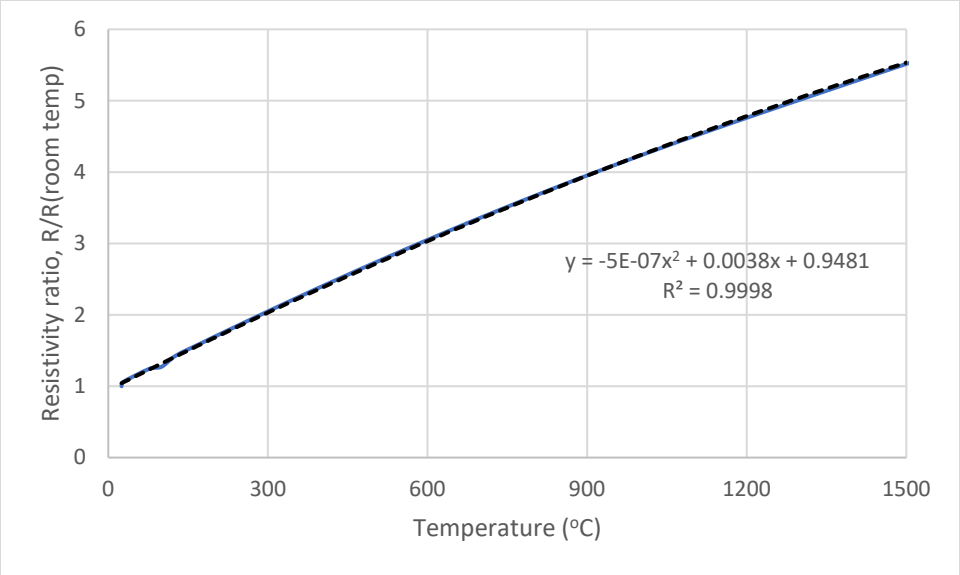

Figure 28: platinum resistivity-temperature trend, used to calculate and subtract R_{Pt} from measurements.

5.2.3 Contact resistivity-temperature measurements

To measure contact resistivity, two cylindrical samples were stacked on top of one another with a bare brick-brick contact between them. The determination of $\rho_{b,avg}$ and $\rho_{m-b,avg}$ can be used to determine an average brick-brick contact resistivity $\rho_{b-b,avg}$:

$$R_{stack} = \rho_{b,avg} \sum_{1}^{X} \frac{t_x}{A_{eff}} + (X-1)\rho_{b-b,avg} A_{nom} + 2\rho_{m-b,avg} A_{nom} + R_{Pt} \tag{26}$$

Here, A_{nom} was chosen as the reference area for brick-brick contact resistance rather than A_{eff}. Depending on the scale of pores relative to surface asperities, the porosity at the sample surface may have a significant reductive effect on the formation of asperity contact sites which is neglected by the use of nominal area. However, the present analysis has not included surface characterization that adequately justifies the use of A_{eff} or another modified area term. In the context of the present work, the use of A_{nom} to calculate $\rho_{b-b,avg}$ and equivalent resistor length is conservative.

To investigate the effect of both load and temperature on $\rho_{b-b,avg}$, multiple ramp/soak cycles were performed, with a load-up and load-down of weight. The weight was applied as alumina shelves supported on one end by the sample and the other end by supports, such that the sample supported approximately half the shelf weight. More shelves could be conveniently added or removed between cycles without disturbing the developed contacts of the previous test. Pressures from 44 kPa to 132 kPa were applied. Prior to any furnace ramp/soak cycles, a simple room temperature load-up and load-down was undertaken.

For all bulk and contact resistivity measurements of the lab-fabricated samples, the ramp/soak program of Figure 29 was used. Heat-up consists of one ramp up to 1500°C over 8 hours, followed by a 7 hour soak, to ensure equilibration of the chamber and provide some sintering time of the platinum paint. Soaks every 100°C were done during cool-down until 900°C. Samples were tested at least twice without removal to see consistency past the first heat-up.

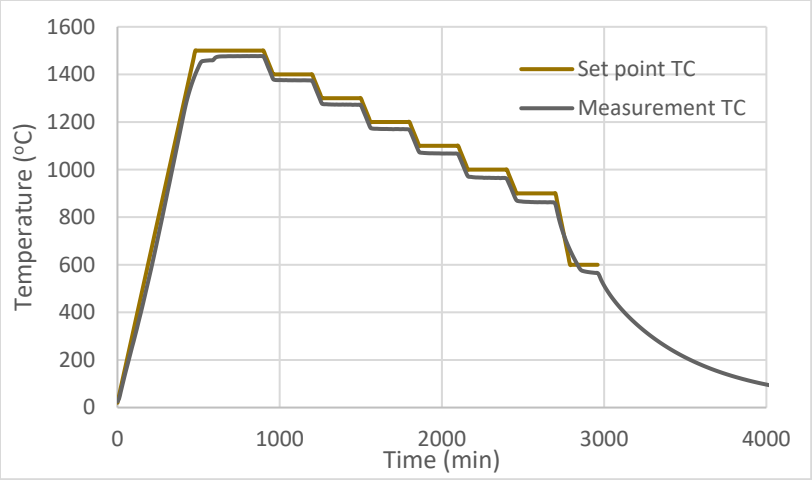

Figure 29: Ramp/soak cycle of lab-fabricated firebrick resistivity-temperature measurements.

5.3 Direct Resistance Heating (DRH) methods

Once contact resistivity measurements of a brick stack were completed, the stack was kept in place to perform a direct resistance heating experiment inside the furnace. A small chamber was built around the stack using highly insulative alumina bricks to reduce heat losses to the surrounding furnace chamber as much as possible. A thermocouple was inserted inside to measure the chamber temperature. Figure 30 shows the chamber and experimental setup.

The same DC power supply and voltmeter were used as before, but the resistor was removed from the circuit. A control program was written to frequently (every 5 seconds) adjust the voltage delivered to the stack as a function of the changing stack resistance, in order to maintain a constant power input during heat-up. Tests were undertaken with input power up to 20W, which corresponds to volumetric heat generation of approximately 8 W/cm^3, and a sample surface wattage loading of 27 kW/m^2. This is similar to typical wattage loadings of commercial SiC heaters [7], which usually have wall characteristic thicknesses of half a centimeter, similar to the test sample. The background furnace temperature was set to 540°C to bring the stack resistance down to a value compatible with the 10V power supply.

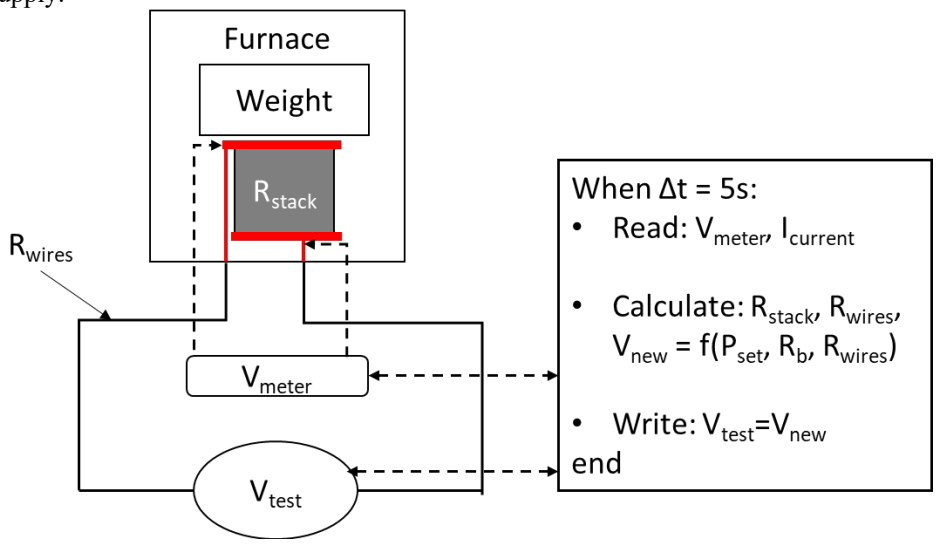

Figure 30: Experimental setup of DRH experiment.

A control program was written to read the voltages and current of the system, calculate the resistances of the stack and wires, and write to the power supply a new voltage that would generate the desired power P_{set} across the stack. The stack was surrounded by insulating bricks to form a small test chamber within the furnace.

6 Experimental results

6.1 Commercial chromia firebrick results

6.1.1 Variability among samples

Figure 31 shows the resistance of five un-fired SERV® 95 DC firebrick samples as a function of load. The sample composition, shown in Table 6 in Section 5.1, is approximately 92% chromia and 5% alumina. Assuming $R_{m\text{-}b}$ is relatively consistent between samples and small at 4500 kPa, samples averaged approximately 1.5 M-ohm (7.5 M-ohm-cm), except for sample B. Variation of resistance across the samples is not unexpected, as they are visibly heterogeneous, with patches of bright green chromia among dark green, typically indicating variations in local composition and grain size [102].

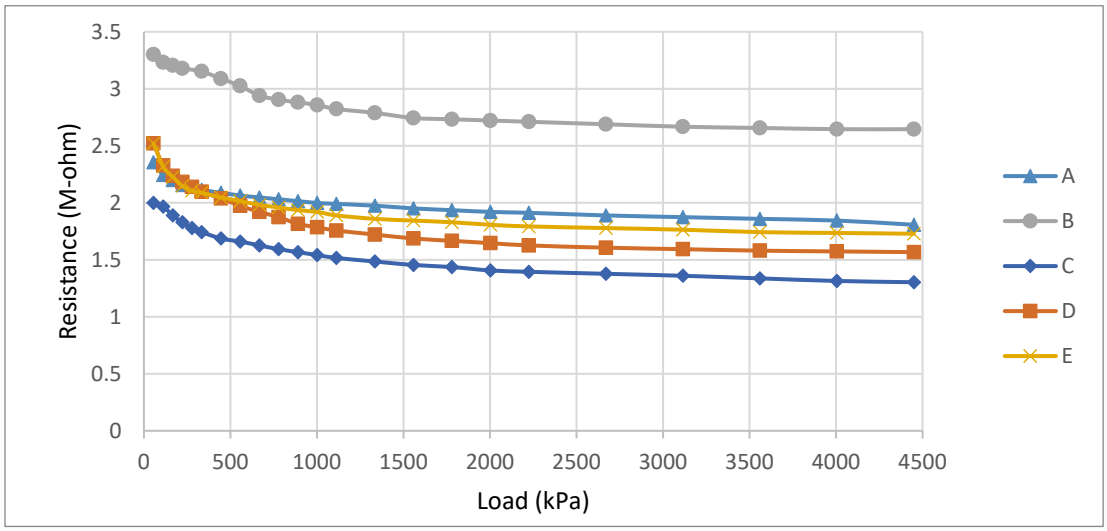

Figure 31: Preliminary resistance measurement of five un-fired SERV® 95 DC firebrick samples as a function of load. The change in resistance is due to reductions in the metal-brick contact resistance between the metal foils and the samples.

Figure 32 shows the resistance vs load of samples A and B before and after a heating cycle of 1200°C for 12 hours. At the highest load all but pre-fired sample A are approximately 2.8 M-ohm (14 M-ohm-cm). The fact that sample B experienced little change suggests that sample B may have been an outlier in pre-fired measurements because it had received more heating during fabrication. However, the steeper rise in resistance at lower loads during load-down suggests the formation of some more elastic character to the surface asperities compared to pre-fired samples. Figure 33 shows the appearance change of brick surfaces after different numbers of thermal cycles. Although some changes in the surface response to loading are evident, it is expected that the changes occurring during heating are throughout the sample volume rather than just at the surface.

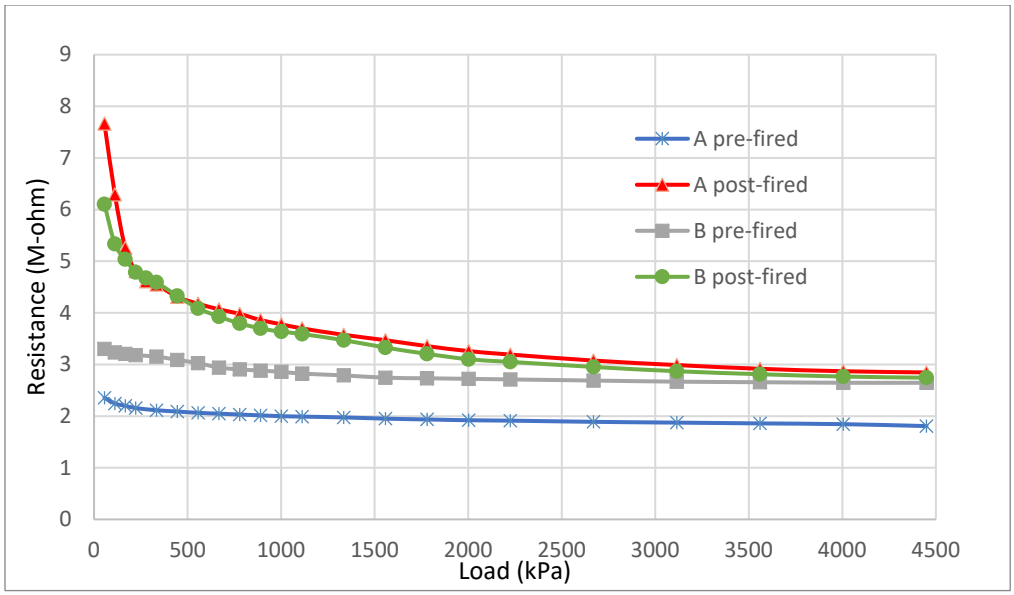

Figure 32: Comparison of sample resistance before and after firing in furnace for 12 hours at 1200°C.


Figure 33: Evolution of brick appearance with thermal cycling.

Top picture: The left-most has never been fired. The middle has been fired once. The right-most has been fired 14 times. Bottom picture: fired once (left) vs never fired (right).

6.1.2 Contact resistivity-load measurements

The post-fired samples A and B were measured in a stack such that a contact resistance $R_{b\text{-}b}$ was introduced in the measurement. The bricks were then platinized and measured again, both individually and stacked. Figure 34 shows the comparison of resistivity-load of the brick stack "A B" and the sum of the individually measured bricks "A+B". The resistivity of the platinized measurements, both individual and stacked, are constant with load, indicating that the highly conductive platinum layer has essentially removed the effect of asperity deformation on contact resistance, and reduced it to nearly zero. The platinized individual measurements are equal to the un-platinized measurements at 4500 kPa, which shows that $R_{m\text{-}b}$ has been reduced to a negligible value at high load. This is to be expected based on the ductility and conductivity of the metal foil. That the platinized brick resistance and the high load brick measurements are equal gives high confidence that the brick bulk resistance $R_b \approx 2.8$ M-ohm for both samples A and B.

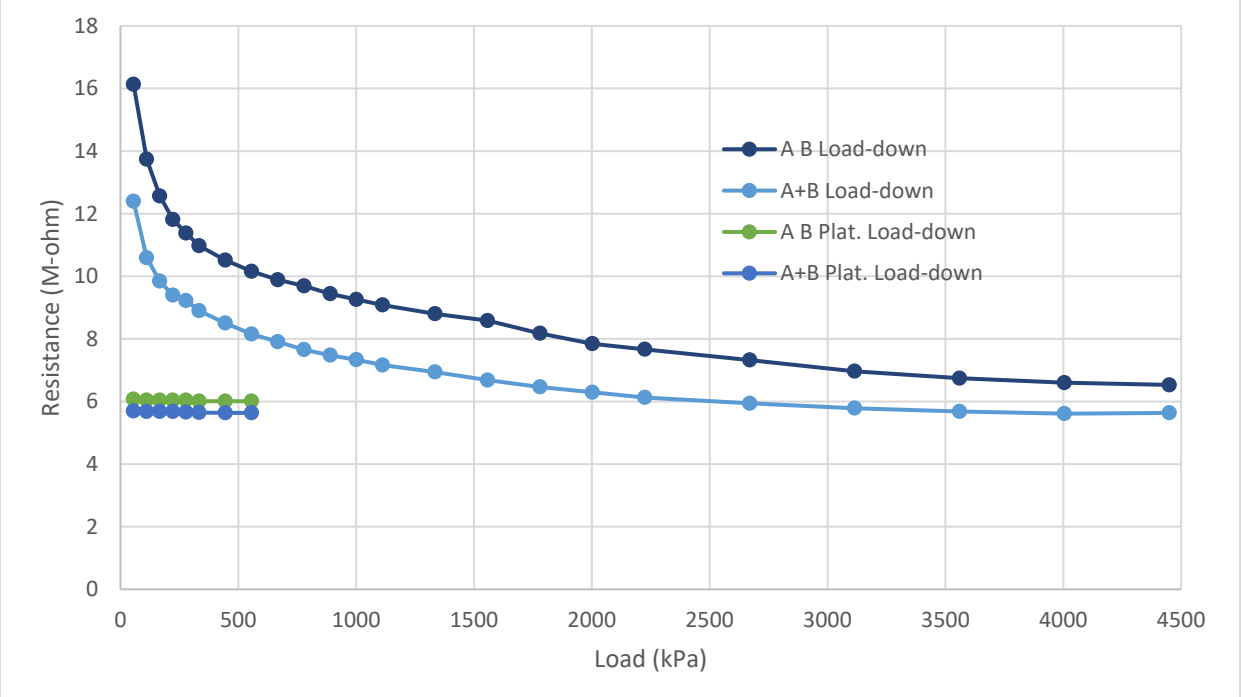

Figure 34: Resistance-load measurements of brick stacks "A B" compared to their summed individual measurements "A+B" before and after platination.

With the load-independent bulk brick resistances R_A and R_B isolated, it is then possible to calculate $R_{m\text{-}b}$ and $R_{b\text{-}b}$. The sum of the measured results R_{A+B} include the now known resistances of brick samples A and B and a total of four metal-brick contacts, which yields $R_{m\text{-}b}$:

$$2R_{m-b} = \frac{R_{A+B} - R_A - R_B}{2} \tag{27}$$

Finally, the measurement of $R_{A\,B}$ includes the known brick bulk resistances and two metal contacts, yielding $R_{b\text{-}b}$:

$$R_{b-b} = R_{A\,B} - R_A - R_B - 2R_{m-b} \tag{28}$$

Figure 35 below shows the contact resistance during both load-up and load-down of of the A B stack, fitted with the power law function. The measurements during load-up were not smooth, perhaps due to more macroscopic features of the samples and the setup. Shifts of components and the more broadly imperfect cuts of the samples themselves may have caused worse contact when increasing from 200lb to 250lb. These features are not seen during load-down. Consistent with theory, both curves are fairly well-fitted by the power law function, with exponents of 0.543 and 0.437 for load-up and load-down, respectively. These values are typical [99, 100]. The difference in exponent between load-up and load-down can be attributed to permanent deformation of surface features that are not lost even when load is reduced. However, the contact area asssociated with these permanent deformations is generally lost when the surfaces are fully separated.

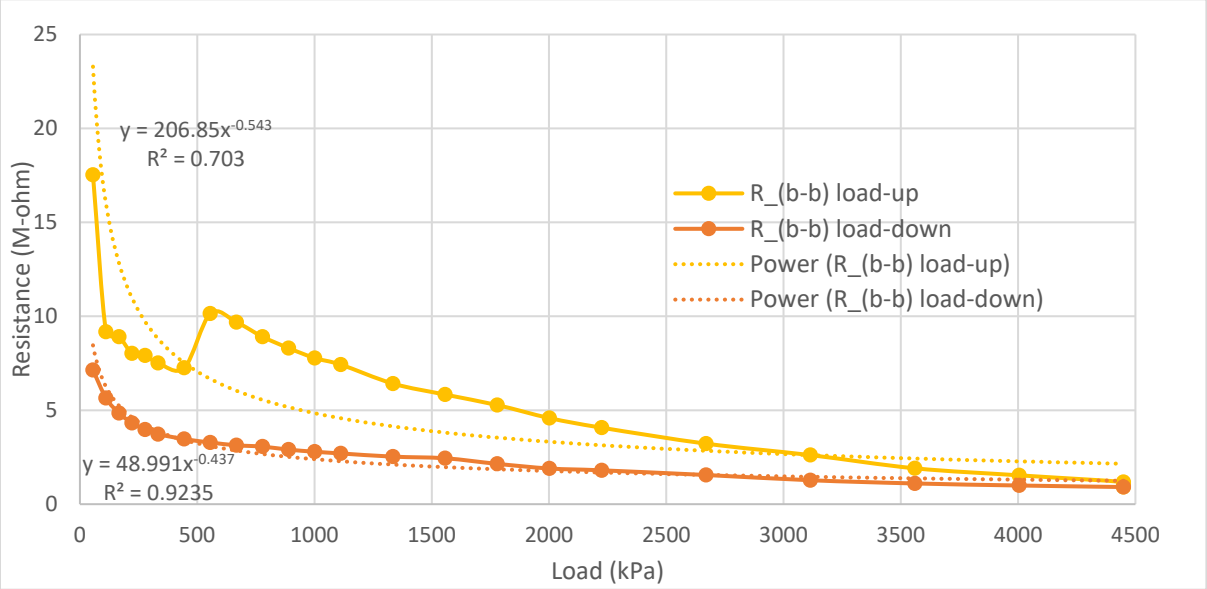

Figure 35: Contact resistance vs load-up and load-down of brick-brick contact of fired samples A and B, fitted with power law functions.

To compare the relative behavior of fired and unfired bricks, the same analysis was done with a stack of three unfired samples C D and E. The samples were not platinized, instead the measured resistance at 4500 kPa was assumed as approximately equal to the bulk resistance R_b of each sample. The sum of the individual samples were taken as 4.5 M-ohm, and each were assumed to have similar contact resistance magnitudes, since each is +/-20% of 1.5 M-ohm. Figure 36 shows the resulting $R_{b\text{-}b}$ with power law fits. The load-up was fit generically with $\alpha = 0.5$ due to the same extraneous factors during load-up mentioned previously, including a drift due to capacitance during the "sit" period at 2000 lb. The load-down is well-fitted.

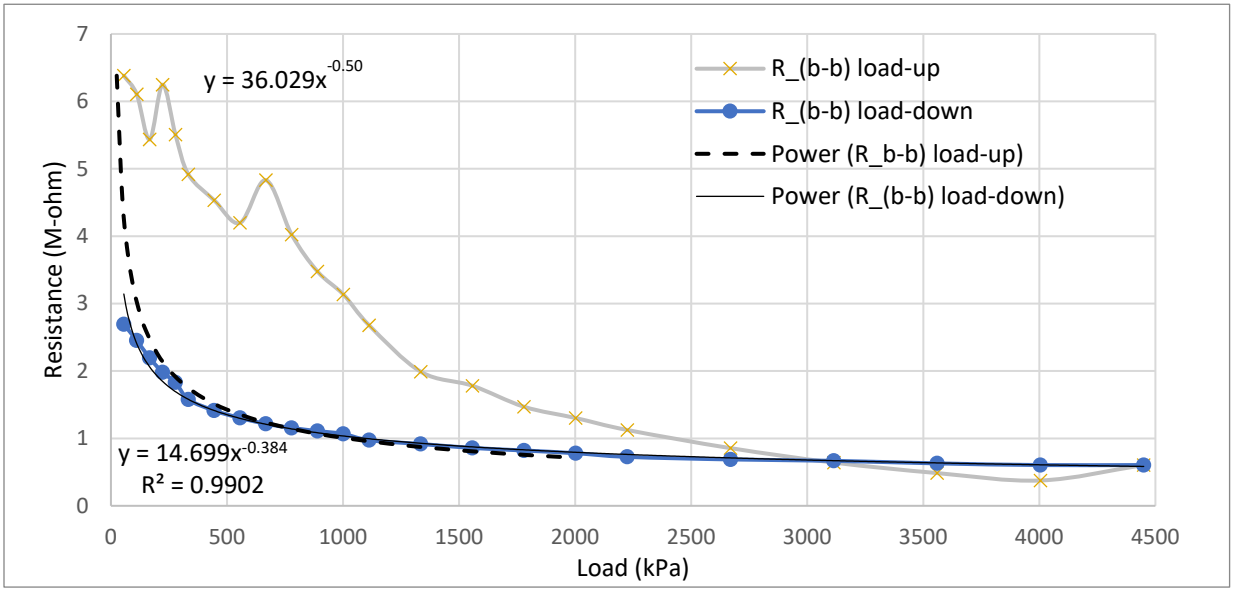

Figure 36: Contact resistance vs load-up and load-down of brick-brick contacts of fired samples C, D and E, fitted with power law functions.

The difference in magnitude of the brick-brick contact resistance of the fired and unfired stacks as a function of load are shown in Figure 37. When multiplying by the contact area (4x5cm^2), a unit resistivity can be calculated (Figure 37a). A more useful and insightful metric may be to consider an "equivalent resistor length" by dividing the contact resistivity by the bulk material resistivity (Figure 37b). This quantity is the equivalent length of firebrick that would pose the same resistance in a circuit, similar to how minor pressure losses in piping systems are sometimes described as an equivalent major loss. The equivalent resistor length is largely independent of (at least one) thermal cycle. Both show equivalent lengths of a few centimeters throughout the loading range, the typical length scale of firebricks in general. This result also supports the claim that the effect of firing samples is largely volumetric rather than at the surface, since a surface effect would not scale appropriately when calculating resistivity. Any discrepancy would be further highlighted by the differing ratios of brick volume and contact area of the two different stacks in the analysis (one brick-brick contact for two bricks versus two brick-brick contacts for three bricks).

The stable contact surface and low contact resistivity of chromia are both promising for its use as an electrically conductive firebrick stack. In contrast, pre-fired brick-brick contact resistance of two commercial SiC varieties (Section 13) was two orders of magnitude higher than the bulk resistance of the bricks themselves, even at the maximum load. Moreover, heating of one of the two SiC types up to only 500ºC oxidized the surface, increasing the measured resistance of an individual brick by orders of magnitude, even across a platinized surface.

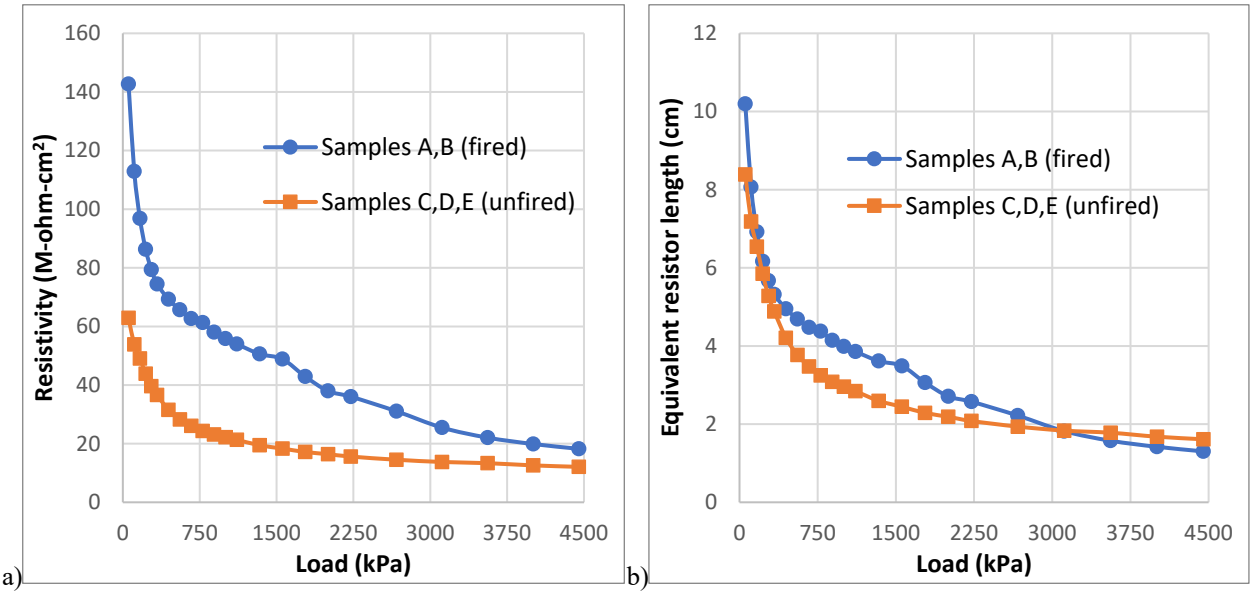

Figure 37: Contact resistivity (a) and equivalent resistor length (b) as a function of load-down of fired and unfired brick stacks.

In the context of a tall electrically heated firebrick stack, the equivalent resistor length intuitively gives a sense of where the voltage drop and heat generation will be experienced. It can be understood that two 10m stacks,

one of 100 bricks each 10cm tall and one of 50 bricks each 20cm tall, will behave differently due to contact resistance. These results will be more contextualized in Section 7, which examines this dynamic in detail.

6.1.3 Resistivity-temperature measurements and cycling

Figure 38 shows the resistivity-temperature behavior of SERV® 95 DC sample A over several cycles. In total, the sample was measured through 13 cycles. As mentioned previously, the measurements during the first 5 cycles experienced problems of "negative" resistances at high temperatures, due to the discharge of capacitance build-up across the brick. There are however some noteworthy features and evolution of the commercial firebrick at lower temperatures. The results shown of these cycles (Figure 38a) are therefore limited to below 1000K. The full temperature regime of cycles 6 through 13 are shown in Figure 38b.

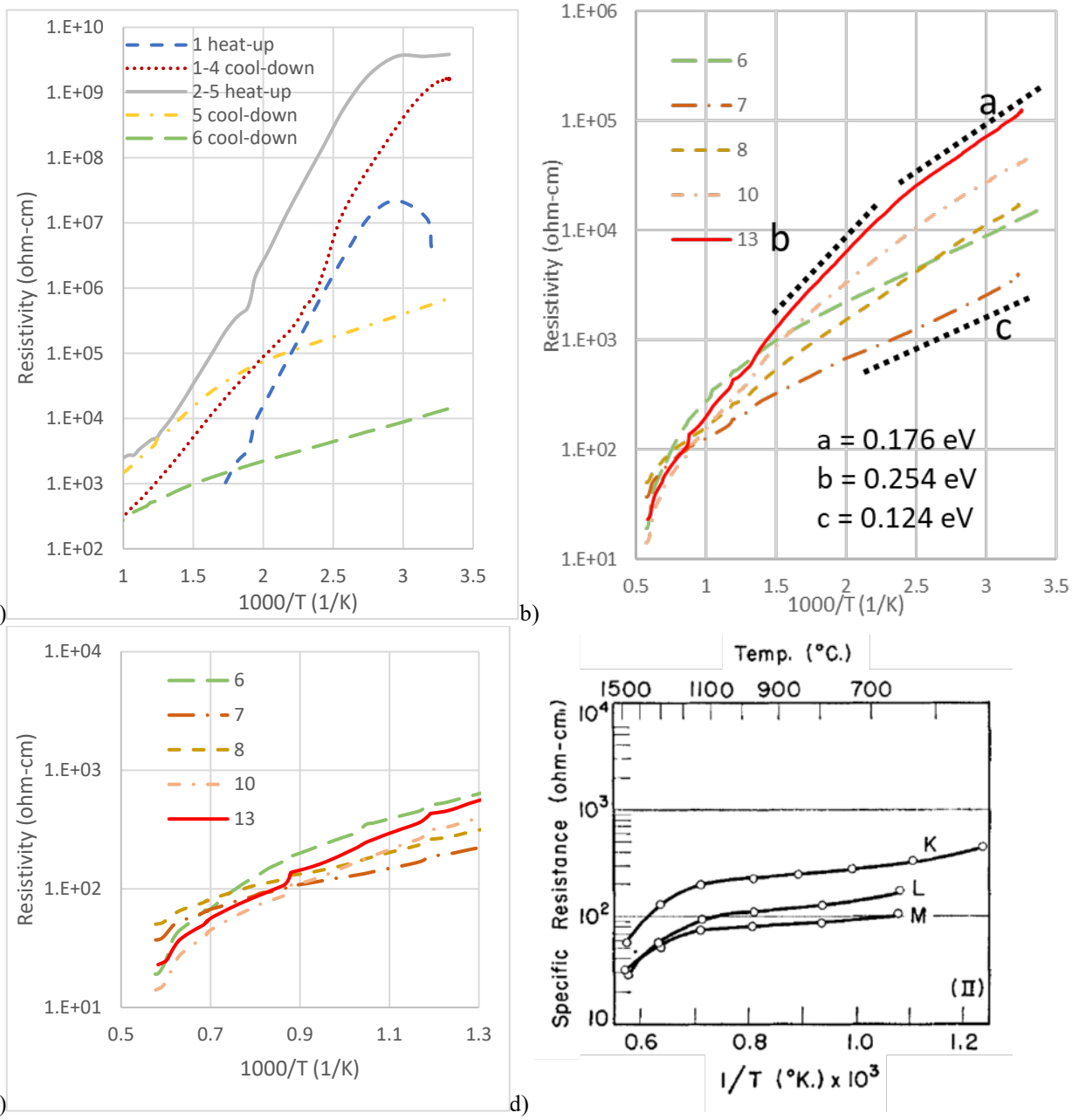

Figure 38: resistivity-temperature trends over 13 cycles of SERV® 95 DC sample A from 25°C to 1500°C.

a): log resistivity vs Arrhenius temperature of cycles 1 through 6. Note the high temperature region is not shown due to capacitance issues. b): log resistivity vs Arrhenius temperature of the cool-down portion of cycles 6 through 13, with annotated activation energies. c): log resistivity vs Arrhenius temperature, scaled to match the data from literature. d): Resistiivity-temperature results from Hensler and Henry [48] of different pure chromia-alumina mixtures. K: 92% Cr_2O_3, 8% Al_2O_3; L: 98% Cr_2O_3, 2% Al_2O_3; M: 100% Cr_2O_3.

The evolution of the sample resistivity with cycling is affected by oxygen non-stoichiometry, the presence of counter-dopants such as Ti, and the diffusion of other impurities present in the commercial mix. As such only a high-level discussion of the evolution with cycling is presented herein.

During the first cycle, the room temperature resistivity of the sample increased by three orders of magnitude, from 10^6 ohm-cm to 10^9 ohm-cm. The sample then followed a near-identical trajectory during subsequent cycling until an abrupt change in the cool-down of cycle 5, where room temperature resistivity decreased by four orders of magnitude, to 10^5 ohm-cm. The large increase after cycle one may have been caused by the movement of impurities to form more resistive grain boundaries, which were not activated by the 1200°C firing performed during contact resistivity testing. It is unclear what caused the abrupt drop in resistivity after cycle 5, but subsequent cycles more closely match the expected behavior of non-stoichiometric chromia.

Beyond cycle 6, the sample shows considerable drift with cycling, flattening out through cycle 7, then rising steeper through cycle 13. Room temperature resistivities vary by 10^3-10^5 ohm-cm. Activation energies varying from a minimum of 0.124eV during cycle 7 to 0.254eV during cycle 13. These activation energies are associated with the ionization of excess oxygen sites to form free electron holes. In Kröger–Vink notation, the reaction can be written:

$$\frac{3}{2}O_2(g) \rightleftharpoons 2V_{Cr}''' + 6h^{\bullet} + 3O_o \tag{29}$$

The equilibrium constant of this reaction increases with temperature such that the number of excess incorporated oxygen molecules increases with temperature. This implies there are two features of activation: the thermally activated incorporation of more excess oxygen (more "dopant") which creates more chromium vacancies, and the thermally activated ionization of the created sites, as discussed in Section 3.1.1. In the lower temperature region, it has been observed that the activation energies may vary dramatically [103], with significant relation to the diffusion of oxygen through the solid. According to Holt and Kofstad, it may take several days or even weeks for centimeter-scale samples to fully equilibrate, even for a porous body at 1200°C. The evolution of the heterogenous brick material may also be affecting the diffusion rate of oxygen with more cycles.

Considering these variables, one possible explanation of the behavior seen in cycle 13 is as follows: during cool-down of cycle 13 (Figure 38b), oxygen diffuses out of the brick, as per the reverse reaction (29), at a higher rate than was seen during the cool-down of other cycles. The loss of excess oxygen coincides with a loss of chromium vacancies, reducing the free carriers with an activation energy "b". Once the kinetics reduce significantly, the resistivity increase is caused by the de-ionization, i.e. freeze-out of the remaining chromium vacancies, associated with activation energy "a". This is supported by the relatively similar slopes of region "a" and "c" between cycles 13 and 7, suggesting that more chromium vacancies were present during cycle 7, and the resistivity-temperature trend was associated exclusively with the ionization of chromium vacancies.

Other than the changing oxygen concentration, the presence of 1.1% titanium (Table 6) may act as a counter-dopant to the excess oxygen if occupying chromia sites. 1% Ti has been demonstrated by Nagai and Ohbayashi to turn chromia into an n-type semiconductor at atmospheric oxygen pressure [64]. The unknown additives that compose 1.6% of the brick may have more competing effects still.

The impact of the titanium and other additives appears small, however, based on a comparison to pure samples in literature. At higher temperatures (Figure 38c) the sample compares well with the resistivity-temperature measurements of pure chromia-alumina mixtures of similar composition (Figure 38d). The frames are identically scaled for ease of comparison. Sample K is closest in composition to SERV® 95 DC, with a chromia-alumina ratio of 92%-8%. Between 500 and 1500°C, the variation between cycles narrows to within the same order of magnitude, suggesting that system conductivity is still controlled by oxygen non-stoichiometry.. The onset of intrinsic behavior is also seen near 1100°C in both the pure and commercial samples. These results suggest that, at the temperatures of interest, the additives and impurities of SERV®95 DC are largely eletrically inactive.

6.1.4 Summary and lessons learned from commercial firebrick testing

The bulk resistivity, contact resistivity-load and bulk resistivity-temperature trends were measured for samples of a commercial high-chromia firebrick, SERV® 95 DC. Samples were within +/-20% of 7.5 M-ohm-cm, with the exception of sample B. The firing of bricks was found to increase their bulk resistivity, but did not form any highly resistive surface phases; firing sample B caused little change.

Load-down measurements found that the brick-brick contact resistivity of samples ranged from 2-10 cm of equivalent resistor length, the same length scale of common firebricks, independent of firing. This outcome shows promise that existing chromia firebrick may form good brick-brick contacts of low resistance in a large electrically conductive firebrick stack. This is in contrast to earlier tests done on commercial SiC bricks, which have equivalent resistor lengths orders of magnitude larger than brick scales, and form insulative oxide layers after one firing. The effects of both temperature and load on contact resistivity is explored for laboratory-fabricated chromia samples in the Section 6.2.2. Modeling of the electrical conductivity and heat generation in larger firebrick stacks as a function of contact resistance is undertaken in Section 7.

The bulk resistivity-temperature behavior of the commercial firebrick evolved considerably with cycling in the lower temperature region (<500ºC), which is mostly likely attributable to changes in the rate of equilibration of oxygen non-stoichiometry, or diffusion of Ti or other additives to grain boundaries or other lattice sites. At higher temperatures (>500ºC), the commercial brick was relatively consistent between cycles, within an order of magnitude, and similar in behavior to that of pure chromia-alumina mixtures with >90% chromia. The processing and additives of existing firebricks therefore does not appear to dramatically influence the electrical character of the chromium oxide.

The testing of a commercial high-chromia firebrick provided many positive indicators for the development of Cr_2O_3-based electrically conductive firebricks for use in a high temperature FIRES system. The key feature to be incorporated is a sufficient quantity of p-type dopant, e.g., 0.5-5 at% Ni or Mg. The development of the specific manufacturing process for a commercial electrically conductive firebrick which exhibits an exhaustion region, without significantly altering the effects granted by other additives, requires more work.

6.2 Lab-fabricated chromia firebrick results

6.2.1 Bulk resistivity-temperature results

Figure 39 shows the bulk resistivity-temperature behavior of 2.00% Ni-doped samples of series 4, based on the deconvolution of R_b and $R_{m\text{-}b}$ and R_{Pt} of samples S4-1, S4-7, and S4-8. There was little discrepancy in the average bulk resistivity value ρ_b (Figure 39a, due to the large geometry differences and smaller impact of poor contacts on the the long narrow form of S4-1. The use of average values of ρ_b, ρ_{m-b} and R_{Pt} can reconstruct the measured behavior of each sample within 10% for the entire temperature range, with the exception of S4-2 below 200ºC, which is within 15%.

The activation energy associated with the ionization of Ni dopant at lower temperatures is approximately 0.31 eV. Following a sharp drop in resistivity by two orders of magnitude from room temperature to 250ºC, values of resistivity are within an order of magnitude above 250ºC through 1500ºC (Figure 39b). This sharp drop in magnitude of the resistivity-temperature derivative RTD is visualized in Figure 39c as a percent change in reciprocal resistivity, i.e. conductivity σ, written as:

$$Percent\ change\ = 100 * \frac{d\left(\frac{1}{\rho_b}\right)}{dT}\rho_b = 100 * \frac{d(\sigma_b)}{dT}\frac{1}{\sigma_b} \tag{30}$$

This formulation is valuable because volumetric heat generation $q''' \propto \frac{1}{\rho_b}$ for a constant voltage system. A 1% increase in this quantity is therefore a 1% increase in power generation. The temperature dependence in the region examined is well-fitted by a power law function. The power increase falls below 1%/K above 500K, and below 0.1%/K above 1000K. Throughout this range, the RTD was found to be negative, i.e. resistivity always decreased with temperature.

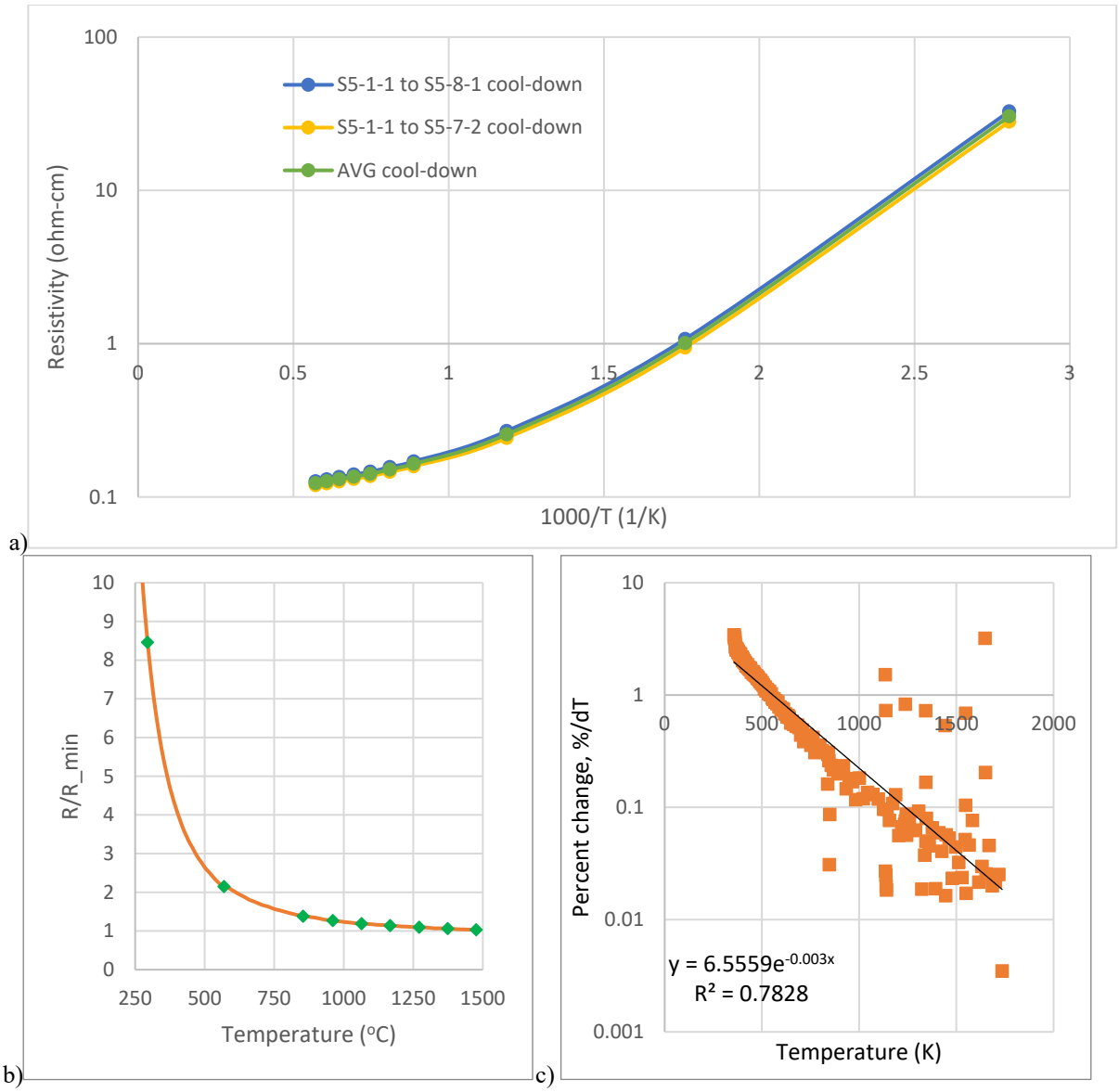

Figure 39: Bulk resistivity-temperature behavior of 2.00% Ni-doped samples, series 4.
a): log resistivity vs Arrhenius temperature. b): Ratio of resistivity to minimum resistivity vs temperature. c): Percent change in reciprocal resistivity per Kelvin vs temperature; see equation (30).

6.2.2 Contact resistivity-load-temperature results

Figure 40 shows the room temperature contact resistivity-load measurements of stacked samples S4-7 and S4-8 (called "S4 stack" herein) during load-up and load-down. The power law exponents in the lab-fabricated samples (Figure 40a) are similar to those found for the commercial samples. The equivalent resistor length (Figure 40b) is between 55 and 25cm during load-down. This is a factor five greater than the 10-5cm result in the same load range for commercial samples, though a direct comparison is not reliable for two reasons: (1) the contact resistivity during load-up of the commercial bricks was measured without a settling time for electrical capacitance effects, introducing error that made the measurements artificially low, especially at low load; (2) The load-downs begin from different maximum loads, because the relatively fragile lab-fabricated samples may have failed under large loads. Figure 40c plots the lab-fabricated and commercial load-ups together, and extrapolates the power law fit of the lab-fabricated samples to the same load range as the commercial brick. It seems likely that in the absence of capatiance effects and with the same maximum loading, a similar result would be found for both samples.

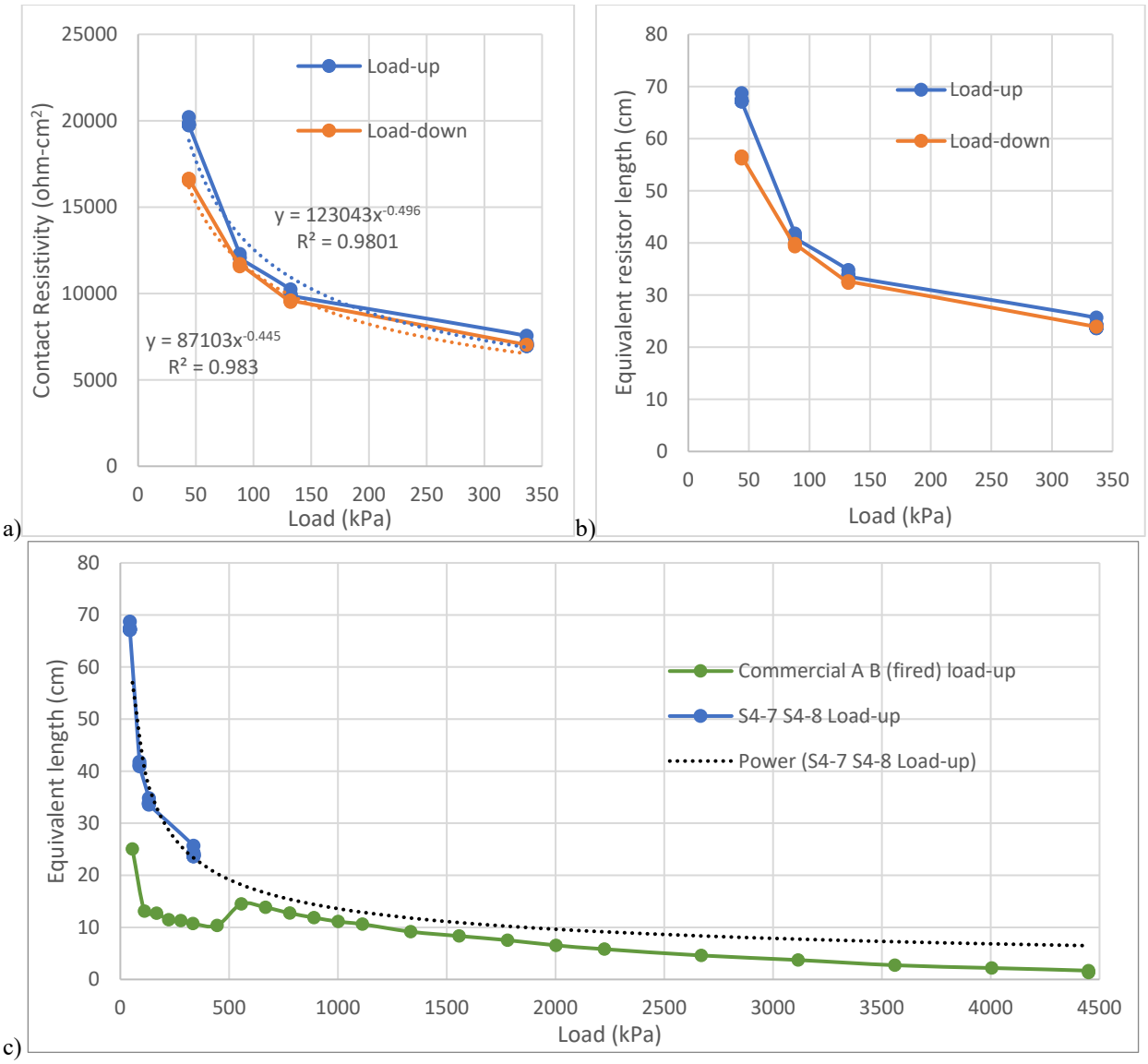

Figure 40: Room temperature contact resistivity-load measurements of stacked samples S4-7 and S4-8.
a): Contact resistivity during load-up and load-down, with power law function fits. b): equivalent resistor length vs load. c): Comparison of extrapolated load behavior of stack S4-7 and S4-8 to commercial firebrick stack A B.

Figure 41 shows the effects of thermal cycling on contact resistance in the S4 stack. During the first thermal cycle (Figure 41a), the resistance of the S4 stack reduces to within the same order of magnitude of the summed resistance of the individual samples. In terms of equivalent resistor length, the change in contact resistivity during the first cycle is a drop from approximately 70cm to approximately 3cm near room temperature.

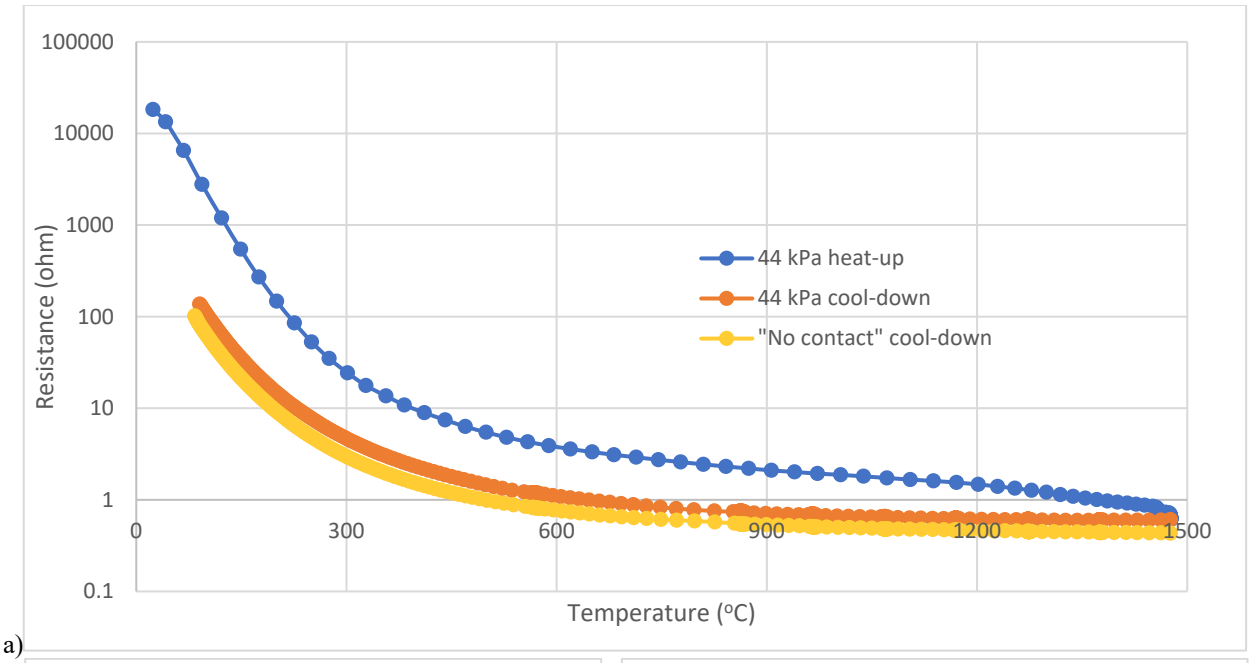

a)

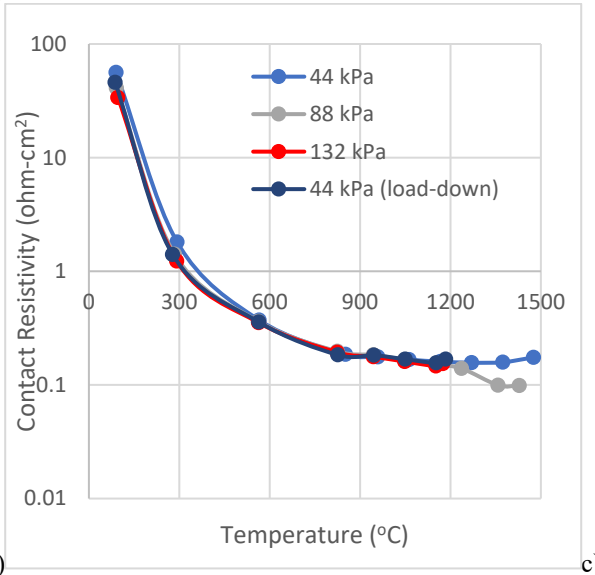

b)

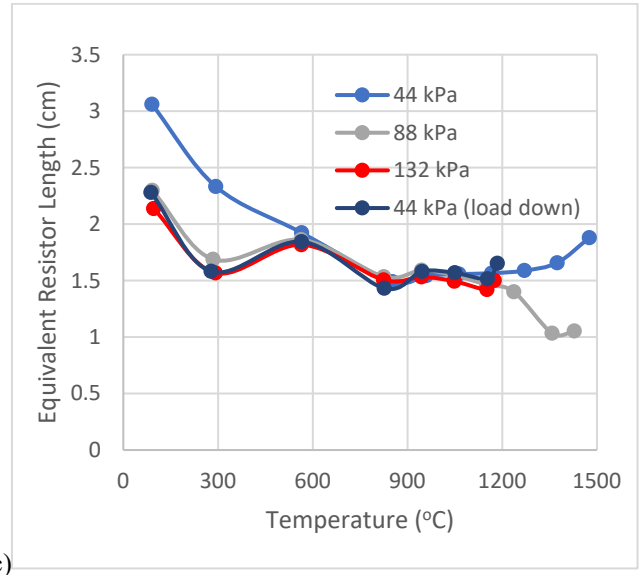

c)

Figure 41: Effects of thermal cycling and loading on contact resistance in the S4 stack.
a): First cycle heat-up and cool-down. The relative magnitude of the contact resistance can be seen in comparison to the "no contact" plot, which sums the individual resistances in the stack. b): contact resistivity vs temperature. c): Equivalent resistor length vs temperature.

Beyond the first cycle, more cycling and greater loads caused relatively minor changes in contact resistivity (Figure 41b). A doubling of load from 44 kPa to 88 kPa impacted the high temperature region, but behavior was identical for most of the temperature range. The subsequent cycles only reached 1200°C rather than 1500°C due to a broken heater rack. These showed no further sensitivity to load, including when load was reduced back to 44 kPa. This is attributable to the lowering of material strength at elevated temperatures, resulting in substantial plastic deformation even under relatively low loads. The change in contact resistivity is most strongly associated with the temperature-dependent material strength rather than the load applied. The equivalent resistor length (Figure 41c) fluctuated between 1 and 2 cm for most of the temperature range of interest, independent of load changes and further cycling.

Another phenomenon that may affect evolution of the contact is the chromia gasification reaction (18). The CrO_3 gas returns to Cr_2O_3 upon deposition. The small air pockets at the brick-brick contact may therefore be a site of

frequent deposition of loose Cr_2O_3 powder, which may be weakly sintered at the interface. A more focused research effort would be necessary to understand the specific effect of the gasification reaction on contact resistivity.

6.2.3 Direct resistance heating experiment results

Figure 42 shows the results of the direct resistance heating experiment of the S4 stack, which was undertaken without moving the stack after contact resistance testing. The steepest temperature ramp rate experienced by the stack was approximately 480°C/hour, and the highest wattage loading was approximately 27 kW/m^2. Such ramp rates and wattage loadings are typical of other heater elements, and are also desirable in the context of a FIRES unit. The stack heated without issue and maintained a steady wattage for 30 minutes at a time. No change was visible to the samples after the experiment.

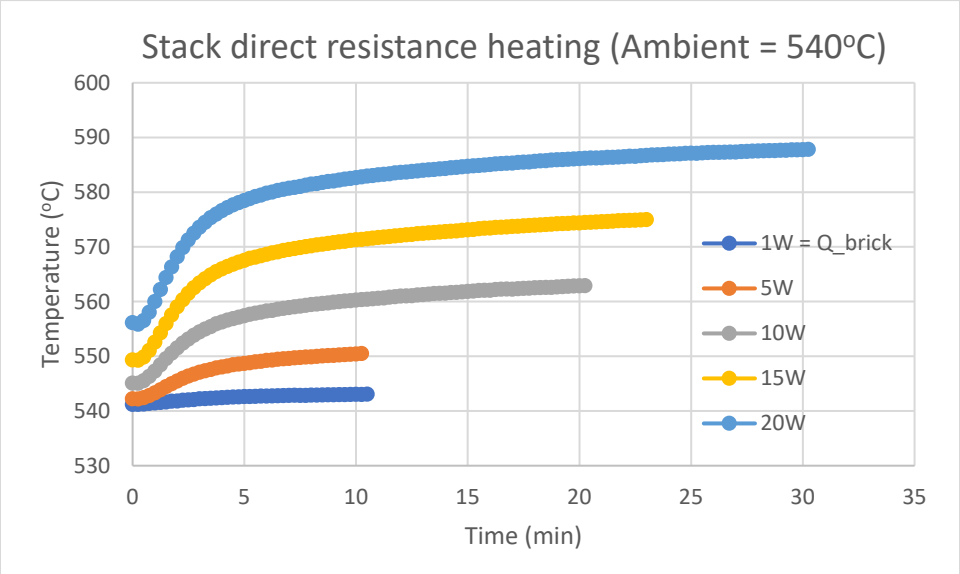

Figure 42: Direct resistance heating experiment of the S4 stack.

The peak temperatures reached during the test was limited by the heat leakage of the small chamber built around the stack. The linearity of the steady state chamber temperature with wattage indicates that conduction through the walls was the limiting thermal resistance of the system, rather than radiation through gaps. Although heavily insulated on the sides, the alumina shelf and plate that the stack was fixed between had a relatively high thermal conductivity. The 20W input was the limit of the power configuration. A hotter operating temperature was therefore not achievable at the time.

Although tested at relatively low temperatures, the ramp rates and wattage loadings demonstrated by the sample in this experiment are again promising for the use of doped chromia in a FIRES unit, or potentially as commercial heater elements.

6.2.4 Findings of previous fabrication series 1, 2 and 3

Figure 43 shows the uncorrected resistivity-temperature behavior of series 1, 2 and 3. Despite issues of poor contacts and platinum resistance, the results warrant some commentary on general trends in dopant activation versus dopant level, and the prospects of creating a positive RTD in doped chromia.

Figure 43a compares the commercial SER® 95 DC result to low-doped samples. The 0.05% Mg-doped sample shows a distinct activation energy of approximately 0.48 eV near room temperature, associated with Mg ionization. The free carriers are far in excess of that attributable to oxygen non-stoichiometry, indicative of the greater activity of the substitutional Mg dopant. The onset of exhaustion is visible, but due to the low dopant level, intrinsic carriers overtake the extrinsic carriers near 1300°C. These same results are shown in Figure 43b against linear temperature for clearer visualization of the temperature dependence. This is only a slight shift towards higher temperatures compared to where intrinsic behavior arose in the undoped commercial sample. Despite the low dopant concentration and high temperature measurements, which should cause a thorough ionization of carriers, no regime

of positive RTD was observed before the onset of intrinsic behavior. At higher levels of 0.25% and 0.50% (Figure 43c) the onset of the intrinsic behavior was pushed beyond 1500ºC, and the magnitude of oxygen non-stoichiometry is lessened as well. However, no positive RTD was observed.

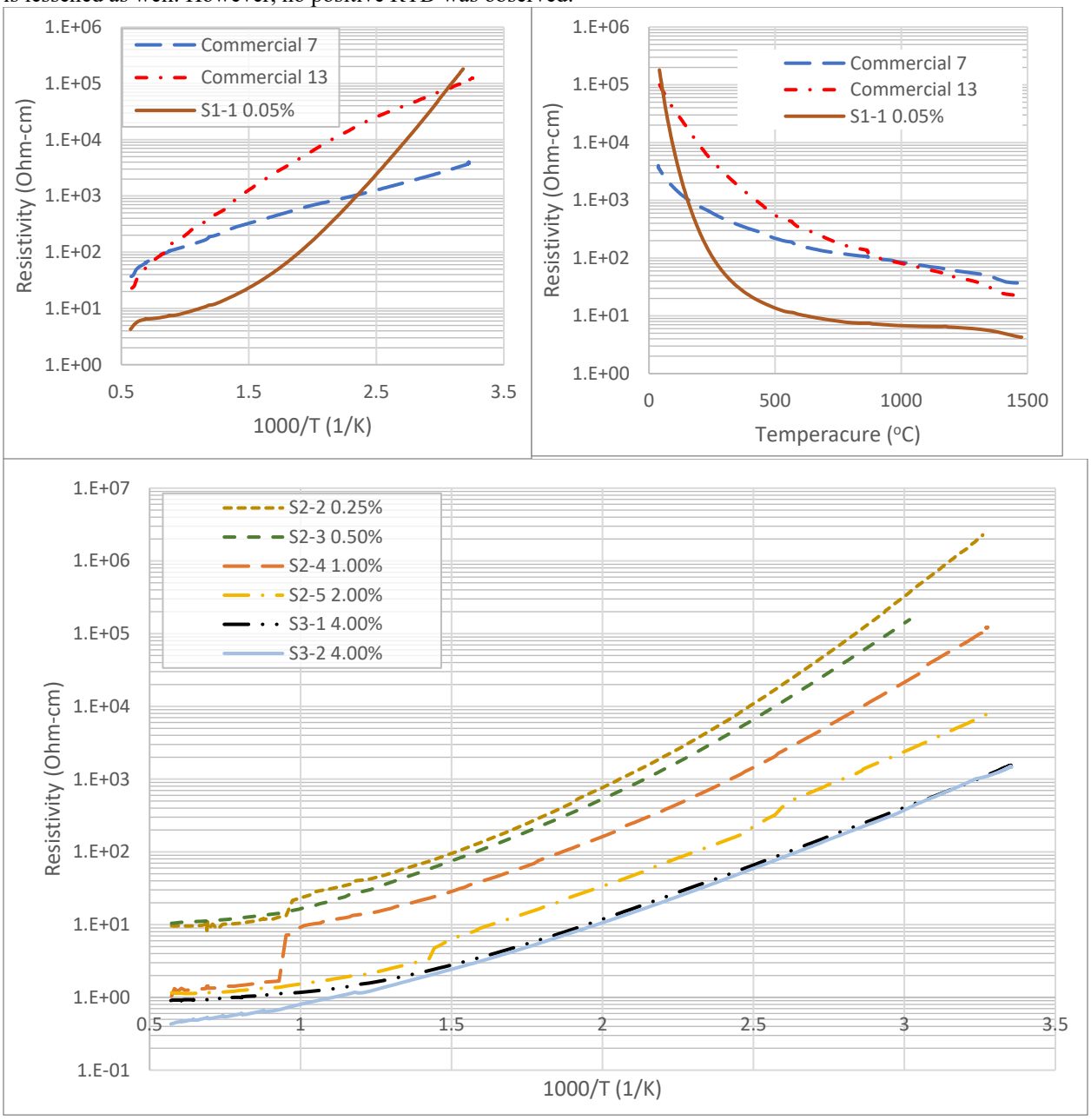

Figure 43: uncorrected resistivity-temperature behavior of samples from series 1 2 and 3.
Results are included for qualitative findings. a): Low-dopant levels and SERV® DC 95 sample A plotted against Arrhenius temperature. b): Low-dopant levels and SERV® DC 95 sample A plotted against linear temperature. c): Dopant levels of 0.25% to 4.00% plotted against linear temperature.

The observed room temperature activation energy associated with dopant ionization gradually decreases with more dopant (Figure 43c), from 0.48 eV at 0.05% to 0.31 eV at 4.00%. This trend has been observed in other highly doped metal oxides, such as Li-doped NiO [46]. Although the formulations of Section 3.1.1 generally identify lower dopant levels as a swifter approach of near-complete ionization levels, a more gradual ionization of dopant with temperature may be acceptable as long as a small RTD is observed. In the work herein and in [46], the higher doped samples are seen to vary by less orders of magnitude over the course of the temperature range of interest.

Regarding solubility limits, X-ray diffraction of 4% Ni-doped Cr_2O_3 (Figure 44) showed weak peaks of nickel-chromate ($NiCr_2O_4$) spinel phase, indicating that the solubility limit of Ni in Cr_2O_3 was reached. Based on the small counts of the spinel, it is suspected that the solubility limit is above 2% and likely only slightly below 4%. This would be an improvement in solubility achieved compared to the 1-2% limit found by Nagai et al. [50] for powder-mixed Ni-doped Cr_2O_3. It is also approximately proportional to the improvement seen by Chen and Colbow [60] when using a sol-gel to produce Mg-doped Cr_2O_3, with a solubility limit near 1.25%, compared to the previously reported 0.5% limit for powder mixing of MgO and Cr_2O_3 by Park and Kim [49].The results are still below what was achieved by Arca et al. [36] in formation of Mg-doped and Ni-doped Cr_2O_3 thin films via PLD, with a pure metastable corundum phase seen as high as 6% and 7%, respectively.

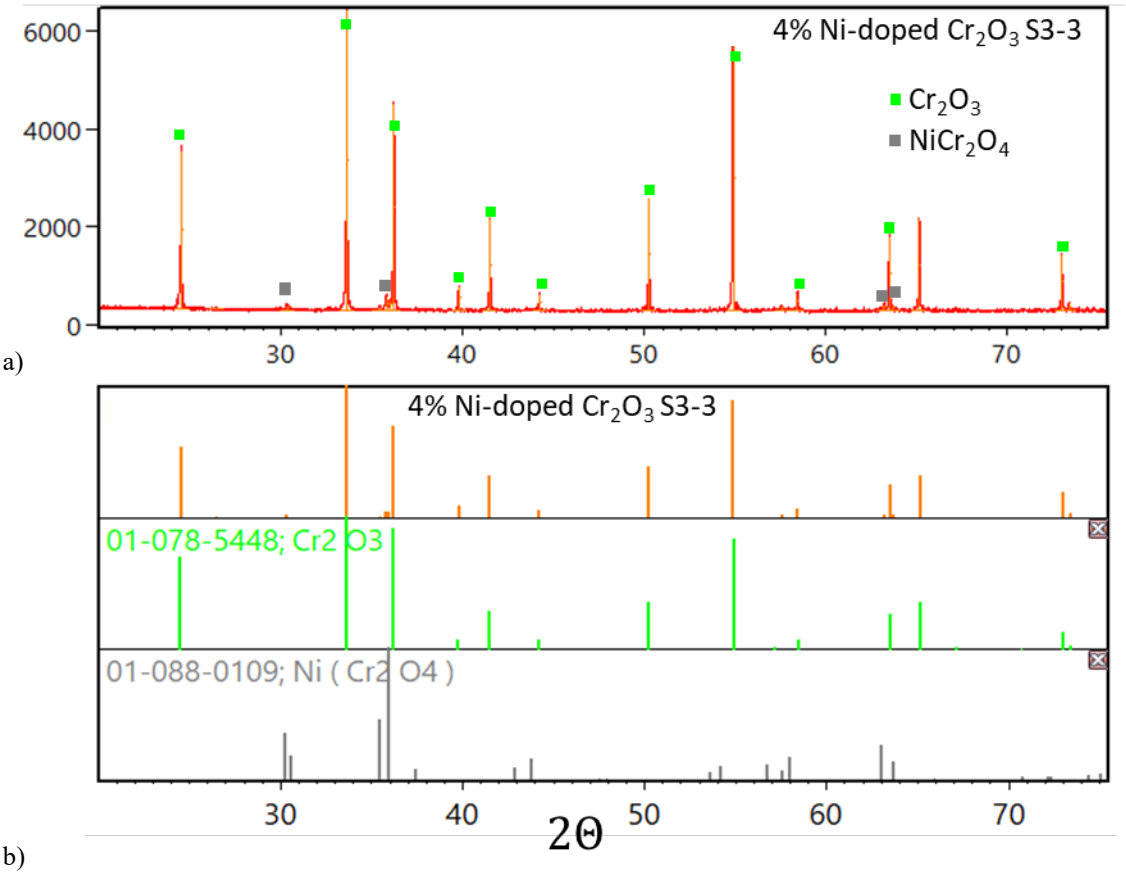

Figure 44: X-ray diffraction of 4% Ni-doped Cr_2O_3, S3-3.
a): XRD line scan. b): Comparison of 4% Ni-doped Cr_2O_3 line patterns with reference line patterns of pure Cr_2O_3 corundum and $NiCr_2O_4$ spinel.

6.2.5 Summary of lab-fabricated chromia firebrick testing

The bulk resistivity and brick-brick contact resistivity of doped chromia samples were measured as a function of load, temperature, and cycling. A negative RTD was observed throughout the temperature range and dopant range explored. However, all resistivity measurements were within an order of magnitude above 250°C, and the percent increase of reciprocal resistivity, i.e. conductivity, was seen to decrease dramatically with temperature, below 0.1%/K near 1000K. This corresponds to a local power generation increase of 0.1%/K for a constant voltage. The temperature-dependent percent increase will be used for stability calculations in Section 8.

Analysis suggests that room temperature brick-brick contact resistivity is very similar to that of commercial bricks as a function of load. However, the contact resistivity decreases dramatically after one thermal cycle, even with relatively low load. The equivalent resistor length of the contact is approximately 2 cm or less at all temperatures, and is load-independent once the surface asperities are plastically deformed. The equivalent resistor length will be used in

Section 7 to determine the relative temperature rise the contacts experience compared to the surroundings, known as the "contact supertemperature," during the charge cycle, to determine if thermal shock or cracking is a threat.

A proof-of-concept DRH test of a two-brick sample stack was undertaken. The stack exhibited a ramp rate of 480°C/hour, corresponding to a volumetric heat generation of approximately 8 W/cm^3, and maintained 27 kW/m^2 loading for 30 minutes without issue. Each of these conditions are in line with the operation expected in FIRES or in commercial heating elements, showing promise for chromia-based joule devices for both. No deterioration of the material was apparent from the test.

The lower limit of doping, where intrinsic behavior dominates in similar fashion to undoped chromia, was found to be near 0.05%. Subsequently higher dopant levels pushed the onset of intrinsic behavior above 1500°C. Despite the general claims that materials of large polaron behavior should exhibit a negative mobility-temperature derivative, and therefore a positive RTD, no positive RTD was observed.

XRD results of 4% doped samples showed the onset of the $NiCr_2O_4$ spinel phase, indicating that solubility was exceeded at 4%. The limit likely lies only slightly below 4%, which would be consistent with solubility improvements seen by sol-gel processes compared to bulk powder mixing reported in other studies. The findings of the lab-fabricated samples are generally positive for the prospects of creating a Cr_2O_3-based DRH-style FIRES unit. A low brick-brick contact resistivity and small percent change in reciprocal resistivity with temperature show promise for a stable stackable joule heating material. The following sections will quantify the performance of the candidate chromia material with respect to contact heating, short circuit instability length scales and thermal runaway timescales, based on the properties measured here.

7 Electrical contact heating and temperature rise in a DRH-style FIRES unit

The resistance of an electrical contact in any system, such as circuit breakers or electrical leads to heater elements, causes greater heat dissipation at the contact, and therefore a higher temperature at the contact, than in the surrounding material. Close attention must be paid to the "contact supertemperature" ΔT_{super} [100] to ensure contacts will not melt or crack due to thermal shock when electricity is supplied. These considerations are especially important to a DRH-style FIRES system, which has electrical contacts integrated throughout the electrical load of the system. This section introduces the theory and relations necessary to calculate contact supertemperature, and derives the relations in terms of parameters of interest for a FIRES unit: ramp rate, material properties and brick dimension. The relations are then used to calculate contact supertemperature over the relevant geometric space and typical operating condition of FIRES, and are briefly discussed with respect to thermal shock.

7.1 Derivation

The voltage-temperature relationship for mono-material electrical contacts is expressed as:

$$\Delta T_{super} = \frac{V_{b-b}^2}{8k\rho_b} \tag{31}$$

where $V_{b\text{-}b}$ is the voltage drop across the brick contact, k is the material thermal conductivity, and ρ_b is the bulk brick resistivity. This relation is commonly used in designing electrical contacts [100]. It assumes symmetry boundaries away from the contact, valid for the highly symmetric stacked brickwork. It is valid for small temperature changes, where changes in ρ_b and k are negligible.

The voltage drop across the contact can be expressed in terms of the geometry and operating conditions, i.e. charge time and temperature range, of the system. Consider a system configuration in Figure 45, where a brickwork consisting of many stacked bricks makes up the DRH mass. Just as a brickwork is made up of many identical bricks, the circuit for the present analysis can be considered as many identical nodes, with identical resistors and voltage drops.

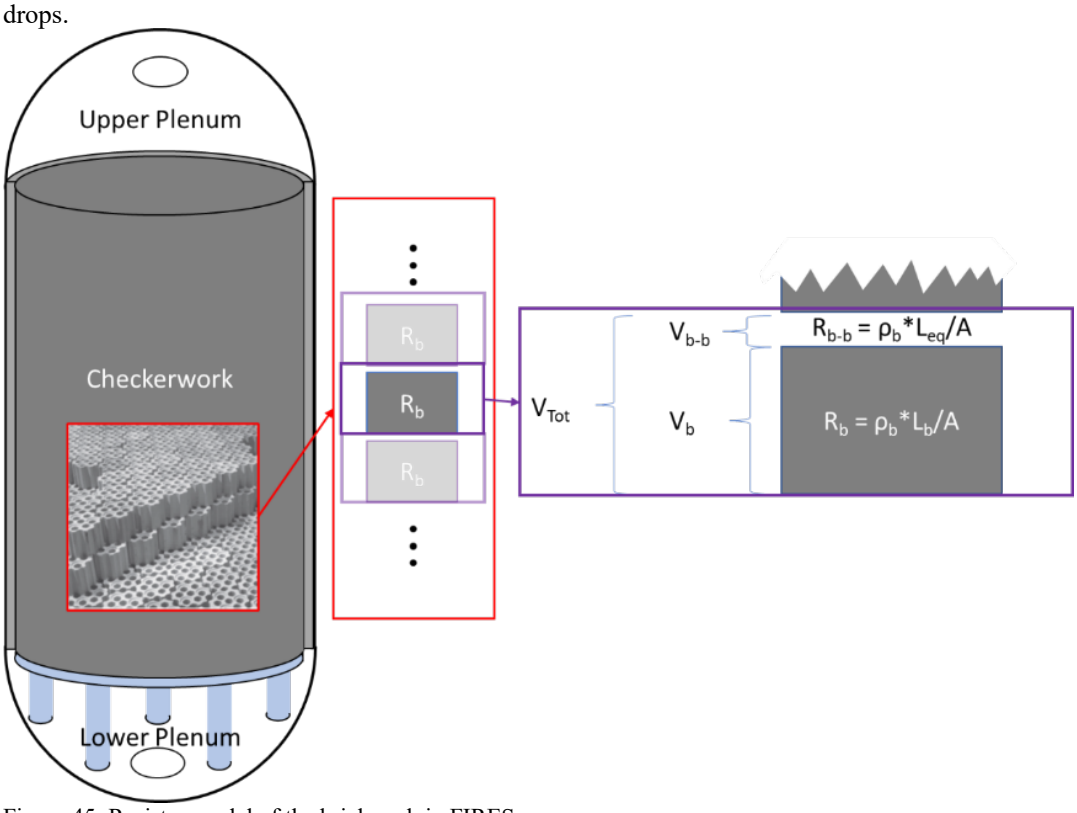

Figure 45: Resistor model of the brickwork in FIRES.

In the circuit, there is a resistance associated with the brick R_b and the brick-brick contact $R_{b\text{-}b}$:

$$R_b = \frac{\rho_b L_b}{A} \tag{32}$$

and

$$R_{b-b} = \frac{\rho_b L_{eq}}{A} \tag{33}$$

Where L_b is the brick length and L_{eq} is the equivalent resistor length of the contact resistance. Here, the distinction between areas A, A_{nom} and A_{eff} is dropped, as the effect of apparent porosity on contact resistance depends on the scale of the pours formed at the surface compared to the deformation scale, which is not considered here. These effects are expected to be generally small, especially at higher densities, and may be captured in the L_{eq} term. The voltage drop across the contact $V_{b\text{-}b}$ can be expressed in terms of the total voltage drop across the circuit V_{tot} by the voltage divider law:

$$V_{b-b} = \frac{V_{tot} R_{b-b}}{R_{b-b} + R_b} = \frac{V_{tot} L_{eq}}{L_{eq} + L_b} \tag{34}$$

Ideally, V_{tot} will be controlled by power electronics to deliver a near-constant power into the system P_{in}:

$$P_{in} = \frac{V_{tot}^2}{(R_b + R_{b-b})} \tag{35}$$

P_{in} is set by the desired charge time and operating temperature range:

$$P_{in} = q''' * Volume = \rho_{mass} c_b \frac{dT}{dt} * L_b * A \tag{36}$$

where ρ_{mass} is the mass density of the brick and c_b is the specific heat. For the present analysis it is assumed that properties are constant with temperature, such that a constant power input implies a constant temperature ramp rate $\frac{dT}{dt}$, which may be expressed in terms of the difference in maximum and minimum system temperatures $T_{max} - T_{min}$, and the charge time t_{Charge}:

$$\frac{dT}{dt} = \frac{T_{max} - T_{min}}{t_{Charge}} \tag{37}$$

By combining the above relations, the contact supertemperature can be described as a function of only $T_{max} - T_{min}$, t_{Charge}, L_b and L_{eq}:

$$\Delta T_{super} = \frac{T_{max} - T_{min}}{t_{Charge}} * L_{eq}^2 * \frac{L_b}{L_b + L_{eq}} * \frac{1}{8\alpha} \tag{38}$$

where α is the thermal diffusivity of the material:

$$\alpha = \frac{k}{\rho_{mass} c_b} \tag{39}$$

7.2 Results and discussion

There are several noteworthy features of relation (38). One is that ΔT_{super} has no dependence on the material bulk resistivity ρ_b. This arises from the assumption made at the outset that ΔT_{super} is only a few degrees, such that

the material resistivity at the contact is not significantly different from the resistivity in the bulk material. Another feature is that ΔT_{super} scales linearly with the temperature ramp rate, and therefore linearly with the charge power P_{in}.

Figure 46 shows the contact supertemperature ΔT_{super} and resistance ratio $R_b/(R_b+R_{b\text{-}b})$ as a function of brick length L_b and the contact equivalent resistor length L_{eq} for typical brick properties and FIRES operating conditions, based on the inputs shown in Table 8. Results from Section 6.2.2 showed L_{eq} values in the range of 1-2 cm above 300°C. ΔT_{super} is between 3 and 13°C for these conditions, which should be well below the worries about hot thermal shock. Previous work [2] has simulated the temperature differences experienced by the brickwork during discharge and compared them to merit indices of thermal shock reported in Lu and Fleck [104]. Although chromia properties are not reported, the cold shock resistance of alumina ranges from approximately ~30 to 300°C. In the case of hot shock, Lu and Fleck report a temperature resistance a factor 3.2 greater, i.e. ~90-900°C.

The ΔT_{super} result is nearly independent of L_b over the range considered, because the term $L_b/(L_b+L_{eq})$ is near unity for most practical brick sizes, i.e. 15-30 cm. Figure 46b shows this ratio, which also indicates the fraction of heat generated in the bulk. Thin bricks on the same scale as the equivalent resistor length would change this behavior. However, very thin bricks violate the assumption of semi-infinite solids, making the present analysis invalid. An analysis of very thin bricks is not considered herein.

Table 8: Inputs to supertemperature ΔT_{super} (38).

Supertemperature Calculation Inputs		
T_{max}	2000	°C
T_{min}	500	°C
t_{Charge}	5	hr
Ramp Rate, dT/dt	300	°C/hr
k	0.01	W/cm-K
c_b	0.87	J/g-K
ρ_{mass}	3.73	g/cm^3
α	0.0031	cm^2/s

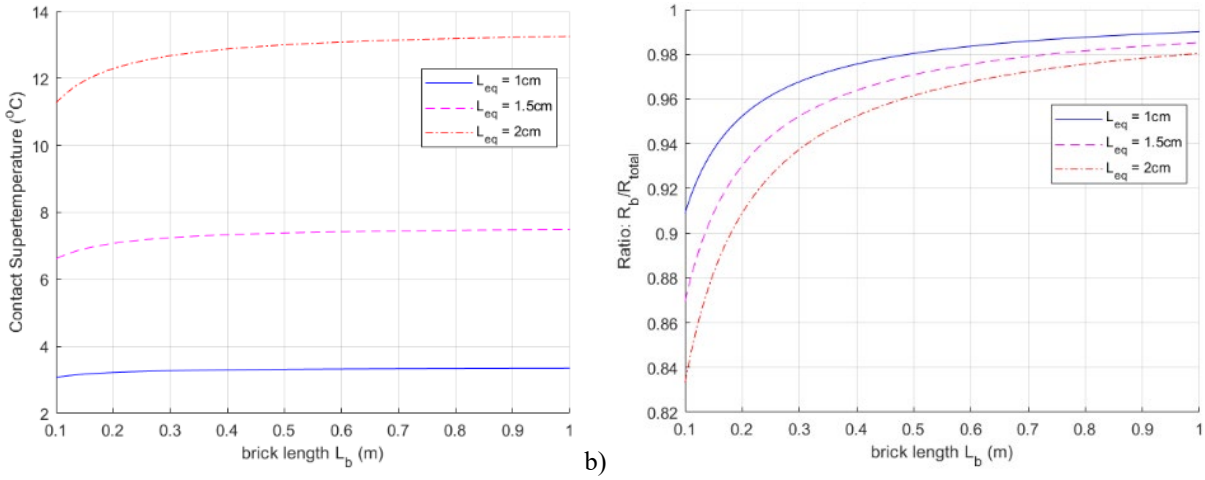

a) b)

Figure 46: a): ΔT_{super} as a function of L_b and L_{eq}. b): resistance ratio $R_b/(R_b+R_{b\text{-}b})$ as a function of L_b and L_{eq}. See Table 8 for inputs.

7.3 Summary of contact heating and temperature rise calculations

The contact supertemperature ΔT_{super} was derived as a function of the key design and operating parameters of a FIRES unit. The derived relation scales linearly with power, and by the square of equivalent resistor length L_{eq}, and is largely independent of the brick length L_b at the expected dimension range of a real FIRES unit. The ability to

adjust ΔT_{super} with geometric or operational design decisions is therefore limited, since L_{eq} is the dominant term and is an extrinsic material property.

Using the equivalent resistor length L_{eq} of brick-brick contacts, a ΔT_{super} of 3-13°C was found for typical FIRES geometry and operating conditions. This is in class with the temperature differences expected during discharge [2], and is well below the temperature differences that cause thermal shock or cracking in most refractory ceramics [104].

The cases where $L_b \approx L_{eq}$ or $L_b \ll L_{eq}$ violate the present analysis and were not explored here. However, there may be merit to a system where most heat is generated at the contacts and conducted through the bulk brick rather than generated volumetrically. More customizability in the stack resistance is one benefit. One could also imagine layers of brick with differing brick lengths L_b, introducing more or less contact resistances in different locations. This may be another method beyond doping that creates regions of differing heat generation.

The low ΔT_{super} of bare brick-brick chromia contacts supports the use of chromia-based firebricks in a DRH-style FIRES system without the need for mortar or other potentially expensive surface engineering.

8 Short circuit instability calculations

The fundamental considerations of materials of different RTD trends in "parallel" and "series" resistor configurations was discussed in Section 3.3. The chromia-based firebrick explored herein has been thoroughly established as a negative RTD material, such that its primary failure mode of concern during resistance heating is short circuit failure. One important point discussed previously was the need to keep RTD relatively small, such that the magnitude of thermal runaway is small and may be mitigated by heat transfer away from the hot spot. This section derives a relation for stability in a system where the temperature profile is somehow perturbed and one portion of material is hotter than another, creating a potential thermal runaway scenario. A critical length of short circuit failure is then plotted as a function of temperature for typical FIRES properties and operating conditions, and the results are discussed in terms of FIRES's design and operation.

8.1 Derivation

It is useful to again consider a 1-D slab, where a region of characteristic length L_{char} may be a small temperature dT hotter than the surrounding material. Figure 47 shows the slab, which represents a generic location in the brickwork, spanning one or multiple bricks. (Note that at most temperatures of interest radiative resistance in the air gaps between bricks or across air channels is negligible compared to the conductive resistance of the bricks themselves).

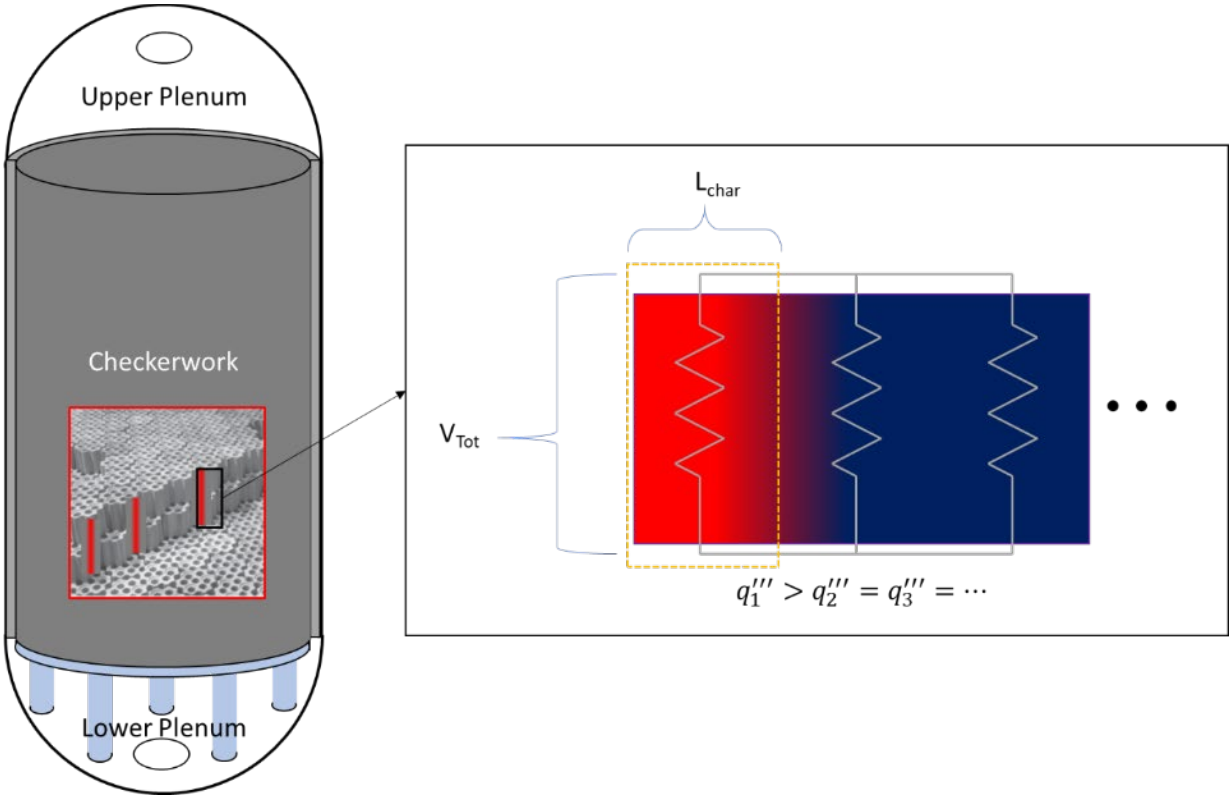

Figure 47: Checkerwork with vertical hot spots in line with electrical flow path.
The zoom represents a region of vertically oriented higher temperature material adjacent to material uniform in temperature, which may lead to a short circuit failure.

The system receives a volumetric heat rate q''' according to a voltage drop V_{tot} across the system height:

$$q''' = \frac{V_{tot}^2}{\frac{\rho_b L}{A}}$$

(40)

Because the material has a negative RTD, the parallel region of L_{char} with a higher temperature possesses a lower resistivity ρ_b, and therefore generates a slightly larger q'''. However, the higher temperature also drives a heat flux q'' towards the lower temperature region. For the present analysis a symmetry boundary condition is assumed on the left extremity of the region.

How the system responds to the small temperature perturbation of the region of L_{char} depends on the ratio of the change in excess heat generated in the region to the change in heat flux out of the region:

$$Stability\ Check = \frac{\frac{d(heat\ generation)}{dT}}{\frac{d(heat\ removal)}{dT}}$$

(41)

If the above relation is <1, then a small temperature perturbation will cool down. If the relation is >1, then the region will heat up further and may exhibit a short circuit failure without intervention. For the present analysis, the region of elevated temperature will be treated as a lumped capacitance system with a uniform temperature. The characteristic length L_{char} will function as a dimension of the heated volume as well as the length of conduction necessary to remove the heat from the region. The stability check may thus be expressed:

$$Stability\ Check = \frac{\frac{dq'''}{dT} * L_{char}}{\frac{dq''}{dT}}$$

(42)

where q'' is the area heat flux. Note that geometric terms for the height and width of the volume are excluded in (42) because they appear in both the numerator and denominator. The change in volumetric heat rate with temperature $\frac{dq'''}{dT}$ is dependent only on the change in reciprocal resistivity $\frac{d\left(\frac{1}{\rho_b}\right)}{dT}$:

$$\frac{dq'''}{dT} = \frac{V_{tot}^2}{\frac{L}{A}} * \frac{d\left(\frac{1}{\rho_b}\right)}{dT}$$

(43)

By rearranging (40) the voltage and geometric terms of (43) may be substituted with $q'''\rho_b$, which yields the fractional change in the reciprocal resistivity $\frac{d\left(\frac{1}{\rho_b}\right)}{dT}\rho_b$ discussed in Section 6.2.1 and measured for the lab-fabricated chromia firebricks:

$$\frac{dq'''}{dT} = q''' \frac{d\left(\frac{1}{\rho_b}\right)}{dT}\rho_b$$

(44)

It was previously derived in Section 7.1 that the volumetric heat rate q''' may be expressed in terms of the temperature ramp rate and firebrick properties, where temperature variation of properties is neglected. The heat generation term may then be written as:

$$\frac{d(heat\ generation)}{dT} = \frac{\rho_{mass} c_b (T_{max} - T_{min})}{t_{Charge}} \frac{d\left(\frac{1}{\rho_b}\right)}{dT}\rho_b * L_{char}$$

(45)

The heat flux term may be substituted with Fourier's law. Data for thermal conductivity of bulk chromia firebrick could not be found. By taking thermal conductivity k as a temperature-independent conservative value in line with other firebricks [53], and substituting dx with the finite value L_{char}, the denominator may be expressed:

$$\frac{d(heat\ removal)}{dT} = \frac{d\left(k\frac{dT}{dx}\right)}{dT} = \frac{k}{L_{char}} \tag{46}$$

The stability check may therefore be expressed:

$$Stability\ Check = \frac{L_{char}^2}{\alpha}\frac{(T_{max} - T_{min})}{t_{Charge}}\frac{d\left(\frac{1}{\rho_b}\right)}{dT}\rho_b \tag{47}$$

8.2 Results and discussion

Figure 48 shows L_{char} as a function of temperature for which the left-hand side of relation (47) is set to unity. Table 9 shows the inputs to the relation. Areas of uneven temperatures smaller than this length scale should not be at risk of a short circuit failure. Areas larger than this length scale will grow hotter in time and may short circuit the FIRES brickwork without intervention.

Table 9: Inputs of stability check calculation (47)

Passive Stability Check Inputs		
Ramp Rate, dT/dt	300	°C/hr
k	0.01	W/cm-K
c_b	0.87	J/g-K
ρ_{mass}	3.73	g/cm^3
α	0.0031	cm^2/s
ρ_b*d(1/ρ_b)/dT	6.5559e$^{(-0.003T(K))}$	1/K

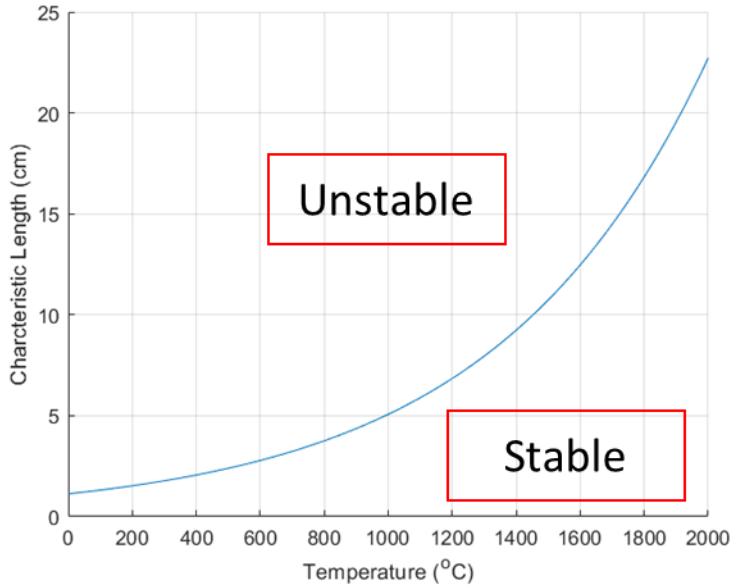

Figure 48: Length scale map of short circuit stability as a function of temperature for chromia.
Hot spots smaller than the stable length will dissipate heat and equilibrate to the surrounding temperature.

From zero to 2000°C, the stable characteristic length of chromia ranges from approximately 1 cm to 23 cm. The manifestation of instability and thermal runaway must consider the stable length scale at the lower bound of temperature operation, which will typically be 400-800°C depending on the application, i.e. 2-4 cm. In the context of operating a DRH-style FIRES unit, the length scale of a few centimeters has two important implications: (1) the stability length matches the length scale of typical firebrick wall thicknesses between air channels, such that a few

degrees temperature difference between the air channel and the inner wall after a discharge period should not be an instability threat. This result is also promising for chromia-based heater elements, typically only 1-2cm wide. (2) Any perturbation beyond normal ideal operation at scales greater than a few centimeters will likely cause thermal runaway, the timescale of which requires further analysis. Instability is even a concern for the scale of the firebricks themselves, which are typically on the order of 15-30 cm. Having passive stability would require a very narrow electrically conductive flow path not in class with the width of one brick, let alone a typical brickwork diameter, usually several meters wide.

8.3 Limitations of short circuit model

Towards designing a practical FIRES system based on the hot blast stove concept, there is a middle ground between the passive stability length scale found here and the typical brickwork length scale found in industry. First, rather than demanding unconditional passive stability, the tendency of thermal runaway may be addressed operationally by allowing an equilibration period after each cycle where any spatial temperature differences may be reduced. For example, in power cycle operations of daily cycling with charge and discharge times of approximately 5 hours and 10 hours respectively, a further 9 hours of the day where the system rests dormant may be adequate for addressing instabilities of a conductive flow path significantly larger than the stability length. The operation of FIRES units of larger dimensions over several cycles, timescale of thermal runaway, and effects of equilibration times is simulated in Section 9.

Second, a real brickwork is more than a 1-D solid media, and also transfers heat via convection and radiation. A stable length scale that includes these heat transfer mechanisms will depend on the system geometry, which has some design options.

Third, a large brickwork several meters wide may still be formed while maintaining a narrow electrical flow path. Such a brickwork may be made up of many vertically parallel portions of conductive brick, insulated from one another with non-conductive brick, besides bridges of conductive bricks at the top or bottom of the brickwork, to form a narrow “snaking” flow path. The brickwork design is discussed in detail in Section 10.

8.4 Summary of short circuit instability calculations

A relation for stability of negative RTD materials that are at risk of the short circuit failure mode was derived in terms of FIRES operating conditions and material properties. The lumped parameter treatment of the characteristic length as well as the imperfect fit of the power law relation used to model the RTD term both make the present analysis approximate only, but the results define the regimes of stability on the scale of 2-20 cm depending on temperature.

The small length scale necessary for passive stability shows that a FIRES system as imagined herein will not be passively stable during charging, since the stable length scale of the conductive flow path is much smaller than typical firebrick dimensions. An equilibration period after each cycle is a straightforward option for addressing the instability. Section 9 simulates the cycling of conductive areas larger than that of passive stability to explore the timescale of thermal runaway.

9 Thermal runaway simulations

The DRH of a chromia-based brickwork with a conductive flow path larger than a few centimeters is prone to thermal runaway via short circuit failure. This section reports the methods, results, and conclusions of 1-D finite difference simulations of the FIRES charge cycles.

9.1 Methods

The methods are presented in four sections. First, a description of the system cycling is provided. Then, the numerical scheme used to simulate the heat generation and heat transfer is detailed. Next, the simulation inputs and rationale are discussed. Finally, the relevant performance characteristics are explained and ultimately a performance criterion is established.

9.1.1 Cycling description

A cycle consists of three sequential periods: charge, equilibration period, and discharge. Each cycle begins with charge. The initial condition of cycling is depicted in Figure 49. The conductive flow path of width w begins with two different temperature regions, one of temperature T_{min} and the other of $T_{min} + \Delta T_{start}$. The hotter region makes up a fraction f_h of the overall width. Throughout the charge period, heat generation and heat transfer throughout the system is simulated. The charge period ends when any section reaches T_{max}.

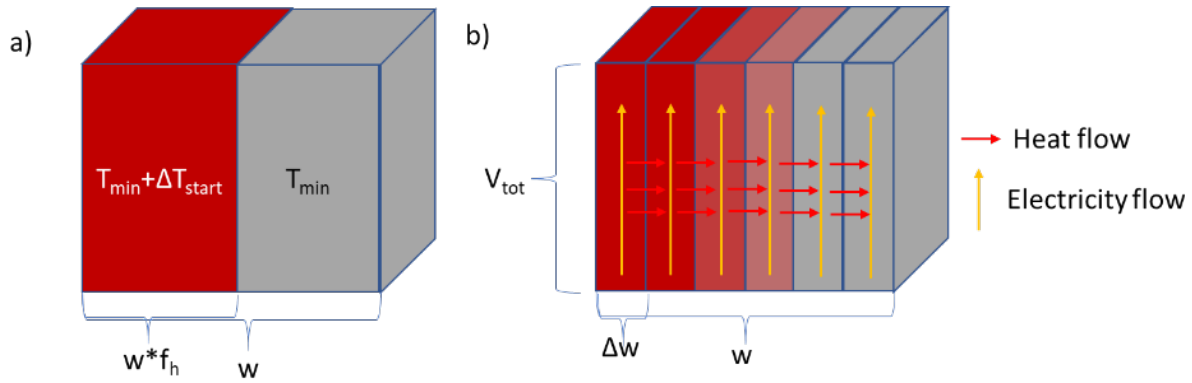

Figure 49: 1-D Modeling of FIRES charge cycling.
a): Initial condition temperature profile. b): Flow path discretization. The voltage V_{tot} applied across the region generates heat at different rates in the different discretized sections. Heat is conducted between adjacent sections. End sections are treated as insulated boundaries.

Following a charge period, an equilibration period of duration t_{equi} is simulated. During this period no electric heating occurs, only conduction through the system. The equilibration period ends after a time of t_{equi} has passed.

The temperature profile at the end of the equilibration period $\boldsymbol{T_{equi}}$ is adjusted according to an "idealized" discharge period, where the system is cooled to a minimum temperature T_{min} without changing the relative temperature profile. As such, the ending temperature profile after a full cycle of charge, equilibration, and discharge, is as follows:

$$\boldsymbol{T_{cycle,end}} = \boldsymbol{T_{equi}} - \min(\boldsymbol{T_{equi}}) + T_{min} \tag{48}$$

The temperature profile $\boldsymbol{T_{cycle,end}}$ of one cycle becomes the initial condition of the next cycle, such that the runaway behavior of multiple cycles may be simulated. For a given scenario at least 5 cycles were generally run to observe the system evolution. More cycles were run in some cases to observe an equilibrium condition, discussed more in results.

A large assumption is made by treating the discharge period as having no net effect on temperature profile. Based on typical operations of convective heat transfer in brickworks, where the plurality of small channels is designed to promote near-uniform flow rates across all channels, it may be expected that the discharge period would aid in

equilibration, since hotter channels would have a higher heat transfer rate to the airstream. On the other hand, imperfections in the brickwork and uneven flow rates may just as likely be the source of an uneven temperature profile and may exacerbate the challenge of thermal runaway. To simplify the present investigation, discharge is therefore assumed to have no effect. The system response to spatial variations in heat removal during discharge is an area of future work.

9.1.2 Numerical scheme

The temperature change due to heat conduction in each discretized section was calculated using methods similar to previous work [2]. The thermal diffusion matrix $\boldsymbol{C}$ with insulated boundary conditions on each end may be written:

$$\boldsymbol{C} = \begin{bmatrix} -1 & 1 & 0 & 0 & \cdots & 0 & 0 \\ 1 & -2 & 1 & 0 & \cdots & 0 & 0 \\ 0 & 1 & -2 & 1 & \cdots & 0 & 0 \\ \vdots & \vdots & \ddots & \ddots & \ddots & \vdots & \vdots \\ 0 & 0 & \cdots & 1 & -2 & 1 & 0 \\ 0 & 0 & \cdots & 0 & 1 & -2 & 1 \\ 0 & 0 & \cdots & 0 & 0 & 1 & -1 \end{bmatrix} \frac{k}{\rho_{mass} c_b \Delta w^2} \tag{49}$$

The dimensions of $\boldsymbol{C}$ is N_w x N_w, where N_w is the number of discretized sections. The time evolution of temperature through the brickwork was solved using the Crank-Nicolson method, which takes the form:

$$(\boldsymbol{I} - \theta \boldsymbol{C} \Delta t)\boldsymbol{T_{new}} = (\boldsymbol{I} + (1-\theta)\boldsymbol{C}\Delta t)\boldsymbol{T_{old}} \tag{50}$$

where $\boldsymbol{I}$ is the identity matrix of equal dimensions to $\boldsymbol{C}$, $\boldsymbol{T}$ is the temperature vector of the discretized brick sections (before or after one time step, Δt, denoted by subscript), and θ is the weighting factor between the implicit and explicit solution methods, which is set equal to 0.5 for the Crank-Nicolson scheme.

Following the heat conduction calculation, the temperature increase of each region due to joule heating in the same time step was calculated separately, with properties evaluated at $\boldsymbol{T_{new}}$. The total input power P_{in} of the system is equal to the sum of the power received by each discretized region, which all experience the same voltage drop:

$$P_{in} = V_{tot}^2 \sum_{n=1}^{N_w} \frac{1}{R_n} = \frac{V_{tot}^2}{R_{eff}} \tag{51}$$

Here R_{eff} represents an effective resistance of the system. By replacing P_{in} with the desired charge rate of FIRES (36), the voltage V_{tot} may be expressed in terms of the effective resistance R_{eff} and the usual FIRES parameters:

$$V_{tot}^2 = w \frac{\rho_{mass} c_b (T_{max} - T_{min})}{t_{Charge}} R_{eff} \tag{52}$$

Note that w is the only dimension necessary to define the volume, and that the height and length dimensions inevitably cancel due to the 1-D geometry. The temperature rise due to joule heating in each discretized region of width Δw may be calculated from the energy delivered to the region in one time step Δt:

$$T_{joule,n} = \frac{R_{eff}}{R_n} \frac{w}{\Delta w} \frac{(T_{max} - T_{min})}{t_{Charge}} \Delta t \tag{53}$$

The sum of the vectors $\boldsymbol{T_{joule}}$ and $\boldsymbol{T_{new}}$ is taken as the new $\boldsymbol{T_{old}}$ for the next time step.

It may be noted that this treatment of heat generation makes this scheme only 1st order accurate, rather than 2nd order accurate as the Crank-Nicolson scheme generally grants. An accurate solution may be obtained with a sufficiently large N_w and small time-step, the computational cost of which is not an issue for the 1-D system simulated herein.

9.1.3 Simulation inputs

The resistance of each section was determined by the section width Δw and the bulk resistivity ρ_b interpolated from the results of lab-fabricated doped chromia in Section 6.2.1. To simulate higher temperature conditions, ρ_b was extrapolated beyond 1500ºC assuming a linear Arrhenius behavior extrapolated from the 1500ºC and 1400ºC soak periods. In reality the curve may flatten, reverse in RTD, or enter the intrinsic regime. Figure 50 shows the resistivity data and extrapolation.

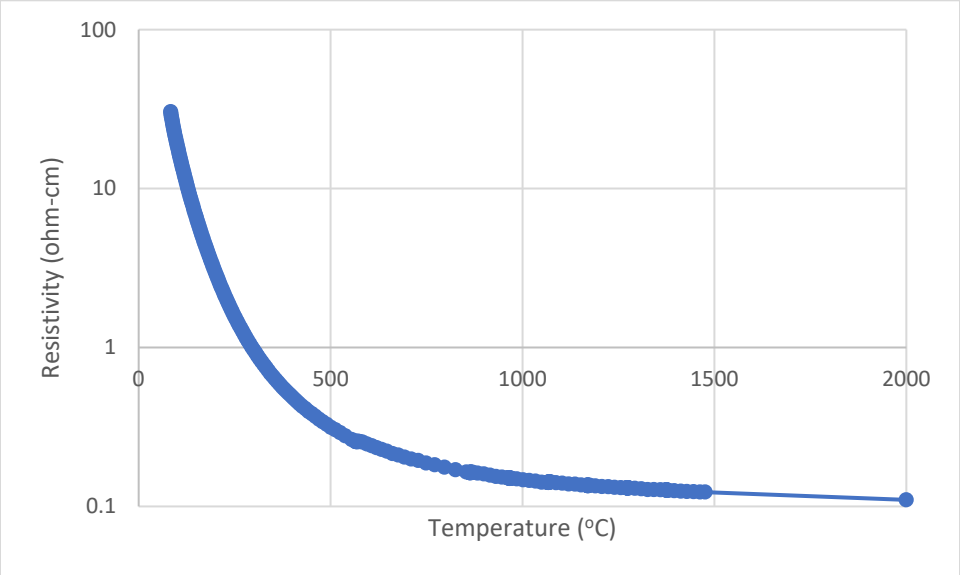

Figure 50: Bulk resistivity ρ_b and extrapolated point to 2000ºC for use in thermal runaway simulations.

Table 10 shows the simulation inputs if the thermal runaway simulations. A T_{max} of 1900ºC and charge time of 5 hours are representative of the expected maximum operating temperatures and charge time of a FIRES unit that may run a variety of applications on a daily cycling basis. Preliminary runs showed that the system was most prone to thermal runaway when the hot material fraction f_h is set near 0.5. This is caused by the large thermal mass of both cold and hot regions and the long characteristic length that heat must travel for equilibration, compared to a relatively thin hot or cold region for f_h near 0 or 1. The value of 0.5 was therefore used for f_h in all scenarios moving forward. The mesh nodes and time step of 100 sections and 5s respectively were found to be broadly acceptable on the overall length scales considered, with no change in results with greater resolution.

The equilibration time was varied between 5 and 10 hours, which, in the context of daily cycling, leaves between 14 and 9 hours for FIRES to discharge each day. Different values of T_{min} were considered with respect to various compressor outlet temperatures of gas power cycles, which may vary between approximately 300ºC and 600ºC, depending on the ambient conditions and compression ratio of the cycle [105]. A slightly wider range than this, 200ºC to 800ºC, was considered.

System width was varied between 0.25m and 0.50m. When considering a real brickwork of air channels, the simulated solid widths correspond to a width approximately 2.5-3 times larger, i.e. 0.6m-1.5m. This arises from the distribution of air channels throughout the mass, which increase the volume and decrease the thermal resistance due to efficient radiative heat transfer throughout most of the temperature range. Though not rigorously proven here, further qualitative discussion is offered in Section 10.

Table 10: Thermal runaway simulation inputs

Thermal Runaway Simulation Inputs		
Constants		
T_{max}	1900	ºC
t_{Charge}	5	hr

f_h	0.5	-
k	0.01	W/cm-K
c_b	0.84	J/g-K
ρ_{mass}	3.73	g/cm^3
Δt	5	s
N_w	100	-
Variables		
t_{equi}	5,8,10	hr
T_{min}	200-800	^oC
w	0.25,0.33,0.41,0.50	m
ΔT_{start}	25-100	^oC

9.1.4 Performance metric considerations

Two key performance characteristics are of interest as FIRES is cycled. One is the fraction of energy that is stored compared to the ideal possible storage. This corresponds to the ending temperature profile of a charge period compared to an ideal spatially uniform temperature of T_{max}. The other characteristic is the maximum thermal stress experienced by the bricks, which depends on the width of the bricks themselves and the temperature difference across them.

Good performance with respect to both characteristics may be adequately indicated by the temperature difference ΔT across the brickwork, where ΔT of a temperature profile $\boldsymbol{T}$ at a given time is simply:

$$\Delta T(t) = \max\big(\boldsymbol{T}(t)\big) - \min(\boldsymbol{T}(t)) \tag{54}$$

The fraction of energy stored at the end of the charge period correlates to the final temperature difference across the system, ΔT_{final}. The maximum stresses experienced by individual bricks correlates to maximum temperature difference across the system during charge, ΔT_{max}.

It was found across most of the simulated space that $\Delta T_{final} \approx \Delta T_{max}$ after 5 cycles, varying by 15% or less for dimensions other than 0.25m, which generally varied by 30% or less. ΔT_{max} may therefore be taken as a conservative metric of stored energy as well as the brick thermal stresses.

For all scenarios, a "passing" criterion was chosen:

$$\Delta T_{max} \leq 100^o C \tag{55}$$

For typical brick dimensions and the T_{min} values tested here, this criterion corresponds to an energy storage fraction of >95%, and a temperature difference across individual bricks of no more than a few 10s of degrees Celsius. This criterion is a useful basis of comparison across the option space considered here.

9.2 Results

Results of thermal runaway simulations are discussed in three parts. First, a select set of results is shown to demonstrate general system dynamics with respect to cycling and the initial condition ΔT_{start}. Then, the $\Delta T_{max} \leq 100^o C$ test is applied across the design space, and tradeoffs of w, T_{min}, and t_{equi} are examined. Finally, the insights and limitations of these findings are discussed with respect to other design considerations.

9.2.1 General system dynamics: ΔT_{start}, cycling, and equilibrium

Figure 51a shows the evolution of the temperature profile at different points of the charge cycle. The initial step change in temperature becomes a smooth gradient. system ΔT steadily increases (Figure 51b) as current preferentially heats the higher temperature region. In the relatively small system shown, $w = 0.25m$, a maximum

ΔT_{max} is reached in the middle of the charge cycle before ΔT begins to fall. This change occurs because at higher temperatures the RTD has sufficiently reduced so that conduction from the hot region to the cold region begins to dominate. For lower T_{min} values such as 200°C and 300°C, the ΔT_{final} is much higher than ΔT_{start} after the first cycle. However, for $T_{min} = 800^o C$, $\Delta T_{final} < \Delta T_{start}$ at the end of the first charge period, signifying that under these conditions the system would converge to $\Delta T = 0$ even without an equilibration period. These features were less common for most conditions in systems of larger *w*, where it was often found that $\Delta T_{final} = \Delta T_{max}$.

Two broad observations may be made regarding the threat of thermal runaway. First, significant thermal runaway occurs on the timescale of hours. Depending on the operating and initial conditions, one or more cycles may occur before temperature differences >100°C are experienced. This supports the assumption made from the outset that an equilibration time between cycles may be a reasonable coping strategy.

Secondly, an equilibrium result is found with enough cycling, where subsequent cycles show a repeated starting profile (Figure 51c), ΔT_{max}, and ΔT_{final} (Figure 51d). This equilibrium result is dependent on t_{equi} and independent of ΔT_{start}. Figure 51e shows an example of different starting temperature conditions ΔT_{start} and the resulting ΔT_{max} over several cycles. ΔT_{start} values of 25°C and 100°C converge to the same ΔT_{max} result, though the number of cycles required to reach the equilibrium increases if ΔT_{start} is far from the starting temperature difference of the equilibrium cycle. So long as a reliable equilibration time is allowed between each cycle, and so long as the heat transfer mechanisms of the system are not fundamentally altered it should be assured that the system will passively remain at or below some equilibrium value of ΔT_{max}.

For the present analysis, the equilibrium result does not necessarily need to be found to conclude whether a system passes or fails the $\Delta T_{max} \leq 100^o C$ criterion; from the results of Figure 51e it could be determined within 5 cycles that the system fails at an equilibration time of 5 hours, and succeeds with an equilibration time of 8 hours. A ΔT_{start} value of 100°C was used as an initial condition for all other cases considered, which guarantees that the passing condition $\Delta T_{max} \leq 100^o C$ is never achieved due to non-equilibrium results.

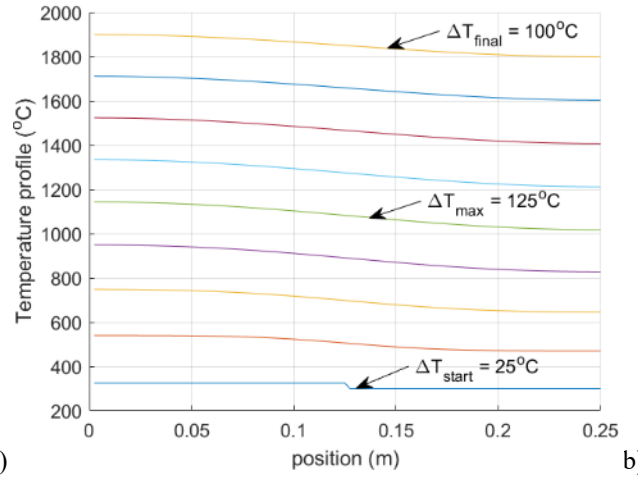

a)

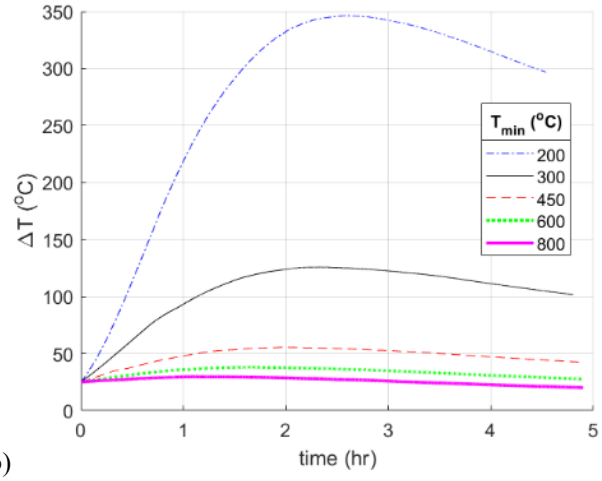

b)

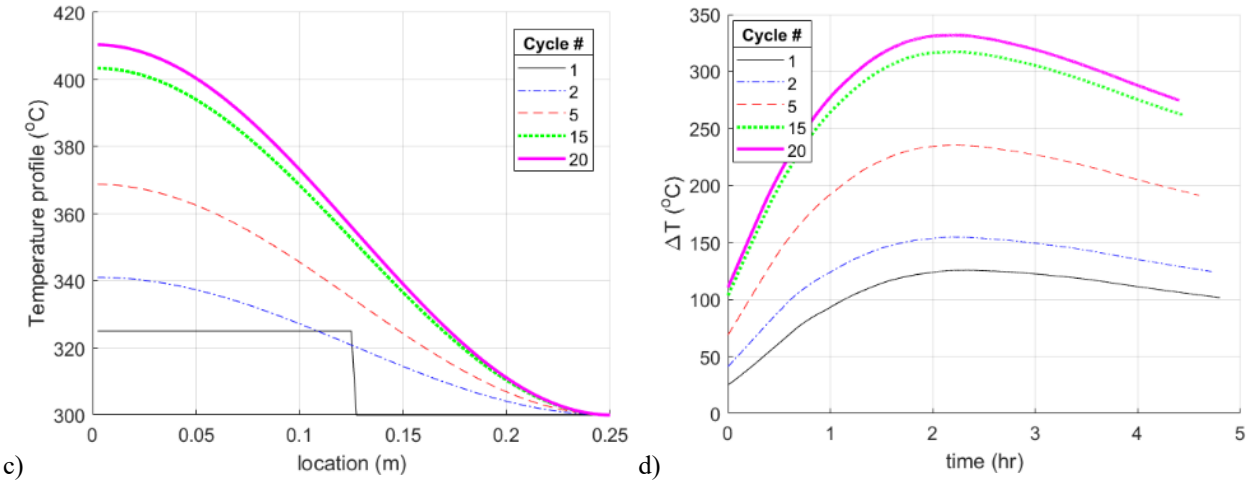

c) d)

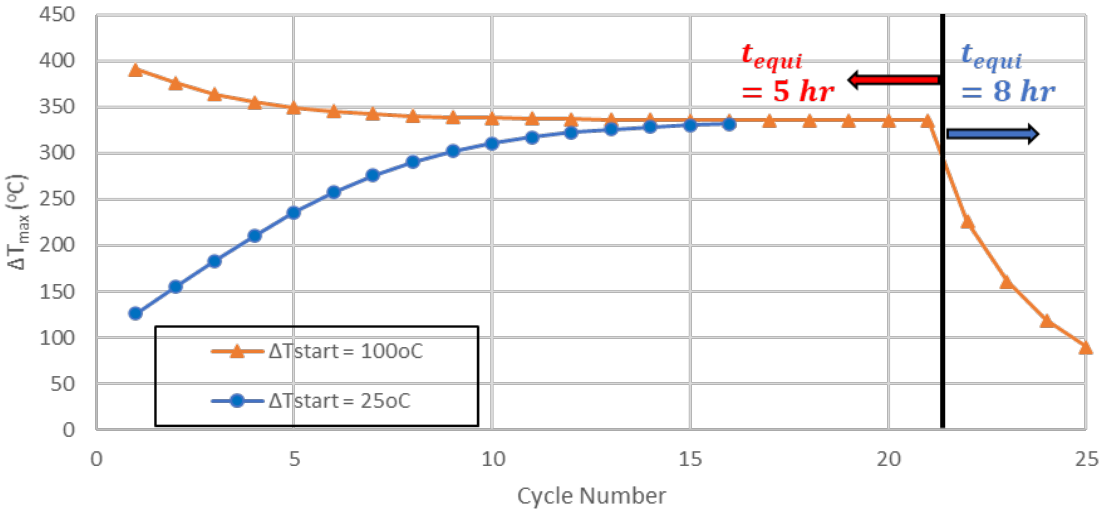

e)

Figure 51: Evolution of temperature and ΔT versus time as a function of varying T_{min} and cycling.
All results for $\Delta T_{start} = 25^oC$, $w = 0.25m$, t_{equi} = 5 hours, unless noted. a): Temperature profiles at different time increments during first cycle charge period, T_{min} = 300°C. b): ΔT versus time during first cycle of various T_{min}. c): Initial temperature profile of 5 subsequent cycles, T_{min} = 300°C. d): ΔT versus time of 5 subsequent cycles, T_{min} = 300°C. e): maximum temperature difference ΔT_{max} across the system during the charge period versus number of cycles for different ΔT_{start} and t_{equi}. T_{min} = 300°C.

9.2.2 The $\Delta T_{max} \leq 100^oC$ criterion: Tradeoffs of w, T_{min}, and t_{equi}

Table 11 shows the equilibration time t_{equi} necessary to achieve $\Delta T_{max} \leq 100^oC$ for scenarios of differing w and T_{min}. Each scenario was run for at least 5 cycles. Additional cycles were run in edge cases where convergence above or below $\Delta T_{max} \leq 100^oC$ remained unclear. The "zero" hours of t_{equi} for temperatures of 700°C and 800°C indicates that $\Delta T_{final} < \Delta T_{start}$ after the first cycle, such that these cases would equilibrate without any additional time. "Fail" conditions are for systems that did not achieve $\Delta T_{max} \leq 100^oC$ even with the maximum tested equilibration time of 10 hours.

Table 11: t_{equi} required to achieve $\Delta T_{max} \leq 100^oC$ as a function of w and T_{min}.

t_{equi} (hr) necessary to reduce ΔT_{max} below 100°C									
T_{min} (°C) / w (m)	200	300	400	450	500	550	600	700	800

0.25	fail	8	5	5	5	5	5	0	0
0.33	fail	fail	10	8	5	5	5	5	5
0.41	fail	fail	fail	fail	10	10	8	5	5
0.5	fail	fail	fail	fail	fail	fail	fail	8	5

The relationships between w, T_{min}, and t_{equi} correspond to the tradeoffs between system complexity, breadth of application viability, and use potential for a given application. The smallest w represents a brickwork of the narrowest electrically conductive path, which therefore requires a more sophisticated brickwork of many snaking paths. The length scale however requires relatively little equilibration time between charge periods, even at relatively low temperatures, making it broadly applicable to the full range of Brayton cycle compressor outlets, and capable of extensive use, since it may discharge throughout the night. Larger w systems may be more practical to build, but require longer equilibration times, higher minimum temperatures, or both. Different options may be best for different scenarios.

9.2.3 Limitation of results

The present analysis describes general tradeoffs of relevant parameters. However, the idealized treatment of the FIRES system and operations makes the results limited in their application to real systems. One key limitation is the neglected discharge dynamics. Variations in flow rates and heat transfer rates within the system require investigation. Another limitation is the assumption that heat transfer through the brickwork is limited conduction. While modern brickworks generally have enclosed chimney air channels, other brick shapes may provide "windows" between channels that enable continuous pathways of radiative heat transfer throughout the brickwork. In this case, the results of Table 11 may change substantially. Another assumption which may be different in practice is that FIRES must take as its inlet whatever the outlet temperature of a compressor or other interfacing process produces. However, heat exchange or gas mixing with the FIRES outlet may be a practical option to ensure FIRES sees a desirable higher inlet temperature. Some of these options are discussed further in Section 10.3.

9.3 Summary of thermal runaway simulations

Thermal runaway was simulated through characteristic systems using 1-D finite difference methods. System dimensions of 0.25m-0.5m were investigated, corresponding to brickwork widths of approximately 0.6-1.5m when accounting for air channel volume and radiative heat transfer across channels. Minimum system temperatures were chosen in class with outlet temperatures of compressors in Brayton power cycles. Equilibration times of 5-10 hours were explored, such that simulated cycles were aligned with daily cycles necessary in a high-solar PV energy market.

General system dynamics showed that the timescale of thermal runaway, i.e. growth of an initial temperature difference from a few 10s of degrees Celsius to over 100°C, takes hours, or multiple charge cycles, which grants the opportunity to include an equilibration period after a charge or discharge period. Additionally, systems cycled enough with a consistent equilibration time each cycle results in an equilibrium result, independent of an initial temperature perturbation. Designing a system with a certain width w and operating it with a consistent equilibration time t_{equi} will ensure that a certain ΔT_{max} is not exceeded. A criterion of $\Delta T_{max} \leq 100^o C$ was chosen as a desirable condition where thermal gradients in individual bricks would be kept to only a few 10s of degrees Celsius, and total storage capacity potential would be realized within 5%. The t_{equi} necessary to meet this criterion was found across the design space, and the tradeoffs of different designs were discussed.

Ultimately, the design and construction of a large conductive brickwork that may achieve stable reliable operation appears achievable with some equilibration time built into each cycle. The analysis herein described general tradeoffs of relevant parameters, with a simplified treatment of discharge and specific system assumptions. Design options that increase radiative heat transfer and increase the inlet temperature of FIRES may increase the viability of the system in different applications and different electricity markets. Section 10 discusses some design options.

10 Conceptual design of a DRH FIRES unit

A design of a DRH-style FIRES unit is presented herein based on the analyses and insights presented in previous sections. The design, as with the general concept, is inspired by hot blast stoves used in the iron blast furnace industry, consisting of a high temperature brickwork contained in an insulated steel vessel. Previous work [2] has detailed the more generic parts of the system and components necessary. The key contributions of the present work are the directly resistance heated (DRH) brickwork and bricks.

First, the brickwork itself is described. The basic composition and function of different regions are detailed, stacking pattern options and electrical charge configurations are presented, and topics of special considerations are discussed. Design characteristics are compared to the results and assumptions from previous sections. Next, brick geometry is explored. Effects of brick shape, width and height are discussed with respect to thermal runaway and contact heating. Finally, high-level flow control design and options for preheating of the FIRES inlet is explored, with an interest of boosting inlet temperatures for reducing thermal runaway effects.

10.1 Brickwork design

Similar to a traditional hot blast stove, the DRH-style FIRES unit consists of a large brick stack within an insulated pressure vessel. To intake an electrical input for charging, the DRH brickwork has a unique layout of firebrick with electrically diverse properties. Figure 52 shows a high-level schematic of the DRH brickwork concept.

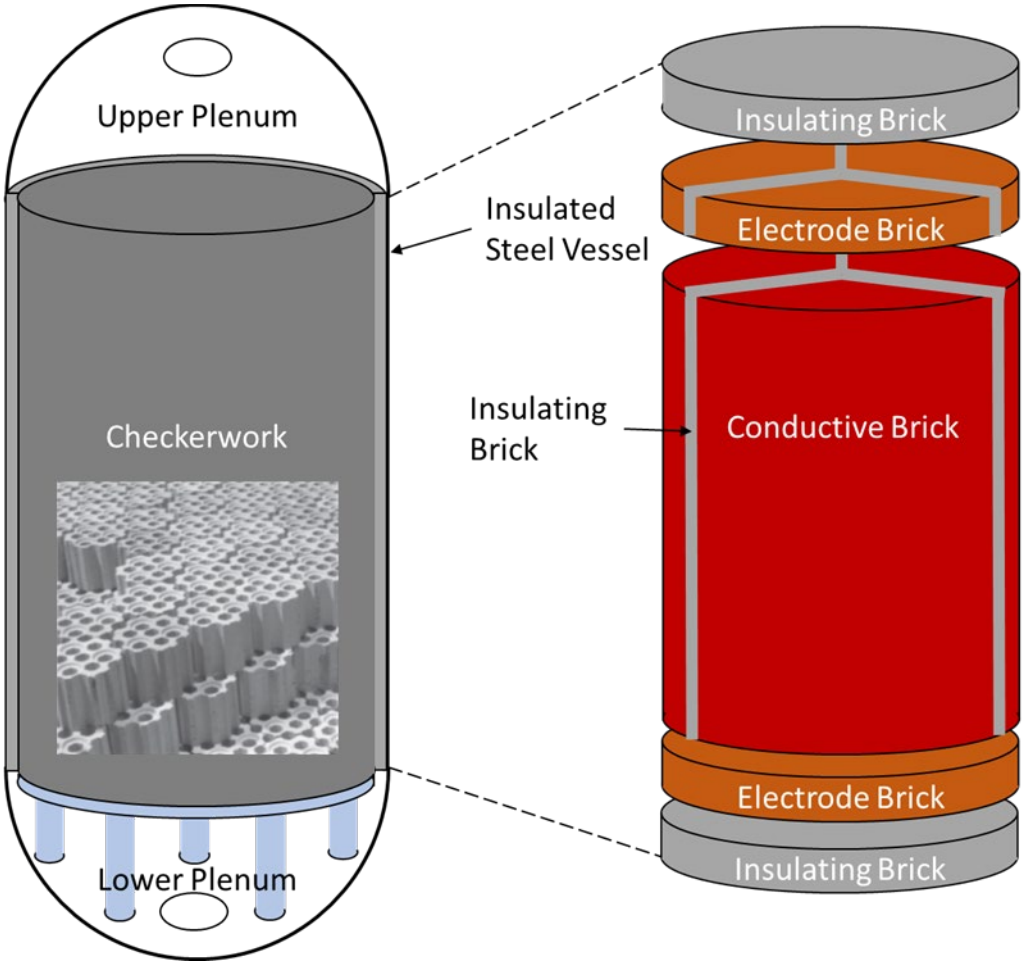

Figure 52: high-level schematic of the DRH brickwork concept. Generic 3-phase wye configuration.

The DRH brickwork is composed of three regions of varying electrical conductivity: the conductive region, electrode region, and insulating region. The characteristics of each region are as follows:

- **The conductive regions** are regions of conductive brick, where the vast majority of heat generation occurs. Bricks in this region are doped at a level that exhibits a gradual RTD such that electrical resistance-heating can be achieved stably and with minimized risk of thermal runaway. The conductive region makes up the majority of the brickwork volume.
- **The electrode regions** are regions of highly conductive brick, approximately an order of magnitude more conductive than conductive brick, where relatively little heat is generated due to the low voltage drop in the region. These regions, located at the top and bottom of the brickwork, represent geometric bottlenecks for electrical flow, the uneven heating of which is prevented by the higher conductivity of the bricks. Doping levels are significantly higher than that of conductive brick, and a gradual RTD is not necessary. The top electrode region interfaces with the electrical penetrations that deliver electricity from the grid or the local zero-carbon electricity source. Placing all electrode penetrations at the top grants easy access for maintenance. The top and bottom electrodes also serve as connections between adjacent electrical flow paths of the conductive region, discussed more below.
- **The insulating regions** are made of electrically insulative bricks, which may be either undoped variants of the conductive bricks or a different composition with a similar coefficient of thermal expansion. Layers of insulating brick at the top and bottom of the stack provide some weight for good electrical contacts in the electrode and conductive regions near the top of the stack, and provide both thermal and electrical insulation to the support structures at the bottom of the stack, respectively. Insulative layers may also cut vertically through the electrode and conductive regions to form isolated flow paths for electricity, such as is necessary for a three-phase AC input, or to reduce the conductive width of the electrical flow path for greater resistance to thermal runaway.

Independent of the varying electrical properties, the geometry of the bricks themselves are identical across regions and form continuous air channels vertically along the brickwork.

10.1.1 "Snaking" electrical flow path, geometry, and power source considerations

Thermal stability calculations (Section 8) and thermal runaway simulations (Section 9) have demonstrated the need to reduce the conductive width of the electrical flow path of FIRES far below the 5-10 meter diameter of a typical brickwork. Vertical insulative layers may be used to further divide the conductive region into a long "snaking" flow path for current, connected by the electrode region at the top and bottom.

In addition to reducing the conductive width, vertical insulative layers define the flow path of electricity through the brickwork, which determines the overall resistance of the system, and determines whether the brickwork electrical load is suited for an alternating current (AC) or direct current (DC) configuration. Figure 53 shows the different general electrical circuit configurations. The brickwork design primarily aims to balance the following needs: a sufficiently narrow electrical flow path, an electrical resistance that is compatible with the voltage being supplied by the power source and the desired ramp rate, and the placement of all steel vessel penetrations at the top of the brickwork for easy access and maintenance. The specific brickwork design is therefore application-specific.

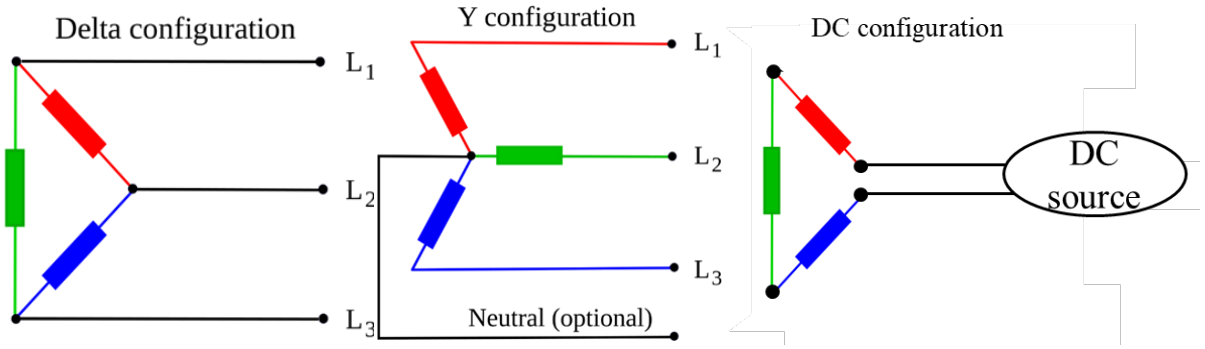

Figure 53: Resistive load configurations of delta, wye, and DC options for FIRES.
Green blue and red elements each represent a different resistor, corresponding to an isolated electrical flow path in the brickwork. L_1, L_2 and L_3 represent a different phase. The DC circuit may be created with the same brickwork configuration as the delta circuit.

Figure 54 depicts one brickwork design, which fits the delta or DC configuration. Here a hexagonal brickwork similar to those in hot blast stoves is used to form the electrically conductive brickwork. The blue layer represents one brick layer of the conductive region, the dark grey represents electrically insulating regions, and the green layer represents the electrode region, which connects the isolated blue regions in a long snaking series circuit. A circumferential region of insulating brick may be added to make the shape more circular, and provide more thermal insulation between the wall and the conductive region.

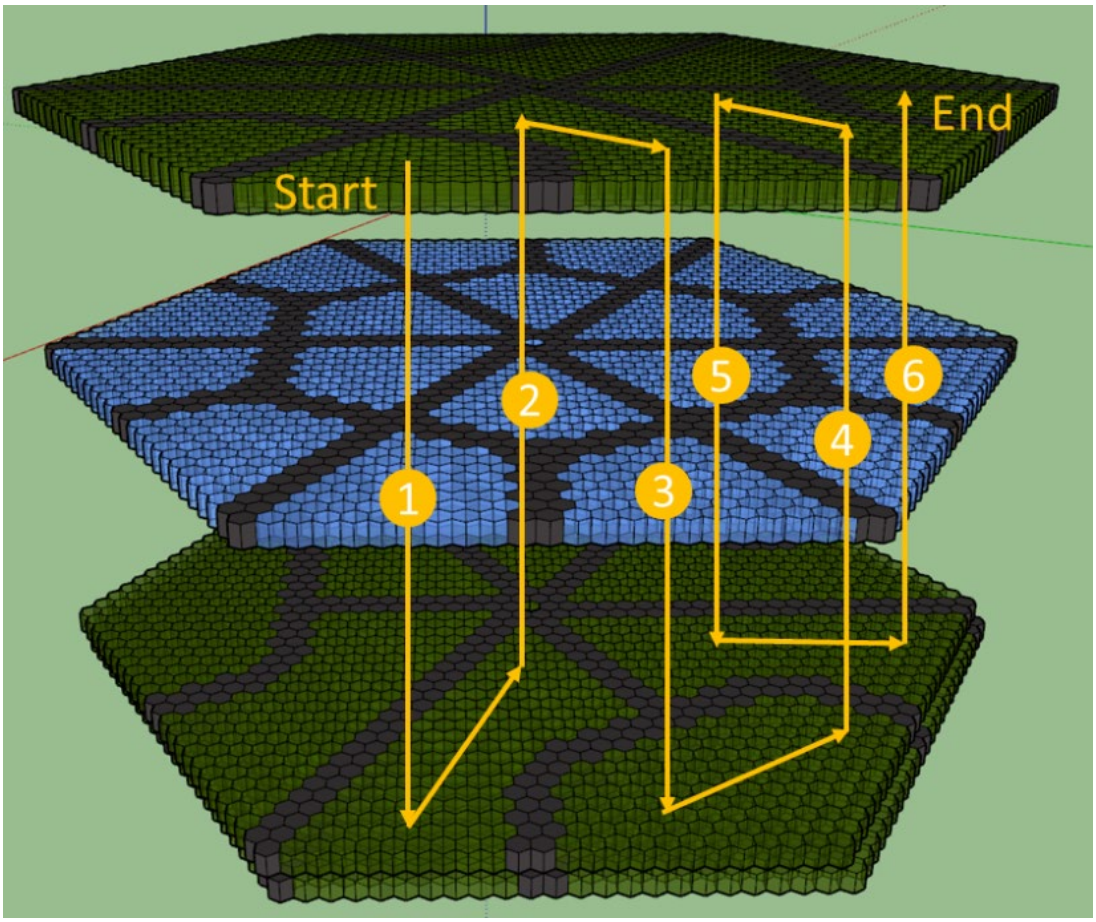

Figure 54: Six-pass delta configuration in a hexagonal brickwork.
The blue layer represents one brick layer of the conductive region. The dark grey represents electrically insulating regions. The green layer represents the electrode region, which connects the isolated blue regions in a long snaking series circuit. Yellow arrows plot the electrical flow path.

The yellow arrows plot the flow of electricity through the conductive regions (blue) and the electrode regions (green) of the brickwork, each outlined by insulating regions (dark grey). Electricity enters at the top of the brickwork, where metallic leads penetrate the steel vessel and interface with the outermost surface of the electrode region. Electricity passes down through the conductive region along an isolated path. At the bottom of the brickwork, electricity moves laterally through the electrode region, then passes back upward through another section of the conductive region, connected in series with the first. In the top electrode region, electricity moves laterally again to connect to the third region. This continues for six passes through the brickwork, before ending at the top electrode region, where another electrical lead penetrates the steel vessel.

The path shown is one-third of the brickwork. In total three identical paths are formed, each of which may receive one phase of a three-phase AC power source. Because the path starts at the top and passes through the brickwork an even number of times, it also ends at the top. Each “start” and “end” point of the three phases may be tied together at the three vertices of the “Δ” in the delta configuration. This can be done outside the vessel with the metallic leads rather than a ceramic interface.

If instead an odd number of passes was made through the conductive region, the electrical path would end at the bottom of the brickwork. To avoid having penetrations at the bottom of the brickwork, which could require the removal of the entire brickwork if repairs are necessary, the wye configuration is used instead. Figure 55 shows the same brickwork geometry divided into a three-pass system. Here each of the three phases has a path ending at a central node, in the middle of the "Y," labeled here as the wye node. In this design the wye node itself is formed by the ceramic electrode brick rather than a metal connection.

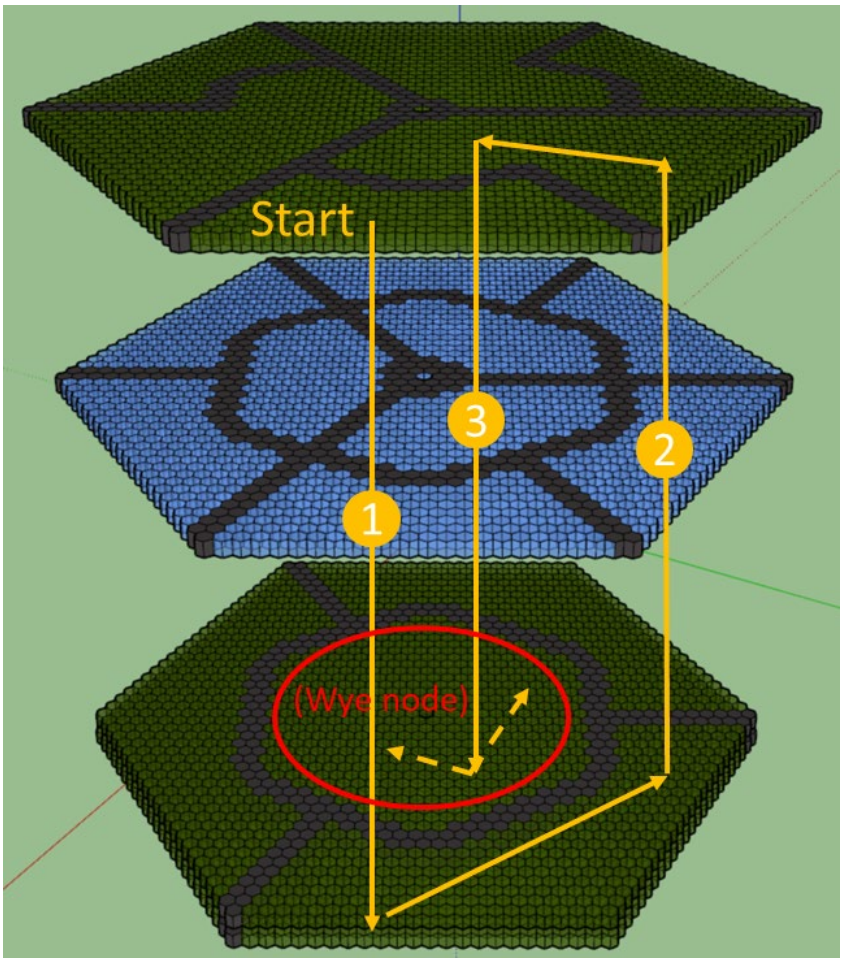

Figure 55: Three-pass wye configuration in a hexagonal brickwork.
The blue layer represents one brick layer of the conductive region. The dark grey represents electrically insulating regions. The green layer represents the electrode region, which connects the isolated blue regions in a long snaking series circuit. Yellow arrows plot the electrical flow path.

Compared to the six-pass delta configuration, the three-pass wye configuration has double the conductive flow area and half the flow length, such that the system is a factor of four less resistive, and requires half the voltage to generate the same power. Design decisions in the brickwork may therefore streamline or otherwise simplify electrical integration. However, thermal runaway of a wider conductive flow path must always be the top consideration over easy integration.

In both the configurations shown above, the paths through the conductive region are the same area as one another so that bottlenecks are not formed in the brickwork. However, they need not be the same shape, as can be seen in the blue region in Figure 55. So long as area is the same among regions, no pass should become significantly hotter than the others.

Hexagonal brickworks are well-suited for cylindrical vessels such as those used in hot blast stoves. Square brickworks are also used industrially in the regenerators of glass furnaces, where the operating pressures is near-atmospheric. Figure 56 shows a three-pass wye configuration of a square brickwork.

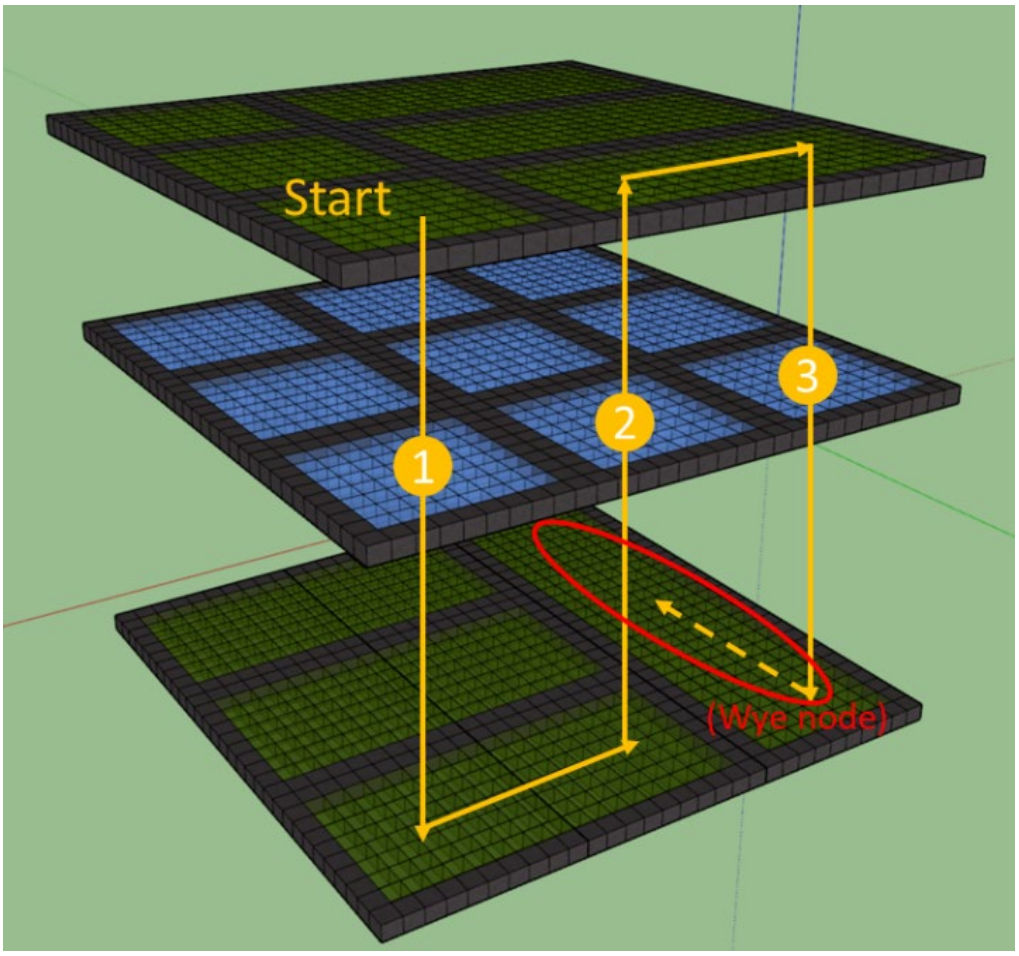

Figure 56: Three-pass wye configuration in a square brickwork.
The blue layer represents one brick layer of the conductive region. The dark grey represents electrically insulating regions. The green layer represents the electrode region, which connects the isolated blue regions in a long snaking series circuit. Yellow arrows plot the electrical flow path.

The same general rules already discussed also apply to square geometries. Note that the wye node, so long as it is sufficiently more conductive than the conductive regions, should not necessarily have to be centered between the three phases in a geometric sense.

Although it is expected that vessel penetrations for delivering electrical power are preferable at the top of the system for easy maintenance access, arguments may also be made for placement at the bottom, where the temperatures will typically be lower. Placement of vessel penetrations at the bottom may be achieved by simply flipping any design shown herein.

10.1.2 Electrode region considerations

Lateral electrical flow in the brickwork occurs in the electrode regions. This is made possible by the stagger of the brick layers, which is also essential for the structural integrity of brick structures. Figure 57 depicts the lateral movement of electricity through the brickwork.

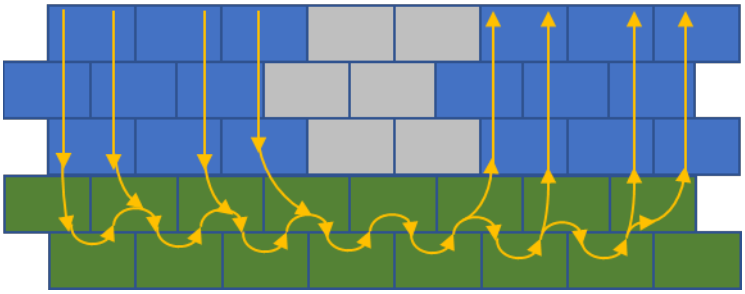

Figure 57: Lateral movement of electricity through the electrode region of the brickwork.
Blue bricks are conductive bricks, green bricks are electrode bricks, and grey bricks are insulating.

In practice there will be more than two layers of electrode brick to ensure a sufficiently low-resistance path. This will depend on how much more conductive the electrode bricks are than the conductive bricks, the limits of which is a function of solubility limits of dopant and other practical considerations regarding the RTD at different dopant levels. One rule of thumb may be to make the electrode region as tall as the conductive region is wide, such that the flow area of each region is similar, and the electricity may take a smooth "U-turn" through the electrode region.

The specific handling of the electrical penetrations to the system, i.e. how metal interfaces with the electrode brick at the top of the brickwork, is not detailed herein. However, a few comments are offered. The metal-ceramic interface presents unique challenges that involve the transfer of electricity from ambient temperature, ambient pressure metal to very high temperature, potentially high pressure ceramic. A key question is the temperature at which ceramic and metal must contact. The tempearture of electrode bricks at the edge of the brickwork may be reduced by several hundred Celsius if heat generation in the region is low and there is significant thermal resistance surrounding it. Platinum leads, the most expensive option, may be used to interface with the ceramic if the temperature is too high for other metals. Fe-Cr-Al wire may also be a candidate to interface with the ceramic. The metal-ceramic interface is an area of future work.

10.1.3 Considerations of insulating region, conductive region, and their volume ratio

Regions of insulating firebrick should ensure that parallel conductive regions do not contact one another even over thousands of thermal cycles, during which bricks might shift or crack. A minimum of two insulating bricks is considered necessary by the author for reliable long-term operation. If only one insulating brick is used, the stagger of different layers of brick in the hexagonal brickwork creates the circumstance where neighboring isolated conductive passes may touch at the corners depending on the brick design.

Whether insulating regions are one, two or more bricks wide, a key consideration is the relative ratio of conductive bricks to insulating bricks within the brickwork. Modeling assumptions used herein assume that the insulating region makes up a relatively small fraction of the volume and thermal mass of the FIRES system. However, the "snaking" flow path requires a non-negligible volume of insulating brick, dependent on the relative number of bricks used in the conductive region. Figure 58 shows the change in the ratio of conductive bricks to total bricks as a function of how wide the conductive region is, while holding the insulating layer thickness at two bricks in any direction. Six identical triangles may be put together to form the hexagonal brickwork shown in Figure 54.

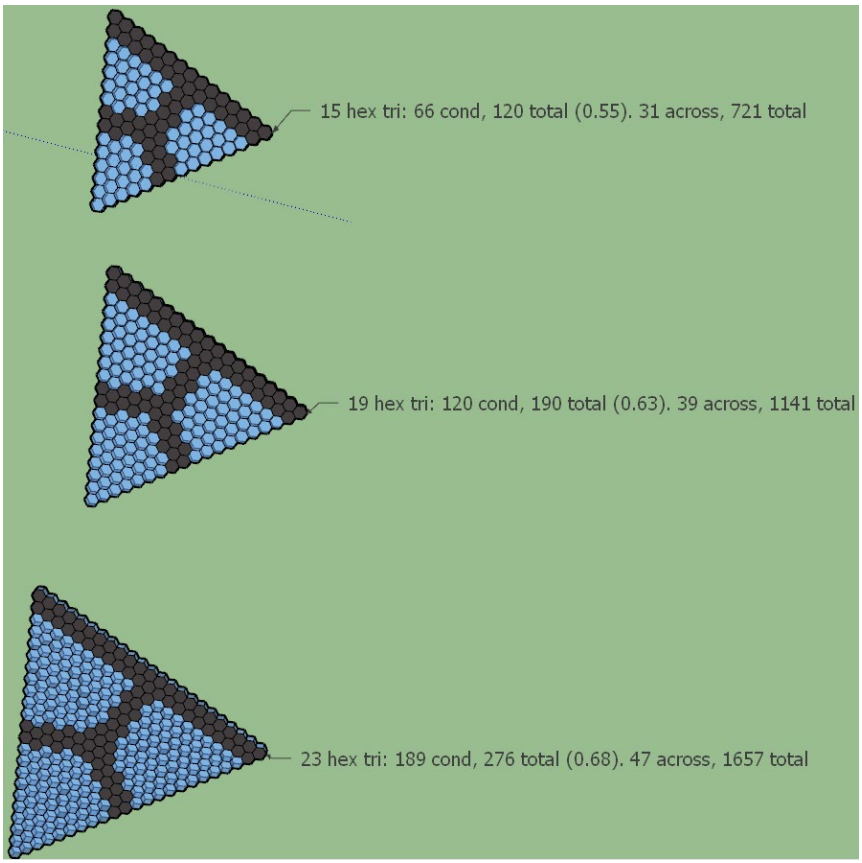

Figure 58: Hexagonal brickwork cross-sections with different widths ratios of conductive and insulating bricks.
The ratio of conductive bricks to total bricks is in parentheses. A larger system has a higher conductive ratio, but is less resistant to thermal runaway. A smaller system is more resistant to thermal runaway, but may have insufficient heat transfer to effectively heat electrically insulative mass. Each effect must be balanced.

A tradeoff must be made between smaller insulating brick fraction and smaller conductive width, or smaller brick size. The smallest triangle in Figure 58 has a conductive brick fraction of 0.55, the remaining 0.45 of which is insulating brick. The largest triangle has a conductive brick fraction of 0.68. The higher conductive fraction means generally more uniform heating, and less temperature gradients. On the other hand, the smaller fraction triangle is less brick widths wide and therefore has a smaller conductive width, i.e. greater resistance to thermal runaway. Insulating bricks are also generally expected to cost less, because their composition may contain less chromia, which is a factor 10 more expensive than alumina.

In designs where the insulating firebrick fraction is large and the conductive firebrick fraction is small, the system dynamics more so resemble a distributed heater system rather than a volumetrically heated system, which has not been simulated herein. Instead, conductive regions with symmetry boundary conditions were used, and insulated regions were neglected, because the relative thickness of the electrically insulating layers between conductive regions was assumed small. Systems with appreciable thermal storage capacity in the insulated regions

One option to keep the conductive width short while also keeping the conductive fraction high is to make the bricks themselves smaller. Typical bricks are 15-30cm wide. Serious deviation from this range may have negative implications on manufacturing and stackability.

10.2 Brick geometry design

Figure 59 shows typical checker firebrick geometries used in regenerative heat exchangers. Divots and protrusions, which can be located respectively on the tops and bottoms of bricks (Figure 59a) or vice versa (Figure 59b), allow them to fit into place and maintain structural order without mortar, even through tens of thousands of cycles of thermal expansion. When stacking, each layer is staggered, such that the center of each brick in one layer are aligned with the vertices of the brick layer below to maintain a strong structure. Unlike typical bricks, FIRES

bricks must encourage even electrical flow throughout the width. It is therefore important that FIRES bricks contact on the broad face of the brick rather than on the small surface area of the protrusions themselves. This may be ensured simply by having deep divots relative to the protruding height, evident in Figure 59b.

The unit cell is the smallest translatable shape that makes up the brickwork, and consists of the air channel and the immediate surrounding brick. The black dotted line of Figure 59d shows the unit cell for the hexagonal system, and typical dimensions: 6cm wide when measured side-to-side, or approximately 7cm when measured point-to-point. Previous work [2] has shown that small cell sizes on the order of a few centimeters have dramatically improved heat transfer rates over larger cells. These cell sizes, typical of hot blast stoves, must be maintained in FIRES brick designs to ensure good heat transfer out of the brickwork during discharge.

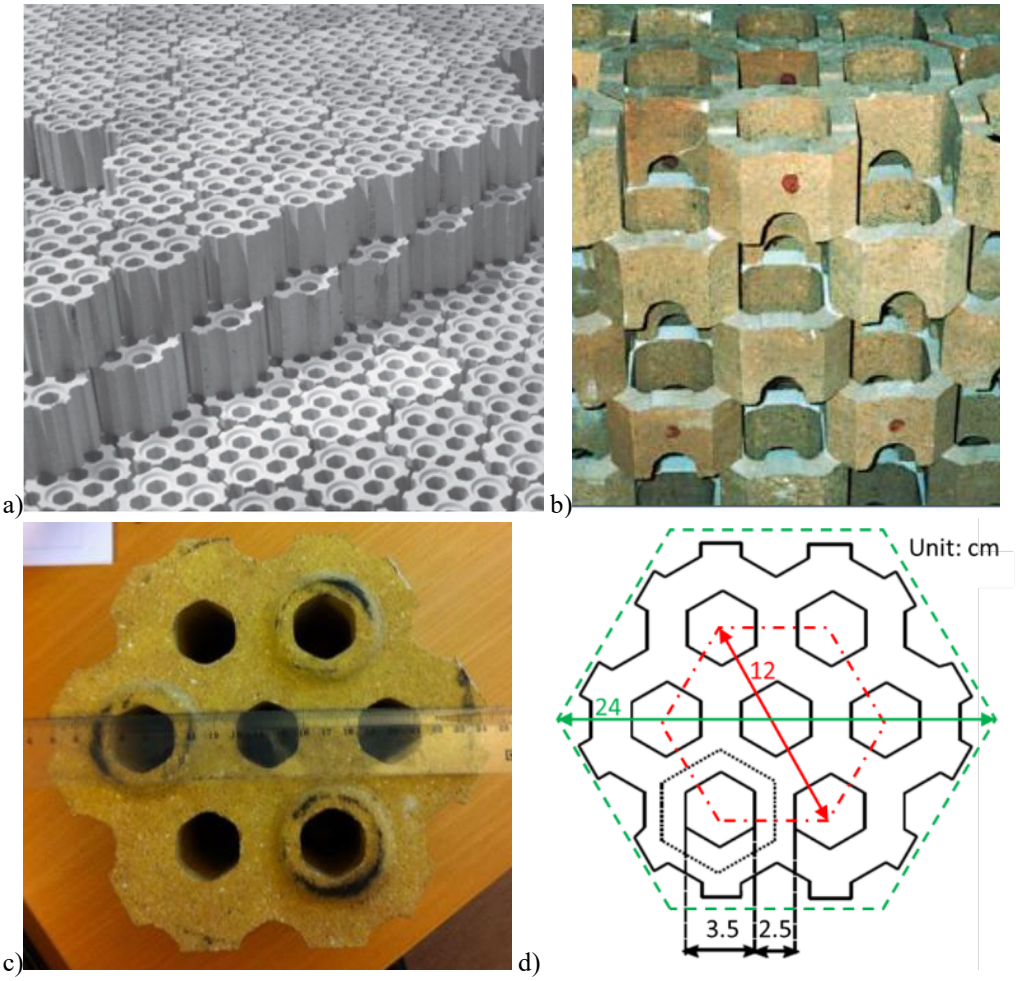

Figure 59: Typical checker firebrick geometries used in regenerative heat exchangers.
a): Hexagonal brick [23]. b): Cruciform brick [2]. c): Single measured hexagonal brick [106]. d): Brick dimension options of hexagonal brickwork, adapted from [106].

10.2.1 Effect of brick width on conductive width of electrical flow path

Reducing the brick width improves charging stability while also maintaining a relatively high conductive volume fraction. These benefits arise simply because the insulating layer should be at least two bricks thick, meaning that smaller bricks reduce this layer thickness in absolute terms. The practical limit of how small the brick may be is set by the desired unit cell size.

Although the unit cell may be repeated to make one layer of the brickwork, a brick that is only one unit cell wide cannot be stacked with a stagger that forms continuous vertical air channels. For this reason, the brick is typically several unit cells wide. The hexagonal bricks shown in Figure 59 each have the equivalent of 12 unit cells (7 full cells, 6 half-cells, and 6 third-cells). The green dashed hexagon that contains the brick is 24cm wide. A smaller option, one-

fourth the size, is marked by the dot-dashed red hexagon: 12cm point-to-point, with 3 unit cells. Figure 60 shows the dimensions and approximate conductive widths of identical hexagonal brickworks made from 12cm and 24cm bricks. Note that unit cell, i.e. the air channel width, are identical in both systems.

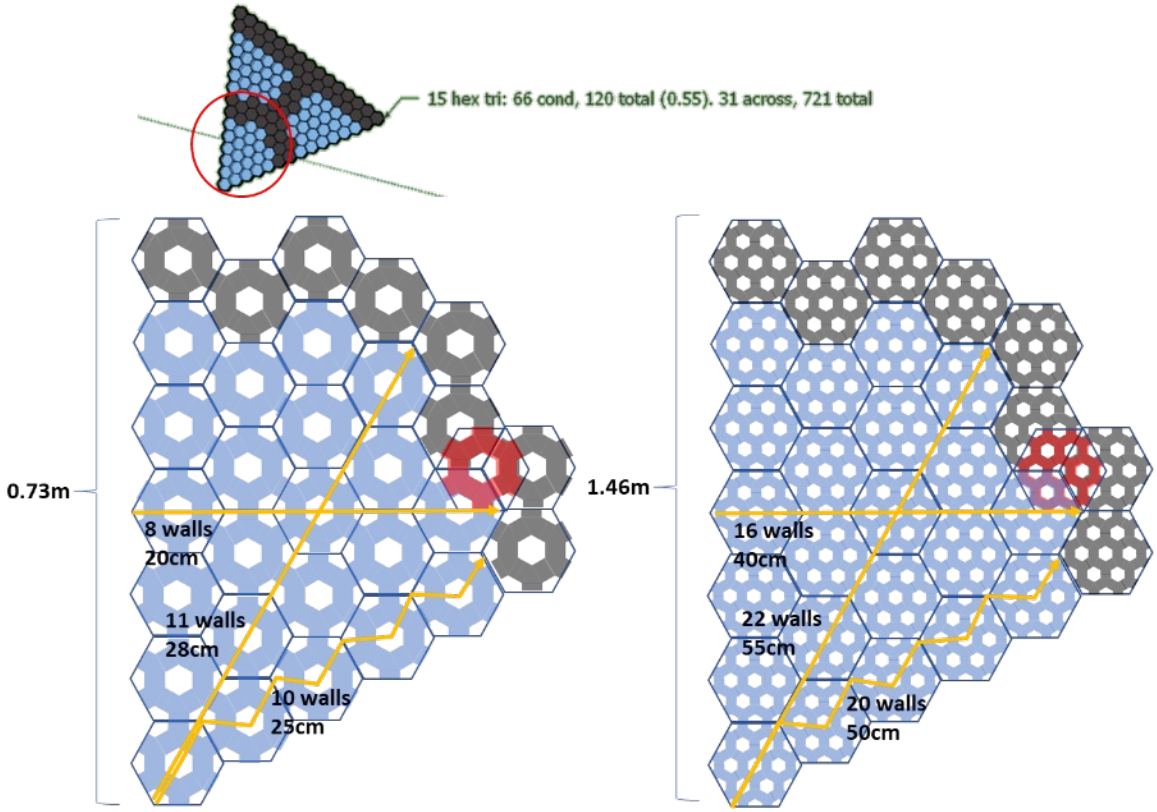

Figure 60: Dimensions and approximate solid conductive widths for two hexagonal brickworks.
a): 12cm bricks. b): 24cm bricks. The red brick shows the staggered stacking pattern of the next layer of brick.

Recall in Section 9, 1-D slabs with solid conductive widths ranging from 0.25m to 0.50m were tested for thermal runaway behavior at a variety of temperatures and equilibration times. In a 2-D system with air channels, the radiative heat transfer across air channels is associated with very little resistance by approximately 500ºC, at which point the effective conductive width can be approximated by how many walls the heat must be conducted through to reach opposite sides of the brickwork. For the brickwork design shown, the conductive widths using 12cm bricks and 24cm bricks roughly correspond to 0.25m and 0.50m of solid conductive width, respectively. The actual brickwork diameters of these designs are 3m and 6m, depending on which brick size is used. Larger patterns may be designed that fit a desired vessel diameter.

10.2.2 Brick height considerations

Brick height affects the ratio of resistance created by the brick itself compared to the brick-brick contact resistance. Results from Section 6.2.2 showed that brick-brick contact resistance for chromia-based firebricks has an equivalent resistor length of approximately 1-2cm. Calculations of contact heating and temperature rise in Section 7 showed that, for a model dominated by bulk brick resistance rather than contact resistance, the temperature rise of the contact may be kept to 3-13ºC for brick heights of approximately 15cm. To keep the majority of heat generation in the volume of the brick itself, bricks in this height range or taller are best. However, brickworks built of shorter brick with a relatively high contact resistance may be viable as well.

Firebricks may be taller (Figure 59a) or shorter (Figure 59b) than they are wide, though the dimensions are generally similar. Bricks with a height of 15cm-30cm and a width of 12cm-24cm are therefore in class with existing bricks and in class with the simulated conditions herein.

10.2.3 Open radiative heat transfer pathways for greater flexibility and stability

Even with air channels included, radiative pathways for heat transfer are always in series with conductive pathways in the traditional hexagonal brick design. That is, after heat radiates across an air channel, it must conduct through the wall before radiating across the next air channel. The thermal resistance throughout the brickwork can be dramatically reduced by pressing bricks that have lateral openings, i.e. "windows" in the air channels. An example of this can be seen in the cruciform bricks of Figure 59b, where the archway in the brick opens a pathway of radiative heat transfer that runs parallel to the conductive heat transfer pathway. This may form a continuous path for radiative heat transfer to equilibrate temperatures across the brickwork. Even with small view factors, the T^4 relationship of radiative heat transfer may dramatically cut down equilibration time, particularly when resting at high temperatures. The opening of wider "windows" between brick air channels comes at the cost of energy density, and may pose a challenge to structural stability of the bricks and brickwork. Brick geometries that promote radiative heat transfer are an area of ongoing research.

10.3 Flow control design and inlet preheating options

The minimum operating temperature of FIRES, which is set by the inlet air, determines how stringently FIRES must be designed and operated to avoid thermal runaway. In thermal runaway analyses of Section 9, it was assumed that the inlet air "seen" by FIRES would be dependent on the application with which it interfaces. This does not necessarily have to be the case if the FIRES outlet is used to preheat the inlet. Presented herein is a qualitative discussion of several design concepts for increasing the FIRES inlet temperature.

Figure 61 shows several flow diagrams of how FIRES may adjust inlet temperature with the introduction of additional components. Option "a" takes the air temperature directly from the application with no modification; options "b" and "c" use the FIRES outlet to preheat the incoming air via direct mixing or heat exchange, respectively. The temperatures shown are example values similar to a typical natural gas power plant application.

a)

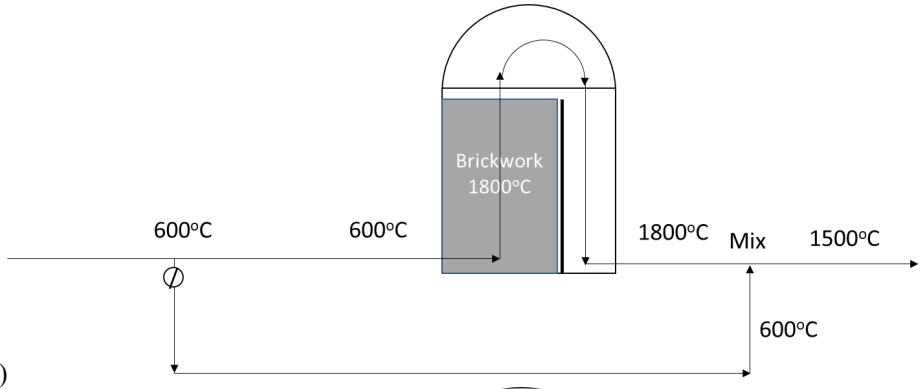

b)

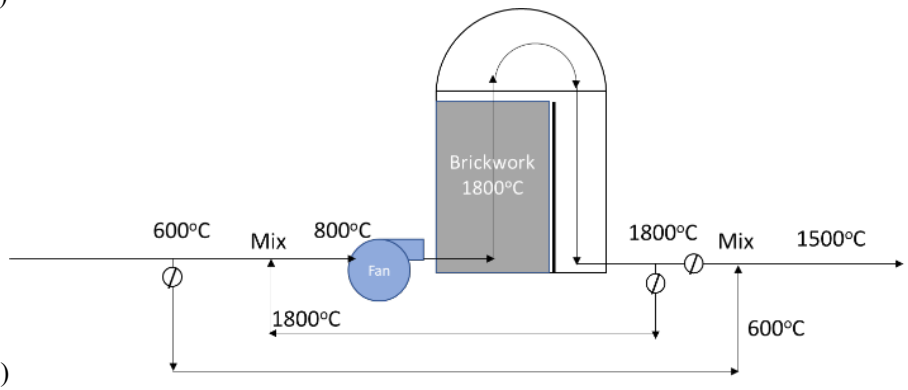

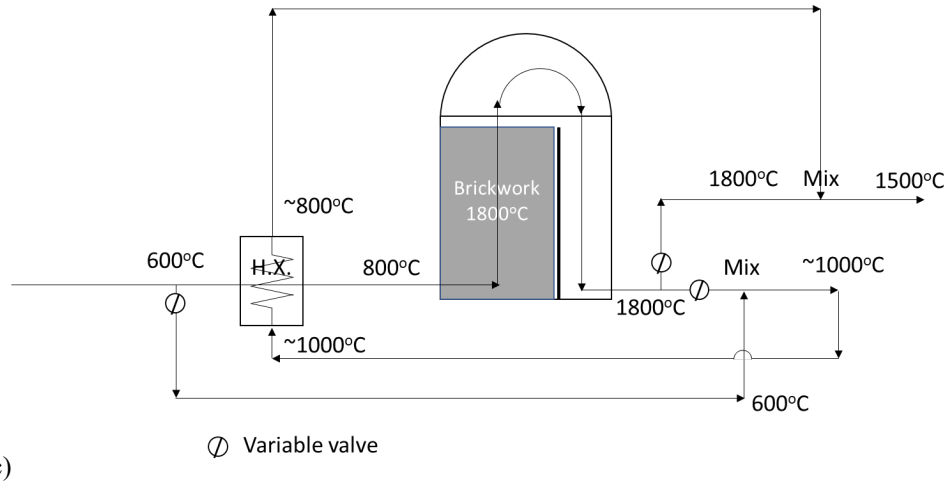

c)

Figure 61: Preheat options for FIRES inlet.
a): No preheat. b): Preheat via fan-driven mixing and recirculation. c): Preheat via heat exchanger. Example temperatures are characteristic of a typical natural gas power plant application: T_{min} = 600°C, $T_{min,mod}$, T_{max} = 1800°C, $T_{desired}$ = 1500°C.

The basic operation of FIRES has been discussed in previous work [2], and was briefly reviewed in Section 2.3. The simplest operating scheme includes one bypass duct, with a variable flow control valve or damper (Figure 61a). The flow rate through the brickwork and through the bypass duct varies as FIRES cools down to ensure that the output always matches the desired temperature $T_{desired}$, in this case 1500°C. When FIRES is nearly depleted and this temperature can no longer be provided, the application operators may choose to combust fuel to maintain constant temperature, or the application may ramp down and shut off. In this simple operating scheme, the FIRES inlet temperature will be whatever the application provides.

Preheating the FIRES inlet with the outlet requires either a fan (Figure 61b) or a heat exchanger (Figure 61c), each of which come with unique technical tradeoffs. Direct mixing of the airstream requires ductwork that connects the outlet back to the inlet, essentially recirculating part of the air. The recirculation requires a pressure rise, and therefore a fan on the flow circuit, or else the air would flow in the wrong direction. The fan may be placed downstream of the mixing step to avoid experiencing the harsh temperatures of the outlet. The operating conditions are at similar pressures and temperatures experienced by compressor blades, and far lower than the temperatures experienced by turbine blades. Based on previous work [2], the pressure rise of the recirculation fan may be limited to a few kilopascals, depending on the desired discharge rate and the density of the airstream itself. As the FIRES exit temperature gradually decreases during discharge, more air will be driven through the brickwork to keep the discharge heat rate constant. This will also require more outlet air to be mixed with the inlet to maintain 800°C. Flow rates may be changed as needed by actuation of valves and with a variable fan drive.

The use of a heat exchanger is an alternative means of preheating the FIRES inlet air that avoids adding a mechanical component to the system. By maintaining the pressure boundary between the inlet and outlet flow of FIRES no pressure rise is required on the hot side. Direct heat exchange between the FIRES outlet (1800°C) and inlet (600°C) poses a material design challenge to the heat exchanger walls. This can be alleviated by the design shown, which instead mixes the bypassed air and the FIRES outlet to a lower temperature (~1000°C) before the heat exchange step. The heat exchanger exit is then recombined with the outlet stream. Careful valve actuation at the bypass and FIRES outlet can control the conditions in the heat exchanger.

In addition to maintaining $T_{desired}$, both alternative schemes must operate with the extra constraint of maintaining $T_{min,mod}$. There will be practical limitations to the variable speed fan and the heat exchanger that may limit the operating window where $T_{min,mod}$ may be maintained. The viability of each scheme and the relative tradeoffs require more analysis and specific considerations of available fan and heat exchanger options at the temperatures and pressures of interest.

A third option not shown here is to split FIRES itself into two sections or chambers: one that operates at lower temperatures heated by commercial metallic or ceramic heaters, and one consisting of the conductive brickwork that can reach very high temperatures. The heater elements in the lower temperature chamber may be selected such that the storage temperature is far below their peak operating temperature (e.g., a SiC chamber reaching 1000°C) to ensure long life. Each chamber may be appropriately sized and equipped with flow control to ensure the outlet of the lower temperature unit is maintained at $T_{min,mod}$ and the outlet of higher temperature portion is maintained at $T_{desired}$.

Practical challenges of this design include the added complexity of the electrical system that provides power to two potentially very different systems.

10.4 Summary of Conceptual design of a DRH FIRES unit

The conceptual design of a directly resistance-heated brickwork was presented. Design options and decisions were discussed. While remaining in class with common brick geometries and brickwork sizes, and based on the performance of chromia, it was found that designs of a snaking brickwork with a solid conductive width of approximately 0.25m-0.50m could be achieved, marking fair resistance to thermal runaway at typical expected inlet temperatures with typical coping times described in Section 9. Contact heating and temperature rise should also be kept to 3^{o}C-13^{o}C based on typical brick heights.

Some of the features of proposed designs deviated from modeled conditions in ways that warrant further investigation. For example, the ratio of conductive brick to insulating brick implies that a fair degree of heat transfer will be necessary through insulating regions, such that assumptions of uniform conductive regions is inaccurate. Other design options that promote better resistance to thermal runaway not included in the calculations or simulations include the addition of "windows" in the brickwork, and preheating of incoming air above the sharpest RTD of the material.

Overall, the design process has shown that there is a relatively large design space for customizing FIRES's performance characteristics with regard to different power systems and vessel sizes and shapes.

11 Retrofits and modifications to applications

Commentary on strategies, advantages and challenges for applying FIRES to existing industrial processes is offered herein. First, the necessary adaptations of hot blast stoves technology to FIRES operating conditions are identified. Next, the approach and challenges of retrofitting cement kilns and blast furnaces are discussed. The chapter concludes discussion of gas turbines, including the presentation of a novel component that may be used to implement FIRES with relative ease.

11.1 Adaptation of hot blast stove designs for FIRES

Modern hot blast stoves come in a large variety of shapes and sizes, which may be suitable for the energy demands of a variety of application. The largest hot blast stoves are up to 11 meters in diameter and 40 meters tall [107]. Such vessels could hold approximately 2 GWh of energy, based on calculations of typical firebrick energy density and typical volume fractions of the brickwork [2].

Figure 62 shows three different designs of hot blast stoves, taken from [108]. The key differentiation of each design is where the combustion of furnace gases occurs: an internal combustion shaft (a), an external combustion shaft (b), or a shaftless or "top combustion" chamber (c). The internal combustion shaft is the most common, but also provides a lower hot blast temperature (900-1100°C). The separate combustion chamber allows for higher output temperatures and a higher volume and surface area for the brickwork, but has been found to cost 30% more due to the more complicated dome structure and the need for more steel. More recently, top combustion chambers have been shown to improve hot blast performance at less cost [108].

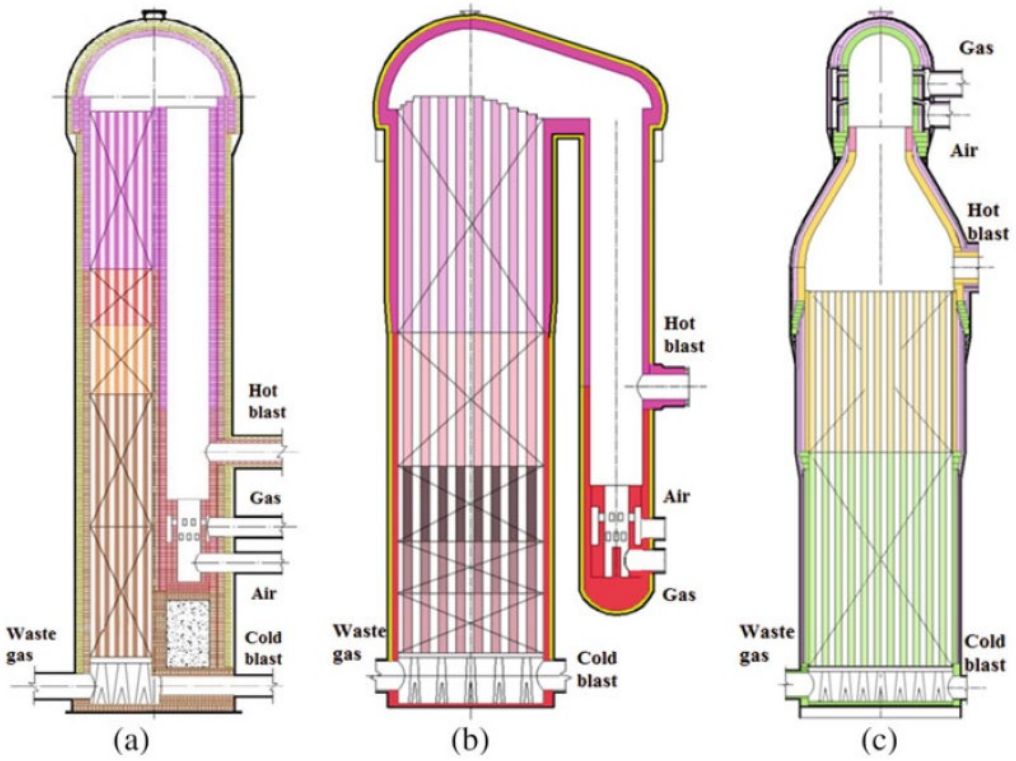

Figure 62: Variations of hot blast stove designs.
a): internal combustion shaft. b): external combustion shaft. c): shaftless or "top combustion" chamber. [108]

Without the need for a combustion chamber, a FIRES unit may simply adapt the structure of the externally-fired stove, with a traditional dome like that of the internally-fired stove, and a hot blast exit port at the top of the brickwork like a top-fired stove. The other option is to use the more common internally-fired stove structure, but use the combustion chamber instead as a mixing chamber for the brickwork flow and the bypassed flow to match the operating temperature during discharge. The recombination and mixing of the bypassed flow with the brickwork outlet may also be done in the dome, or immediately outside the exit.

FIRES is expected to operate with peak temperatures of 1700-2000°C, and will likely require higher temperature insulation than presently used in hot blast stoves, which typically operate with a peak temperature of 1300-1600°C at the top of the stove today [23]. Insulating firebricks of greater than 90% alumina content may be rated in the range of 1700-2000°C [54]. The tradeoffs of storage temperature and insulation cost must be considered with respect to the application.

The operating pressure of FIRES may be anywhere from near-atmospheric up to 25 bar depending on the application. Operating pressure of hot blast stoves typically range from 3 to 5 bar [109]. Particularly in gas turbine applications, where the FIRES unit must be kept within the pressure boundary of the system, a thicker steel vessel will be required.

11.2 Retrofit of cement kilns with FIRES

Cement kilns are used to produce cement clinker, primarily through the process of calcination of $CaCO_3$, and partial melting and sintering of CaO. Approximately half the heating load is in the precalciner, where most calcination occurs, and half is in the rotary kiln, where melting and sintering occur [110]. Approximately one third of carbon emissions from cement production are associated with direct energy use [19, 111], which can potentially be fully replaced with zero-carbon FIRES heat with relatively little change to the process.

The maximum temperature requirements of the processes themselves are approximately 1000°C for calcination and 1550°C for sintering. The flame and gas temperatures used to deliver the heat may be closer to 1800-2000°C depending on the fuel used. Pulverized coal has been conventionally preferred over natural gas based on cost and due to its hotter and higher emissivity flame. However, recent experience with natural gas has shown similar performance at lower flame temperatures [110].

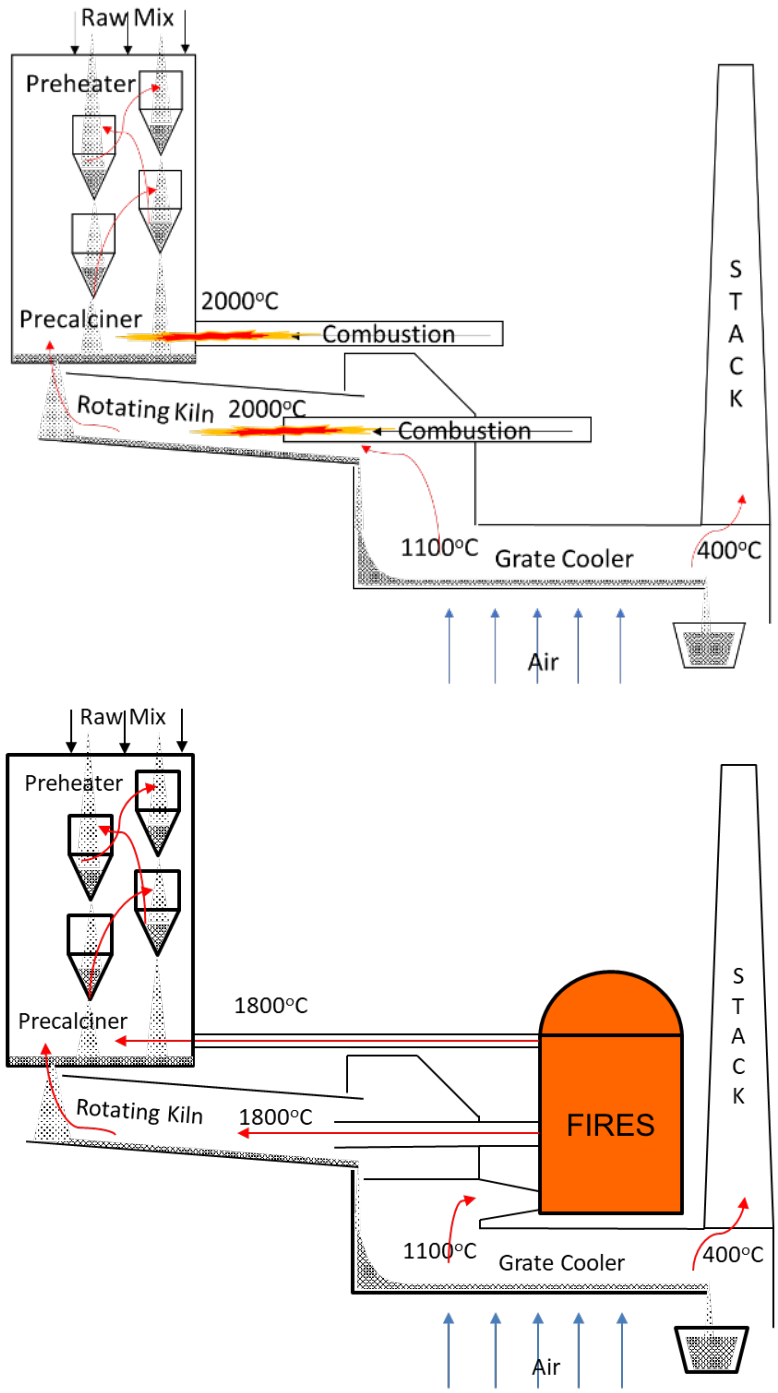

Figure 63: General schematic of a cement plant without (top) and with FIRES (bottom).

Inclusion of FIRES at a modern cement clinker plant, depicted in Figure 63, involves three general modifications: The inclusion of a flow baffle that may direct the grate cooler air into FIRES, a port that delivers FIRES air into the rotary kiln, and a port that delivers FIRES outlet to the precalciner. The baffle may be open and close such that it blocks the flow to FIRES and allows air to flow as normal through the kiln when FIRES is depleted of heat. It may be possible to use the lance that delivers combustion heat to also deliver FIRES heat.

A practical challenge of operating cement kilns with FIRES is the lack of combustion products in the hot gas, which normally create the intense flame that radiatively delivers the heat to the clinker. There are several approaches to improving the radiative heat transfer of a non-combustion gas. One option is to make use of excess particulate from

the clinker itself, captured in the cyclones and other parts of the process. A certain fraction of particulate normally contributes to the emissivity of the hot gas [110], and will still be present when operating with FIRES. Another option is to recirculate CO_2 released from the calcination process through the rotary kiln. The CO_2 may introduced either through the grate cooler or at the FIRES inlet or outlet, depending on the flow rate necessary. The introduction of CO_2 will increase the emissivity of the flowing gas through the kiln. Running a higher concentration CO_2 stream may also improve the prospects of carbon capture options as well. One competing effect is the higher temperatures required to fully calcine $CaCO_3$ in the presence of a higher CO_2 partial pressure. The mixing of CO_2 and grate cooler air may also be used to adjust the incoming temperature to FIRES. The grate cooler outlet is typically near 1100°C, which is beneficial with respect to charging stability of FIRES but puts more stringent requirements on the lower structural supports of the brickwork inlet.

11.3 Retrofit of iron blast furnaces with FIRES

Iron blast furnaces are used to produce molten iron via smelting, i.e., reduction and melting of the iron ore. The main feedstocks of the process are iron ore and coke. Figure 64 shows the schematic of a generic iron blast furnace with and without FIRES (note temperatures are approximate in all cases). Here hot blast stoves are used in cyclic fashion to capture and reuse exhaust energy from the blast furnace. Air passes through the hot blast stove that is "on blast:" the air flows upward and is heated up to 1300°C in the case of modern stoves. The air is then fed into the blast furnace through tuyeres at the bottom, where combustion of coke occurs and heats the chamber approximately 1800-2000°C. The hot gases flow upward in the furnace, through which carbon and carbon monoxide reduce the iron ore as it flows downward and melts. The blast furnace gas (BF gas) exits and is cleaned of particulate before entering the hot blast stove that is "on gas:" here the BF gas, relatively rich in CO, is mixed with air and sometimes natural gas, and is combusted in the combustion chamber to recover this chemical energy. The hot gas flows down through the brickwork, which captures the heat to be used in the next cycle.

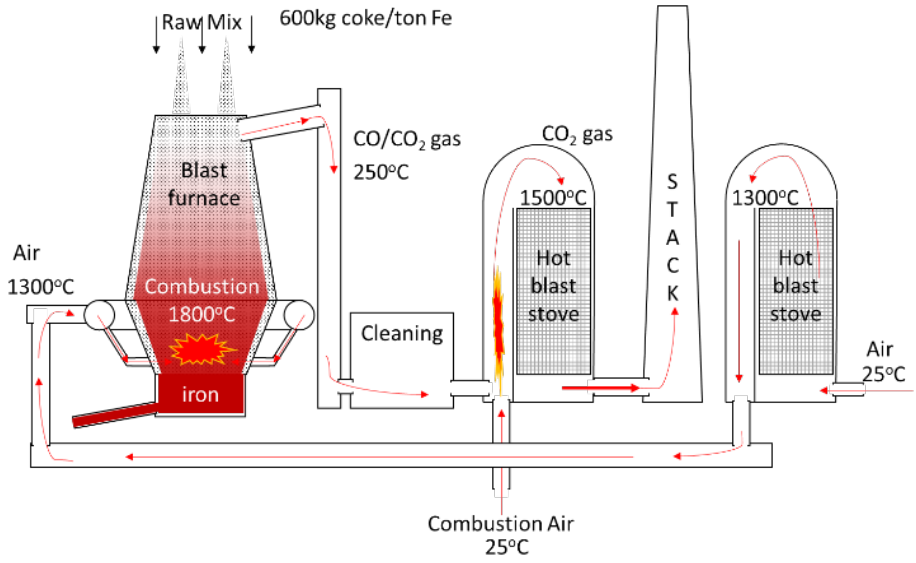

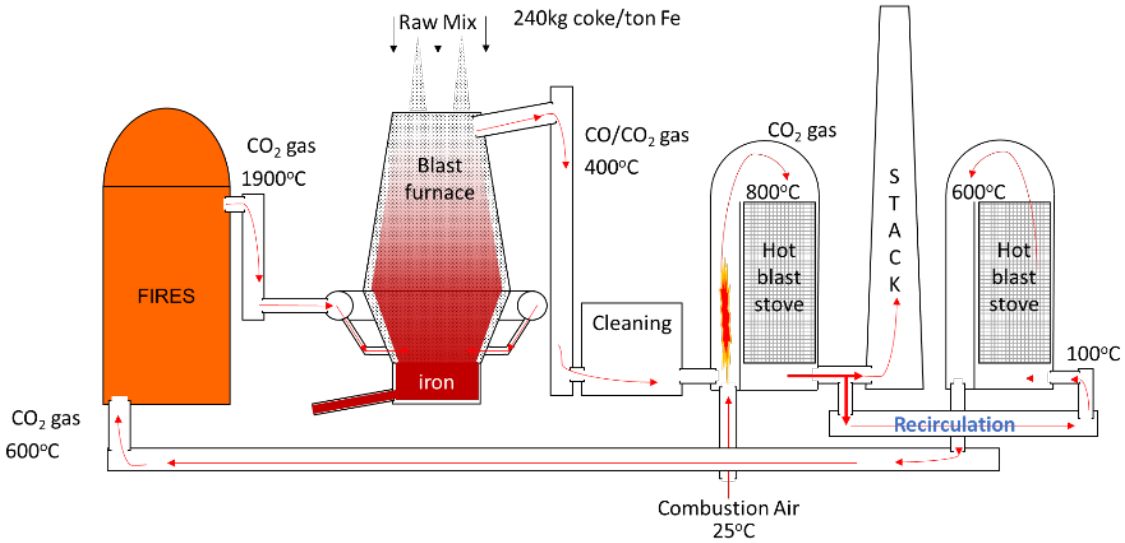

Figure 64: General schematic of a blast furnace without (top) and with FIRES (bottom).

In the FIRES variant of the system, FIRES is fed the outlet of the hot blast stove, and provides heat to the blast furnace up to 1800-2000°C. The region of the blast furnace that usually receives the hot blast may need to be lined with higher performance insulation, due to the higher inlet temperatures provided by FIRES. The use of FIRES reduces how much coke is fed into the furnace because heat from combustion is not necessary.

The $N_2/CO/CO_2$ mixture that exits is cleaned and combusted in the on-gas stove, with two differences from nominal: (1) Only just enough air is added to combust the CO in the mixture, and (2) most of the gas is recirculated following combustion. By recirculating gas, the oxygen content may be kept low, which prevents the reaction of coke with free O_2 and better utilizes it for iron ore reduction. By combusting the CO to form CO_2, the heating value may still be captured in the hot blast stove, and the firebrick within FIRES and the hot blast stoves will not be at risk of reduction reactions by CO.

According to the World Coal Association, The production of one ton of iron consumes 600 kg of coke, which is derived from approximately 770 kg of coal [112]. The coke serves three purposes: chemical reducing agent of the iron ore, heating source, and porous media for promotion of flow. FIRES may theoretically replace the fraction of coke not used for reduction of the iron ore, and a proportional fraction of total CO_2 emissions. This fraction can be estimated by inspection of the chemical balance of iron ore reduction:

$$2Fe_2O_3(s) + 3C\ (s) \rightarrow 4Fe(s) + \ 3CO_2(g) \tag{56}$$

Where 3 moles of carbon produces 4 moles of iron metal, the minimum carbon requirement is 161 kg C/ton Fe. If a carbon content of a few wt% is desirable for later processing, this value may be closer to 200 kg C/ton Fe. This is approximately 27%-33% of total coke consumption. FIRES may therefore theoretically reduce coke consumption and carbon emissions by approximately 67-73%.

There are however issues of practical limitation. The calculations above assume full oxidation of carbon. In practice, CO is the prominent reducing agent, and the carbon leaves as a mixture of CO/CO_2. The worst-case carbon usage may be determined where all carbon exits as CO; in this case, 322-362 kg C/ton Fe, or 54-60% of the current coke usage would remain. In this scenario, FIRES would enable emissions reductions of 40% or more. Presuming a mixture of CO/CO_2, a 60% reduction seems reasonable. Another potential challenge of lowering the amount of coke in the blast furnace is impact pressure losses and flow restrictions in the process without enough porous media, which may be examined in future work.

11.4 Modification of gas turbines with FIRES

The addition of FIRES to a gas turbine power plant allows the power plant to operate similar to an electrical battery, with potentially far improved economics. Previous work [2, 21, 22] has discussed the coupling of FIRES with gas turbines. Two configurations of interest are the common natural gas combined cycle plant (NGCC), which today

reaches efficiencies as high as 63%, and the reheat air-Brayton combined cycle (RACC), developed at UC Berkeley [105] for the fluoride salt-cooled high temperature reactor (FHR). The RACC is a modified NGCC concept optimized for the relatively low temperatures of zero-carbon heat sources: next generation nuclear plants or concentrated solar power plants, both of which operate at approximately 600-700°C. The RACC allows for baseload efficiency of approximately 40%, similar to steam cycle option that solar and nuclear plants traditionally use. However, the RACC allows for the addition of higher temperature heat sources to boost the output of plants at times of high demand. The incremental heat-to-electricity efficiency of this process is over 66%, and may reach 70% based on newer turbine technology. A FIRES unit attached to these systems would therefore operate with roundtrip efficiencies near 63% and 70%, respectively, assuming negligible heat leakage and parasitic losses. Figure 65 and Figure 66 show the power cycle diagrams with FIRES included.

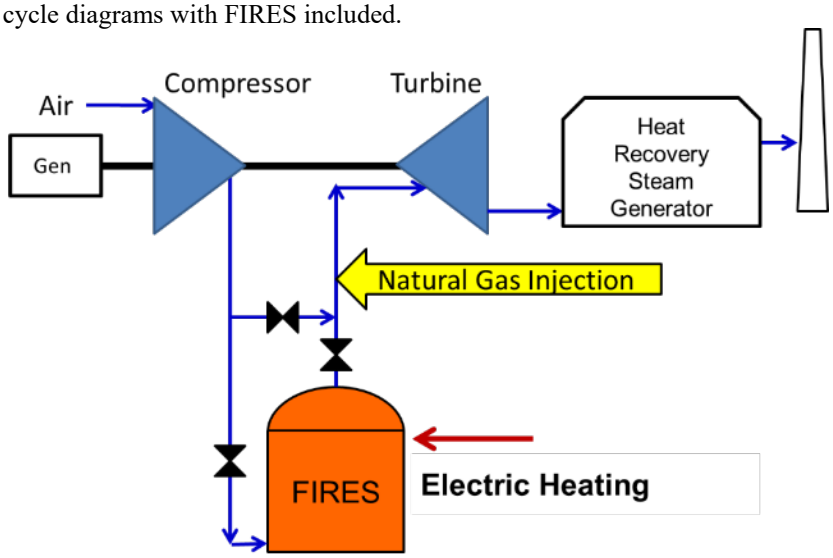

Figure 65: FIRES coupled with natural gas combined cycle (NGCC) plant. Roundtrip efficiencies up to 63%.

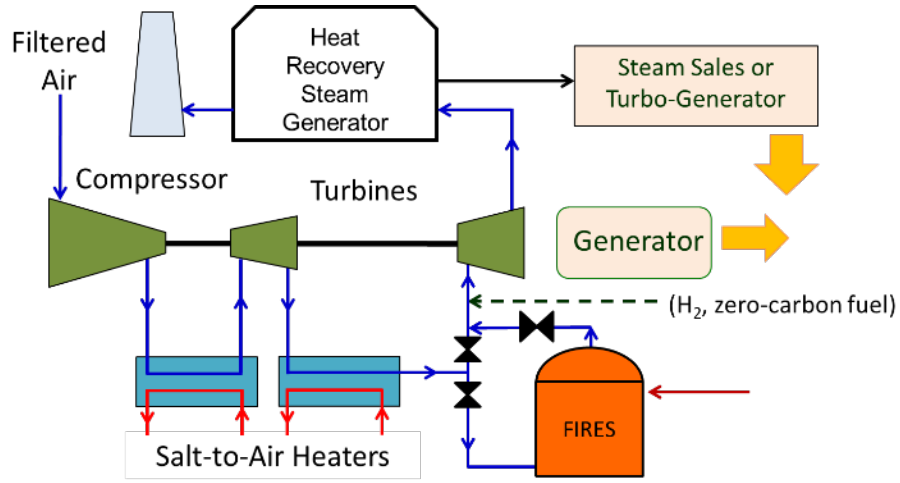

Figure 66: FIRES coupled with reheat air-Brayton combined cycle (RACC) plant.
FIRES heat addition step may boost turbine temperatures from that of a "baseload" condition operating from zero-carbon heat source: a high temperature nuclear reactor, or concentrated solar power plant. Roundtrip efficiencies near 70%. [105]

To attach FIRES to a gas turbine, the pressurized air downstream of the compressor must be routed from the turbine assembly into a refractory-lined pipe that leads to FIRES. The heated high pressure air must then be returned to the turbine assembly and directed to the turbine. It was previously proposed [2] that an exit guide vane and diffuser into aerodynamic scroll baffle may be used, such as those used in intercooling applications [113]. However, retrofitting existing turbines with scroll baffles would require a great deal of modification to the gas turbine.

A new approach proposed herein is to interface directly with the combustion cans of the gas turbine. Figure 67 shows a cutaway of a typical large gas turbine used for power generation in an NGCC plant. The combustion cans

are located concentrically around the turbine. The combustion can itself can be removed from the turbine casing with relative ease, making it a relatively easy point to modify with minimal broader modifications.

Figure 68 examines the combustion can more closely. The compressed gas from the compressor flows primarily through an annular region before reaching the far end of the can, where it turns in towards the center of the combustion chamber where the natural gas burning occurs.

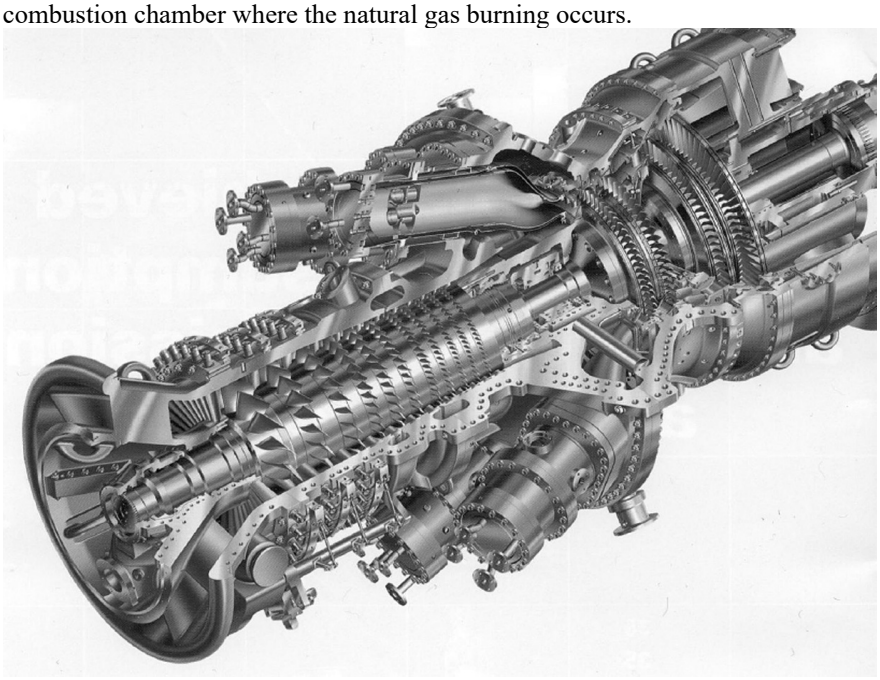

Figure 67: Cross section of typical gas turbine. [114]

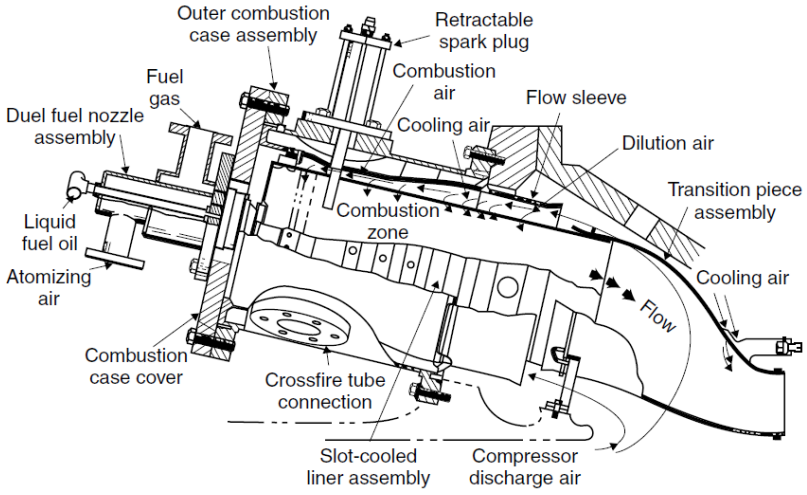

Figure 68: A typical reverse-flow diffusion can-annular combustor. [114]

Figure 69 shows a high-level diagram of how FIRES may interface with the concentrically located combustion cans of a gas turbine. A custom double-walled torus may replace the individual combustion cans and fit into the same locations within the turbine casing. The compressed "cold" annular flow of the combustion can instead flow in the outer annulus of the torus, shown as blue. The outer torus transitions to a thick insulation-lined pipe that delivers the compressed air to FIRES. After appropriate mixing the return pipe feeds into the inner torus and delivers ~1500°C air to the turbine through the same flow path as the traditional combustion can.

Different portions of the torus may be insulated as needed with ceramic to lower requirements on the metal. In the immediate site of the turbine interface, bare metal will be exposed to approximately 1500°C gas, with colder air of approximately 500°C gas flowing annularly to keep the walls cool.

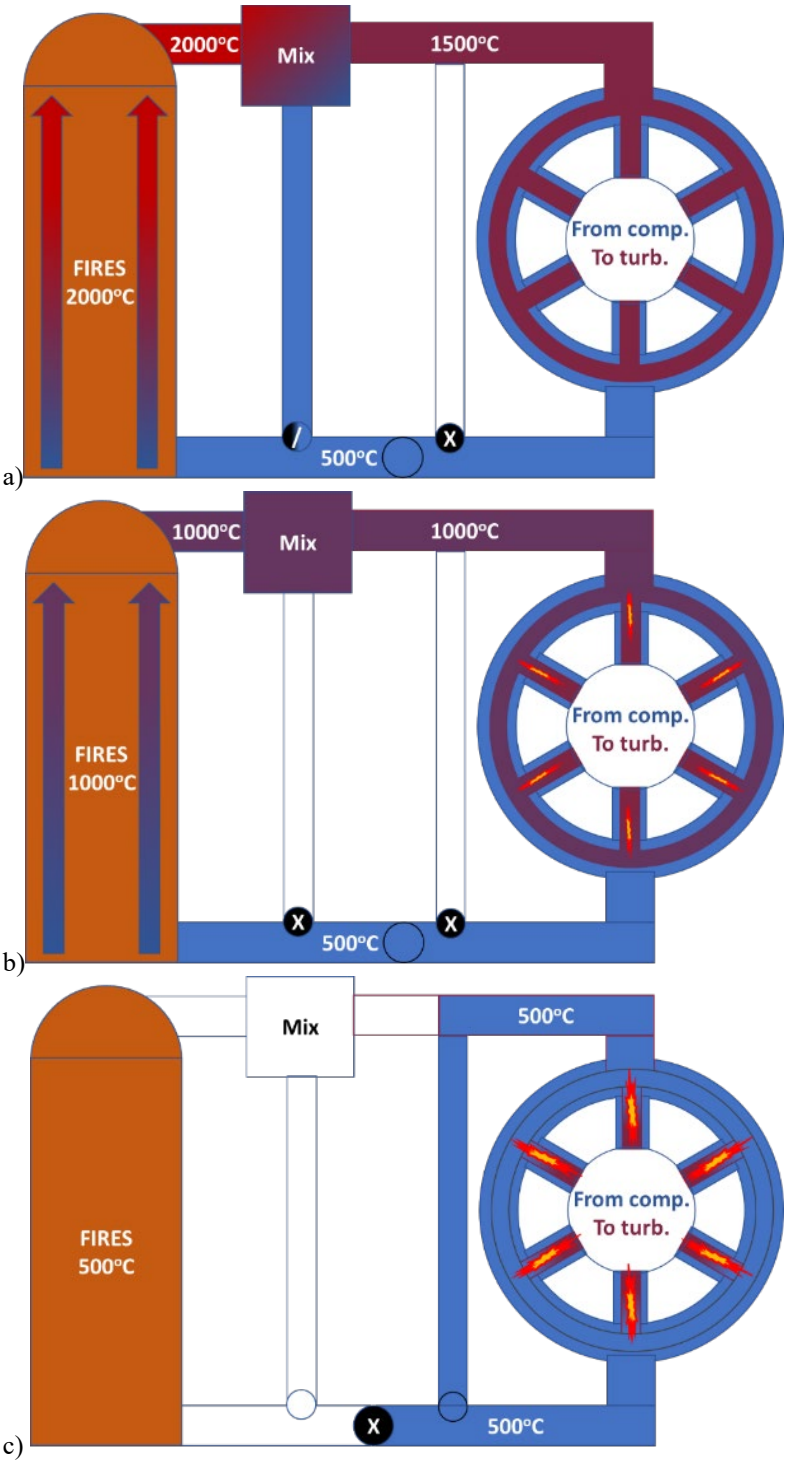

Figure 69: Interface and operating mode of FIRES with a natural gas turbine.
a): FIRES provides all heat to the gas turbine, with no combustion required. b): FIRES provides partial heat to the turbine, with a weak natural gas flame making up the balance. c): The flow bypasses FIRES and the turbine is fully fired by natural gas.

When FIRES cools down, there may be the option to inject gas to increase the temperature as needed (Figure 69b). This would depend on the specific requirements of stable flame operation and emissions controls when burning at preheated conditions. Alternatively, complete transition to natural gas may be made, or FIRES may solely run the turbine at increasingly lower part load as it depletes. When FIRES is fully cooled (Figure 69c), the flow path to FIRES

may be bypassed to avoid the pressure loss, and solely natural gas may be used when desired, for assured capacity to the grid.

Further research is required to address the challenges of the double-walled torus. One challenge involves the dilution ports typically used to keep the walls cool when they are exposed to flame temperatures. Dilution ports in the present design may significantly cool the air coming from FIRES and reduce the turbine efficiency. On the other hand, operation with natural gas without dilution ports may place serious burdens on the metal walls and may pose issues of viability. One answer to this challenge may simply be a lower operating temperature when burning natural gas. The lower efficiency may be acceptable given the societal goals of phasing out natural gas, and given the broader advantages of this configuration, i.e., the arbitrage between heat sources, and the option to run the power plant as a zero-carbon "renewable heat" facility. Whether the facility will operate predominantly with FIRES or with natural gas may inform whether dilution ports are included.

11.5 Usage of FIRES in other applications

Cement and iron production are discussed in detail here due to their unique importance and challenge in the context of decarbonization: high share of global CO_2 emissions and high process temperatures. Other applications such as glass and ceramics production, metal heat treating, coking and chemical processing may also be adapted to use FIRES heating instead of fossil fuels.

FIRES may also be used to run lower-temperature industrial processes, such as boilers in most steam-driven industrial processes. The integration with most steam systems is expected to be relatively simple because the FIRES stream may be a closed loop that passes through a heat exchanger with the steam feedwater system. The steam systems operate at temperatures near 600^{o}C or lower, such that the very high storage temperatures of FIRES are not required from an operational perspective; commercially available heaters may be effectively used for the same purpose as electrically conductive bricks [2]. However, the high storage temperatures of a DRH-style FIRES unit create a higher energy density system, which may yield a cost advantage over other options. The need for less thermal storage material may reduce shipping costs and space costs. Whether the DRH-style FIRES concept is a winning option for decarbonizing steam-driven industries likely depends on the ratio of traditional (less expensive) firebricks to conductive (more expensive) firebricks in the system.

11.6 Summary of retrofits and modifications to applications

General points and approaches of modifying and retrofitting industrial applications with FIRES were discussed. Existing hot blast stoves come in customizable shapes and sizes. FIRES applications will generally be higher temperature and, in the case of gas turbine applications, higher pressure, which will require thicker steel, and thicker and higher temperature insulation.

FIRES may replace all the fossil fuels used for precalcining and sintering in cement kilns, preventing approximately 45-50% of CO_2 emissions. A baffle that may direct air into FIRES from the grate cooler, and the inclusion of recirculated CO_2 or particulate for increased radiative heat transfer are two key modifications necessary, as are ports that allow FIRES heat to flow into the precalciner and rotary kiln. It is believed FIRES can replace near 60% coke consumption in blast furnace operation, and prevent 60% of CO_2 emissions. FIRES may simply be installed at the outlet of the hot blast stoves. The piping that feeds the hot blast through the furnace tuyeres may need improved insulation to account for the higher inlet temperatures provided by FIRES.

There is promise that FIRES may be retrofitted to existing natural gas power plants with a relatively simple modification to the combustion can assembly. The development of a component similar to the double-walled torus shown herein may avoid more costly modifications to the broader turbine assembly and components.

The use of FIRES in each application requires some degree of modification to mature, capital-intensive technologies, which may generally be considered risky or expensive by the respective industry. However, in the context of societal goals and pressure to combat climate change by phasing out fossil fuels, the changes outlined herein to electrify these processes appear relatively non-disruptive.

12 Conclusions

12.1 Summary of work

A high-temperature firebrick resistance-heated energy storage (FIRES) concept based on electrically conductive firebricks may be used to convert low-carbon electricity at times of low prices into high-temperature stored heat to provide on-demand heat at temperatures comparable to fossil fuels. FIRES may be used to replace fossil fuels in high-temperature, high-emissions industrial processes such as iron and cement production, or it may be used to run a fossil fuel power plant with no emissions and roundtrip efficiencies of 60% or more. This approach to energy storage shows promise for solving problems of decarbonization in the electricity sector as well as the industrial heating sector at lower cost than other electricity storage or low-carbon heating options, such as Li-ion batteries or renewable H_2 production. The present work has attempted to advance the commercialization of this technology by systematically developing the concept, from materials design and fabrication, to performance simulations, and application of results to system design and retrofit considerations.

Fundamental physics and design considerations of joule-heating devices were presented with a focus on extrinsic semiconductors. The role of the resistivity-temperature derivative (RTD) in charge stability and failure modes was related to extrinsic semiconductor properties, such as dopant level and small or large polaron mobility. Evaluation of different high-temperature ceramic options that may constitute the basis of an electrically conductive firebrick was based on these insights and other consideration, such as thermal and chemical stability, industrial maturity, and cost. Chromium oxide (chromia), nickel oxide and zinc oxide were identified as top candidates. Chromia was selected for the focus of experimental efforts due to its existing use as a refractory ceramic.

Experimental efforts with chromia were undertaken to understand the prospects of directly resistance-heating a freely stacked mass of chromia firebricks. Electrical resistivity measurements of some commercial chromia firebricks, as well as fabrication, resistivity measurements and experimentation with doped chromia firebricks were undertaken. Temperature-dependent values of electrical resistivity and brick-brick contact resistivity were obtained, and DRH experimentation was conducted on a small stack as a proof of concept. The material RTD significantly decreased at temperatures above 250°C, coinciding with the onset of exhaustion of dopant activation. With a small applied pressure, brick-brick contact resistance became equivalent to 1-2 cm of bulk resistance with the same electrical flow area. This result was found to be nearly constant with temperature. The DRH experiments exposed the stack to ramp rates and heat generation rates similar to commercial heating elements, with no apparent deterioration of the material during the 30 minute testing periods. Temperatures only reached approximately 600°C in these tests due to limits of the insulation surrounding the sample.

Calculations and simulations were performed to contextualize the experimental results with respect to charging conditions of interest. Key questions concerned whether or not temperatures would significantly rise at the brick-brick contact during charging, and whether short circuit failure might occur in the event of an uneven temperature profile. Relations were derived to calculate contact supertemperature and short circuit failure outcomes based on the desired starting temperature, ending temperature, ramp rate, system geometric parameters, and material properties of the firebrick. Contact supertemperature was kept to reasonable temperatures of 3-13°C for typical brick geometry and operating conditions, which presents manageable temperature gradients for the ceramic. The stable conductive width that avoids short circuit failure was found to be 2-20cm depending on the temperature. The small length scale shows that a FIRES system as imagined herein would not be passively stable during charging, since the stable length scale of the conductive flow path is much smaller than typical firebrick dimensions, and smaller than the width of a large brickwork, typically several meters wide. Thermal runaway simulations were conducted to explore the evolution of an uneven temperature profile during charge cycles, with an allowed period of thermal equilibration during each cycle. Using finite difference methods on a 1-D chromia slab without air volume, conductive widths of 0.25-0.50m were found to be cyclable without significant thermal runaway, depending on the starting temperature and allowable equilibration time.

Conceptual designs for large electrically conductive brickworks was presented. Designs of a “snaking” electrically conductive flow path used conductive bricks and insulating firebricks to construct a brickwork several meters wide while maintaining an equivalent solid conductive width similar to the 0.25-0.50m widths found workable in the simulations. The comparison of the brickwork dimensions and the simulated 1-D solid conductive width dimension was made with the simplifying assumption that radiative heat transfer across channels has negligible resistance at most temperatures of interest. The designs proposed are workable using firebricks with dimensions

similar to commercial firebricks. One important feature of the designs not accounted for in thermal runaway simulations is the effect of the insulating firebrick regions, which are relatively substantial in size due to the relative scale of bricks: potentially 30-45% of the thermal mass of the system. However, at the present level of conceptual design, the indicators are positive for proving a design that is both stable and high-performance. Thermal equilibration may be dramatically improved by designing bricks with "windows" between channels for a sufficient radiative view factor that allows radiative heat transfer throughout the conductive width. Inlet temperature control via preheating is another option for expanding the viability of FIRES to lower-temperature application inputs.

The retrofits and modifications necessary to apply FIRES to some industrial processes were discussed. Hot blast stoves are customizable in size and shape relative to the heating demands of a given application, up a approximately 2 GWh for the largest vessels. Improved insulation and a thicker steel vessel will be required for the higher temperatures and pressures of FIRES. Reduction of CO_2 emissions in iron and cement production may be between 45 and 60%. Radiative heat transfer in the flowing FIRES gas may be improved by recirculating a combination of CO_2 and particulate matter of the process. In gas turbine applications, a double-walled torus component may be installed in place of the traditional gas combustion cans. The component allows flow to and from the turbine system without serious modifications. The technical developments necessary to realize these modifications are, in the view of the author, relatively minor with respect to the potential impact.

12.2 Future work

The work herein has attempted to identify and address a breadth of questions and challenges in developing the DRH-style FIRES system. Lab-scale fabrication of small high-purity samples and 1-D simulations of conductive firebrick slabs are only starting points for proofing the technological viability of FIRES. The next steps toward commercialization the technology must include a three-prong effort.

The first prong is further materials development. Commercial viability will likely require industrial-grade bulk powder mixing to produce the bricks rather than the Pechini sol-gel method. Tests of commercial chromia bricks and review of the literature suggest that samples of reasonable performance and uniformity may be achieved by bulk powder mixing. Samples of chromia alumina mixtures that demonstrate long term air stability at high temperature is also necessary. Failure to achieve this would likely require a pivot to another material option. Once the bricks are proven, a small laboratory facility that contains electrically conductive brick stack in a vessel with flowing gas may be tested as a prototype.

The second prong is more sophisticated simulations, in a commercial 3-D multi-physics framework. Simulation of charge and discharge cycling are instrumental to the iteration of design and proving robust operation and stability in a variety of perturbations, such as uneven gas flow and uneven brick properties. Radiative heat transfer through the brickwork is a key missing component in the present work, which becomes particularly important as more complex brick geometries are considered for the specific needs of a FIRES system. Lateral electrical flow through the electrode regions, and the heating of the different regions as a function of different electrical properties must also be explored in detail.

The third prong is the development of relationships with the industrial players, governmental institutions and regulatory bodies necessary for the adoption of the FIRES technology. Collaborative efforts are necessary to develop the technology for the easy retrofit to existing processes. The owners of power plants, cement kilns, and blast furnaces, as well as the manufacturers of the equipment, must be aligned regarding the goal of technology adoption. This alignment may be aided by governmental offices, such as National Energy Technology Laboratory (NETL), and office of Energy Efficiency and Renewable Energy (EERE), which are concerned with technologies that may decarbonize manufacturing processes and fossil energy systems. This third prong of action must be taken alongside the other two if FIRES is to become more than an academic endeavor.

13 Appendix material

13.1 Tests of commercial silicon carbide samples

Because of the maturity of SiC as both commercial heater and a firebrick, early work explored the prospects of using SiC-based firebricks for construction of a DRH-style FIRES unit. Samples of two commercial SiC bricks provided by HWI were explored: HARBIDE and NISIC 20, shown in Figure 70. The test results eliminated SiC-based firebricks as a top candidate, due mostly to challenges of oxidation and poor indicators of brick-brick contact resistance based on room temperature measurements. Electrical resistivity measurements at room temperature and elevated temperatures were taken with methods very similar to those discussed in Section 5.1. Only the main points of the results are summarized here.

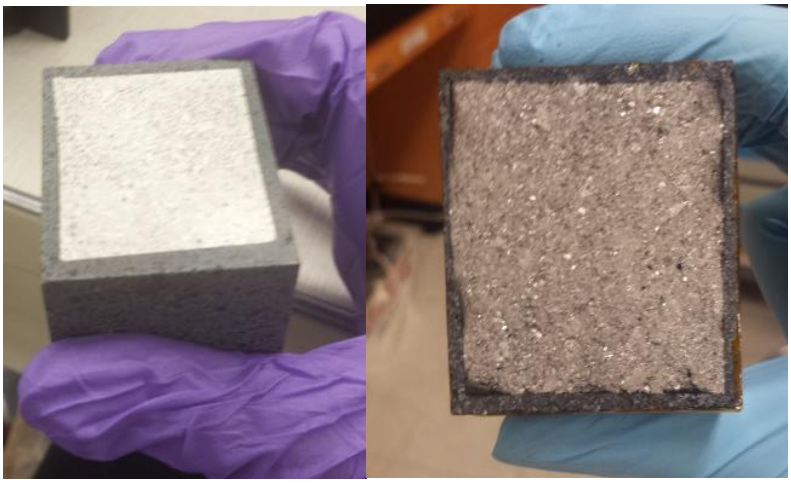

Figure 70: Platinized samples of NISIC 20 (left) and HARBIDE (right), provided by HWI.

13.1.1 HARBIDE results and discussion

Figure 71 shows room temperature electrical resistance measurements as a function of load for bare and platinized HARBIDE, pressed between two metal foils. Even at maximum load of 2000 lb (4500 kPa), the bare brick result is nearly double the platinized result, indicating large contact resistance. This is markedly different from the behavior of the SERV 95 DC, where the platinized and bare brick results were within a few percent of one another above a 1000 lb load. A two-brick stack of HARBIDE was found to be approximately a factor 25 more resistive than the sum of the individual bricks, corresponding to an equivalent resistor length of approximately 2 meters. This is a factor 100 larger than that found for SERV 95 DC at room temperature load tests and for lab-fabricated chromia samples at high temperature.

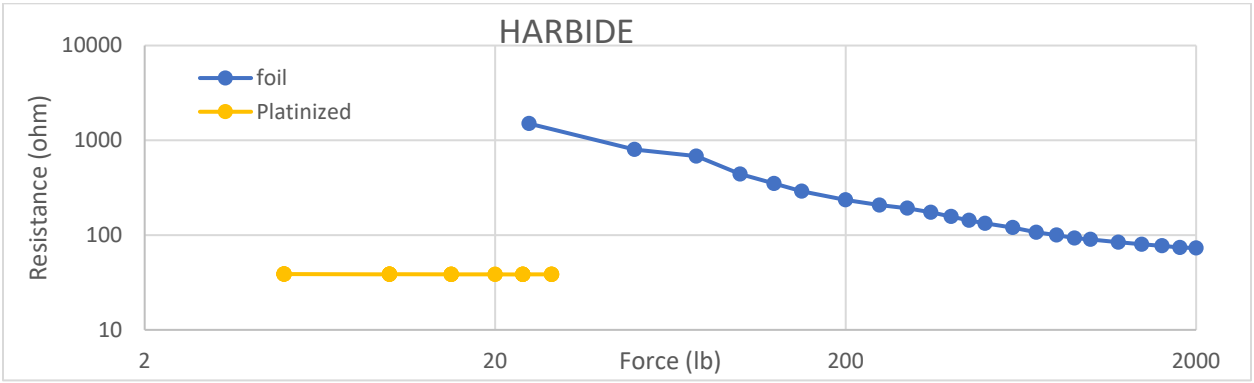

Figure 71: Measured electrical resistance versus load of bare and platinized HARBIDE.

The first furnace-heated resistivity measurements were conducted manually with a HARBIDE sample, shown in Figure 72. ramping at 200ºC/hour with a soak period for 30 minutes every 100ºC, or until a settled resistance value was observed. Though the test was originally intended to reach 1500ºC, during the first heat-up, resistivity of the sample began to climb exponentially while soaking at 500ºC. The sample was allowed to soak at 500ºC for one hour until cool-down was initiated. The sample room temperature resistivity was a factor 50 larger than before. The second heat-up was conducted in a similar fashion, until again 500ºC was reached, at which time the sample was left to soak for 72 hours, with one measurement taken every 24 hours.

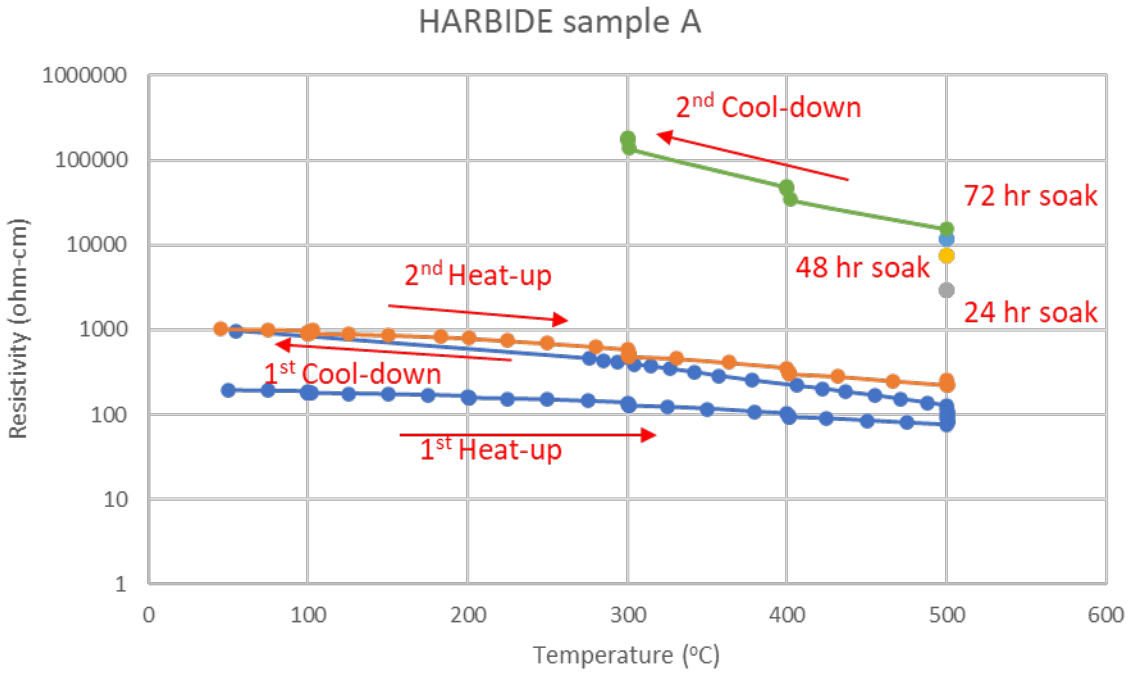

Figure 72: Resistivity versus temperature of HARBIDE up to 500ºC over a customized ramp/soak operation. Resistivity increased while at constant temperature due to development of oxidized layer below the platinized surface.

Oxidation of the SiC to SiO_2 below the platinized surface was the cause of the rising resistivity, apparently activate at 500ºC. The second cool-down shows an Arrhenius resistivity-temperature behavior characteristic of SiO_2 and most other insulating oxide materials. In contrast, the first heat-up of HARBIDE was markedly flat, suggesting that this commercial SiC composition may have been doped in such a way that resulted in favorable electrical properties with a low-temperature extrinsic region. No further investigations into HARBIDE were conducted due to the relatively low-temperature surface oxidation challenges.

13.1.2 NISIC 20 results and discussion

To avoid the effort of platinizing SiC bricks that would ultimately oxidize in the furnace, NISIC 20 bricks were heated and measured at room temperature several times before conducting furnace measurements. Each heating was conducted at 1200ºC for 12 hours. Figure 73 shows NISIC 20 electrical resistance measurements and mass gain over several heating cycles.

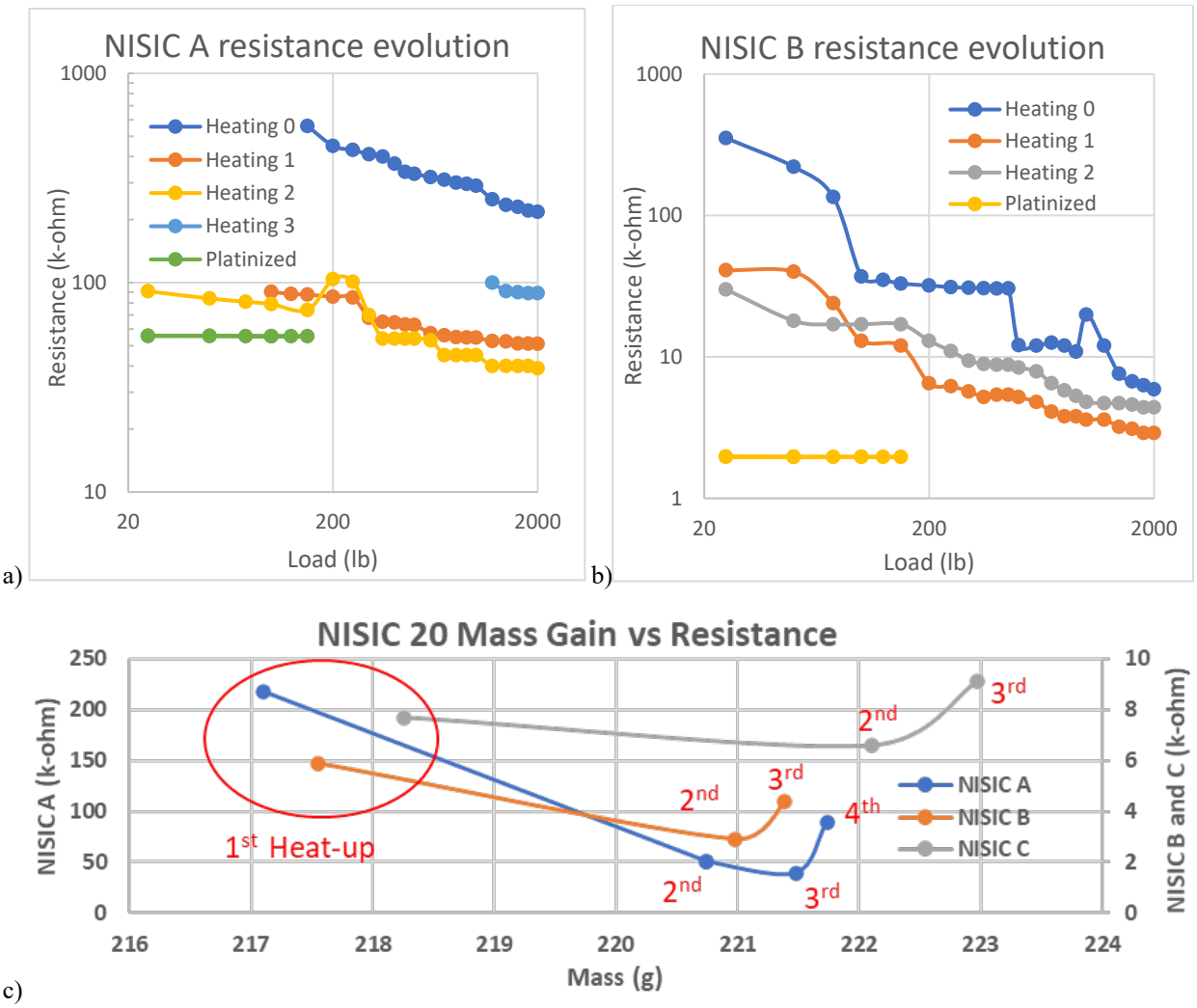

Figure 73: NISIC 20 electrical resistance measurements and mass gain over several heating cycles.
a): Measured resistance versus load of bare and platinized sample A. b): Measured resistance versus load of bare and platinized sample B. c): Mass gain and resistivity change for samples A, B, and C.

Similar to HARBIDE, NISIC 20 resistance was also found to be approximately 50-100% greater than the platinized result (note: samples were platinized after the final heating, such that platinized results should be compared to the final heating result). Again, the brick-brick contact resistance of the sample was more than an order of magnitude higher than the individual bricks. Where samples B and C individually summed to 13 k-ohm at 2000 lb, the stack of B and C measured over 1.125 M-ohm – the limit of the ohmmeter used in the tests – indicating a factor 100 or more increase, or 4 meter L_{eq}.

Unlike HARBIDE, NISIC 20 did not become exponentially more resistive when heated, and initially became more conductive. The resistance to forming an insulative SiO_2 layer is likely due to the 20% Si_3N_4 content of NISIC 20 (hence the name). Other noteworthy features of the samples tested was a large variance in resistivity values, approximately a factor of 5-10 between samples A, B and C. The source of variance is not hypothesized herein.

Because NISIC 20 was more resistive to oxidation, the samples were platinized and prepared for in-furnace measurement. Figure 74 shows electrical resistivity as a function of temperature of NISIC 20. Unlike HARBIDE, the NISIC 20 behavior was found to be exponential with temperature, and very similar to results published by Chiochetti and Henry [115].

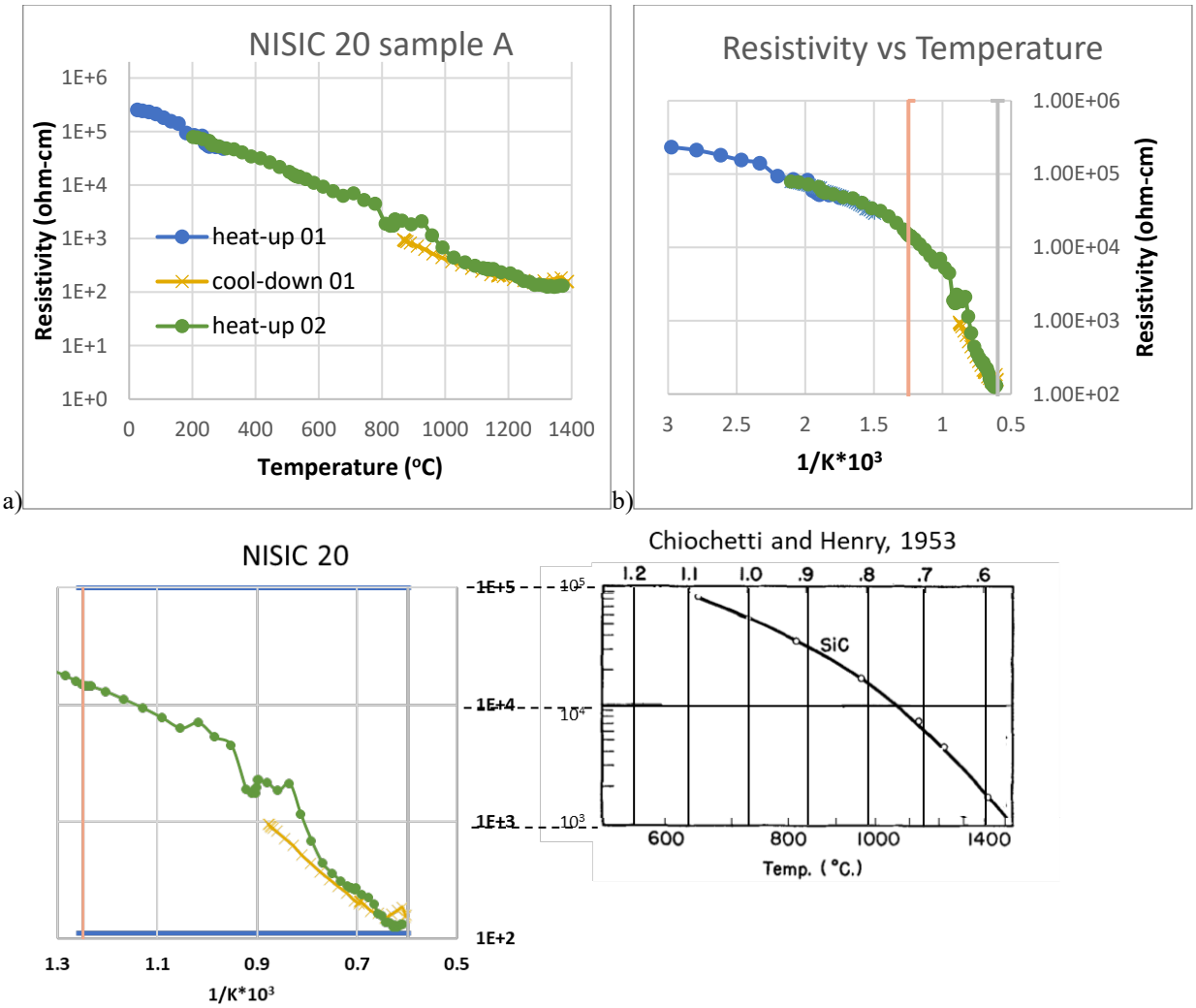

Figure 74: Resistivity versus temperature of NISIC 20.
a) resistivity versus linear temperature. b) resistivity versus Arrhenius temperature (inverted). c) Aligned comparison of this work (left), and Chiochetti and Henry [115].

It may yet be possible to form a freely stacked electrical circuit using a nitride-bonded SiC brick that resists oxidation, if challenges of doping the multi-phase mixture can be overcome. This is not trivial if the mechanism for oxidation protection is the formation of a highly resistive Si_3N_4 layer. It would also require a much larger factor of reduction in brick-brick contact resistance at high temperatures than what was seen in the chromia samples. Nitride-bonded SiC was not investigated further given these challenges.

14 References

1. United Nations, *Paris Agreement*. 2015.
2. Stack, D.C., D. Curtis, and C. Forsberg, *Performance of firebrick resistance-heated energy storage for industrial heat applications and round-trip electricity storage.* Applied Energy, 2019. **242**: p. 782-796.
3. Cole, W. and A.W. Frazier, NREL, *Cost projections for utility-scale battery storage*. 2019.
4. Schmidt, O., et al., *The future cost of electrical energy storage based on experience rates.* Nature Energy, 2017. **2**(8).
5. Friedmann, S.J.F., Zhiyuan; Tang, Ke, *LOW-CARBON HEAT SOLUTIONS FOR HEAVY INDUSTRY, SOURCES, OPTIONS, AND COSTS TODAY.* 2019.
6. Kanthal, *Resistance heating alloys and systems for industrial furnaces*, Sandvik. 2011.
7. Kanthal, *Kanthal Silicon Carbide Electric Heating Elements*, Sanvik.
8. Kanthal, *Kanthal Super Electric heating elements*, in *Products and accessories*, Sandvik. 2012.
9. Denholm, P., et al., NREL, *Overgeneration from solar energy in California - a field guide to the duck chart*. 2015.
10. MIT, *The Future of Solar Energy*. 2015.
11. Denholm, P. and R. Margolis, NREL, *Energy Storage Requirements for Achieving 50% Penetration of Solar Photovoltaic Energy in California*. 2016.
12. Blanke, A., CAISO, *2019 Q3 Report on Market Issues and Performance*. 2019.
13. Schmidt, O., et al., *Projecting the Future Levelized Cost of Electricity Storage Technologies.* Joule, 2019. **3**(1): p. 81-100.
14. DOE, *Quadrennial Technology Review: An assessment of energy technologies and research opportunities*. 2015.
15. LLNL, *Estimated U.S. Energy Consumption in 2018: 101.2 Quads*. 2018; Available from: https://flowcharts.llnl.gov/content/assets/images/charts/Energy/Energy_2018_United-States.png.
16. EIA, *Annual Energy Outlook 2020 with projectons to 2050*. 2020.
17. Agora Verkehrswende, Agora Energiewende and Frontier Economics, *The future cost of electricity-based synthetic fuels*. 2018.
18. EIA, *International Energy Outlook 2019*, in *With projections to 2050*. 2019: https://www.eia.gov/ieo.
19. IEA, *The challenge of reaching zero emissions in heavy industry*. 2020; Available from: https://www.iea.org/articles/the-challenge-of-reaching-zero-emissions-in-heavy-industry.
20. Gil, A., et al., *State of the art on high temperature thermal energy storage for power generation. Part 1—Concepts, materials and modellization.* Renewable and Sustainable Energy Reviews, 2010. **14**(1): p. 31-55.
21. Forsberg, C.W., et al., *Converting excess low-price electricity into high-temperature stored heat for industry and high-value electricity production.* The Electricity Journal, 2017. **30**(6): p. 42-52.
22. Stack, D., et al. *Conceptual Design and Market Assessment of Firebrick Resistance Heated Energy Storage (Fires)-Avoiding Wind and Solar Electricity Price Collapse to Improve Nuclear, Wind, and Solar Economics*. in *International Congress Advanced Nuclear Power Plants (ICAPP), San Francisco, CA, Apr*. 2016.
23. Laing, D. and S. Zunft, *Using concrete and other solid storage media in thermal energy storage (TES) systems*, in *Advances in Thermal Energy Storage Systems*. 2015. p. 65-86.
24. Willmott, A.J., Thermopedia, *REGENERATIVE HEAT EXCHANGERS.*
25. Danieli Corus, *IRONMAKING AND STEELMAKING - Hot Blast Stoves*. 2021 [cited 2021 18 January]; Available from: https://www.danieli.com/en/products/products-processes-and-technologies/hot-blast-stoves_26_69.htm.
26. Stupich, M., Wikipedia, *Blast furnace (left), and three Cowper stoves (right) used to preheat the air blown into the furnace*. 1989; Available from: https://en.wikipedia.org/wiki/Hot_blast.
27. China Household Electrical Appliances Association, *China's coal-to-electricity policy to further boost market growth, setting central heating a new trend*. 2018 [cited 2021 18 January]; Available from: https://en.cheaa.org/contents/476/7689.html.
28. Siemens Gamesa, *Electric Thermal Energy Storage (ETES)*. 2021 [cited 2021 13 January]; Available from: https://www.siemensgamesa.com/en-int/products-and-services/hybrid-and-storage/thermal-energy-storage-with-etes.
29. Zhou, C., Shanghai Institute of Applied Physics, *Current energy situation & application prospect of FIRES in China*. 2017, TMSR-SINAP-CAS.

30. Dimplex, *VFMQ Storage Heaters*. 2013 [cited 2021 18 January]; Available from: https://www.dimplex.com/en/page.php?id=27&p=819&s=59.
31. Mitsubishi Heavy Industries, *MHI Achieves 1,600°C Turbine Inlet Temperature in Test Operation of World's Highest Thermal Efficiency "J-Series" Gas Turbine*. 2011 [cited 2021 13 January]; Available from: https://www.mhi.com/news/1105261435.html#:~:text=World's%20Highest%20Thermal%20Efficiency%20%22J%2DSeries%22%20Gas%20Turbine&text=Tokyo%2C%20May%2026%2C%202011%20%2D,J%2DSeries%22%20gas%20turbine.
32. Deshmukh, Y.V., *Electric Resistance Heating*, in *Industrial Heating: Principles, Techniques, Materials, Applications, and Design*. 2005, Taylor & Francis Group: Boca Raton, FL.
33. Thermcraft Inc., *ELECTRICAL RESISTANCE HEATING ELEMENTS: AN OVERVIEW*. 2016.
34. Pieper, R.J. and S. Michael, *Comprehensive Analytical Approach to Predicting Freeze-Out and Exhaustion for Uniform Single-Impurity Semiconductors in Equilibrium.* IEEE Transactions on Education, 2005. **48**(3): p. 413-421.
35. Pieper, R.J. and S. Michael, *An exact analysis for freeze-out and exhaustion in single impurity semiconductors*. 2005: Proceedings of the 2005 American Society of Engineering Education Annual Conference.
36. Arca, E., et al., *Valence band modification of Cr2O3 by Ni-doping: creating a high figure of merit p-type TCO.* Journal of Materials Chemistry C, 2017. **5**(47): p. 12610-12618.
37. Streetman, B.G. and S.K. Banerjee, *Solid State Electronic Devices*, ed. V. O'brien. 2006: Pearson Prentice Hall.
38. Zeghbroeck, B.V., *Principles of Semiconductor Devices*. 2011.
39. Lany, S., *Semiconducting transition metal oxides.* J Phys Condens Matter, 2015. **27**(28): p. 283203.
40. Naik, I.K. and T.Y. Tien, *Small-polaron mobility in nonstoichiometric cerium dioxide.* J Phys Chem Solids, 1978. **39**: p. 5.
41. Bosman, A.J. and H.J. van Daal, *Small-polaron versus band conduction in some transition-metal oxides.* Advances in Physics, 1970. **19**(77): p. 1-117.
42. Gnesin, G.G., V.K. Zakharenkov, and L.A. Shipilova, *VOLUME ELECTRICAL RESISTIVITY OF SILICON CARBIDE HEATING ELEMENTS.* Poroshkovaya Metallurgiya, 1978. **1**: p. 6.
43. Lely, J.A. and F.A. Kroger, *Optical Properties of Pure and Doped SiC.* Semiconductors and Phosphors, 1958.
44. Pelissier, K., T. Chartier, and J.M. Laurent, *Silicon Carbide Heating Elements.* Ceramics International, 1998. **24**: p. 7.
45. Prot, D. and C. Monty, *Self-diffusion in α–Al2O3. II. Oxygen diffusion in 'undoped' single crystals.* Philosophical Magazine A, 2006. **73**(4): p. 899-917.
46. Bosman, A.J. and C. Crevecoeur, *Mechanism of the Electrical Conduction in Li-Doped NiO.* Physical Review, 1966. **144**(2): p. 763-770.
47. Nagaraja, A.R., et al., *Band or Polaron: The Hole Conduction Mechanism in the p-Type Spinel Rh2ZnO4.* Journal of the American Ceramic Society, 2012. **95**(1): p. 269-274.
48. Hensler, J.R.H., E.C., *Electrical Resistance of Some Refractory Oxides and Their Mixtures in the Temperature Range 600 to 1500 C.* Journal of the American Ceramic Society, 1953. **36**(3): p. 8.
49. Park, S.J.K., H.G., *Electrical Conductivity and Defect Models of MgO-Doped Cr2O3.* Journal of the American Ceramics Society, 1988. **71**(3): p. 4.
50. Nagai, H., T. Fujikawa, and K. Shoji, *Electrical Conductivity of Cr2O3 Doped with La2O3, Y2O3 and NiO.* Transactions of the Japan Institute of Metals, 1983. **24**(8): p. 8.
51. Bennett, J.P., et al., *AN ANALYSIS OF THE CAUSES OF FAILURE IN HIGH CHROME OXIDE REFRACTORY MATERIALS FROM SLAGGING GASIFIERS.* DOE/NETL-IR-2006-183, 2006.
52. Bennett, J.P. and K.-S. Kwong, *Failure Mechanisms in High Chrome Oxide Gasifier Refractories.* Metallurgical and Materials Transactions A, 2011. **42**(4): p. 888-904.
53. Martienssen, W. and H. Warlimont, *Springer Handbook of Condensed Matter and Materials Data*. 2005: Springer Berlin Heidelberg.
54. Harbison-Walker, *Harbison-Walker Handbook of Refractory Practice*. 2005: HarbisonWalker International.
55. Muan, A. and S. Somiya, *Phase Equilibrium Studies in the System Iron Oxide-Al2O3-Cr2O3.* Journal of the American Ceramic Society, 1959. **42**(12): p. 11.
56. Crawford, J.A. and R.W. Vest, *Electrical Conductivity of Single-Crystal Cr2O3.* Journal of Applied Physics, 1964. **35**(8): p. 2413-2418.

57. Park, J.H. and K. Natesan, *Electronic Transport in Thermally Grown Cr2O3.* Oxidation of Metals, 1990. **33**: p. 24.
58. Kehoe, A.B., et al., *Assessing the potential of Mg-doped Cr(2)O(3) as a novel p-type transparent conducting oxide.* J Phys Condens Matter, 2016. **28**(12): p. 125501.
59. Arca, E., M.A. McInerney, and I.V. Shvets, *Band alignment at the interface between Ni-doped Cr2O3 and Al-doped ZnO: implications for transparent p-n junctions.* J Phys Condens Matter, 2016. **28**(22): p. 224004.
60. Chen, Z. and K. Colbow, *MgO-doped Cr2O3, solubility limit and the effect of doping on the resistivity and ethanol sensitivity.* Sensors and Actuators, 1992. **9**: p. 5.
61. Arca, E., et al., *Effect of Chemical Precursors On the Optical and Electrical Properties of p-Type Transparent Conducting Cr2O3:(Mg,N).* The Journal of Physical Chemistry C, 2013. **117**(42): p. 21901-21907.
62. HUANG, R.F., A.K. AGARWAL, and H.U. ANDERSON, *Oxygen activity dependence of the electrical conductivity of Li-doped Cr2O3.* Journal of the American Ceramic Society, 1983. **67**(2): p. 5.
63. CALLISTER, W.D., et al., *Sintering Chromium Oxide with the Aid of TiO2.* Journal of the American Ceramic Society, 1979. **62**(3-4): p. 4.
64. Nagai, H. and K. Ohbayashi, *Effect of TiO2 on the Sintering and the Electrical Conductivity of Cr2O3.* Journal of the American Ceramic Society, 1989. **72**(3): p. 4.
65. GRAHAM, H.C.D., H.H, *Oxidation and Vaporization Kinetics of Cr2O3.* Journal of the American Ceramic Society, 1971. **54**(2): p. 5.
66. Hirata, T., K. Akiyama, and H. Yamamoto, *Sintering behavior of Cr2O3-Al2O3 ceramics.* Journal of the European Ceramic Society 2000. **20**: p. 5.
67. Prostakova, V., et al., *Experimental study and thermodynamic optimization of the CaO–NiO, MgO–NiO and NiO–SiO2 systems.* Calphad, 2012. **37**: p. 1-10.
68. Lin, Y., et al., *Polarization of High-Permittivity Dielectric NiO-Based Ceramics.* Journal of the American Ceramic Society, 2005. **88**(7): p. 1808-1811.
69. Ismail, A.A. and D.W. Bahnemann, *Photochemical splitting of water for hydrogen production by photocatalysis: A review.* Solar Energy Materials and Solar Cells, 2014. **128**: p. 85-101.
70. Zaleska, A., *Doped-TiO2: a Review.* Recent Patents on Engineering, 2008. **2**(3).
71. Hitosugi, T., et al., *Properties of TiO2-based transparent conducting oxides.* physica status solidi (a), 2010. **207**(7): p. 1529-1537.
72. Baumard, J.F. and E. Tani, *Electrical conductivity and charge compensation in Nb doped TiO2 rutile.* The Journal of Chemical Physics, 1977. **67**(3).
73. Özgür, Ü., et al., *A comprehensive review of ZnO materials and devices.* Journal of Applied Physics, 2005. **98**(4).
74. Janotti, A. and C.G. Van de Walle, *Fundamentals of zinc oxide as a semiconductor.* Reports on Progress in Physics, 2009. **72**(12).
75. ZIEGLER, E., et al., *Electrical Properties and Non-Stoichiometry in ZnO Single Crystals.* physica status solidi (a), 1981. **66**: p. 14.
76. TAKATA, M., D. TSUBONE, and H. YANAGIDA, *Dependence of Electrical Conductivity of ZnO on Degree of Sintering.* Journal of the American Ceramic Society, 1976. **59**(1-2): p. 5.
77. Du, M.-H. and S.B. Zhang, *Impurity-bound small polarons in ZnO: Hybrid density functional calculations.* Physical Review B, 2009. **80**(11).
78. MOHAPATRA, S.K. and F.A. KROGER, *Defect Structure of α-Al2O3 Doped with Magnesium.* Journal of the American Ceramic Society, 1976. **60**(3-4): p. 8.
79. MOHAPATRA, S.K. and F.A. KROGER, *Defect Structure of a-Al2O3 Doped with Titanium.* Journal of the American Ceramic Society, 1977. **60**(9-10): p. 8.
80. BROOK, R.J., J. YEE, and F.A. KROGER, *Electrochemical Cells and Electrical Conduction of Pure and Doped Al2O3.* Journal of the American Ceramic Society, 1971. **54**(9): p. 8.
81. WARMAN, J.M., et al., *ELECTRONIC PROCESSES IN SEMICONDUCTOR MATERIALS STUDIED BY NANOSECOND TIME-RESOLVED MICROWAVE CONDUCTIVITY-III. A12O3, MgO and TiO2 POWDERS.* Radiat. Phys. Chem., 1991. **37**(3): p. 10.
82. Shluger, A.L., et al., *Theoretical simulation of localized holes in MgO.* J. Phys: Condens. Matter, 1992. **4**: p. 12.
83. Stoneham, A.M., *Small polarons and polaron transitions.* J. Chem. Soc., Faraday Trans. 2, 1989. **85**(5): p. 12.

84. Shluger, A.L. and A.M. Stoneham, *Small polarons in real crystals: concepts and problems.* J. Phys.: Condens. Matter, 1993. **5**: p. 39.
85. French, R.H., *Electronic band structure of Al2O3, with comparison to AlON and AlN.* Journal of the American Ceramic Society, 1990. **73**(3): p. 13.
86. Varley, J.B., et al., *Role of self-trapping in luminescence andp-type conductivity of wide-band-gap oxides.* Physical Review B, 2012. **85**(8).
87. Smith, J.G., et al., *Intrinsic Conductivity in Magnesium–Oxygen Battery Discharge Products: MgO and MgO2.* Chemistry of Materials, 2017. **29**(7): p. 3152-3163.
88. Kosacki, I., et al., *Electrical conductivity of nanocrystalline ceria and zirconia thin films.* Solid State Ionics 2000(136-137): p. 9.
89. Chang Ho Lee and G.M. Choi, *Electrical conductivity of CeO2-doped YSZ.* Solid State Ionics 2000(135): p. 9.
90. Badwal, S.P.S., *Electrical conductivity of single crystal and polycrystalline yttria-stabilized zirconia.* JOURNAL OF MATERIALS SCIENCE 1984. **19**: p. 10.
91. Chu, S.H. and M.A. Seitz, *The ac electrical behavior of polycrystalline ZrO2-CaO.* Journal of Solid State Chemistry, 1978. **23**: p. 18.
92. Quemener, V., *Electrical Characterization of Bulk and Thin Film Zinc Oxide*. 2012, University of Oslo. p. 106.
93. Praveen, C.S., V. Timon, and M. Valant, *Electronic band gaps of ternary corundum solid solutions from Fe2O3–Cr2O3–Al2O3 system for photocatalytic applications: A theoretical study.* Computational Materials Science, 2012. **55**: p. 192-198.
94. Schonberger, U. and F. Aryasetiawan, *Bulk and surface electronic structures of MgO.* Phys Rev B Condens Matter, 1995. **52**(12): p. 8788-8793.
95. Siddique, M.N., A. Ahmed, and P. Tripathi, *Electric transport and enhanced dielectric permittivity in pure and Al doped NiO nanostructures.* Journal of Alloys and Compounds, 2018. **735**: p. 516-529.
96. Lany, S., *Band-structure calculations for the 3dtransition metal oxides inGW.* Physical Review B, 2013. **87**(8).
97. Hutson, A.R., *Hall Effect Studies of Doped Zinc Oxide Single Crystals.* Physical Review, 1957. **108**(2): p. 222-230.
98. Look, D.C., et al., *Electrical properties of bulk ZnO.* Solid State Communications, 1997. **105**(6): p. 3.
99. Koch, S., *Contact resistance at ceramic interfaces and its dependence on mechanical load.* Solid State Ionics, 2004. **168**(1-2): p. 1-11.
100. Timsit, R.S., *Electrical Contact Resistance: Fundamental Principles*, in *Electrical Contacts: Principles and Applications*, P.G. Slade, Editor. 2014, Taylor & Francis Group: Boca Ranton, FL.
101. Dimesso, L., *Pechini Processes: An Alternate Approach of the Sol–Gel Method, Preparation, Properties, and Applications*, in *Handbook of Sol-Gel Science and Technology*. 2016. p. 1-22.
102. ROY, S.N., S.R. SAHA, and S.K. GUHA, *Sintering kinetics of pure and doped chromium oxide.* Journal of Materials Science, 1986. **21**: p. 4.
103. Holt, A. and P. Kofstad, *Electrical conductivity and defect structure of Cr2O3. II. Reduced temperatures (below 1000°C).* Solid State Ionics, 1994. **69**: p. 7.
104. Lu, T.J. and N.A. Fleck, *Thermal Shock Resistance of Solids.* Acta materialia, 1998. **46**(13): p. 14.
105. Andreades, C., et al., *Reheat-Air Brayton Combined Cycle Power Conversion Design and Performance Under Nominal Ambient Conditions.* Journal of Engineering for Gas Turbines and Power, 2014. **136**(6).
106. Zetterholm, J., *Modelling of a Hot Stove for the Blast Furnace.* Luleå University of Technology, 2014. **M.S. Thesis**.
107. Danieli Corus, *Danieli Corus: Once in a Lifetime*, in *Product Brochure*.
108. Aksyushin, M., et al., *Improvement of the energy efficiency of hot blast stove performance*, in *Advanced Methods and Technologies in Metallurgy in Russia*, C. Brebbia and J. Connor, Editors. 2018, Springer.
109. Institute for Industrial Productivity, *Blast Furnace System*. [cited 2021 January 19]; Available from: http://www.iipinetwork.org/wp-content/Ietd/content/blast-furnace-system.html.
110. Akhtar, S.S., et al., *From coal to natural gas - Its impact on kiln production, Clinker quality and emissions.* IEEE Cement Industry Technical Conference 2013, 2013.
111. Rissman, J., et al., *Technologies and policies to decarbonize global industry: Review and assessment of mitigation drivers through 2070.* Applied Energy, 2020. **266**.
112. World Coal Association, *How is steel produced?* [cited 2021 January 21]; Available from: https://www.worldcoal.org/coal/uses-coal/how-steel-produced.

113. Min, J.K., et al., *High temperature heat exchanger studies for applications to gas turbines.* Heat and Mass Transfer, 2009. **46**(2): p. 175-186.
114. Boyce, M.P., *Advanced industrial gas turbines for power generation*, in *Combined Cycle Systems for Near-Zero Emission Power Generation*. 2012. p. 44-102.
115. Chiochetti, V.E.J. and E.C. Henry, *Electrical Conductivity of Some Commercial Refractories in the Temperature Range 600° to 1500°C.* Journal of the American Ceramic Society, 1953. **36**(6): p. 5.